

Académie de Nantes

ECOLE DOCTORALE DE L'UNIVERSITÉ DU MAINE
LE MANS, FRANCE

THÈSE DE DOCTORAT
Spécialité : ACOUSTIQUE

présentée par

Philippe TESTUD

pour obtenir le titre de Docteur d'Université

**AÉRO-ACOUSTIQUE DES DIAPHRAGMES EN CONDUIT:
SIFFLEMENT ET CAVITATION**

Soutenue le 20 octobre 2006

devant le jury composé de :

Y. AURÉGAN	Chargé de recherche au CNRS, LAUM, Le Mans	directeur de thèse
J. BORÉE	Professeur des Universités, LEA, Poitiers	examineur
E. DE LANGRE	Professeur des Universités, LadHyX, Palaiseau	président du jury
A. HIRSCHBERG	Professeur des Universités, TU/e, Eindhoven (Pays-Bas)	examineur
D. JUVÉ	Professeur des Universités, ECL, Lyon	rapporteur
J. KERGOMARD	Directeur de Recherche au CNRS, LMA, Marseille	rapporteur
P. MOUSSOU	Ingénieur-chercheur, EDF R&D, Clamart	examineur

Remerciements

La réalisation d'une thèse me semble proche d'un accouchement (expérience que j'aurai par ailleurs rarement l'occasion de connaître). Il s'agit d'avoir une idée originelle, puis de lui donner vie scientifiquement. Sans vouloir risquer la comparaison trop loin, il est indéniable que la réalisation technique est un travail personnel, mais qui doit beaucoup aux indispensables personnes qui l'encadrent et l'accompagnent... J'ai plaisir ici à témoigner ma gratitude à ces personnes, comme il est de coutume dans cette sorte d'éloge funèbre pour la thèse (cependant encore vivante) qu'est cette partie remerciements.

Pour la soutenance de thèse, je remercie M. Jacques Borée d'avoir accepté d'être membre du jury, et M. Emmanuel De Langre d'avoir accepté d'être président du jury. De même, je remercie M. Daniel Juvé et M. Jean Kergomard d'avoir accepté la difficile tâche d'être rapporteur de la thèse. Leur relecture et leurs remarques m'ont permis d'améliorer la version finale du manuscrit.

Ce travail a été effectué au Laboratoire de Mécanique des Structures Industrielles Durables, UMR-CNRS EDF 2832. Je remercie Stéphane Andrieux de m'avoir permis de travailler dans ces bonnes conditions de travail. Je remercie Géraldine, dont la compétence, la disponibilité et la gentillesse sont très appréciables au quotidien. Je la remercie notamment de m'avoir aidé au moment délicat de la préparation de la soutenance de thèse. Pendant les deux dernières années, j'ai passé de bien bons moments parmi les thésards du LaMSID: Docteur Sam, Thomas le gentil barbare, Josselin oeil-de-lynx, Khaled futur ministre (mektub), Amine artiste-philosophe, Pierre-Emmanuel l'homme aux 36 projets, Benjamin le Normand et Mohammed. Je pense qu'un livre d'entretien entre PE et Amine, sorte d'aperçu des plus grands débats qu'on a eus à table, serait un best-seller assuré (et si Khaled fait la préface, alors là!). Bon courage à vous tous pour votre dernière année de thèse!

Au sein du groupe T63 règne une ambiance très conviviale. Il y est particulièrement agréable d'y travailler. Je remercie les agents du groupe, et en particulier Michel qui y est pour beaucoup je pense. Ce fut un plaisir de travailler avec Sébastien, Philippe, Fabien, et de cotôyer les autres membres du groupe (je leur fais confiance, ils se reconnaîtront: j'évite ici une liste trop longue, pénible à lire pour le lecteur impatient et tendu qui n'aurait pas encore trouvé son nom...). A AMA, je remercie particulièrement Pierre Sans pour ses précieux conseils en informatique (notamment pour arriver à manipuler la mystérieuse et délicate LADY).

Je remercie Yves, mon directeur de thèse, pour la haute qualité technique et la fiabilité de son encadrement. C'est un privilège pour un expérimentateur d'utiliser la boucle de mesure du LAUM,

facile d'utilisation et permettant d'obtenir des données de très bonne qualité.

Je remercie Mico pour sa profonde gentillesse et le soutien précieux qu'il apporte, tant scientifiquement qu'humainement. Entre autres choses, sa capacité d'être présent dans les moments difficiles a été exceptionnelle, et je lui en suis particulièrement reconnaissant. Ce fut agréable et instructif de travailler avec quelqu'un d'aussi passionné par la science, avec une approche originale, à la fois ludique et rigoureuse. Je remercie Monique, Lionel et Michel pour leur accueil, et les nombreux repas sympathiques que nous avons partagés chez eux à Veldhoven. Je souhaite une très bonne continuation à Lionel et à Michel.

Enfin, je remercie Pierre qui a été mon responsable quasi-quotidien durant ces trois années à EDF. Ce fut un enrichissement et un plaisir. Si la thèse s'est bien passée, et représente pour moi une expérience constructive, c'est avant tout grâce à lui. Au quotidien, j'ai apprécié les discussions agréables, intéressantes et motivantes. D'un point de vue technique, sa vigilance, sa rigueur, son enthousiasme et sa curiosité scientifiques (amoindris pour les corrections de bout) m'ont été très profitables.

J'arrive maintenant, et en même temps que le lecteur se rend compte avec perspicacité de la gradation progressive, à cet ultime paragraphe. Il me reste donc à remercier les amis indéfectibles, Éric, Thierry, Vincent, Mél, Laurent, Perrine, Lorena, Zag, et les autres que je n'ai pas oubliés en fait (le lecteur déçu de ne pas voir son nom pourra donc se mettre dans cette liste, ou la précédente d'ailleurs, cela me va bien aussi). Et enfin pour terminer, je remercie, et beaucoup plus encore, mes parents et mes deux sœurs, pour tout leur soutien et leur amour.

PS: comme ceci est dit dans le genre 'Repose en paix, thèse...', je précise, si besoin est, que cette thèse ne doit pas être enterrée sur-le-champ (ou pire, utilisée comme cale... celle-ci est trop épaisse de toute façon).

Contents

Introduction générale	1
1 Experimental study of a whistling criterion for singularities in air pipe flow	5
1.1 Introduction	5
1.1.1 Motivations	5
1.1.2 Abstract	5
1.2 Bibliography introduction to self-sustained oscillations in confined flow	6
1.2.1 Aeroacoustics	6
1.2.2 Plane-wave propagation in duct with uniform mean flow	6
1.2.3 Self-sustained oscillations	8
1.3 Presentation of the whistling criterion	11
1.3.1 Configuration of study: a singularity in straight pipe under constant flow	11
1.3.2 Elaboration of the whistling criterion	11
1.3.3 Formulation of the whistling equations	13
1.4 Measurements configurations	18
1.4.1 Experimental set-up of the LAUM	18
1.4.2 Measurement procedures	20
1.5 The whistling criterion on circular centred orifices	23
1.5.1 Orifices tested	23
1.5.2 Scattering matrix coefficients	26
1.5.3 Potentially whistling frequencies	29
1.5.4 Strouhal numbers	30
1.5.5 Conditions of whistling for the incident waves	39
1.5.6 Non-dimensional potentially whistling eigenvalues	42
1.6 The whistling criterion on other singularities	44
1.6.1 Importance of the bevel for the whistling of orifices	44
1.6.2 Smile shaped slits	49
1.7 Whistling configurations	51
1.7.1 Whistling configuration	51
1.7.2 Comparison between whistling frequencies and potentially whistling frequencies	51
1.7.3 Comparison between whistling frequencies in air and in water	53
1.7.4 A model to predict the instability frequency	56
1.7.5 A failed model to predict the instability with Bode-Nyquist idea	61

1.8	Broadband noise	65
1.8.1	Broadband spectra	65
1.8.2	Lighthill scaling laws	65
1.9	Conclusion	68
2	Aeroacoustical behaviour of a single expansion with the multimodal method	75
2.1	Introduction	75
2.2	Analytical problem	76
2.2.1	Problem to solve	76
2.2.2	Geometry and flow hypothesis	76
2.2.3	Assumption of non-expansion of the main flow	76
2.2.4	Equations of the problem	77
2.2.5	Method of resolution	78
2.2.6	Solutions: acoustic, evanescent and hydrodynamic modes	79
2.2.7	Determination of the scattering matrix	81
2.3	The multimodal method	82
2.3.1	Imposed flow profile	82
2.3.2	Schlichting turbulent pipe flow profile	82
2.3.3	Comparison of the two flow profiles	83
2.3.4	Discretization of the variables	83
2.3.5	Derivatives expressions in the finite difference scheme	84
2.3.6	Discretized equations	85
2.3.7	Modes determination in duct I	86
2.3.8	Modes determination in duct II	87
2.3.9	Numerical classification of the modes	88
2.3.10	Scattering matrix determination	90
2.4	Single expansion calculations	92
2.4.1	Modes obtained in duct I and duct II	92
2.4.2	Convergence results	99
2.4.3	Visualization of the excited fields	101
2.4.4	Difficulties in the calculation	108
2.5	Single expansion results	110
2.5.1	Results without flow: comparison with a model	110
2.5.2	Results with flow: comparison with experimental data	112
2.5.3	Transition to unstable hydrodynamic mode	120
2.5.4	Comparison between circular and rectangular duct	121
2.6	Conclusion	124
3	Aeroacoustical behaviour of a whistling expansion	129
3.1	Introduction	129
3.2	Configuration studied	129
3.3	Experimental results: the configuration is potentially whistling	130
3.4	Description of the numerical calculation method	130

3.4.1	Scattering matrix of the constriction	132
3.4.2	Scattering matrix of the double expansion with the multimodal method	135
3.4.3	Scattering matrix of the double expansion: method by assemblage of successive matrices	135
3.4.4	Scattering matrix of the double expansion: method by direct calculation	137
3.5	Validation of the calculations	138
3.5.1	Comparison with experimental data - without flow	138
3.5.2	Comparison with experimental data - with flow	140
3.5.3	Effect of the saturation of the unstable hydrodynamic mode	144
3.6	Whistling ability of the configuration	147
3.6.1	Whistling ability of the configuration	147
3.6.2	Comparison with the whistling ability of a single expansion configuration	149
3.6.3	Parametric study on the Strouhal number	151
3.7	Conclusion	156
4	Noise generated by cavitating single-hole and multi-hole orifices in a water pipe	161
4.1	Introduction	161
4.1.1	Motivations	161
4.1.2	Literature	161
4.2	Experimental set-up	164
4.2.1	Tested orifices	164
4.2.2	Test rig	165
4.2.3	Experimental conditions	166
4.2.4	Distinction of two cavitation regimes	167
4.2.5	Acoustic analysis method	168
4.2.6	Acoustic boundary conditions on both sides of the orifice	169
4.3	Cavitation regimes	170
4.3.1	Hydraulic model for the pressure drop ΔP across the single-hole orifice	170
4.3.2	Hydraulic model for the pressure drop ΔP across the multi-hole orifice	174
4.3.3	Developed cavitation visualization and time signal	176
4.3.4	Whistling phenomenon in developed cavitation	178
4.3.5	Super cavitation visualization and typical time signal	180
4.4	Results in the developed cavitation regime	181
4.4.1	Acoustic features	182
4.4.2	Noise spectra generated downstream	183
4.4.3	Nondimensional analysis and representation	186
4.5	Results in the super cavitation regime	188
4.5.1	Acoustic features	188
4.5.2	Noise spectra generated downstream	190
4.6	Conclusion	191

5	End correction of single expansions and orifices	197
5.1	Introduction	197
5.2	End correction: single expansion without flow	197
5.2.1	Model of end correction: single expansion without flow	197
5.2.2	Determination of the end correction from multimodal calculation: single expansion without flow	198
5.2.3	Literature data: single expansion without flow	199
5.2.4	Numerical results: single expansion without flow	200
5.3	End correction: orifice without flow	202
5.3.1	Determination of the end correction from measurements: orifice without flow	202
5.3.2	Literature data and models: orifice without flow	202
5.3.3	Experimental results: orifice without flow	203
5.4	End correction: single expansion with flow	207
5.4.1	Model of end correction: single expansion with flow	207
5.4.2	Determination of the end correction from measurements: single expansion with flow	207
5.4.3	Literature data: single expansion with flow	207
5.4.4	Numerical results: single expansion with flow	208
5.5	End correction: orifice with flow	208
5.5.1	Determination of the end correction from measurements: orifice with flow	208
5.5.2	Models using literature data: orifice with flow	208
5.5.3	Experimental results: orifice with flow	209
5.6	Conclusion	212
	Conclusion générale	214
	A Measurements on orifices: potentially whistling frequencies	221
	B Measurements on double orifices: potentially whistling frequencies	235
	C Acoustical propagation equations under sheared mean flow	241
	D Demonstration of the continuity of the acoustic variables at the expansion	245
	D.1 Continuity of the acoustic variables	245
	D.2 Continuity of the derivatives of the acoustic variables	246
	E Acoustic analysis method	247

Introduction générale

Contexte de l'étude

Des obstacles d'écoulement de type diaphragmes (vanne, robinet, ...) sont présents dans les tuyaux de centrales nucléaires d'EDF, afin de contrôler ou mesurer le débit sur une ligne. Sous de forts débits d'écoulement, cette perturbation de l'écoulement peut engendrer un bruit important, d'origine aéroacoustique, c'est à dire non pas engendré par les vibrations des structures, mais par les fluctuations inhomogènes instationnaires qui se développent dans les régions de fortes turbulences en aval proche de l'obstacle.

Ces bruits peuvent être de plusieurs types:

- dans tous les cas, un bruit de turbulence apparaît, prenant naissance dans la région de fortes turbulences résultant de la déstabilisation de l'écoulement par l'organe en aval proche du diaphragme;
- en écoulement d'eau, un bruit de cavitation peut être observé. Il correspond à l'implosion de bulles de vapeur et d'air, issues de la vaporisation du liquide dans les zones de fortes fluctuations locales de pression, en aval proche du diaphragme. Ce phénomène de cavitation intervient lorsque les conditions hydrauliques sont particulièrement fortes, c'est à dire lorsque la différence de pression statique de part et d'autre du diaphragme est particulièrement importante (dizaines de bar);
- dans certaines conditions, des sons de sifflement peuvent être observés, en eau ou en air, et en conditions de fonctionnement industrielle à EDF. Le sifflement correspond à l'auto-entretien (c'est à dire, entretien par l'écoulement lui-même) d'une amplification d'une fluctuation acoustique au niveau de la couche cisailée qui se forme par contraction de l'écoulement au passage du diaphragme, auto-entretenu.

Au sein d'EDF R&D, ces bruits aéro-acoustiques sont étudiés afin de limiter, d'une part, la fatigue vibratoire des tuyaux, et d'autre part, le bruit engendré dans les installations et à l'extérieur des installations. Les bruits les plus nocifs de ce point de vue sont les bruits de cavitation et de sifflement. Ainsi, des études sont menées à EDF R&D sur le bruit causé par des singularités d'écoulement en conduit. Les travaux de la présente thèse s'inscrivent dans ce cadre.

Cadre de l'étude

L'objectif de ce travail est de mieux comprendre les mécanismes de génération de bruit par les singularités en conduit sous écoulement. Nous avons étudié principalement le bruit de sifflement

(chapitres 1 à 5). Des analyses approfondies de bruits de cavitation ont été également effectuées (chapitre 4).

La configuration d'étude est un tuyau droit sous écoulement uniforme et stationnaire, passant au travers d'une singularité d'écoulement. Les conditions d'écoulement étudiées sont les suivantes:

- l'écoulement est turbulent, avec un nombre de Reynolds dans le tuyau de l'ordre de 10^4 à 10^5 ;
- l'écoulement est subsonique, avec un nombre de Mach dans le tuyau de l'ordre de 10^{-3} en eau, et 10^{-2} en air.

Les singularités d'écoulement étudiées sont majoritairement les diaphragmes circulaires centrés et fins (chapitre 1). Nous avons également étudié des diaphragmes multitrou (chapitre 4) et des fentes (chapitre 1).

Les vibrations de structures sont négligées dans cette étude.

Plan de l'étude

Rappels

Le phénomène de sifflement est une auto-oscillation entretenue par un phénomène de rétroaction. Cette auto-oscillation résulte de l'amplification d'une instabilité de type Kelvin-Helmholtz, c'est à dire une instabilité d'une couche de cisaillement formée par décollement de l'écoulement, apparaissant en aval immédiat du diaphragme. Cette instabilité est caractéristique du jet qui se forme par contraction de l'écoulement au niveau du diaphragme. On parle de fréquence d'instabilité de couche de cisaillement.

Chapitre 1

L'idée du chapitre 1 est de tester expérimentalement un critère de prédiction des fréquences d'instabilité d'une singularité sous écoulement. Ce critère est proposé par Aurégan & Starobinsky (1999), et nous appliquons en propagation d'ondes planes dans les tuyaux.

Ce critère est un bilan de puissance acoustique global effectué de part et d'autre du diaphragme. Il repose sur la représentation en matrice de diffusion du comportement acoustique du diaphragme soumis à des ondes planes incidentes. C'est l'hypothèse d'un comportement acoustique linéaire du diaphragme. Les fréquences d'instabilité de ce critère sont comparées, également par nos mesures, à des fréquences de sifflement effectivement observées. Ainsi, le critère peut être validé et permet d'obtenir des fréquences potentielles de sifflement d'une singularité sous écoulement.

Pour cela, nous utilisons la boucle de mesure du LAUM (Laboratoire d'Acoustique de l'Université du Maine, Le Mans) en air. La validation de cette boucle de mesure a été effectuée précédemment (cf. thèse de Grégoire Ajello, 1997)) et a montré que les données acoustiques obtenues sous écoulement constant sont parmi les plus précises actuellement (au moins dans la gamme de fréquence 30-800 Hz).

Les géométries les plus simples sont testées pour commencer cette étude: des diaphragmes monotrou, circulaires centrés, et fins. D'autres singularités sont testées par la suite, dans une plus faible mesure: diaphragmes biseautés, fentes.

Chapitres 2 et 3

Le travail expérimental mené au chapitre 1 apporte des données quantitatives sur le sifflement, mais a besoin d'être enrichi, et c'est l'objet des chapitres 2 et 3. En effet, le critère étudié dans le chapitre 1 se place assez loin du diaphragme, et ne permet pas de comprendre ce qui se passe localement, au niveau de la zone de développement de l'instabilité. C'est l'objet d'une étude d'une configuration précise, une expansion sifflante, constituée par un diaphragme biseauté en aval suivi d'un double élargissement brusque. Un calcul numérique est ainsi développé pour simuler le comportement aéroacoustique de cette configuration, pour mieux comprendre le phénomène d'instabilité et l'importance de la zone d'amplification. L'objectif est d'obtenir la matrice de diffusion de cette singularité, afin de pouvoir appliquer le critère de sifflement et le comparer aux résultats expérimentaux. L'objectif est aussi en complément d'obtenir une visualisation des champs acoustiques dans la configuration, pour mieux comprendre ce qu'il s'y passe.

La première étape dans le calcul numérique est de valider la méthode multimodale. Cela est effectué en appliquant le calcul à un élargissement brusque. C'est l'objet du chapitre 2. Les résultats obtenus sont comparés aux données expérimentales (Ronneberger) et numériques (Boij) de la littérature. Cette étape permet d'étudier et de valider cette méthode sur une configuration simple.

Le chapitre 3 présente l'application de la méthode multimodale à une configuration de diaphragme sifflante. Les résultats obtenus sont comparés aux données expérimentales que nous avons mesurées pour cette configuration. L'analyse des résultats permet de mieux comprendre l'importance de la zone d'amplification, et notamment l'évolution de la fréquence d'instabilité en fonction des paramètres géométriques de cette zone.

Le développement d'un critère d'instabilité, suivi d'une compréhension plus fine du mécanisme d'instabilité, forme une base cohérente permettant de mieux appréhender le phénomène de sifflement de diaphragme en conduit. En pratique, d'autres problèmes se posent et nous avons complété cette étude par deux études supplémentaires, constituées par les chapitres 4 et 5.

Chapitre 4

En eau, le phénomène de sifflement peut apparaître en présence de cavitation, comme cela est observé par des mesures industrielles. Il est intéressant de confronter les résultats obtenus en air au chapitre 1 avec ces sifflements obtenus en condition industrielle en eau. C'est l'objet du chapitre 4.

Pour cela, nous analysons des expériences précédemment menées à EDF, sur des diaphragmes monotrou et multitrou. Les conditions de débit et de pression sont typiques du régime de fonctionnement de centrale nucléaire (nombre de Reynolds de l'ordre de 10^5). Les spectres de bruit obtenus dans ces conditions de cavitation sont aussi analysés.

Chapitre 5

Les phénomènes de sifflement sont liés à des résonances de conduit, et la prise en compte de la correction de longueur pour un diaphragme sous écoulement permet d'affiner le calcul de ces fréquences de résonance. C'est l'objet du chapitre 5 d'étudier ce modèle de correction de longueur.

Nous étudions le modèle de correction de longueur sur des diaphragmes et des élargissements brusques. Nous utilisons les données expérimentales présentées au premier chapitre sur les diaphragmes,

et nous utilisons la méthode numérique présentée aux chapitres 2 et 3, sur un élargissement brusque. Les données obtenues sont comparées aux données disponibles dans la littérature, concernant le comportement acoustique des diaphragmes sans écoulement et le comportement aéro-acoustique des terminaisons de tuyau.

L'objectif de cette étude est de vérifier, dans le cas sans écoulement, la validation des résultats de la littérature avec nos données expérimentales et théoriques, et d'autre part, de présenter nos données expérimentales avec écoulement, données qui sont rares dans la littérature.

Nota Bene

Les chapitres ont été rédigés en anglais par commodité pour la collaboration avec les étudiants de l'Université Technique d'Eindhoven (chapitre 2 et 3), et dans l'optique de la rédaction de publication dans une revue internationale (chapitre 1).

Collaborations

Cette thèse est une collaboration entre, d'une part, le Laboratoire d'Acoustique de l'Université du Maine (LAUM, UMR CNRS 6613) au Mans, et l'entreprise EDF. La direction de la thèse a été assurée par Yves Aurégan du LAUM.

Le thésard a effectué sa thèse au sein d'EDF R&D (Clamart), dans le Département AMA, groupe T63: 'Acoustique, vibrations sous écoulement et dynamique des machines', et dans le Laboratoire de Mécanique des Structures Industrielles Durables (LaMSID, UMR CNRS 2832).

De plus, une collaboration a été entretenue tout au long de la thèse avec Mico Hirschberg de l'Université Technique d'Eindhoven (Pays-Bas). Nous avons également pu y discuter de la méthode multimodale avec Gerben Koojmann (thésard).

Chapter 1

Experimental study of a whistling criterion for singularities in air pipe flow

1.1 Introduction

1.1.1 Motivations

Whistling is sometimes observed in piping systems of nuclear plants, in duct with water (see the study of whistling orifices in water at chapter five). It may drive pipe vibrations, and thus can damage the structure. The study of whistling provides information to understand the phenomenon, to predict its occurrence, and to design safe orifices and other singularities.

The present experimental work is carried out in air, as it is expected that the whistling phenomenon is similar in air and in water (hypothesis that we evaluate in this work). The main differences should be the occurrence of cavitation and a stronger coupling with the pipe walls (due to the higher compressibility) in water.

1.1.2 Abstract

An experimental study on the acoustic response of single-hole orifices under constant flow is presented, assuming plane wave propagation in the ducts. An energetic criterion derived by Aurégan and Starobinsky (1999) is used to predict, from the measured scattering matrix, the conditions under which whistling could occur. The idea is to apply an energetic acoustic balance from both sides of the singularity to detect the so-called potentially whistling frequencies for which there is production of acoustic power by the singularity. Results obtained are compared with experimental data from literature (Anderson), and from other experiments at EDF in water (presented in chapter 4).

1.2 Bibliography introduction to self-sustained oscillations in confined flow

1.2.1 Aeroacoustics

Acoustics is the study of sound: its generation, transmission and reception. Aeroacoustics is a branch of acoustics: it is the study of the sound generated in a fluid flow, when interacting with a solid surface or with another flow. It is a relatively young discipline, considered as born in the 1950's after Lighthill's work.

The fundamental issue of aeroacoustics is that the noise is constituted of acoustic fluctuations which have amplitudes compared to the main flow pressure and velocities, which is itself quite difficult to know as fluid mechanics equations are not solvable in a general case. No complete theory of the generation of noise by aerodynamic flows has yet prevailed until now. However, the so-called aeroacoustic analogies are an efficient way to study most practical aeroacoustic issues. An analogy consists in writing the acoustic equations under some assumptions, in a form similar to the wave equation of classical acoustics, so that propagation terms and source terms can be unambiguously identified.

In theory, an infinite number of analogies can exist, but by far the most common and widely used is Lighthill's aeroacoustic analogy, first proposed by James Lighthill (1952) when noise generation associated with the jet engine was beginning to be placed under scientific scrutiny. This theory is consequently particularly adapted to study the noise generated by a turbulent flow. It assumes that the sound is produced by the instationary inhomogeneities of the fluctuations in the flow, that is, the local fluctuations in space and time of the flow. In other terms, the quiescent flow is taken as the reference flow, where no sound is created.

In this work, we are concerned with a particular noise, different from a purely turbulent one: the whistling, associated with self-sustained oscillations. This is an exotic phenomenon, encountered sometimes in everyday life (human whistling, whistler), but also in duct flow of nuclear plants.

1.2.2 Plane-wave propagation in duct with uniform mean flow

We present briefly the equations describing the acoustic propagation in the plane wave approximation for an isentropic and constant mean flow. More details can be found in Rienstra and Hirschberg (2003), Ajello (1997), Davies (1988), Pierce (1981).

First, we suppose the mean flow to be uniform, of Mach number $\mathbf{M}_0 = \frac{U_0}{c_0} \mathbf{e}_x$, where U_0 is the flow velocity, \mathbf{e}_x is the unitary vector in the direction of the duct and orientated in the flow way (see Fig. 1.2), and c_0 is the speed of sound in the fluid.

Second, we neglect any visco-thermal dissipation effects.

To determine the acoustic propagation, the acoustic variables are defined as first order of the total fluid mechanics variables, and denoted ρ' (acoustic volume density), p' (acoustic pressure), \mathbf{u}' (acoustic velocity). Hence equations of propagation for the acoustic field are given by the first order of fluid mechanics equations applied to the total flow:

- the acoustic mass conservation equation:

$$\frac{D_0 \rho'}{Dt} = -\rho_0 \operatorname{div}(\mathbf{u}'); \quad (1.1)$$

- the acoustic momentum conservation equation:

$$\rho_0 \frac{D_0 \mathbf{u}'}{Dt} = -\mathbf{grad} p'; \quad (1.2)$$

- the fluid constitutive law:

$$c_0^2 = \frac{p'}{\rho'}, \quad (1.3)$$

where $D_0/Dt = \partial/\partial t + \mathbf{U}_0 \cdot \mathbf{grad}$ is a specific convective derivative. It is used conveniently due to the assumptions of the mean flow: uniform, incompressible and stationary (so that the terms $grad(\mathbf{U}_0)$, $div(\mathbf{U}_0)$ and $\partial \mathbf{U}_0/\partial t$ vanish in the first order equations).

The combination of those previous equations gives the general equation of acoustic propagation. Written for the acoustic pressure, it takes the form:

$$\Delta p' - \frac{1}{c_0^2} \frac{D_0^2 p'}{Dt^2} = 0, \quad (1.4)$$

completed by a boundary equation, such as the rigidity of the duct walls.

The solutions of this equation are found by looking for harmonic solutions at the pulsation frequency ω . A denumerable set of solutions is obtained, and called modes. This set of modes represents a basis in the space of solutions. The modes are either propagative either evanescent. In particular, below the so-called cut-off frequency of the duct, only the first mode propagates, while the other are evanescent. This first mode is the plane wave mode. For this mode, the acoustic variables are only function of x and ω and satisfy the propagation equation (this writing is particular to a uniform, incompressible, stationary mean flow):

$$\left[(1 - M_0) \frac{\partial}{\partial x} - j k_0 \right] \left[(1 + M_0) \frac{\partial}{\partial x} + j k_0 \right] p' = 0, \quad (1.5)$$

with $k_0 = \omega/c_0$ the wave number in a quiescent fluid.

The solution of this equation is constituted by two plane waves, so that the acoustic pressure p' in the duct is the sum of the two plane waves: $p' = P^+ + P^-$, with:

- a downstream propagating wave P^+ :

$$P^+ = P^+(0) e^{j(\omega t - k^+ x)}, \quad (1.6)$$

where $k^+ = k_0/(1 + M_0)$ is the downward wave number under constant flow M_0 ;

- an upstream propagating wave P^- :

$$P^- = P^-(0) e^{j(\omega t + k^- x)}, \quad (1.7)$$

where $k^- = k_0/(1 - M_0)$ is the upward wave number under constant flow M_0 .

1.2.3 Self-sustained oscillations

1.2.3.1 The physical mechanism of self-sustained oscillations: feedback loop

This section is a brief presentation of self-sustained oscillations. It follows literature, and particularly Aurégan et al. (2002), Rienstra and Hirschberg (2003), Billon (2003).

Self-sustained oscillations differ from turbulence oscillations as they generate very specific sounds, like whistling sound, characterized by a high intensity and a spectrum with discrete frequencies (that is the whistling frequency and harmonics).

The term used 'self' signifies that these oscillations occur without imposing any external force. They occur spontaneously in the flow, but under quite particular conditions. These conditions are the following, and are illustrated in Fig. 1.1:

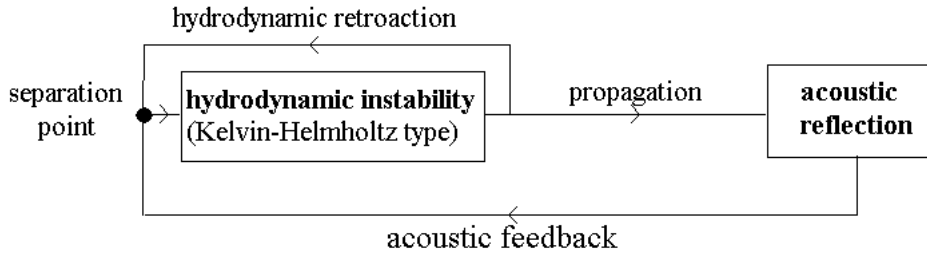


Figure 1.1: Mechanism of self-sustained oscillations with acoustic feedback (from Rienstra and Hirschberg (2003)).

- the presence of a localized region of the flow very sensitive to small fluctuations so as to be able to amplify those fluctuations. The main flow and the fluctuations are strongly coupled, an energy transfer from the main flow to the fluctuations occurs. In many cases (and in particular in this study), this region is an unstable shear layer, coming from a separation point of the flow, such as the one of a jet or a wake. The instability is a Kelvin-Helmholtz type one (Drazin and Reid, 1981);
- far away from this localized region of amplification, the fluctuations, which have been propagated, have to be sufficiently reflected at some point. The reflection can come either from an obstacle of the flow (hence producing an hydrodynamic feedback), either from an acoustic reflection (acoustic feedback). Thus, an important part of the fluctuations is redirected towards the amplification region;
- in the region of amplification, the phase of the reflected fluctuations has to be identical to the one of the newly rising fluctuations. Thus, the amplitude of the fluctuations rises in each loop.

This linear description gives theoretically infinite amplitude of the fluctuations. Actually, a saturation amplitude is reached, stabilizing the amplitude of the fluctuations (an infinite amplitude would correspond to an infinite acoustic energy, which contradicts the principle of conservation of energy).

The feedback characterizes the self-sustained oscillations. Two main types of feedback are differentiated: (Rienstra and Hirschberg, 2003):

- hydrodynamic feedback: the feedback is created by an incompressible flow due to the presence of an obstacle (for instance, the phenomenon of edge tone, hole tone, ...) ;
- acoustic feedback: the feedback is created by an acoustic reflection (for instance, a side branch in a pipe, a sudden enlargement, or an open pipe termination). This is the case studied in this work.

The whistling associated with hydrodynamic feedback is the most extensively discussed in literature (Blake and Powell, 1986; Rockwell, 1983). In particular, edge tone whistling constituted by a jet impacting an edge.

On the contrary, there are few references quantitatively describing whistling of an orifice with acoustic feedback. The phenomenon is well described in overviews (Blake, 1986; Rienstra and Hirschberg, 2003) but quantitative studies are scarce. The only reference found is Anderson papers (Anderson, 1952, 1953, 1953^b, 1954, 1955, 1955^b, 1956), which deals with the whistling of orifice in a pipe with a jet termination (that is, an open air exit after the orifice). In our configuration, that is the whistling of a thin orifice in a confined duct with acoustic feedback, no studies have been found.

1.2.3.2 The linear assumption when studying self-sustained oscillations

We want to insist here on the necessary distinction to be made between the instability frequency, and the whistling frequency. This distinction is made throughout this chapter.

The process of amplification is a linear one. The most unstable 'Kelvin-Helmholtz type' frequency of the shear layer is amplified exponentially due to this linear amplification. We can call this frequency the frequency of oscillation.

The process of saturation is a non-linear phenomenon. It is not modelled, and very little is known about this phenomenon. All we can say is that the frequency of oscillation can be theoretically subjected to a shift in the saturation process: the resulting frequency obtained, that we can call the whistling frequency, has to be differentiated from the oscillation frequency.

Hence the frequency for which the instability begins to growth, that is, the frequency of oscillation, and the frequency for which the amplification process saturates, that is, the whistling frequency, are theoretically different frequencies. They should be distinguished (Sarpkaya, 2004), as the whistling frequency comes from a non-linear saturation process: a shift in the frequency may arise during this non-linear saturation. The fundamental assumption adopted usually is that those two frequencies coincide, or at least are close. This is a very practical assumption, as it allows studying the whistling frequency with a linear theory of amplification.

In our work, the two frequencies are naturally differentiated: our potentially whistling frequency corresponds to the frequency of oscillation, and we show that when using reflecting conditions in the duct, the observed whistling frequencies are close to this potentially whistling frequency.

1.2.3.3 Theory for self-sustained oscillations: vortex sound

The analogy of Lighthill is not suited to the study of sound generated by self-sustained oscillations, as it assumes no retroactive effect of the acoustic perturbations on the main flow. Another analogy is

used efficiently: the ‘vortex sound theory’. It comes from the pioneer work of Powell (1964), and its latter generalization by Howe (1975).

In this approach, we call vortices all points where the vortex vector $\omega = rot(\mathbf{v})$ (where v is the flow velocity) is non-vanishing. The finding is that a vortex is associated to a source of sound, of a dipole type (produced by an external force), which is efficient (energy transfer from the flow to the acoustic flow) when the acoustic velocity is non-vanishing at this point. This has been a major advance in the domain, as using this theory, the problem is no more a dynamic one but becomes a kinematic one: how do vortices evolve (in non-viscous flow, the circulation of vortices is conserved).

The work of Howe gives an understanding of the creation/dissipation of acoustic energy by the flow. It assumes low Mach number, high Reynolds number and isentropic flow. The analogy decomposes the mean flow velocity \mathbf{v} into irrotational and incompressible parts:

$$\mathbf{v} = \mathbf{grad}(\phi) + rot(\psi). \tag{1.8}$$

The acoustic velocity is defined as the non-stationary part of the irrotational part of the mean flow:

$$\mathbf{v}_{ac} = grad(\phi'). \tag{1.9}$$

The power \mathcal{P} generated by the vorticity field $\omega(\mathbf{x}, t)$ (\mathbf{x} is the position vector) in the flow field $\mathbf{v}(\mathbf{x}, t)$ and the acoustic field $\mathbf{v}_{ac}(\mathbf{x}, t)$ is then given by:

$$\mathcal{P} = -\rho_0 \int_T \left[\iiint_{\mathcal{V}} [\omega(\mathbf{x}, t) \wedge \mathbf{v}(\mathbf{x}, t)] \cdot \mathbf{v}_{ac}(\mathbf{x}, t) d\mathbf{x} \right] dt, \tag{1.10}$$

where ρ_0 is the average fluid density, \mathcal{V} is a volume of non-vanishing $\omega(\mathbf{x}, t)$, and T is an acoustic period.

As an application, the case of the shedding of vortices by an orifice is considered. At the point of location of the developed vortex, just downstream of the orifice, the flow vector is assumed to be in the longitudinal flow direction, hence the vectorial product $\omega \wedge \mathbf{v}$ is in the transverse direction. It appears that the quantity $(\omega \wedge \mathbf{v}) \cdot \mathbf{v}_{ac}$ depends on the transverse component of the acoustic velocity. Consequently, this model enhances the importance of the transverse acoustic velocity in the power generated by the vorticity field in the acoustic field.

1.3 Presentation of the whistling criterion

This section presents the idea of Aurégan and Starobinsky (1999) to detect potentially whistling frequencies for singularities in confined flow. This theory is applied to our configuration of study: an orifice in pipe flow with plane wave propagation.

1.3.1 Configuration of study: a singularity in straight pipe under constant flow

The configuration of study is presented in Fig. 1.2: a singularity placed in a straight rigid pipe and subjected to a constant flow of Mach number M_0 is considered. Plane wave propagation is assumed.

The singularity is an obstacle of the flow, dissipating hydraulic energy and hence creating a static pressure drop across the orifice. It can be of any forms, but single-hole orifices, multi-hole orifices and valves are the most common ones in piping systems of nuclear power plants.

Two regions are differentiated (see Fig. 1.4): the first one corresponds to the upstream of the orifice (subscript 1), and the second to the downstream of the orifice (subscript 2), so that we use the following notation for the acoustic pressure:

$$\text{upstream: } p_1'(x, \omega) = P_1^+ e^{j(\omega t - k^+ x)} + P_1^- e^{j(\omega t + k^- x)}, \quad (1.11)$$

$$\text{downstream: } p_2'(x, \omega) = P_2^+ e^{j(\omega t - k^+ x)} + P_2^- e^{j(\omega t + k^- x)}. \quad (1.12)$$

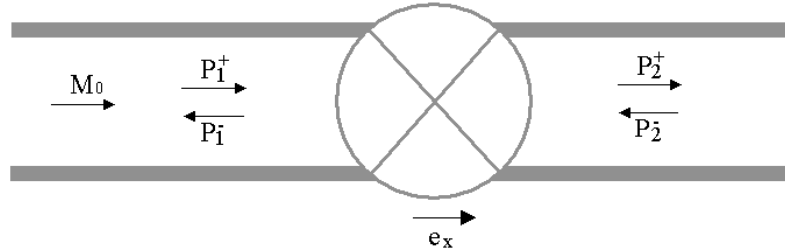


Figure 1.2: Configuration studied: singularity in a constant uniform pipe flow M_0 .

1.3.2 Elaboration of the whistling criterion

The fundamental idea to characterize the whistling of the singularity is to apply an acoustic energy balance in a region of study enclosing the source region. The acoustic power going out of the region is denoted \mathcal{P}_{out} , and the acoustic power going in the region is denoted \mathcal{P}_{in} . When whistling occurs, acoustic energy is produced in the source region:

$$\mathcal{P}_{out} > \mathcal{P}_{in}. \quad (1.13)$$

This is a necessary condition for whistling, which we use as a criterion to detect whistling.

At that point, the energy balance can be elaborated. The important point is that, in uniform flow, the definition of the acoustic energy is non-equivocal, as demonstrated by Morfey (1971): it satisfies

the linearized equations of mass, momentum and energy conservation as well as the standard energy conservation form. In instantaneous form, it is written:

$$\frac{\partial E}{\partial t} + \nabla \cdot \mathbf{I} = -\mathcal{D}, \quad (1.14)$$

where E is the density of acoustic energy, \mathbf{I} the intensity flux of acoustic energy and \mathcal{D} the rate of acoustic energy dissipation per unit volume.

To express those quantities, the variables of the acoustic mass velocity \mathbf{m}' and the acoustic total enthalpy Π' are introduced. They are convenient variables when in presence of flow. They are defined as (Morfey, 1971):

$$\mathbf{m}' = \rho_0 \mathbf{v}' + \frac{p'}{c_0} \mathbf{M}_0, \quad (1.15)$$

$$\Pi' = \frac{p'}{\rho_0} + c_0 \mathbf{v}' \cdot \mathbf{M}_0, \quad (1.16)$$

where \mathbf{v}' is the acoustic velocity, ρ' the acoustic density. One should note that the variables $(\rho_0 \Pi', \mathbf{m}'/\rho_0)$ are similar to (p', \mathbf{v}') without flow. In our configuration of a uniform flow, these quantities from both sides of the singularity get simple expressions ($i = 1$ for upstream, $i = 2$ for downstream):

$$m'_i = \frac{1}{c_0} (\Pi_i^+ - \Pi_i^-), \quad (1.17)$$

$$\Pi'_i = \frac{1}{\rho_0} (\Pi_i^+ + \Pi_i^-), \quad (1.18)$$

with:

$$\Pi_i^+ = (1 + M_0) P_i^+, \quad (1.19)$$

$$\Pi_i^- = (1 - M_0) P_i^-. \quad (1.20)$$

One should note that the terminology ‘acoustic total enthalpy’ refers to acoustic exergy multiplied by the density of the fluid: $\Pi' = \rho_0 B'$ where B' is the acoustic total enthalpy defined as $B' = p'/\rho_0 + U_0 u'$ (Rienstra and Hirschberg, 2003), neglecting the variation of entropy (hence total enthalpy and exergy are the same).

With these notations, the density of acoustic energy is recalled to be:

$$E = \frac{1}{2} (\mathbf{v}' \cdot \mathbf{m}' + \rho' \Pi'), \quad (1.21)$$

and the intensity flux of acoustic energy, \mathbf{I} , which will be used in the following, is given by:

$$\mathbf{I} = \Pi' \mathbf{m}'. \quad (1.22)$$

In integral form, using the control volume defined previously, of volume V , enclosed by a surface S and with outer normal vector \mathbf{n} , and applying the theorem of Gauss to transform the intensity flux expression, we get:

$$\frac{\partial}{\partial t} \iiint_V E + \iint_S \mathbf{I} \cdot \mathbf{n} = - \iiint_V \mathcal{D}. \quad (1.23)$$

In time average, as we consider acoustic fields, the average of the density of acoustic energy $\langle E \rangle$ is constant on an acoustic period, hence we get:

$$\mathcal{P} = \iint_S \langle \mathbf{I} \cdot \mathbf{n} \rangle = - \iiint_V \langle \mathcal{D} \rangle, \quad (1.24)$$

defining \mathcal{P} as the total acoustic power going through the surface S and the time average:

$$\langle X \rangle = \lim_{T \rightarrow +\infty} \frac{1}{T} \int_{t=0}^T X. \quad (1.25)$$

In plane-wave propagation, the acoustic intensity flux on a given surface can be decomposed in 2 terms: one corresponding to a propagation of the flux downstream I^+ , the other one corresponding to a propagation of the flux upstream I^- .

Also, the total surface S is made of 2 terms: the surface upstream, and the surface downstream S_2 (see Fig.1.3). We can hence define the time-averaged acoustic power going out of the control volume, denoted \mathcal{P}_{out} , and the time-averaged acoustic power going in the control volume, denoted \mathcal{P}_{in} :

$$\mathcal{P}_{in} = \iint_{S_1} \langle \mathbf{I}^+ \cdot \mathbf{n} \rangle + \iint_{S_2} \langle \mathbf{I}^- \cdot \mathbf{n} \rangle, \quad (1.26)$$

$$\mathcal{P}_{out} = \iint_{S_1} \langle \mathbf{I}^- \cdot \mathbf{n} \rangle + \iint_{S_2} \langle \mathbf{I}^+ \cdot \mathbf{n} \rangle. \quad (1.27)$$

The application of the idea of the whistling criterion gives:

- if $\mathcal{P}_{out} < \mathcal{P}_{in}$: the acoustic power going out of the singularity is a fraction of the acoustic power incident on the singularity. The singularity dissipates a part of the incident acoustic energy;
- if $\mathcal{P}_{out} = \mathcal{P}_{in}$: the acoustic power going out of the singularity is equal to the acoustic power incident on the singularity. This case is obtained when there is no energy exchange between the flow and the acoustic fluctuations;
- if $\mathcal{P}_{out} > \mathcal{P}_{in}$: the acoustic power going out of the singularity is higher than the acoustic power incident on the singularity. The singularity produces acoustic energy. This production corresponds to a conversion of the aerodynamic energy into an acoustic energy in the shear layers formed just downstream of the singularity.

1.3.3 Formulation of the whistling equations

1.3.3.1 Influence of the singularity: the scattering matrix

Assumptions for the model of the scattering matrix

A so-called scattering matrix describes the acoustic influence of the singularity. The following assumptions are made to use this model.

Firstly, the singularity is assumed to be acoustically compact: the characteristic length of the singularity is far smaller than the wavelength. In this assumption, the flow through the singularity can be considered as locally incompressible.

Secondly, a control volume is defined, enclosing the singularity. The boundaries of this control volume are chosen such that upstream and downstream of its boundaries the flow is uniform, as illustrated in Fig. 1.3.

The acoustic behaviour, inside and outside this volume, is described as the following:

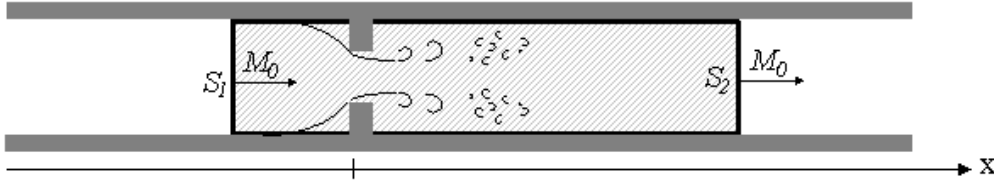


Figure 1.3: Definition of the control volume to apply the energy balance.

- outside the volume: plane-wave propagation is assumed;
- inside the volume: an incompressible flow behaviour is assumed. The control volume acts as a discontinuity for the far field (see Fig. 1.4). A linear acoustic behaviour is assumed in the control volume, so that the outgoing plane waves P_1^- and P_2^+ are linked to the incoming plane waves P_1^+ and P_2^- by the scattering matrix at $x = 0$.

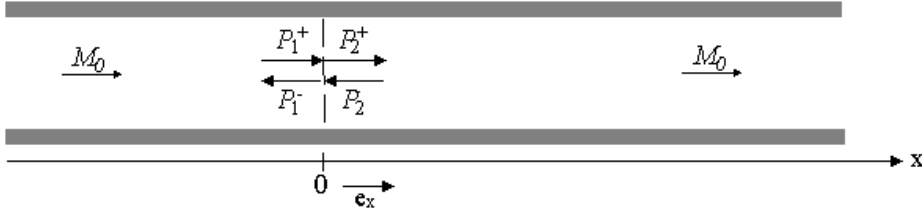


Figure 1.4: The acoustic scattering matrix of the singularity under constant pipe flow M_0 .

The scattering matrix in terms of pressure (measured)

In the linear approximation, anechoic acoustic reflection coefficients R^+ , R^- and transmission coefficients T^+ , T^- describe completely this scattering process representing the acoustic influence of the singularity. It can be conveniently written in a 2x2 matrix system:

$$\begin{pmatrix} P_2^+ \\ P_1^- \end{pmatrix} = \begin{pmatrix} T^+ & R^- \\ R^+ & T^- \end{pmatrix} \begin{pmatrix} P_1^+ \\ P_2^- \end{pmatrix}, \tag{1.28}$$

taking the phase origin at $x = 0$.

The matrix is called the scattering matrix, and noted S :

$$\mathbf{S} = \begin{pmatrix} T^+ & R^- \\ R^+ & T^- \end{pmatrix}. \quad (1.29)$$

This is a 2x2 complex matrix characterizing the acoustic influence of the singularity in terms of pressure. It depends only on the singularity, on the flow M_0 and on the pulsation frequency ω . It does not depend on the acoustic boundary conditions upstream and downstream of the singularity, as long as a linear behaviour prevails.

Similarly to this definition, a scattering matrix in terms of enthalpy is introduced, in order to present the whistling criterion.

The scattering matrix in terms of total enthalpy

In order to determine the acoustic energy of the plane waves, formulation into total enthalpy waves rather than pressure waves has to be used. Indeed, the time-averaged acoustic intensity flux is function of the amplitude of the acoustic total enthalpy waves, in a duct section ($i=1$ for upstream, $i=2$ for downstream), following Morfey (1971); Doak (1995); Aurégan and Starobinsky (1999):

$$\langle \mathbf{I}_i \rangle = \frac{1}{\rho_0 c_0} (\Pi_i^+{}^2 - \Pi_i^-{}^2) \mathbf{e}_x, \quad (1.30)$$

where ρ_0 is the density of air and \mathbf{e}_x the unitary vector in the direction of the flow (see Fig.1.4).

The scattering process, formulated previously in pressure waves (Eq. 1.28), is then formulated similarly in terms of total enthalpy waves:

$$\begin{pmatrix} \Pi_2^+ \\ \Pi_1^- \end{pmatrix} = \begin{pmatrix} T_e^+ & R_e^- \\ R_e^+ & T_e^- \end{pmatrix} \begin{pmatrix} \Pi_1^+ \\ \Pi_2^- \end{pmatrix}. \quad (1.31)$$

The matrix S_e is the scattering matrix for enthalpy waves:

$$\mathbf{S}_e = \begin{pmatrix} T_e^+ & R_e^- \\ R_e^+ & T_e^- \end{pmatrix}. \quad (1.32)$$

The coefficients of the scattering enthalpy matrix S_e are simply determined from the coefficients of the measured scattering pressure matrix S by:

$$T_e^+ = T^+, \quad T_e^- = T^-, \quad (1.33)$$

$$R_e^+ = \frac{1 - M_0}{1 + M_0} R^+, \quad R_e^- = \frac{1 + M_0}{1 - M_0} R^-. \quad (1.34)$$

1.3.3.2 The acoustic energy balance across the singularity

In this section, the acoustic energy balance across the singularity is made using the scattering matrix in terms of enthalpy.

Following Morfey (1971), the expression of the time-averaged acoustic power in presence of uniform flow is, in a duct section ($i=1$ for upstream, $i=2$ for downstream):

$$\mathcal{P}_i = S_p \langle \mathbf{I}_i \rangle \cdot \mathbf{e}_x. \quad (1.35)$$

If the incoming enthalpy waves and outgoing enthalpy waves are written in a column vector:

$$\mathbf{\Pi}_{in} = \begin{pmatrix} \Pi_1^+ \\ \Pi_2^- \end{pmatrix}, \quad \mathbf{\Pi}_{out} = \begin{pmatrix} \Pi_2^+ \\ \Pi_1^- \end{pmatrix}, \quad (1.36)$$

then the acoustic powers going in and out of the singularity are function of their respective wave vector and take the form (Aurégan and Starobinsky, 1999):

$$\mathcal{P}_{in} = S_p \|\mathbf{\Pi}_{in}\|^2, \quad \mathcal{P}_{out} = S_p \|\mathbf{\Pi}_{out}\|^2, \quad (1.37)$$

where S_p is the pipe cross-section, and $\|\mathbf{\Pi}_{in}\|^2 = (\mathbf{\Pi}_{in}, \mathbf{\Pi}_{in})$ is the square of the norm, defining the scalar product $(\mathbf{X}, \mathbf{Y}) = {}^T \mathbf{X} \mathbf{Y}$, the notation T standing for the Hermitian transpose (complex conjugate transpose). One should note that, by definition, those acoustic power are always positive.

The scattering matrix in terms of total enthalpy (see Eq. 1.31) is used to link the incoming and outgoing energies. As:

$$\mathbf{\Pi}_{out} = \mathbf{S}_e \mathbf{\Pi}_{in}, \quad (1.38)$$

the acoustic power going out of the orifice is only function of the incoming waves vector $\mathbf{\Pi}_{in}$:

$$\mathcal{P}_{out} = S_p {}^T \mathbf{\Pi}_{in} {}^T \mathbf{S}_e \mathbf{S}_e \mathbf{\Pi}_{in}. \quad (1.39)$$

To apply the whistling criterion idea, the sign of the acoustic energy dissipated by the singularity $\mathcal{P}_{in} - \mathcal{P}_{out}$ has to be determined:

$$\mathcal{P}_{in} - \mathcal{P}_{out} = S_p {}^T \mathbf{\Pi}_{in} (\mathbf{I}_d - {}^T \mathbf{S}_e \mathbf{S}_e) \mathbf{\Pi}_{in}, \quad (1.40)$$

where \mathbf{I}_d is the identity matrix.

The hermitian 2x2 matrix $\mathbf{I}_d - {}^T \mathbf{S}_e \mathbf{S}_e$ is self-adjoint. Hence it is diagonalizable with real eigenvalues ξ_{min} and ξ_{max} , sorted so that $\xi_{min} \leq \xi_{max}$, associated with orthonormalized eigenvectors $\mathbf{\Pi}_{min}$ and $\mathbf{\Pi}_{max}$. It is worth noting that the application of an algebra theorem (see for instance Lang (2004)), because the eigenvalues of ${}^T \mathbf{S}_e \mathbf{S}_e$ are positive or null, the eigenvalues of $\mathbf{I}_d - {}^T \mathbf{S}_e \mathbf{S}_e$ are inferior to unity: $\xi_i \leq 1$. This is the mathematical consequence of the physical fact that the acoustic powers are defined positive.

In the basis $(\mathbf{\Pi}_{min}, \mathbf{\Pi}_{max})$ of the eigenvectors, the acoustic dissipated power, seen as a quadratic form function of $\mathbf{\Pi}_{in}$, takes the expression:

$$\mathcal{P}_{in} - \mathcal{P}_{out} = \xi_{min} |(\mathbf{\Pi}_{in}, \mathbf{\Pi}_{min})|^2 + \xi_{max} |(\mathbf{\Pi}_{in}, \mathbf{\Pi}_{max})|^2. \quad (1.41)$$

The minimum and maximum of this quadratic form are obtained for $\mathbf{\Pi}_{in} = \mathbf{\Pi}_{min}$ and $\mathbf{\Pi}_{in} = \mathbf{\Pi}_{max}$, so that:

$$\xi_{min} = \min_{\mathbf{\Pi}_{in}} \left(\frac{\mathcal{P}_{in} - \mathcal{P}_{out}}{\mathcal{P}_{in}} \right), \quad \xi_{max} = \max_{\mathbf{\Pi}_{in}} \left(\frac{\mathcal{P}_{in} - \mathcal{P}_{out}}{\mathcal{P}_{in}} \right). \quad (1.42)$$

Consequently the eigenvalues give a bracket of the non-dimensional acoustic power $(\mathcal{P}_{in} - \mathcal{P}_{out})/\mathcal{P}_{in}$ dissipated by the singularity:

$$\xi_{min} \leq \frac{\mathcal{P}_{in} - \mathcal{P}_{out}}{\mathcal{P}_{in}} \leq \xi_{max}. \quad (1.43)$$

The sign of the minimum eigenvalue determines the whistling criterion:

- if $\xi_{min} \geq 0 \Rightarrow \mathcal{P}_{out} \leq \mathcal{P}_{in}$, for any \mathbf{Pi}_{in} :
the singularity dissipates the incoming acoustic energy, whatever the incoming waves. The singularity can not whistle at that frequency, whatever the reflections outside of this system;
- if $\xi_{min} < 0 \Rightarrow \mathcal{P}_{out} > \mathcal{P}_{in}$, for some \mathbf{Pi}_{in} :
there exists some couples of incident total enthalpy waves for which the acoustic power going out of the singularity is larger than the incoming acoustic power. For those incident waves, the singularity is potentially producing acoustic energy. It is consequently prone to whistle at that frequency, depending on the acoustic boundary conditions.

1.3.3.3 Models for the scattering matrix coefficients

A simple models is used to determine the scattering matrix coefficients, assuming an incompressible and quasi-stationary behaviour. It is experimentally evaluated in section 1.5.2.1.

An incompressible and quasi-stationary model is introduced (see scheme in Fig. 1.5). It is a classical model, described in details in Ajello (1997); Hofmans (1998); Hofmans et al. (2000); Durrieu et al. (2001). Two regions are distinguished: the first one includes the region upstream of the turbulent mixing region (also called *vena contracta*) where the linearized Bernoulli equation and the linearized mass conservation are applied; the second one includes the region downstream of the jet, where the linearized conservation of momentum quantity and the linearized mass conservation are applied. The reflection and transmission coefficients corresponding to this model are the following:

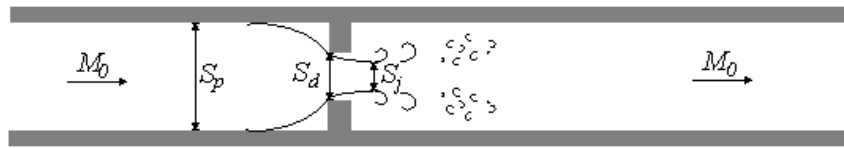


Figure 1.5: Scheme of the flow and notations for the quasi-stationary incompressible model.

$$R_{quasi-stat}^+ = R_{quasi-stat}^- = \frac{M_0\beta}{2 + M_0\beta}, \quad (1.44)$$

$$T_{quasi-stat}^+ = T_{quasi-stat}^- = \frac{2}{2 + M_0\beta}, \quad (1.45)$$

$$\text{with } \beta = \left(\frac{S_p}{S_j}\right)^2 - 1, \quad (1.46)$$

where S_j is the section of the jet. The contraction coefficient α is introduced, as usual, as $\alpha = S_j/S_d$.

1.4 Measurements configurations

1.4.1 Experimental set-up of the LAUM

1.4.1.1 Set-up

The set-up is illustrated in Fig. 1.6 and described in the following (see also (Auregan and Leroux, 2003)). It consists out of an open loop with a steel circular duct of inner diameter $D = 30$ mm and a thick and smooth wall (thickness $e = 4$ mm, roughness of the order of the micrometer).

In absence of flow, the cut-off frequency of the duct is equal to $f_{cut-off} = 6.7$ kHz, as calculated from (Angot, 1972; Pierce, 1981):

$$f_{cut-off} \approx \frac{1.84 c_0}{\pi D}, \quad (1.47)$$

where D is the pipe diameter, and c_0 the speed of sound in quiescent fluid. We use the speed of sound in air, under $P_0 = 1$ atm, and neglecting the effect of dampness (Wong, 1985):

$$c_0 = 343.2042 \sqrt{\frac{T_0 + 273.15}{293.15}}, \quad (1.48)$$

where T_0 is the ambient temperature expressed in Celsius degrees.

A constant air flow is generated by a compressor *Aerzen Delta blower GM10S* (nř1 in Fig. 1.6). The volume flow rate is measured with a flow meter *ITT Barton 7402* (nř2) with an accuracy of 10^{-2} m s^{-1} .

Two acoustic sources are present, one upstream (nř4) and one downstream (nř8) of the orifice. They are made of a loudspeaker and a compression chamber. They allow an acoustic level up to 160 dB in the measurement frequency range 400-5000 Hz.

Anechoic terminations are placed upstream (nř3) and downstream (nř9) of the measurement zone. They are presented in section 1.4.1.3.

The duct is 2 m long upstream of the 4 upstream microphones to allow a fully developed turbulent flow.

The temperature is measured with two transducers, each on one side of the orifice, with an accuracy of 10^{-2} K.

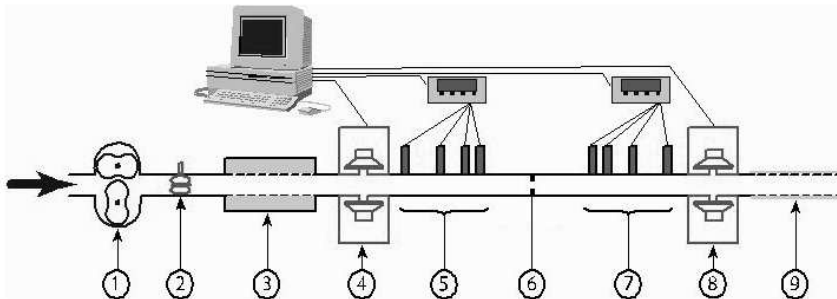


Figure 1.6: The experimental set-up.

1.4.1.2 Test section

Fig. 1.7 illustrates the test section. The singularity (n°6 on the figure) is located at the middle of the test section. Measurements are made with 2 series of 4 pressure transducers (microphone *B&K 4938* 1/4", preamplifier *B&K 2670* with *Nexus*) from both sides of the singularity :

- one series of 4 microphones upstream (n°5 in Fig. 1.6), denoted u_1 to u_4 while increasing index going away from the singularity;
- one series of 4 microphones downstream (n°7 in Fig. 1.6), denoted d_1 to d_4 while increasing index going away from the singularity;

The use of 2x4 microphones allows an over-determination, hence a better determination, of the transmitted and reflected waves.

The distance between consecutive microphones of a series is not constant: going away of the orifice, it equals 10.0 mm, 37.48 mm and 59.67 mm (that is: $x_{u1} - x_{u2} = x_{d1} - x_{d2} = 10.0$ mm, $x_{u2} - x_{u3} = x_{d2} - x_{d3} = 37.48$ mm, $x_{u3} - x_{u4} = x_{d3} - x_{d4} = 59.67$ mm). The choice of these distances allows to avoid the problem of measurement precision when half of the acoustic wavelength is close to the distance between 2 microphones (Boden and Abom, 1986).

The distance between microphone u_1 and the singularity is of the order of $12D$. The distance between the singularity and microphone d_1 is of the order of $20D$.

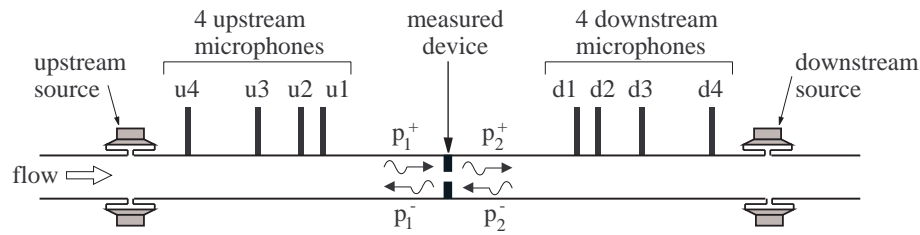


Figure 1.7: The measurement zone.

1.4.1.3 Acoustic boundary conditions of the test section

This experimental set-up is designed to measure the scattering matrix of a singularity. This matrix is independent of the acoustic boundary conditions of the set-up, as long as the singularity does not whistle. To avoid any whistling, it is preferable to have low reflecting acoustic boundary conditions of the test rig. The use of such anechoic boundary conditions also appears to enhance the accuracy in the measurement.

- upstream of the measurement zone, (about 2 m from the singularity), an expansion is placed, imposing a low upstream reflection coefficient: $|R_u| < 0.2$. Data for R_u are shown in Fig. 1.8;
- downstream of the measurement zone, (about 3 m from the singularity), a quasi-anechoic termination is arranged: holes are non-uniformly arranged in the wall of the duct of a length of tens of centimetres and covered with a piece of textile. The textile gives a resistance to the

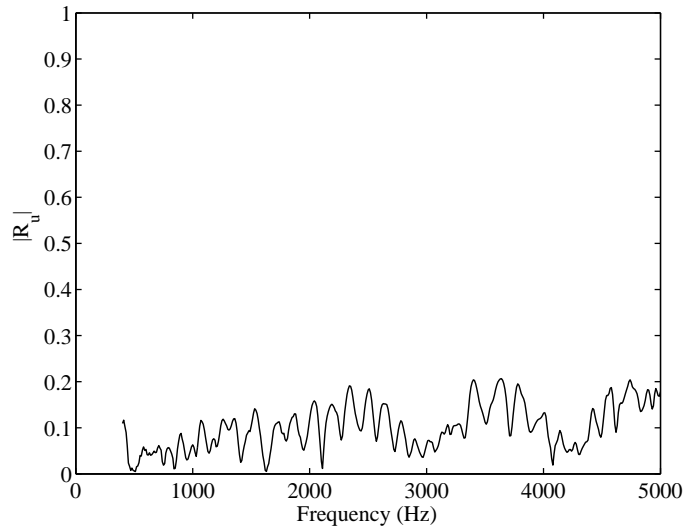


Figure 1.8: Upstream reflection coefficient of the measurement zone, without flow.

holes and secondarily prevents whistling due to the grazing flow. This configuration imposes a low reflection coefficient: $|R_d| < 0.4$.

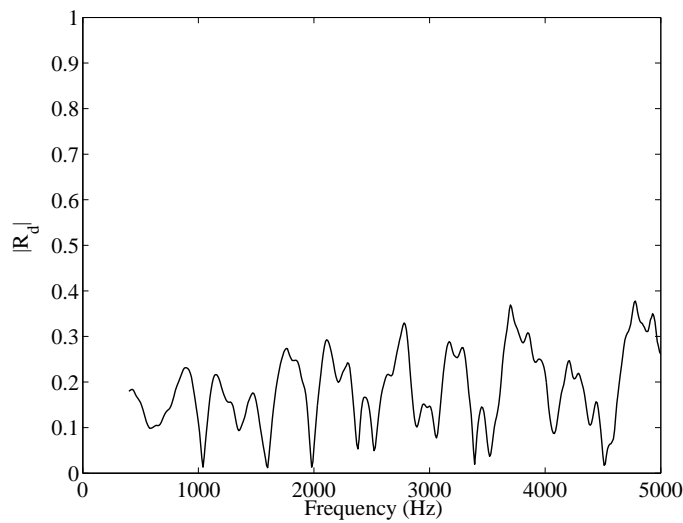


Figure 1.9: Downstream reflection coefficient of the measurement zone, without flow.

Those acoustic boundary conditions suppress whistling in most of our cases.

1.4.2 Measurement procedures

Preliminarily of any series of measurement, a calibration of the microphones is needed. Then, two types of measurements are made with this experimental set-up: the measurement of the scattering

matrix of the singularity (using the loudspeakers), and the measurement of the sound generated in the pipe (without using the loudspeakers).

1.4.2.1 Calibration of the microphones

The calibration of the 8 microphones is needed to link the responses of the microphones to each other. The calibration procedure uses a reference microphone. The transfer function between this reference microphone and the microphone being calibrated is measured, using the source and a constant distance between both microphones. The calibration provides 8 transfer functions that are used as a correction of the signals obtained from the microphones.

The quality of the measurements depends critically on the quality of the calibration. Hence an estimation of the quality of the calibration is helpful. A possible way to verify the calibration is to do a measurement without orifice and without flow. The scattering matrix of a pipe without flow is obtained. From it, two estimations can be made:

- the phase of the transmission coefficient gives the distance between the first upstream microphone (u_1) and the first downstream microphone (d_1), as there is no singularity in this measurement. The value obtained is compared to the actual length. A typical result for such a measurement is given in Fig. 1.10. The distance between the first upstream microphone and the first downstream microphone is typically obtained with an uncertainty less than 2 mm (that is 2% of error), in our frequency range of study: 400-5000 Hz.

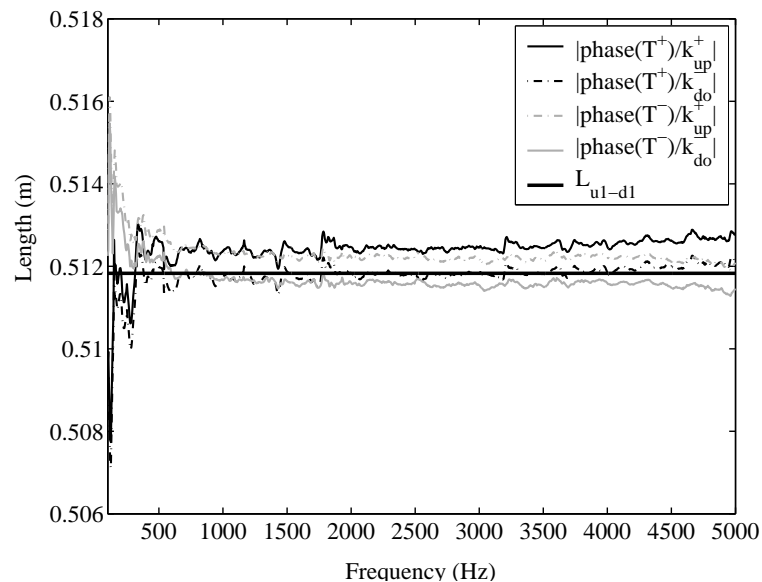


Figure 1.10: Experimental determination of the distance between microphones u_1 and d_1 , measuring when the singularity is replaced by a straight tube, and without flow.

- the magnitude of the transmission coefficient is determined by the attenuation of the waves between the first upstream microphone (u_1) and the first downstream microphone (d_1). This

attenuation is compared to the computed one, using the model of Kirchhoff (Ajello, 1997; Peters et al., 1993) (no fitting variables):

$$k^\pm = \frac{\omega}{c_0} K_0, \tag{1.49}$$

taking into account damping due to viscosity (with the shear number $Sh = \frac{D}{2} \sqrt{\frac{\omega}{\nu}}$) and temperature (with the Prandtl number $Pr = \nu/\kappa$, with ν the cinematic viscosity and κ the thermal conductivity; $Pr = 0.71$ for air):

$$K_0 = 1 + \frac{1}{Sh} \frac{1-j}{\sqrt{2}} \left(1 + \frac{\gamma-1}{\sqrt{Pr}} \right), \tag{1.50}$$

where γ is the ratio of specific heats at constant volume and pressure ($\gamma = 1.4$ for air). This expression is valid for low Helmholtz numbers $ka \ll 1$.

A typical result is given in Fig. 1.11. The model is found very satisfactory up to 4 kHz. Beyond 4 kHz, the Helmholtz number is not negligible, as $kD/2 \geq 1.1$, hence the theory is no more valid.

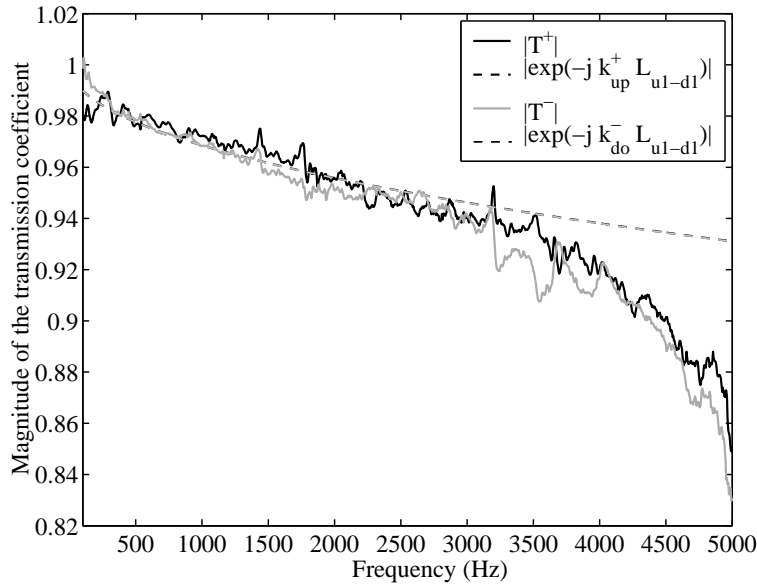


Figure 1.11: Experimental determination of the quality of the attenuation model for the wave number applied from Kirchhoff theory, measuring when the singularity is replaced by a straight tube, and without flow.

1.4.2.2 Measurement of the scattering matrix

The method to measure the scattering matrix of the singularity is a 2 sources method, which is described in details in Ajello (1997). Two measurements are made: one using the upstream loudspeaker (sending a plane wave P_1^+); the other one using the downstream loudspeaker (sending a plane wave P_2^-). The

coefficients (R^+, R^-, T^+, T^-) of the scattering matrix are determined from those two measurements:

$$\begin{pmatrix} \left(\frac{p_1^-}{p_1^+} \right)^{UP} & \left(\frac{p_1^-}{p_2^-} \right)^{DOWN} \\ \left(\frac{p_2^+}{p_1^+} \right)^{UP} & \left(\frac{p_2^+}{p_2^-} \right)^{DOWN} \end{pmatrix} = \begin{pmatrix} T^+ & R^- \\ R^+ & T^- \end{pmatrix} \begin{pmatrix} 1 & \left(\frac{p_1^-}{p_2^-} \right)^{DOWN} \\ \left(\frac{p_2^+}{p_1^+} \right)^{UP} & 1 \end{pmatrix}. \quad (1.51)$$

The upstream plane waves are determined using transfer functions $H_{u_n u_m}$ ($n \neq m, n \in [1, 4], m \in [1, 4]$) between the different upstream microphones u_n, u_m :

$$\frac{p_1^-}{p_1^+} = \frac{H_{u_n u_m} e^{-jk^+ x_{u_m}} - e^{-jk^+ x_{u_n}}}{e^{jk^- x_{u_n}} - H_{u_n u_m} e^{jk^- x_{u_m}}}. \quad (1.52)$$

Similarly, the downstream plane waves are determined using transfer functions $H_{d_n d_m}$ ($n \neq m$) between the different downstream microphones d_n, d_m ($n \in [1, 4], m \in [1, 4]$). Those transfer functions are obtained by the measurement. The wave numbers k^+ and k^- are determined with the model of Kirchhoff (Ajello, 1997) taking into account visco-thermal dissipation in the propagation.

The parameters used for the measurement of the scattering matrix are the following. The typical frequency range of our measurements is 400-4000 Hz (sometimes 400-5000 Hz), with a frequency resolution of 10 Hz (sometimes 5 Hz). A HP-software drives the measurement as a ‘Swept Sine’ type measurement. The source level is approximately 130 dB (SPL) and chosen in relation to the flow rate in order to avoid non-linear effects due to an excessive source level. For each frequency, the settle time before each measurement is 1000 cycles and the integration time is 1000 cycles. This range of parameters is chosen in order to reduce the error to an acceptable level.

1.4.2.3 Measurement of the broadband noise

The measurement of the flow sound generated in the pipe (without drive of exterior sources) is made with a ‘Frequency Response’ type measurement.

The parameters used for the measure of the noise are the following. The frequency range is 0-6400 Hz, with 4 Hz of frequency resolution. The spectra obtained represent an average of 50 data acquisition.

1.5 The whistling criterion on circular centred orifices

1.5.1 Orifices tested

Single-hole orifices are the main singularities tested. Indeed, they represent the simplest geometry to begin with the study of the whistling criterion.

The orifices tested (see Fig. 1.12) are of aluminium, with a circular and centred single hole. The edges of the hole are neat sharp angle edges (no bevel is visible on both sides).

In total, 19 orifices have been tested with different thickness t and diameter d , see Tab. 1.5.1 and Fig. 1.13. The range of thickness-to-diameter ratio is $0.15 \leq t/d \leq 1.5$. This range corresponds to thin orifices, according to Idel’cik (1969): $t/d \lesssim 2$.

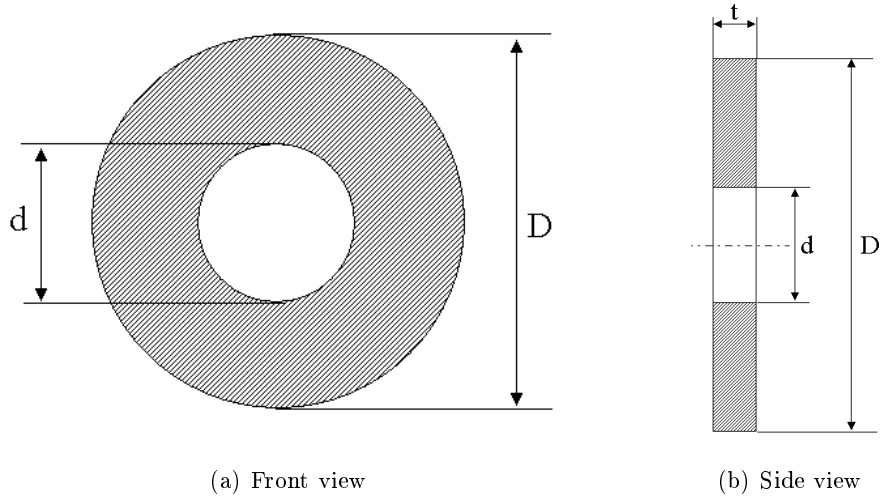


Figure 1.12: Tested single-hole circular-centred orifices with no bevel.

t/d	0.15	0.20	0.22	0.24	0.26	0.29	0.30	0.29	0.33	0.40
orifice	CC1	CC16	CC2	CC3	CC4	CC5	CC6	CC7	CC8	CC9
t (mm)	3	5	5	5	5	7	3	5	5	8
d (mm)	20	25	23	21	19	24	10	17	15	20
t/d	0.42	0.50	0.50	0.62	0.67	0.67	0.71	1.00	1.50	
orifice	CC17	CC10	CC18	CC11	CC12	CC19	CC13	CC14	CC15	
t (mm)	10	5	10	5	6	10	5	10	15	
d (mm)	24	10	20	8	9	15	7	10	10	

Table 1.1: Features of the single-hole orifices (no bevel).

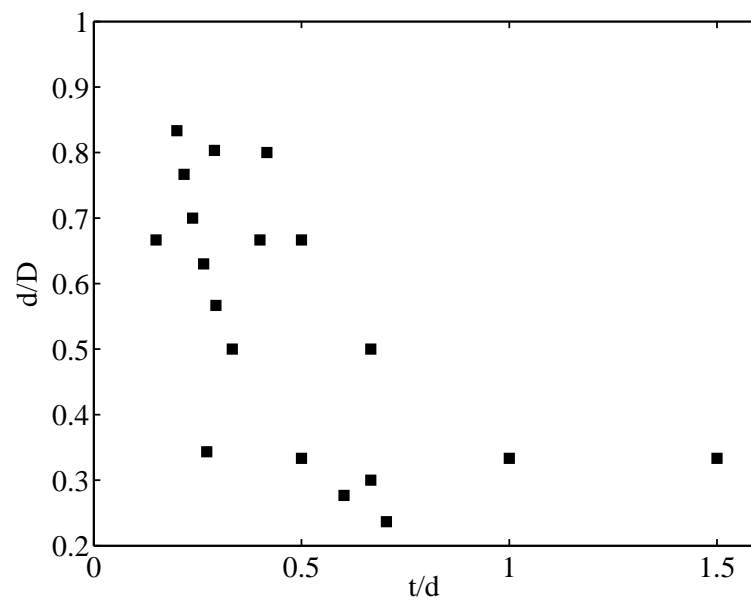


Figure 1.13: Characteristics of the orifices tested: circular centred orifices with no bevel.

1.5.2 Scattering matrix coefficients

1.5.2.1 Typical coefficients of the scattering matrix

Typical coefficients obtained for the scattering matrix are presented in Fig. 1.14 and 1.15 and analysed in the following:

- First, the low-frequency behaviour of the scattering matrix coefficients is well described by an incompressible quasi-stationary model (introduced in section 1.3.3.3).

This model depends on the vena-contracta coefficient α . Different values of α are used to compare to measurements in the limit of vanishing frequency. Results are indicated in Tab. 1.5.2.1. A fair agreement is obtained with $\alpha=0.70$ (see figures), which is known (Blevins, 1984) as being a reasonable value for an orifice with no visible bevel in a fully-developed turbulent flow ($Re \gtrsim 5 \cdot 10^3$).

Also, the assumption of incompressibility and no dissipation, giving the relation $|R^+| + |T^+| = |R^-| + |T^-| = 1$ (see section 1.3.3.3) is well satisfied for low Strouhal numbers fd/U_d , as illustrated in Fig. 1.16.

α	0.65	0.70	0.75
R^+, R^-	0.32	0.29	0.26
T^+, T^-	0.68	0.71	0.73

Table 1.2: Evaluation of a quasi-steady acoustic model to predict the scattering matrix at low frequency.

- Second, the transmission coefficient exhibit values with an amplitude above 1. This is an usual experimental observation. This behaviour corresponds to a production of acoustic energy by the orifice, which is consequently potentially whistling at those frequencies. This behaviour is hence directly linked with the whistling criterion, and further commented in section 1.5.2.1.

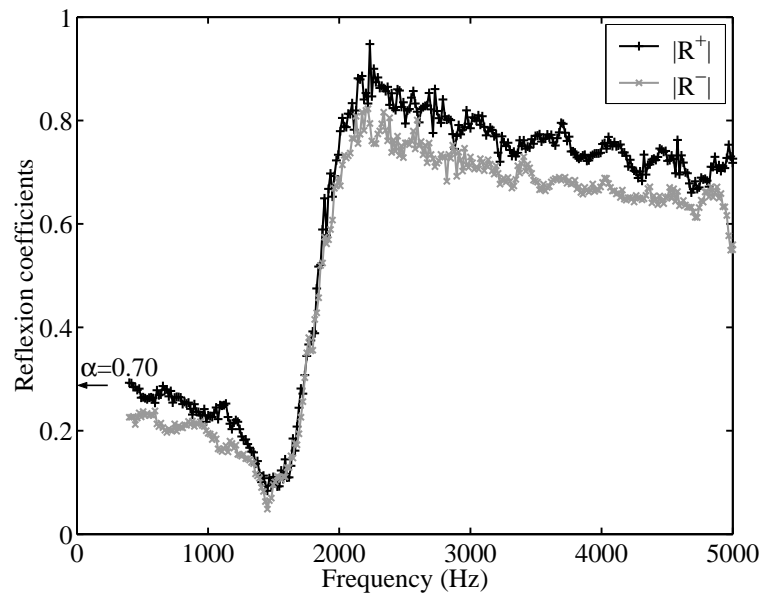


Figure 1.14: Typical reflection coefficients obtained from measurements of circular centred single-hole orifices - orifice $t = 5$ mm, $d = 15$ mm with $M_0 = 2.60 \cdot 10^{-2}$. The arrow indicates the incompressible and quasi-stationary model limit, using a contraction coefficient $\alpha = 0.70$.

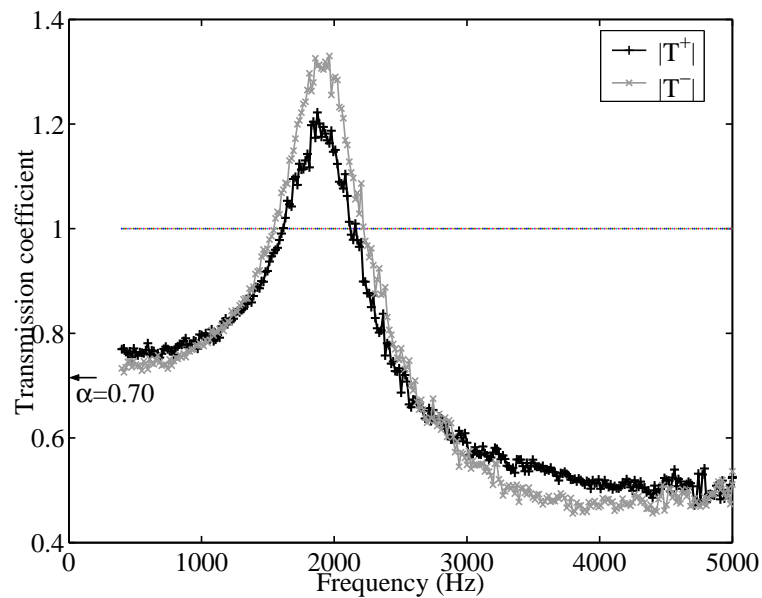


Figure 1.15: Typical transmission coefficients obtained from measurements of circular centred single-hole orifices - orifice $t = 5$ mm, $d = 15$ mm with $M_0 = 2.60 \cdot 10^{-2}$. The arrow indicates the incompressible and quasi-stationary model limit, using a contraction coefficient $\alpha = 0.70$.

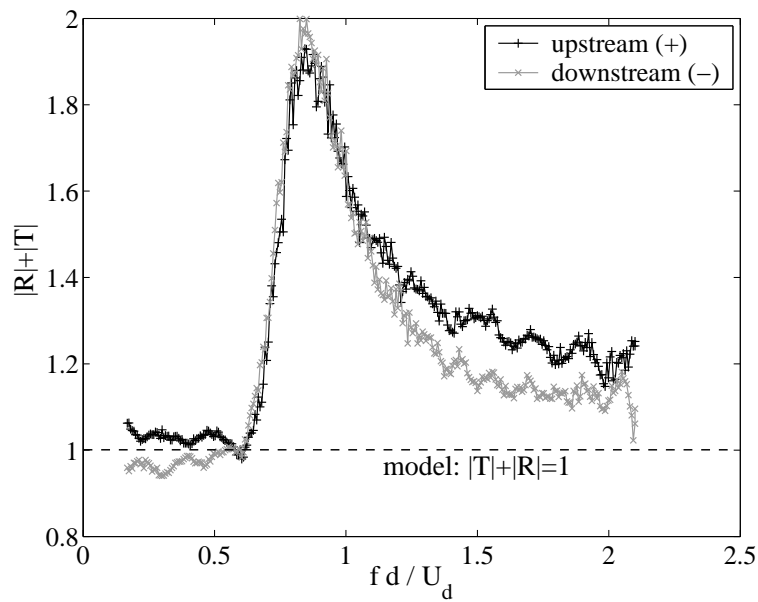


Figure 1.16: Evaluation of the incompressible and lossless model compared with measurements: for low Strouhal numbers, the behaviour of the scattering matrix coefficients follows the model - orifice $t = 5$ mm, $d = 15$ mm with $M_0 = 2.60 \cdot 10^{-2}$.

1.5.2.2 Non linear behaviour due to high level of the excitation source

The ‘2 sources method’ assumes a linear acoustic behaviour of the system. In this assumption, the determination of the scattering matrix coefficients is independent of the level of the excitation source. In our experiments, we limited our source amplitude in order to avoid non-linear effects. So as to determine the amplitudes at which such effects occur, we present data for increasing levels.

As illustrated in Fig. 1.17 and 1.18, these non-linear effects are observed for frequencies identified as potentially whistling frequencies. Instead of a typically linear hump form, a threshold is observed, exhibiting a saturation phenomenon.

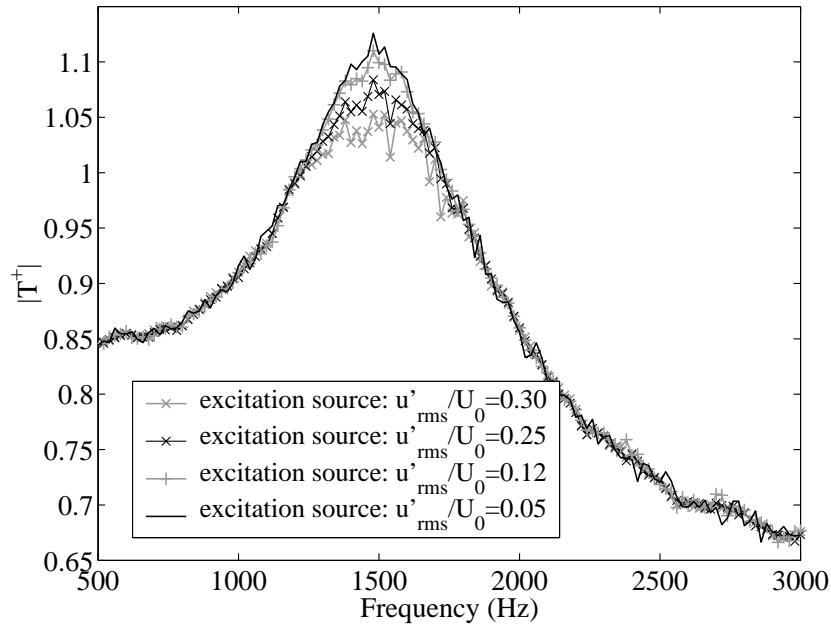


Figure 1.17: The level of the excitation amplitude of the source loudspeaker has an influence on the scattering matrix coefficients, here for $|T^+|$ - orifice $t = 5$ mm, $d = 17$ mm with $M_0 = 2.59 \cdot 10^{-2}$.

Investigations indicate that for a level value of $u'_{rms}/U_0 \approx 10^{-1}$, such non-linear effects become significant under conditions at which whistling can occur $\mathcal{P}_{out} > \mathcal{P}_{in}$. When absorption prevails $\mathcal{P}_{out} < \mathcal{P}_{in}$, the response is almost independent of the amplitude up to $u'_{rms}/U_0=0.3$.

1.5.3 Potentially whistling frequencies

In this section, the application of the whistling criterion is studied. The evolutions of the eigenvalues ξ_{min} and ξ_{max} of the matrix $I - {}^T S_e S_e$ are investigated.

Typical evolutions obtained for these eigenvalues are shown in Fig. 1.19:

- the two eigenvalues can clearly be distinguished: the first one (denoted ξ_{nonevo}) close to zero, and another one (denoted ξ_{evo}), taking both positive and negative values;
- the evolving eigenvalue ξ_{evo} shows a hump form as visible in the figure. This form is systematic for circular-centred orifices without bevel;

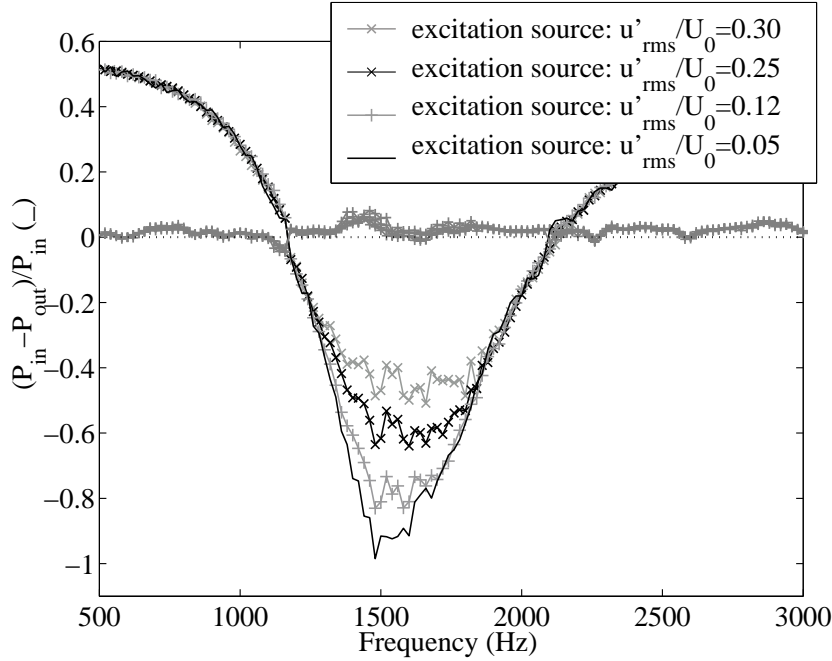


Figure 1.18: The level of the excitation amplitude of the source loudspeaker has an influence on the eigenvalues obtained from measurements of scattering matrix coefficients - orifice $t = 5$ mm, $d = 17$ mm with $M_0 = 2.59 \cdot 10^{-2}$.

- a major experimental result is obtained: ranges of frequencies exist for which the minimum eigenvalue is negative. Following the whistling criterion, these ranges of frequency correspond to potentially whistling frequencies. In the figure, two ranges of frequencies are observed, corresponding to two different hydrodynamic modes of whistling.

In order to test the consistency of this whistling indicator, an orifice with a bevel on one side is studied. The idea is to test the influence of the side of the bevel on the whistling criterion: bevel upstream, bevel downstream. Results are given in Fig. 1.20:

- bevel upstream: the eigenvalues are always positive: for all frequencies, the orifice dissipates acoustic energy, and will never whistle. This observation agrees with literature, as this configuration is well-known to be a typical non-whistling one (Rienstra and Hirschberg, 2003).
- bevel downstream: a frequency range, 2200-3700 Hz, is found for which the orifice can produce acoustic energy. This also confirms literature as the configuration of a bevel downstream is known to be a typical whistling configuration (Wilson et al., 1971; Hirschberg et al., 1989).

1.5.4 Strouhal numbers

Considering a range of potentially whistling frequency, the amplitude of the eigenvalue takes a hump form, so that a peak frequency, denoted f_{peak} , corresponding to the minimum amplitude reached by the evolving eigenvalue, is identifiable (as shown in Fig. 1.21). This frequency represents the highest

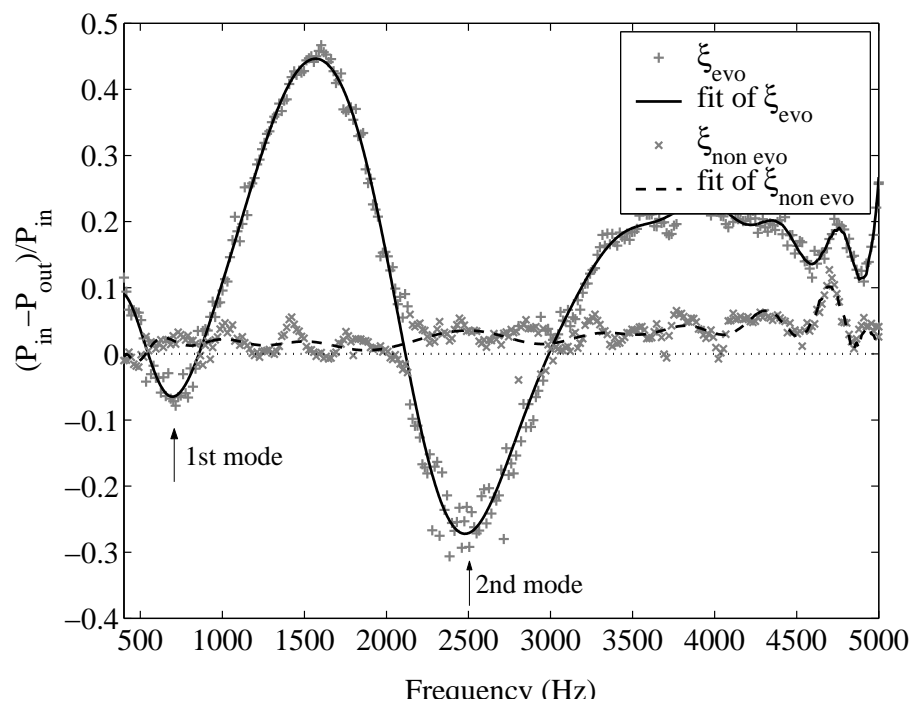


Figure 1.19: Potentially whistling eigenvalues ξ_{evo} and ξ_{nonevo} of the matrix $I^{-t} S_e S_e$: a typical hump evolution is found, exhibiting typical successive acoustic whistling modes - orifice $t = 8$ mm, $d = 20$ mm with $M_0 = 3.28 \cdot 10^{-2}$.

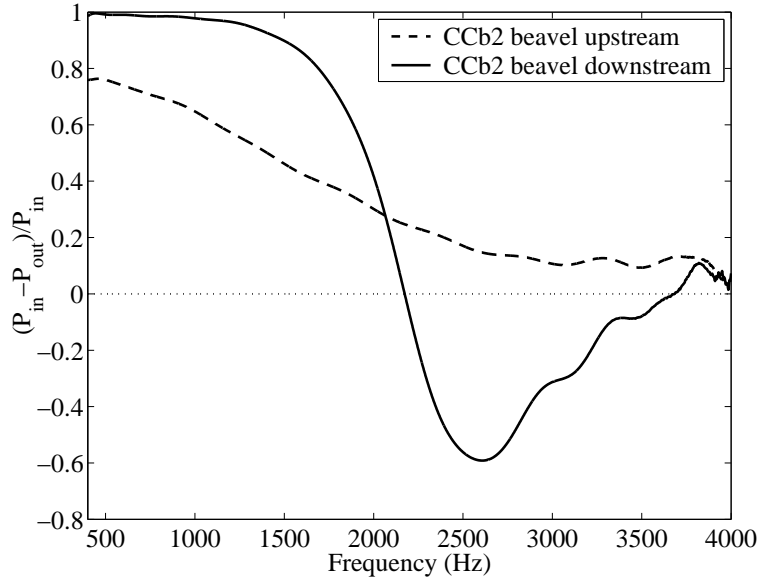


Figure 1.20: Influence of the bevel on the whistling criterion using the potentiality of whistling with the evolving eigenvalue ξ_{evo} : no whistling potentiality is found when the bevel is placed at the upstream edge of the orifice, whereas a range of potentially whistling frequencies is found (here 2200-3700 Hz) when the bevel is placed at the downstream edge of the orifice - orifice with a bevel $r_{bevel}=1$ mm, $t = 5$ mm, $d = 10$ mm (CCb2) with $M_0 = 7.6 \cdot 10^{-3}$.

potential whistling frequency for this whistling mode. Results obtained for this frequency are studied in this section.

The peak frequency f_{peak} is made non-dimensional, using the orifice thickness t and the orifice velocity $U_d = U_0 (D/d)^2$, hence defining the Strouhal number:

$$St_{peak} = \frac{f_{peak}t}{U_d}. \tag{1.53}$$

An example of a collapse in x-coordinate with this Strouhal number is given in Fig. 1.22 (to be compared with Fig. 1.21).

The best collapse of peak Strouhal numbers obtained with this choice of these scaling variables t and U_d . Other scaling variables have been tested and lead to less satisfactory collapse: lengths $d, D, (D - d)/D$ and velocity U_0 . For instance, the choice of a Strouhal based on the orifice diameter d leads to a far less satisfactory collapse, as illustrated in Fig. 1.24 (compared with Fig. 1.23, where the Strouhal is based on the orifice thickness t).

Distinction of flow regimes for the Strouhal number

Strouhal numbers $f_{peak}t/U_d$ obtained for all orifices are given in Fig. 1.23 for the first whistling mode, as function of the pipe Reynolds number $Re_D = U_0D/\nu$. In the range of Reynolds number studied ($2 \cdot 10^3 \leq Re_D \leq 8 \cdot 10^4$), Strouhal numbers appear to vary significantly. Two main regions can be discerned:

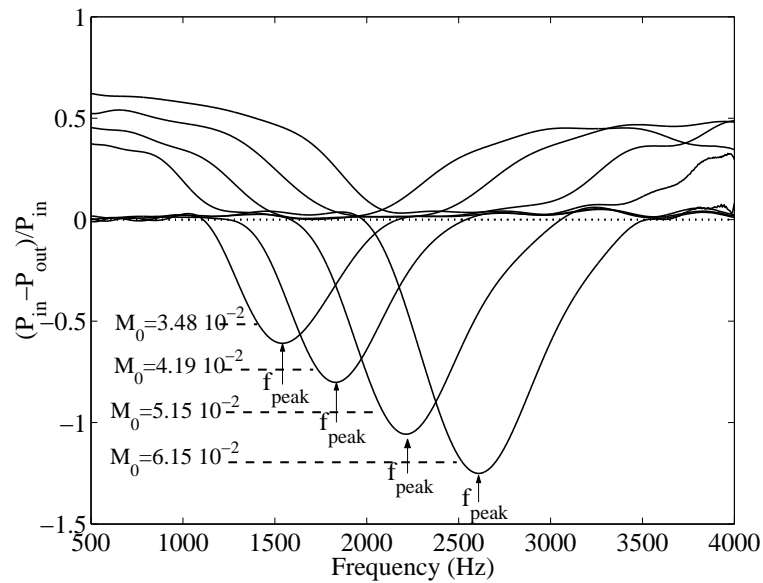


Figure 1.21: Identification of the frequency peak f_{peak} corresponding to the potentially maximum frequency for one mode of whistling identified with the evolving eigenvalue ξ_{evo} - orifice $t = 5$ mm, $d = 19$ mm with various Mach numbers.

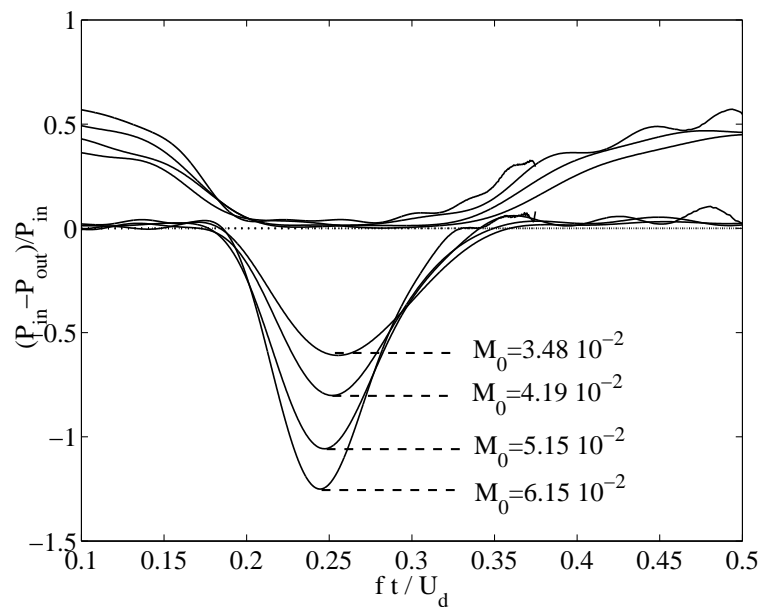


Figure 1.22: Representation in Strouhal number $St = ft/U_d$ of the eigenvalues determining the potentially whistling frequencies: a very good collapse is obtained - orifice $t = 5$ mm, $d = 19$ mm with various Mach numbers.

- a flow below or close to the laminar-turbulent transition: $Re_D \lesssim 5 \cdot 10^3$;
- a fully turbulent flow: $Re_D \gtrsim 5 \cdot 10^3$, most of the cases.

The Strouhal numbers for low-Reynolds number are significantly higher, up to 50%, compared with those obtained for a fully turbulent main flow. Explanations of this observation may be the following: Firstly, for a flow in laminar state, the main flow impacting the upstream edge of the orifice is very different from a flow in turbulent state.

Secondly, for low Reynolds numbers, the jet vena-contracta section in the orifice is known (see Tab.1.5.4 from Blevins (1984)) to vary very much compared to its high Reynolds number value, as indicated in Tab.1.5.4.

DIAMETER RATIO d/D	DISCHARGE COEFFICIENT, C							
	Orifice Reynolds Number $(UD/\nu) (D/d)$							
	10	60	100	500	10^3	10^4	10^5	10^6
0.3	0.47	0.64	0.67	0.72	0.70	0.60	0.60	0.60
0.5	0.46	0.66	0.69	0.74	0.72	0.61	0.60	0.60
0.7	0.42	0.67	0.72	0.81	0.83	0.65	0.61	0.60

Table 1.3: Strong variations of the jet vena-contracta section for pipe Reynolds numbers between 10^3 and 10^4 from Blevins (1984).

For this latter reason, the Strouhal number ft/U_j based on the jet velocity should be more precise than the one used in this study ft/U_d . However, the value of U_j is experimentally difficult to obtain; U_j can be estimated from the measure of the pressure drop across the orifice. This requires static pressure transducers from both sides of the orifice, which were not available in our experiments.

Strouhal numbers are constant for turbulent flow regime

The main result of this Strouhal number study is that for most of the cases, that is for fully turbulent Reynolds numbers ($5 \cdot 10^3 \leq Re_D \leq 810^4$), Strouhal numbers obtained are almost constant: Strouhal numbers (mode 1) are in the range 0.2-0.3 (cf. Fig. 1.23). This is in close agreement with literature. Anderson (1953^b) indicates a value around 0.26-0.29 for thin orifices ($0.1 \leq t/d \leq 0.5$) in a configuration of a free jet (exit towards free space). The comparison is shown in Fig. 1.26) using the representation given by Blake (1986).

For turbulent Reynolds numbers ($5 \cdot 10^3 \leq Re_D \leq 10^5$), various linear fits on data with multiple parameters have been used to estimate the importance of different parameters on the Strouhal number: $1/Re_D^\alpha$, $\ln(Re_D)$, $(d/D)^\alpha$, $(t/d)^\alpha$, $[D/(D-d)]^\alpha$, with $\alpha > 0$. It is found that the Strouhal number varies mainly with two parameters: the Reynolds number Re_D

and the distance to the wall $D/(D-d)$. For the first hydrodynamic mode, the linear regression giving the least standard deviation on data is the following:

$$St_{peak} = 0.2048 \left(1 + \frac{57.6936}{\sqrt{Re_D}} + 0.0596 \frac{D}{D-d} \right), \quad (1.54)$$

giving a standard deviation of $1.6 \cdot 10^{-3}$ on 65 data points;

Hydrodynamic modes of higher orders (≥ 2) are given in Fig. 1.25. The Strouhal numbers are significantly higher than for the first whistling mode. The values obtained are consistent with data from Anderson (1954).

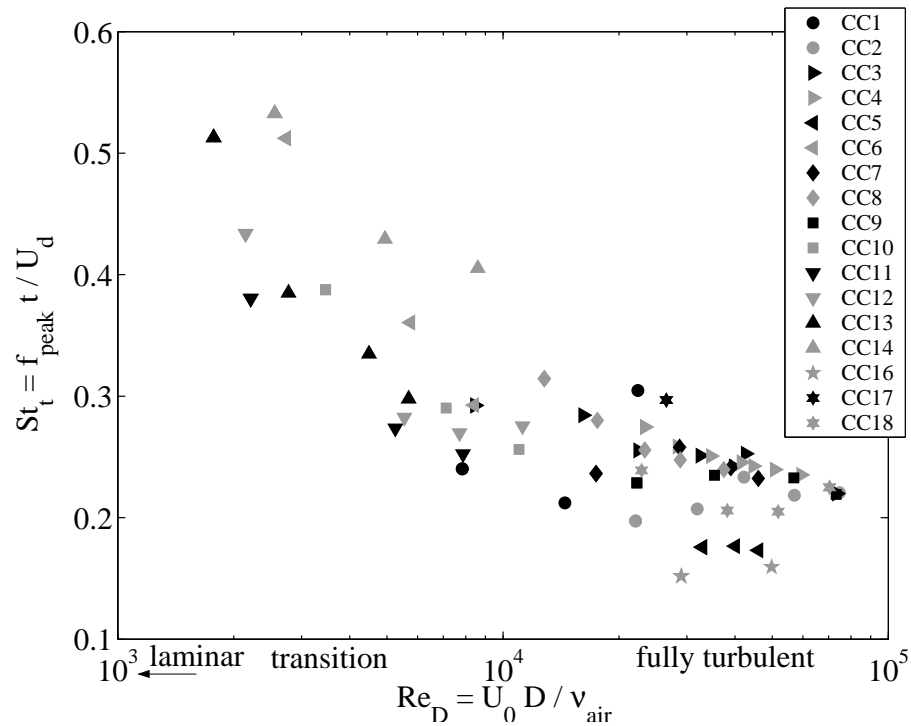


Figure 1.23: Strouhal numbers associated with the potentially whistling ‘peak’ frequency identified for the first whistling mode - all measurements with circular-centred single-hole and no bevel orifices.

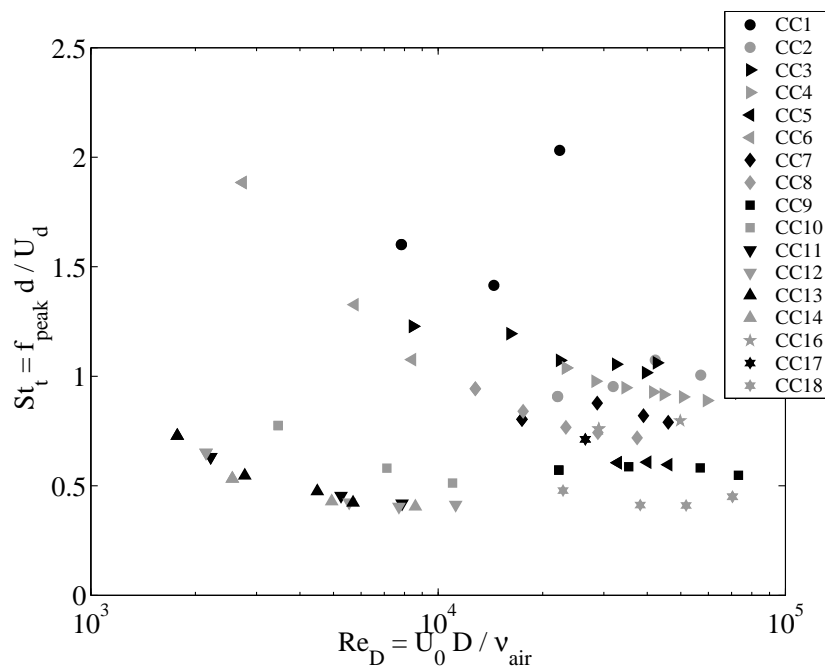


Figure 1.24: Strouhal numbers based on the scaling length d associated with the potentially whistling ‘peak’ frequency identified for the first whistling mode: the scaling length d is unsatisfactory - all measurements with circular-centred single-hole and no bevel orifices.

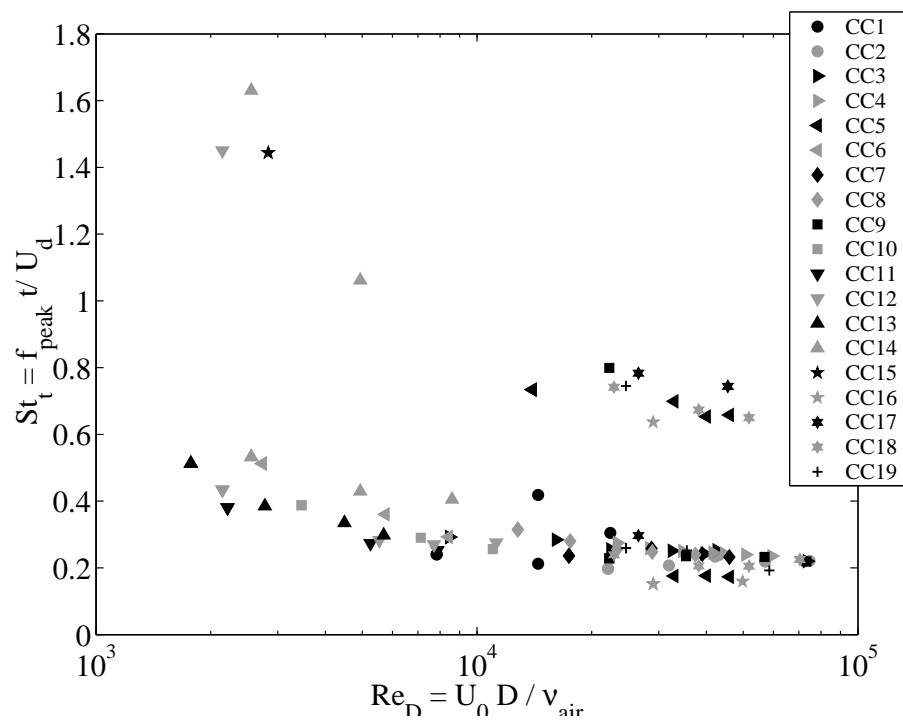


Figure 1.25: Strouhal numbers associated with the potentially whistling ‘peak’ frequency identified for the first and second whistling mode - all measurements with circular-centred single-hole and no bevel orifices.

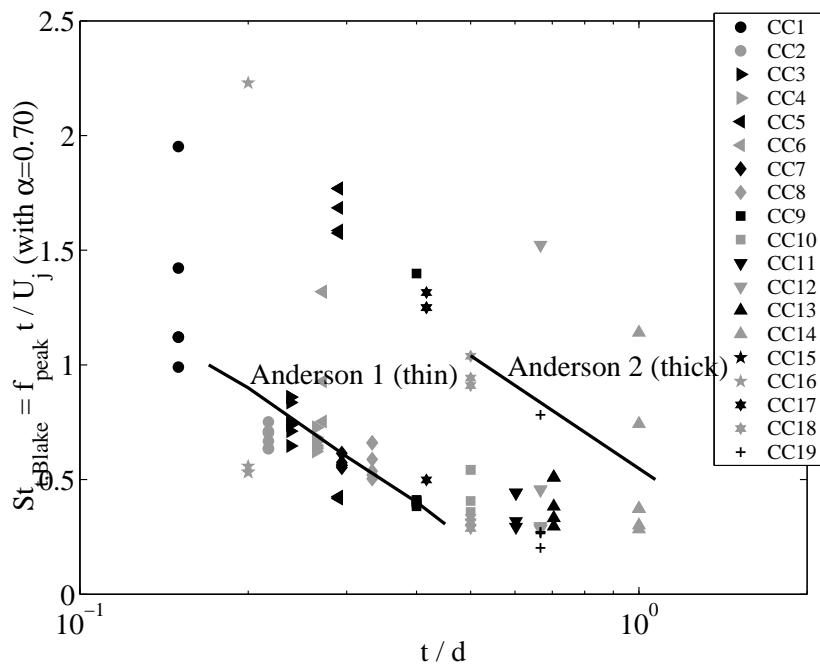


Figure 1.26: Comparison of our measured Strouhal numbers with Anderson data, for thin ($0.1 \leq t/d \leq 0.5$) and thick ($0.5 \leq t/d \leq 1.2$) orifices, reported by Blake: the representation of Blake is unsatisfactory.

1.5.5 Conditions of whistling for the incident waves

So far the eigenvalues of the scattering matrix have been analysed. The analysis of the corresponding eigenvectors is done in this section, in order to investigate the conditions linked to whistling and non-whistling behaviour.

The eigenvectors Π_1 and Π_2 , associated with the eigenvalues ξ_1 (minimum) and ξ_2 (maximum), are considered (see an example illustrated in Fig. 1.29). Their components are denoted a_i and b_i :

$$\Pi_1 = \begin{bmatrix} a_1 \\ b_1 \end{bmatrix}, \quad \Pi_2 = \begin{bmatrix} a_2 \\ b_2 \end{bmatrix}. \quad (1.55)$$

The components of the eigenvectors correspond to the incident total enthalpy waves, so that:

$$\Pi_i = \begin{bmatrix} a_i \\ b_i \end{bmatrix} \equiv \begin{bmatrix} (1 + M_0)p_1^+ \\ (1 - M_0)p_2^- \end{bmatrix}. \quad (1.56)$$

The evolution of the components of the eigenvectors Π_1 and Π_2 is given in Fig. 1.27 and 1.28. First, it is observed that the imaginary part of the components can be neglected compared to the real part. Second, the real part appear clearly to get two values: +1 or -1 broadly (in first order analysis). Those two values correspond to different excitation conditions for the incident enthalpy waves:

- $a_i/b_i \approx 1$ corresponds to an excitation $(1 - M_0)p_1^- - (1 + M_0)p_2^+ \approx 0$. This is a condition of the type of an acoustic velocity node $v' \approx 0$.
- $a_i/b_i \approx -1$ corresponds to an excitation $(1 - M_0)p_1^- + (1 + M_0)p_2^+ \approx 0$. This is a condition of the type of an acoustic pressure node $p' \approx 0$.

The conditions obtained are plotted in Fig. 1.29:

- strong energy exchange between the acoustic field and the main flow (that is passive dissipation and whistling behaviours) occurs when a pressure node condition $p' = 0$ is formed at the orifice by the excitation waves;
- inversely, no energy exchange between the acoustic field and the main flow is obtained for a velocity node type.

These results confirm very well what is known on whistling and non-whistling condition.

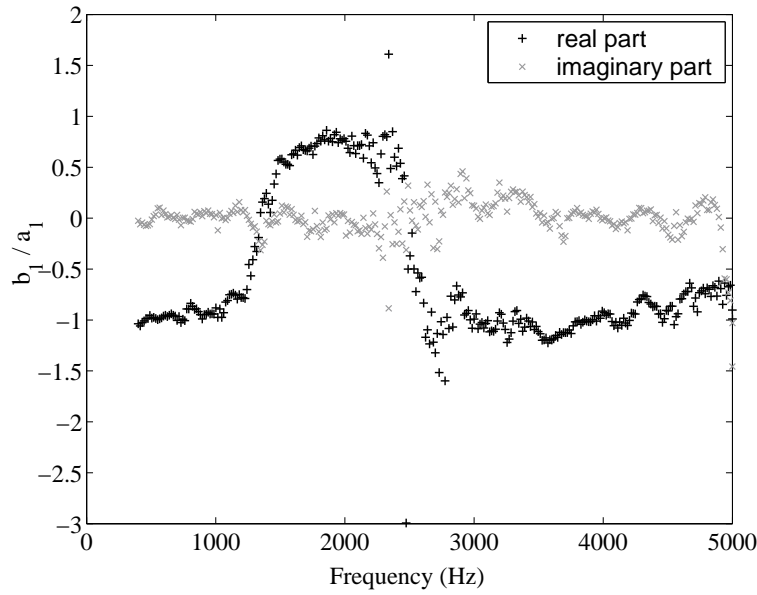


Figure 1.27: Representation of the wave (eigenvector) corresponding to the eigenvalue ξ_1 (see Fig. 1.29) in a non-dimensional representation $b_1/a_1 = [(1 - M_0)p_2^-]/[(1 + M_0)p_1^+]$ - orifice $t = 5$ mm, $d = 19$ mm with $M_0 = 4.19 \cdot 10^{-2}$.

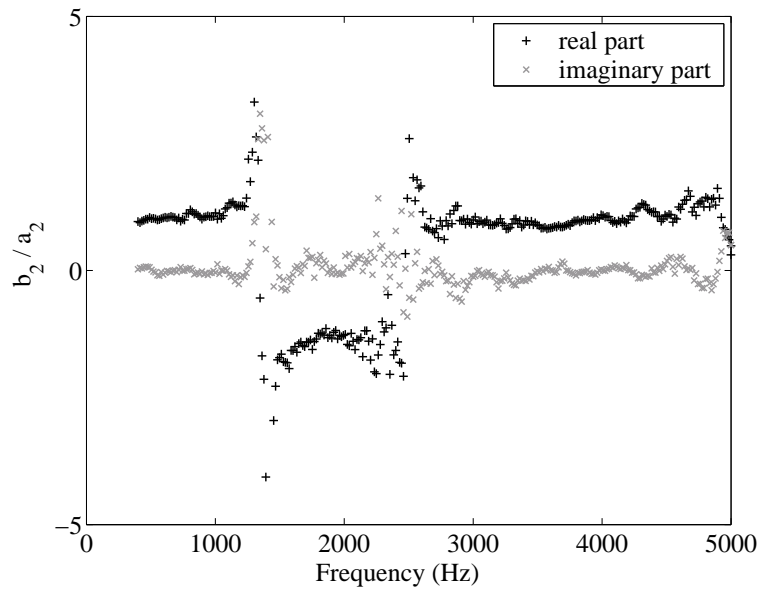


Figure 1.28: Representation of the wave (eigenvector) corresponding to the eigenvalue ξ_2 (see Fig. 1.29) in a non-dimensional representation $b_1/a_1 = [(1 - M_0)p_2^-]/[(1 + M_0)p_1^+]$ - orifice $t = 5$ mm, $d = 19$ mm with $M_0 = 4.19 \cdot 10^{-2}$.

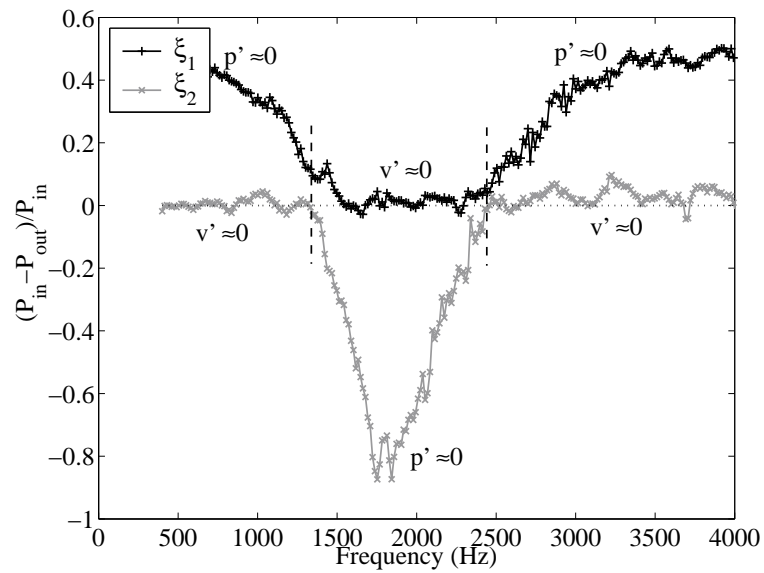


Figure 1.29: Potentially whistling eigenvalues and the corresponding wave conditions in terms of acoustic pressure p' and acoustic velocity v' at the orifice ($x = 0$) - orifice $t = 5$ mm, $d = 19$ mm with $M_0 = 4.19 \cdot 10^{-2}$.

1.5.6 Non-dimensional potentially whistling eigenvalues

The magnitude of the eigenvalue is a ratio of potentially dissipated acoustic energy. In this section, a secondary dimensionless representation is proposed.

The amplitudes corresponding to the peak potentially whistling frequencies are considered. A satisfactory dimensionless representation is obtained: they are proportional to the Mach number as illustrated in Fig. 1.30 and 1.31.

The dipole associated to whistling explains the proportionality with the Mach number, as in a quasi-

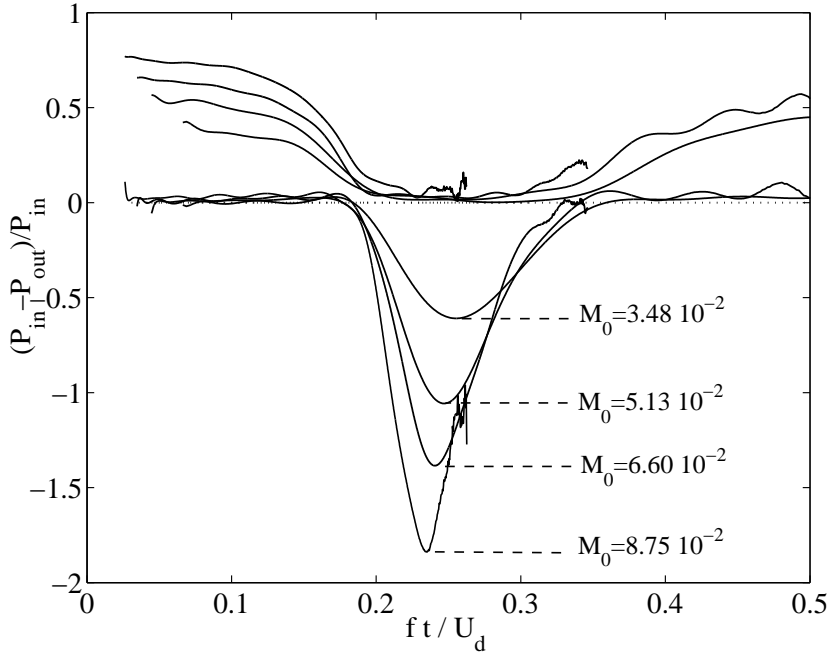


Figure 1.30: Representation of the potentially whistling eigenvalues for a given orifice at different Mach number: the magnitudes evolve strongly - orifice $t = 5$ mm, $d = 19$ mm.

steady approximation for a free jet emerging in free space, one gets:

$$\Delta p = \frac{1}{2} \rho_0 U_0^2 \Rightarrow \Delta p' = \rho_0 c_0 M_0 u', \tag{1.57}$$

where Δp is the static pressure drop across the orifice, $\Delta p'$ the acoustic pressure drop across the orifice, u' the acoustic velocity in the pipe.

The Mach number is not the only scaling variable: the ratio of the peak eigenvalue to the Mach number is found to depend on the geometry of the orifice, as shown in Fig. 1.32. Globally $(\xi_{evo})(f_{peak})/M_0$ depends linearly on the contraction ratio D/d . However, data are not sufficient to find another scaling variable of this quantity.

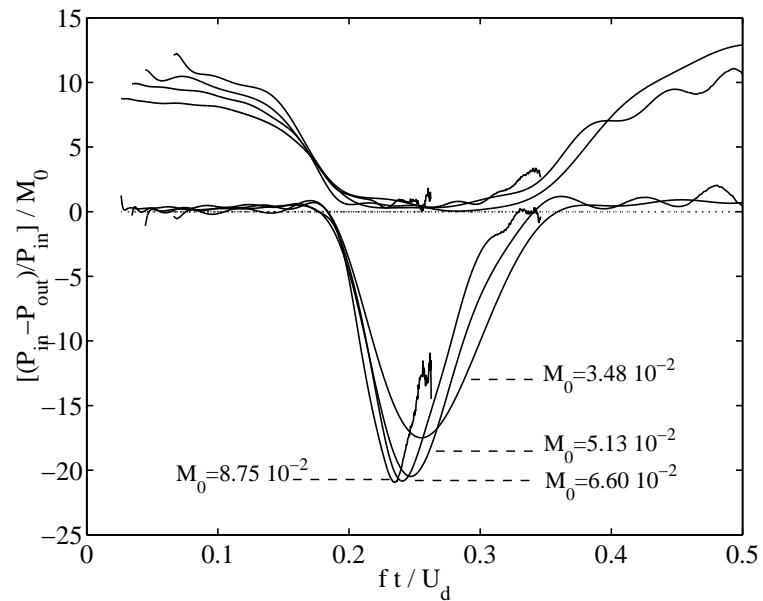


Figure 1.31: Non-dimensional representation of the magnitude of the potentially whistling eigenvalues for a given orifice at different Mach number: the non-dimensional representation is satisfactory for a given orifice: the non-dimensional representation needs improvement - orifice $t = 5$ mm, $d = 19$ mm.

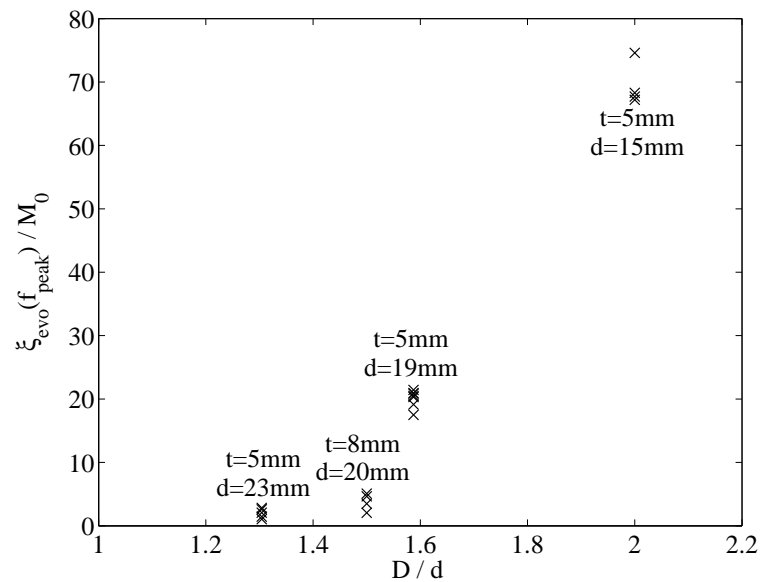


Figure 1.32: From the non-dimensional representation of the potentially whistling frequencies, the values of the ratio $\xi_{evo}(f_{peak})/M_0$ appear to vary a lot when varying the orifices.

1.6 The whistling criterion on other singularities

Additionally to the circular centred orifices, other singularities have been tested: orifices with bevel and smile shaped slits.

1.6.1 Importance of the bevel for the whistling of orifices

Orifices with bevels are schematised in Fig. 1.33 and their features are given in Tab. 1.6.1. Two types of bevels are studied: a rounded bevel and a straight bevel.

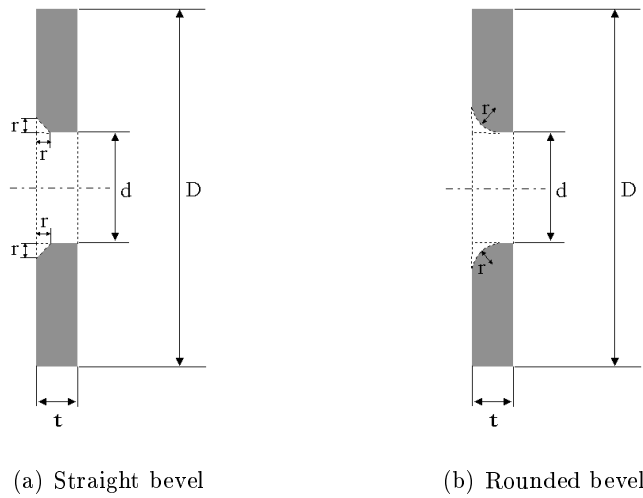


Figure 1.33: Scheme of tested circular-centred single-hole orifice with bevel.

orifice	CCb1	CCb2	CCb3
t (mm)	5	5	5
d (mm)	10	10	10
bevel	1 side	1 side	both sides
bevel type	rounded	straight	straight
r (mm)	≈ 3	1	1

Table 1.4: Features of the single-hole orifices with bevel (r is the bevel radius of curvature).

The idea is to compare the reference orifice, without bevel, illustrated in Fig. 1.34 to a large rounded bevel orifice, placed upstream for Fig. 1.35 or downstream for Fig. 1.36, to a small straight orifice, placed upstream for Fig. 1.37 or downstream for Fig. 1.38, and to a both sides bevel orifice is presented in Fig. 1.39.

Results obtained demonstrate the importance and the position, whether upstream or downstream, of the bevel, on the potentiality of whistling of an orifice:

- a bevel placed on the upstream edge of the orifice attenuates strongly the potentiality of whistling of the orifice. In general, an orifice with a bevel upstream has no whistling potentiality. It is

illustrated in Fig. 1.35 and Fig. 1.37, compared to the reference Fig. 1.35. One potentially whistling case is found in Fig. 1.37 because the bevel is straight, hence a vena-contracta is forming for sufficiently high velocities, which favours potential whistling;

- on the contrary, a bevel placed on the downstream edge of the orifice enhances the potentiality of whistling of the orifice. In general, an orifice with a bevel downstream is potentially whistling. It is illustrated in Fig. 1.38 and Fig. 1.39, compared to the reference Fig. 1.34. An exception is illustrated in Fig. 1.39, where the presence of the rounded bevel downstream decreases the whistling potential ratio of the orifice. This latter result needs further study.
- the form, rather than the size of the bevel, is critical. A very small bevel can prevent from whistling, if placed on the upstream edge of the orifice, as illustrated in Fig. 1.35.

The theory of Howe gives a model to understand qualitatively those results on the importance of the bevel (see (Hirschberg et al., 2002; Hourigan et al., 1990))

It appears that the collapse in Strouhal number ft/U_d for orifices with bevel is not so good as for orifices without bevel. However, the same Strouhal numbers values are approximately found. An increase in the Strouhal number is found for orifices with a bevel downstream: the Strouhal numbers shift from 0.3 without bevel towards 0.5 with bevel (Fig. 1.36, 1.38 and 1.39).

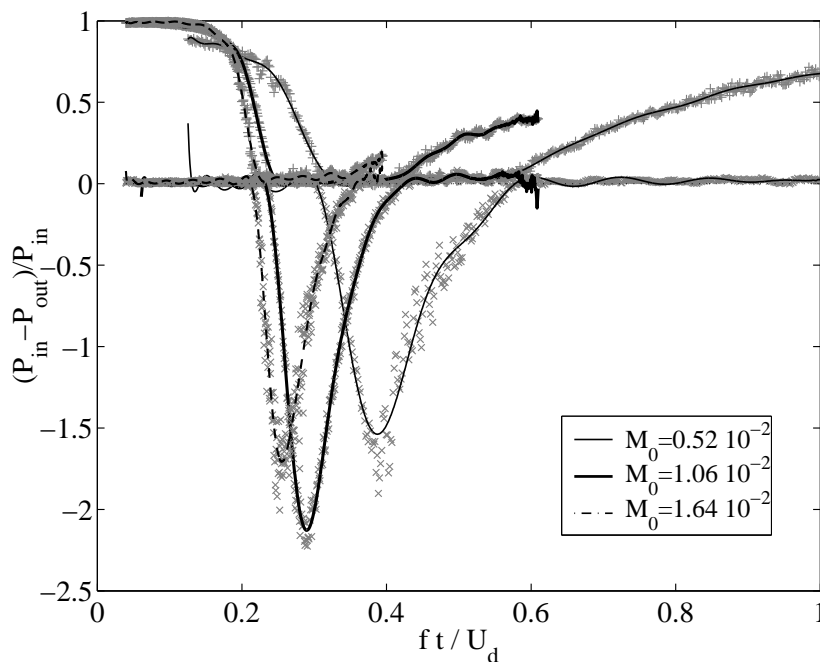


Figure 1.34: Orifice without bevel: potentially whistling eigenvalues obtained for orifice $t = 5$ mm, $d = 10$ mm (CC10).

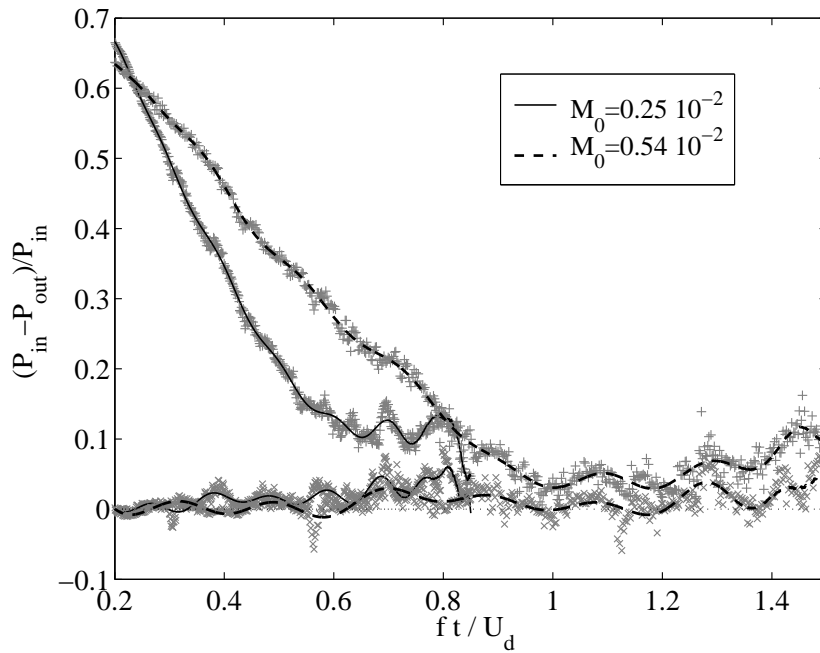


Figure 1.35: Orifice with a large ($r = 3$) rounded bevel on the upstream edge: potentially whistling eigenvalues obtained for orifice $t = 5$ mm, $d = 10$ mm (CCb1).

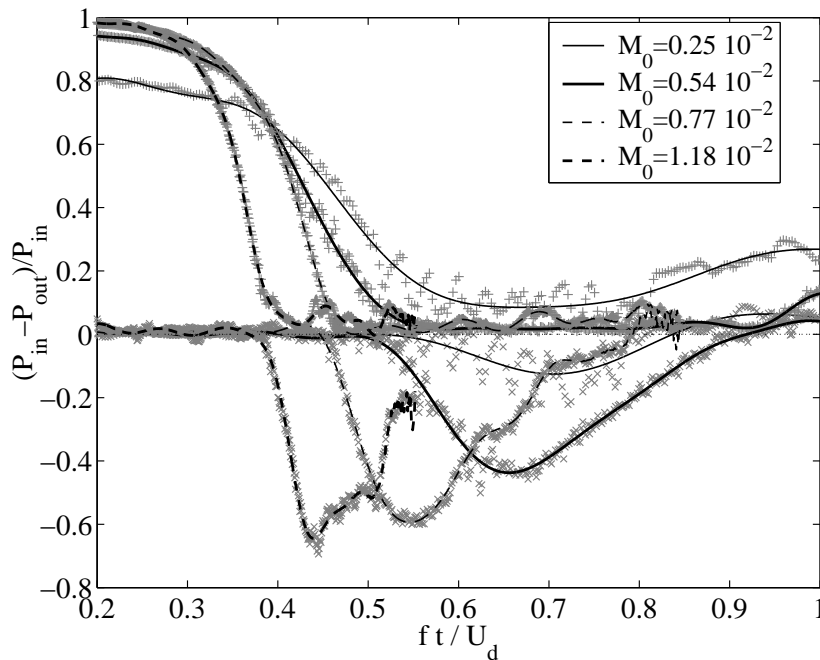


Figure 1.36: Orifice with a large ($r = 3$) rounded bevel on the downstream edge: potentially whistling eigenvalues obtained for orifice $t = 5$ mm, $d = 10$ mm (CCb1).

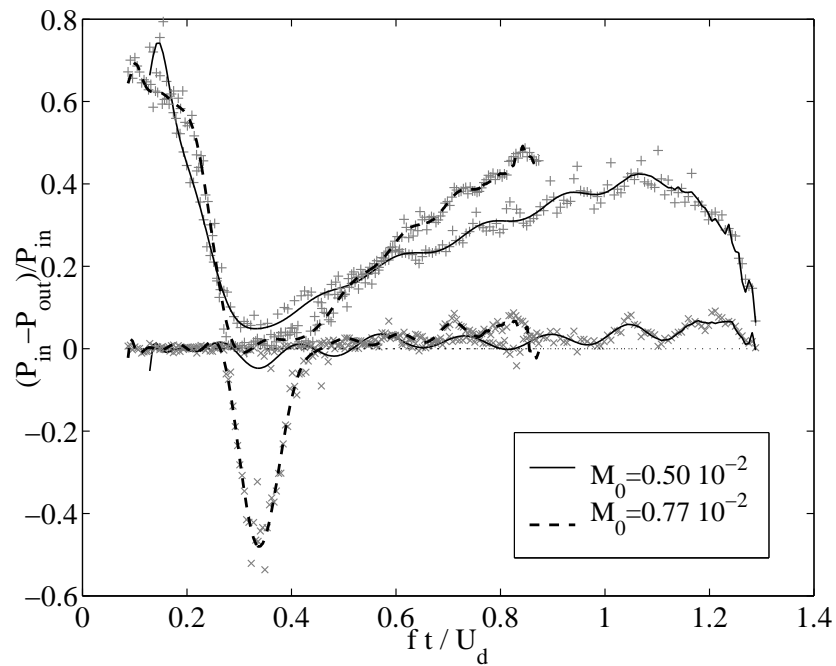


Figure 1.37: Orifice with a small ($r = 1$) straight bevel on the upstream edge: potentially whistling eigenvalues obtained for orifice $t = 5$ mm, $d = 10$ mm (CCb2).

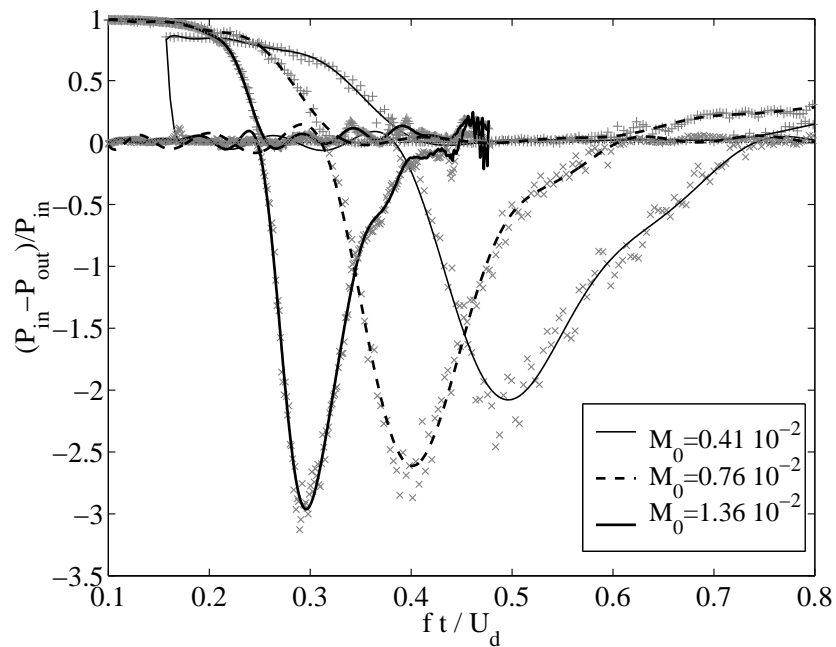


Figure 1.38: Orifice with a small ($r = 1$) straight bevel on the downstream edge: potentially whistling eigenvalues obtained for orifice $t = 5$ mm, $d = 10$ mm (CCb2).

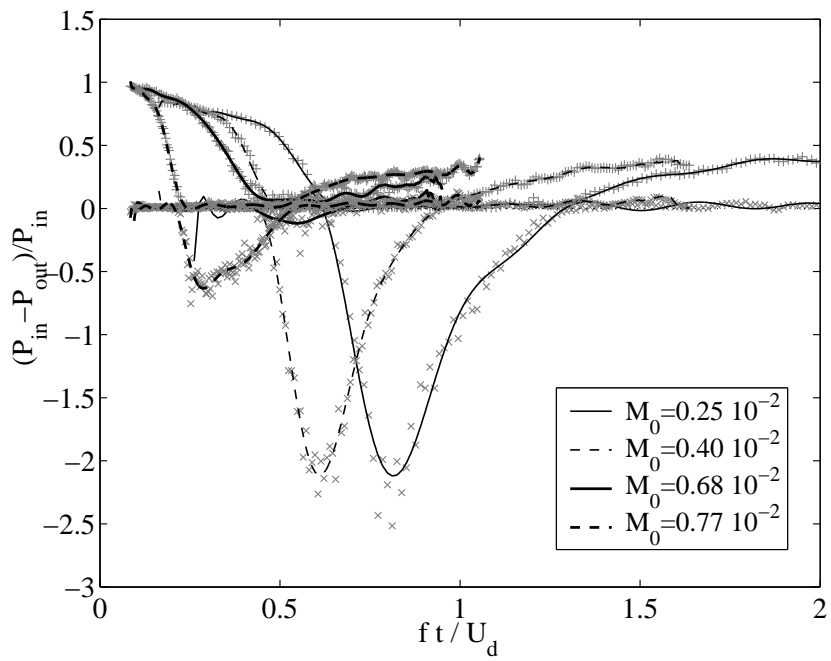


Figure 1.39: Orifice with a small ($r = 1$) straight bevel on both edges: potentially whistling eigenvalues obtained for orifice $t = 5$ mm, $d = 10$ mm (CCb3).

1.6.2 Smile shaped slits

Two smile shaped slits have been tested. They are schematised in Fig. 1.40 and their features are given in Tab. 1.6.2.

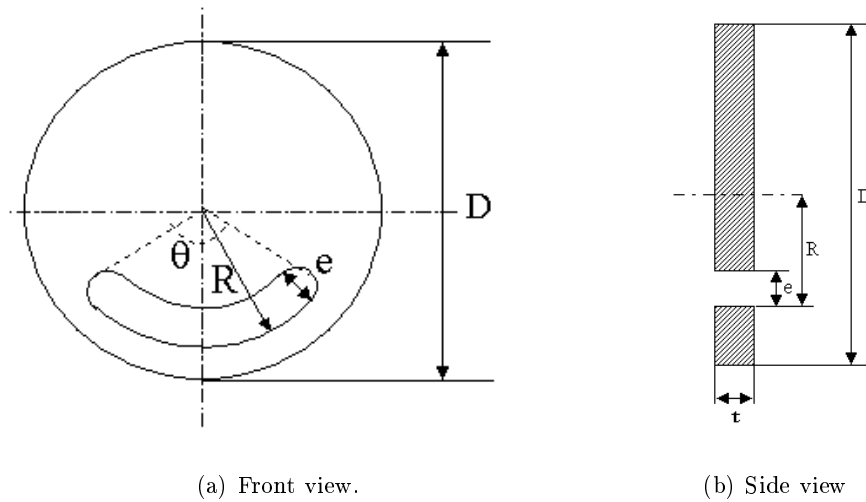


Figure 1.40: Tested smile shaped slits.

smile shaped slit	F1	F2
e (mm)	5	5
R (mm)	15	8
θ (rad)	$\pi/2$	0.69

Table 1.5: Features of the smile shaped slits.

The idea is to compare this non-circular geometry with the previous circular orifices. It appears that these smile shaped slits are potentially whistling (Fig. 1.41 and 1.42). Also, the Strouhal number is very similar (slightly higher) than the one obtained for circular orifices.

These results on smile shaped slits could indicate that any form of slit or orifice would be potentially whistling. Indeed, all orifices and slits tested in this study are potentially whistling, exception made by orifices with a bevel on its upstream edge. This extension of the results needs further study.

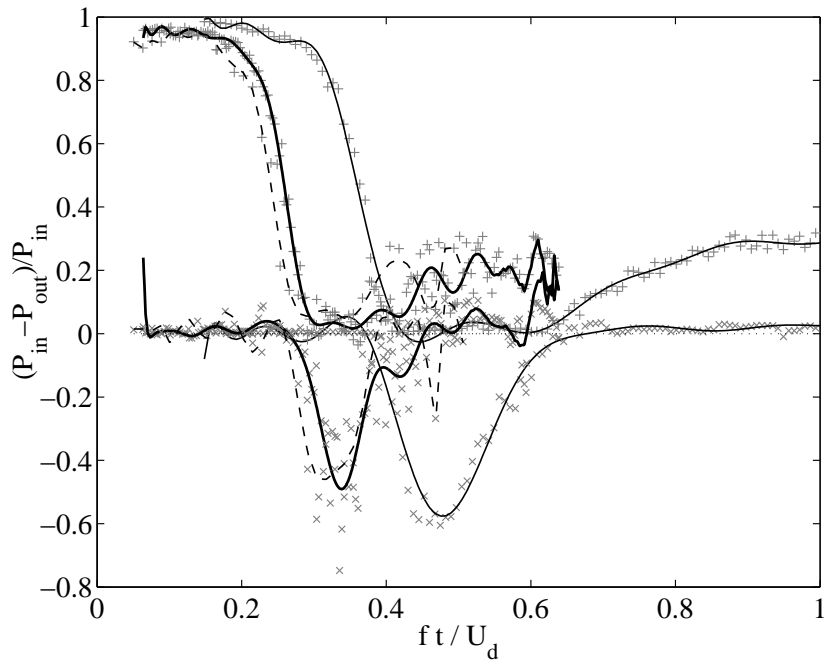


Figure 1.41: Smile shaped slit (F1): potentially whistling eigenvalues - $t = 5 \text{ mm}$, $S_d = 63 \text{ mm}^2$.

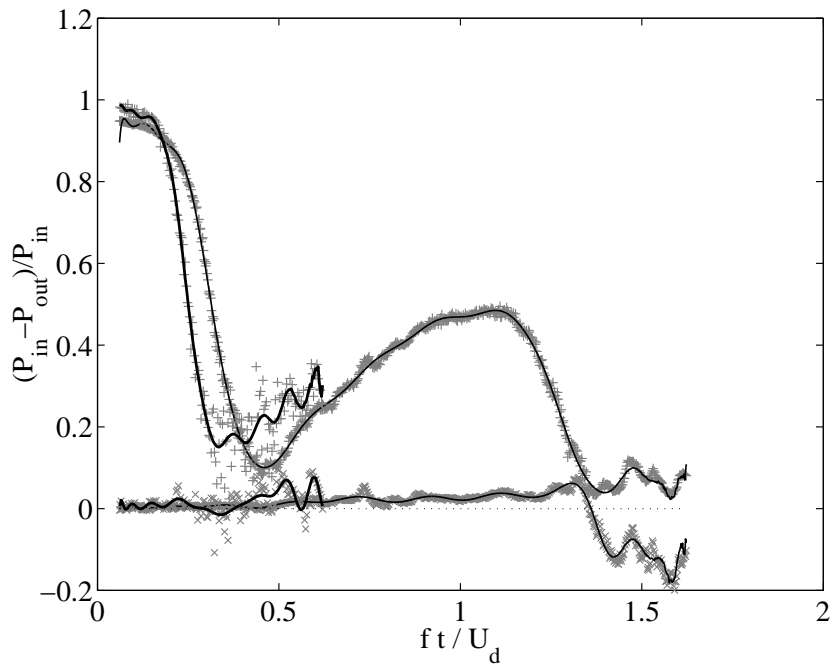


Figure 1.42: Smile shaped slit (F2): potentially whistling eigenvalues - $t = 5 \text{ mm}$, $S_d = 63 \text{ mm}^2$.

1.7 Whistling configurations

In this section, configurations with no exterior source are investigated. Acoustical reflections from both sides of the orifice are placed, in order to make the orifice spontaneously whistle for certain ranges of flow regime. The objective is to link the experimentally observed whistling frequencies with the previously presented potentially whistling frequencies.

It is not difficult to obtain whistling from a potentially whistling orifice. One has to place acoustic reflection conditions from at least one side of the orifice. We focus in the following in a particular configuration, to describe more quantitatively those results when the orifice under flow whistles spontaneously.

1.7.1 Whistling configuration

The following whistling configuration is studied. In order to provide the acoustic feedback necessary for whistling to occur, acoustic reflections coefficients upstream and downstream of the orifice have to be sufficiently high. For the example described in this section, the configuration used is shown in Fig. 1.43. The orifice tested is $t = 5$ mm, $d = 10$ mm (CC10). The acoustic reflections used are the following:

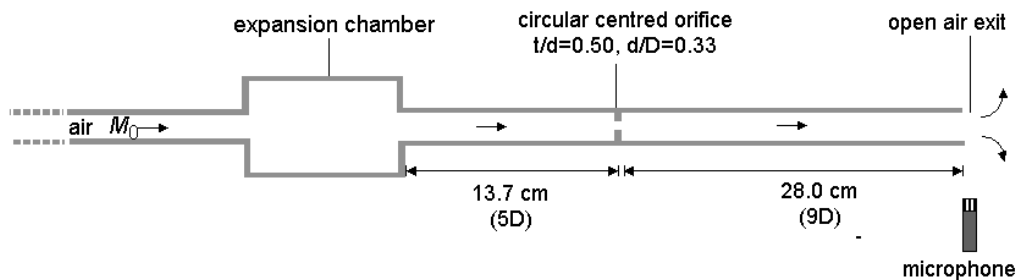


Figure 1.43: The studied whistling configuration: an orifice; upstream of the orifice, an expansion chamber; downstream of the orifice, an open pipe termination, to allow sufficient acoustic feedback.

- upstream of the orifice (at 0.137 m from the upstream edge of the orifice): an expansion chamber imposes a high reflection coefficient: $|R_u| \approx 0.8$ in the frequency range 400 - 2500 Hz, weakly dependent on the flow velocity (Fig. 1.44);
- downstream of the orifice (at 0.270 m from the upstream edge of the orifice): an unflanged open pipe termination. It imposes a high reflection coefficient: $|R| > 0.4$ in the frequency range 400 - 2500 Hz (Fig. 1.45);

1.7.2 Comparison between whistling frequencies and potentially whistling frequencies

Whistling frequencies, as illustrated in Fig. 1.46 and Fig. 1.47, correspond to Strouhal numbers $f_{whistling}t/U_d$ of 0.2 - 0.4 . They are in well agreement with the potentially whistling frequencies

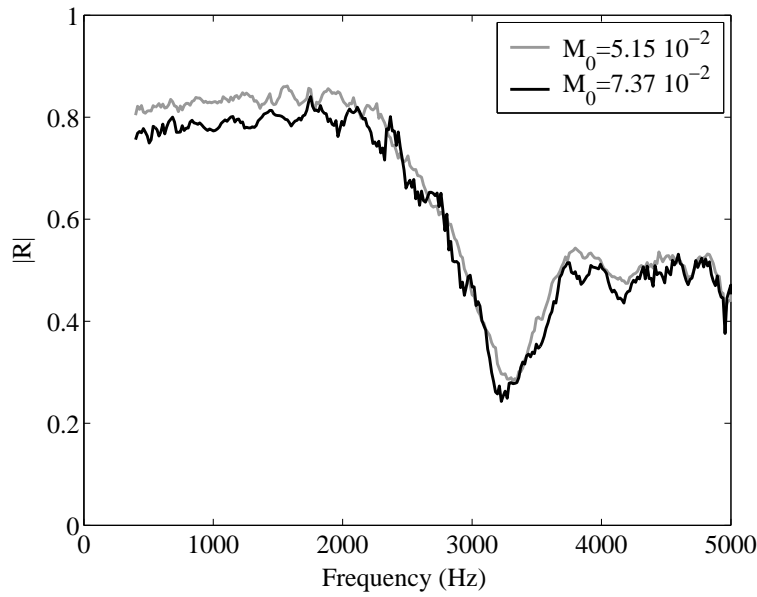


Figure 1.44: Characteristics of the whistling configuration: the reflection coefficient of the expansion chamber (seen from the orifice).

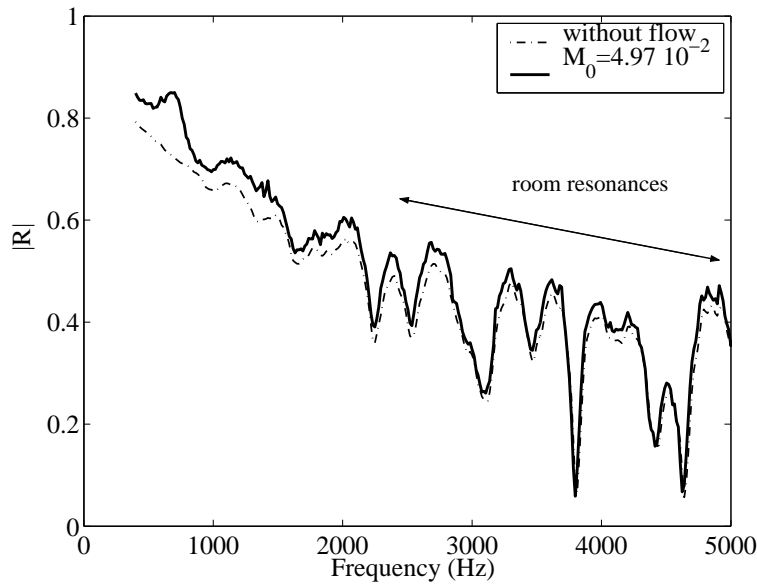


Figure 1.45: Characteristics of the whistling configuration: the reflection coefficient of the unflanged open pipe end (seen from the orifice).

determined by the whistling criterion (and presented in Fig.A.10). There is a slight discrepancy for the low limit, but a good agreement in tendency.

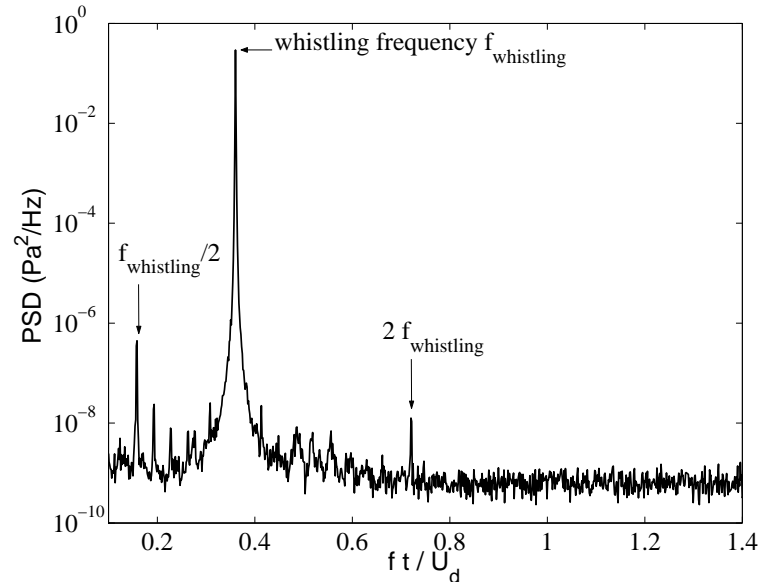


Figure 1.46: In the whistling configuration, example of typical SPD spectrum obtained far downstream of the orifice (at microphone d4), exhibiting whistling frequency and harmonics ($M_0 = 4.62 \times 10^{-3}$).

The discrepancy corresponds to a discrepancy in the Strouhal number of 0.03 and in frequency of 140 Hz at its maximal value, around $M_0 = 7.7 \times 10^{-3}$. This may be due to the different flow condition impacting the upstream edge of the orifice, because the expansion chamber is only at $5D$ upstream of the orifice. Hence the flow conditions between the non-whistling and whistling configurations may be different.

1.7.3 Comparison between whistling frequencies in air and in water

We add in this section the results obtained in chapter 4, when analysing measurements in water in an industrial loop, with high reflecting acoustic boundary conditions. Whistling frequencies have been observed, in presence altogether of cavitation phenomena.

The comparison between our measured instability frequencies in air is plotted in Fig.1.48. This is a spectacular result. The values observed in water are quite close to the values obtained for the potentially whistling frequencies for thin circular centred orifices in air. That gives a strong indication that the Strouhal number is not highly sensitive on the compressibility of the fluid, on the presence or not of cavitation, on the pipe diameter and on the static pressures in the pipe. This completes satisfactorily our study of the Strouhal number, as we have not varies those parameters.

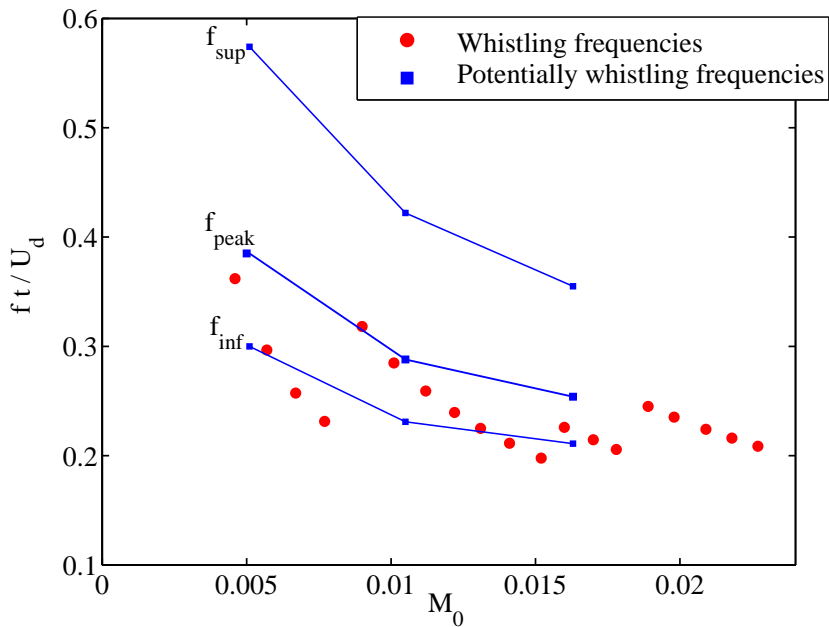


Figure 1.47: Comparison of the whistling frequencies observed and the potentially whistling frequencies measured (f_{inf} and f_{sup} are respectively the inferior and superior frequencies of the potentially whistling first mode, f_{peak} is the frequency in this range corresponding to the maximum ratio of produced acoustic power).

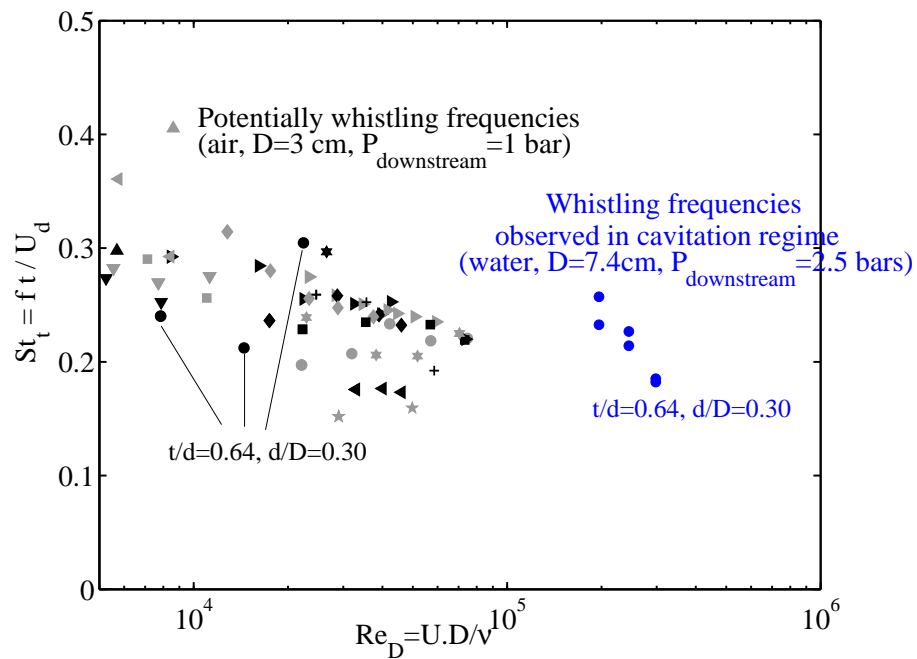


Figure 1.48: Comparison between the whistling frequencies observed in industrial measurements in water for a circular centred orifice (analysed in chapter 4), and the potentially whistling frequencies of circular centred orifices obtained with the whistling criterion.

1.7.4 A model to predict the instability frequency

In this section, we propose a simple model to predict the whistling frequency (as shown in the previous section) of an orifice in an acoustic system with reflection coefficients.

The configuration of the model is illustrated in Fig. 1.49. An orifice under constant flow in a duct is considered. It is represented by its scattering matrix under this flow \mathbf{S}_e . The upstream R_u and downstream R_d acoustic reflections are localized at L_u and L_d from the upstream edge of the orifice.

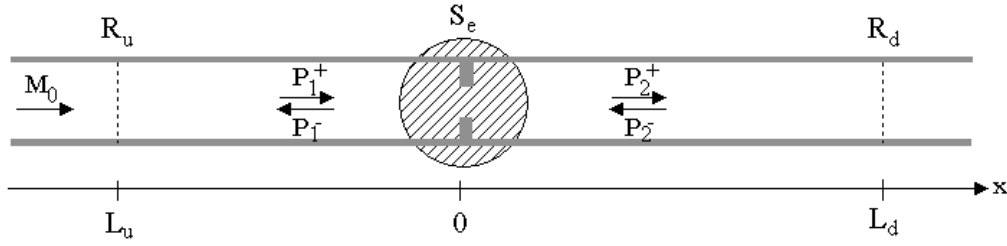


Figure 1.49: Scheme of the model to predict the whistling frequency, in plane wave approximation, using the scattering matrix of the singularity S_e and the characteristics of the acoustic reflections R, L upstream and downstream of the singularity.

The idea is to use a linear model of basic acoustic propagation equations to identify frequencies for which stationary plane waves exist. Then by feedback loops, it is assumed that these stationary frequencies can be amplified to create whistling. Hence the frequency of whistling is deduced. It is assumed that there is no shift in frequency during the amplification and saturation of the waves. This hypothesis is impossible to estimate, as our model is linear, and amplification and saturation phenomena are non-linear.

The plane waves propagate in the ducts assuming no attenuation:

$$p_1^+(x, \omega) = P_1^+ e^{j(\omega t - kx)}, \quad p_1^-(x, \omega) = P_1^- e^{j(\omega t + kx)}, \tag{1.58}$$

$$p_2^+(x, \omega) = P_2^+ e^{j(\omega t - kx)}, \quad p_2^-(x, \omega) = P_2^- e^{j(\omega t + kx)}. \tag{1.59}$$

The acoustic propagation equations in this configuration can be expressed at $x = 0$. The influence of the orifice:

$$\begin{pmatrix} P_2^+ \\ P_1^- \end{pmatrix} = \mathbf{S}_e \begin{pmatrix} P_1^+ \\ P_2^- \end{pmatrix}, \tag{1.60}$$

with:

$$\mathbf{S}_e = \begin{pmatrix} T_e^+ & R_e^- \\ R_e^+ & T_e^- \end{pmatrix} \tag{1.61}$$

and the upstream and downstream reflections:

$$P_1^+ = R_u(x = 0, \omega) P_1^-, \tag{1.62}$$

$$P_2^- = R_d(x = 0, \omega) P_2^+, \tag{1.63}$$

where $R_u(x=0, \omega) = R_u(x=L, \omega) e^{2jkL}$ and $R_d(x=0, \omega) = R_d(x=L, \omega) e^{-2jkL}$.

In this system, there are four unknowns, $P_1^+, P_1^-, P_2^+, P_2^-$, with four equations:

$$\begin{pmatrix} 1 & -R_u & 0 & 0 \\ 0 & 0 & -R_d & 1 \\ R_e^+ & -1 & 0 & T_e^- \\ T_e^+ & 0 & -1 & R_e^- \end{pmatrix} \begin{pmatrix} P_1^+ \\ P_1^- \\ P_2^+ \\ P_2^- \end{pmatrix} = \begin{pmatrix} 0 \\ 0 \\ 0 \\ 0 \end{pmatrix}. \quad (1.64)$$

There exists a non-vanishing solution if the determinant of the system is zero: this corresponds to the existence of stationary plane waves at that frequency, such that:

$$R_u R_d (T_e^+ T_e^- + R_e^+ R_e^-) - R_u R^+ - R_d R^- + 1 = 0 \quad (1.65)$$

The study of the cancellation of the determinant should hence give the whistling frequencies reported in the previous section.

We apply this model to the whistling configuration described in the previous section. The scattering matrix coefficients used are the ones measured. The reflection coefficients used have been simplified compared to experiment. The loss is mainly on the phase information, but end corrections are taken into account (see Fig. 1.50):

$$R_u(x=0, \omega) = -0.8 e^{2jk(Lu+0.82a)} \quad (1.66)$$

$$R_d(x=0, \omega) = -[0.73 - 1.5 \cdot 10^{-4} (f - 1000)] e^{-2jk(Ld+t+0.61a)} \quad (1.67)$$

In this latter, we have used the end correction of an exit of a tube with thin walls (formula of Levine and Schwinger (1948)). Results are illustrated in Fig. 1.51, 1.52 and 1.53. Although reflection coefficients used are approximate, the model seems to give satisfactory results. However, further study is needed to obtain more data and confirm this result.

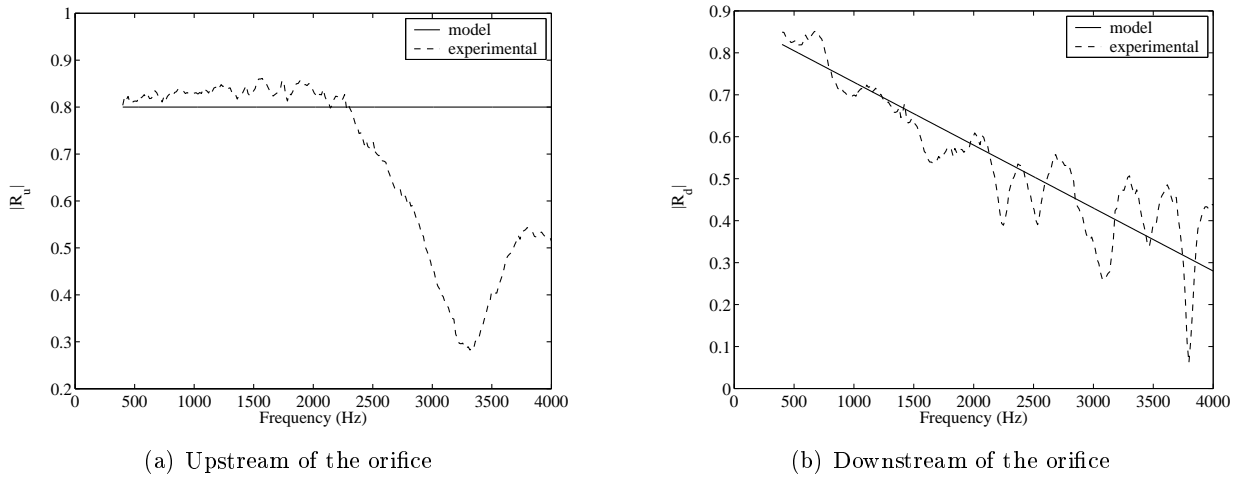


Figure 1.50: Model to predict the whistling frequency: simplified reflection coefficients are applied compared to measurements.

A parametric study is done on the upstream reflection coefficient, as illustrated in Fig. 1.54. When varying its magnitude, it is observed that the whistling frequency does not change much (few Hz).

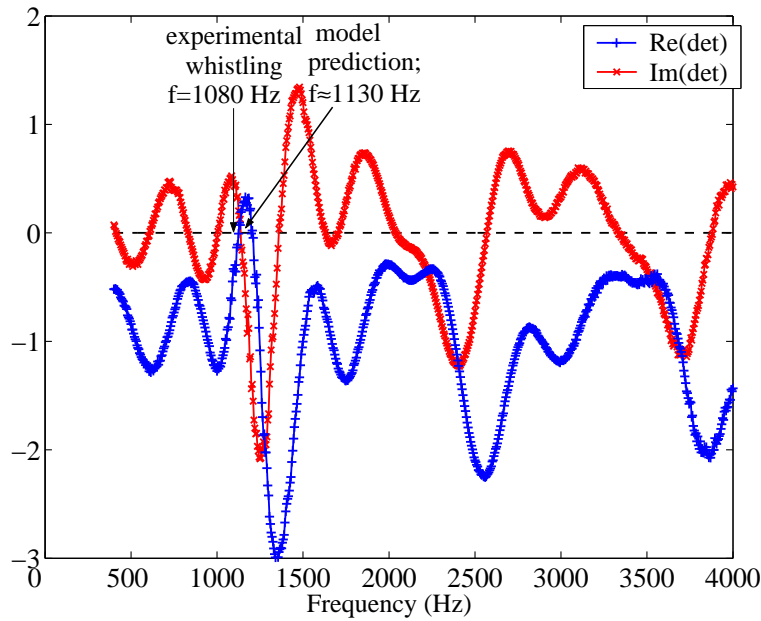


Figure 1.51: Model to predict the whistling frequency, example 1: the model gives a satisfactory prediction of the measured whistling frequency - $M_0 = 5.2 \cdot 10^{-3}$.

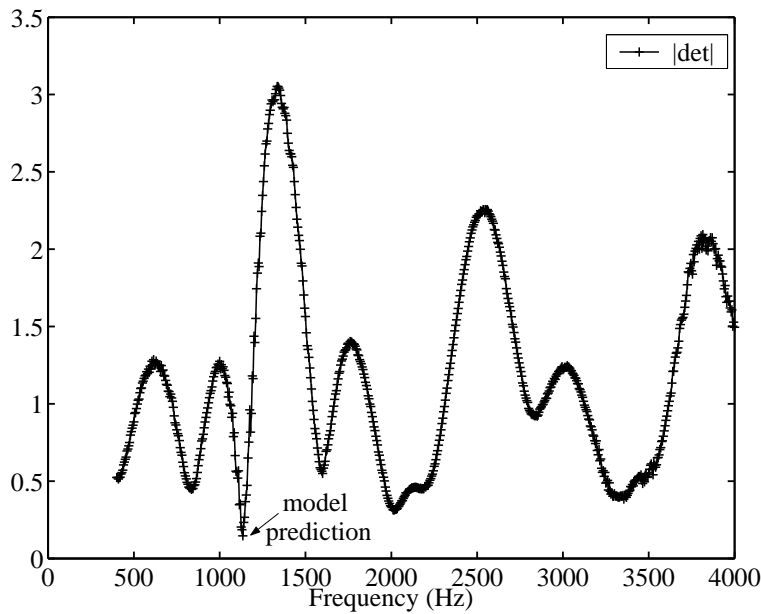


Figure 1.52: Model to predict the whistling frequency, example 1: the model gives a satisfactory prediction of the measured whistling frequency - $M_0 = 5.2 \cdot 10^{-3}$.

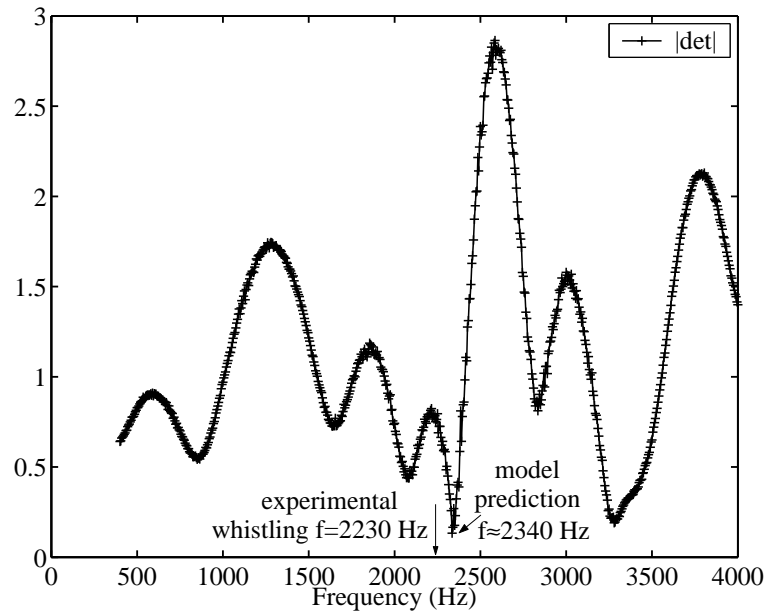


Figure 1.53: Model to predict the whistling frequency, example 2: the model gives a satisfactory prediction of the measured whistling frequency - $M_0 = 1.64 \cdot 10^{-2}$.

Below a certain value of the reflection coefficient, the model predicts no whistling. This is in agreement with experiments: both reflections, upstream and downstream, are necessary to obtain whistling. It is also observed that the whistling frequency, as illustrated in Fig. 1.54, is close to a $\lambda/2$ type frequency of the resonator of length L_u .

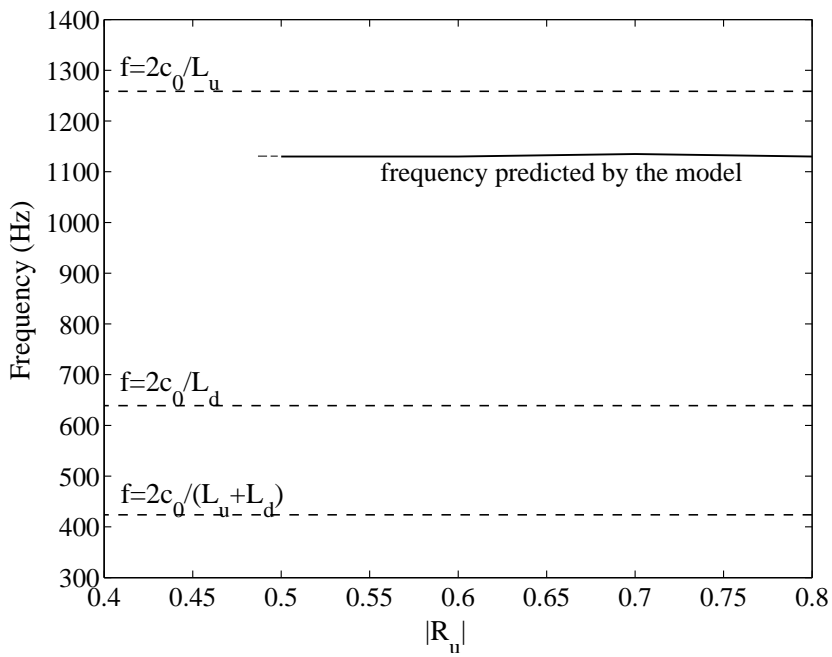


Figure 1.54: Model to predict the whistling frequency: parametric study varying the magnitude of the upstream reflection coefficient. The frequency obtained with the model does not vary with the magnitude, and no whistling is obtained when the magnitude of the reflection coefficient is low enough (<0.5 here) - $M_0 = 1.64 \cdot 10^{-2}$.

1.7.5 A failed model to predict the instability with Bode-Nyquist idea

Another model has been tried to predict the instability frequency of an orifice in an acoustic system with reflection coefficients. This model uses the ideas of Bode and Nyquist for the amplification of open system. However, it has not given satisfactory results. The idea is however presented in the following.

Experimentally, it is found (see section 1.5.5) that the scattering matrix, in the new basis of vectors $(-1,1);(1,1)$, can be approximately written:

$$\mathbf{S}'_e \approx \begin{pmatrix} \mu & 0 \\ 0 & 1 \end{pmatrix}, \quad (1.68)$$

where μ is the gain associated to the vector in phase opposition $(-1,1)$. The vector in phase $(1,1)$ is unaltered when going through the orifice.

The source generates upstream and downstream plane waves. Each waves couple can be decomposed on the basis of vector: $(-1,1); (1,1)$. From the previous analysis of S'_e , the potentially amplified wave is the one in phase opposition, collinear to the vector $(-1,1)$: the source is a dipole. Hence if the source generates $(-\Pi_{1s}^-, \Pi_{2s}^+)$, it comes after an upstream and downstream acoustic feedback in the system an amplification of :

$$\begin{pmatrix} -\Pi_{1s}^- \\ \Pi_{2s}^+ \end{pmatrix} \longrightarrow \begin{pmatrix} -R_u \Pi_{1s}^- \\ R_d \Pi_{2s}^+ \end{pmatrix} = \frac{R_u + R_d}{2} \begin{pmatrix} -\Pi_{1s}^- \\ \Pi_{2s}^+ \end{pmatrix} + \frac{-R_u + R_d}{2} \begin{pmatrix} \Pi_{1s}^- \\ \Pi_{2s}^+ \end{pmatrix}, \quad (1.69)$$

where R_u and R_d are upstream and downstream reflection coefficients.

Next, this wave is amplified by the scattering matrix: the amplification of the complete return path (or open loop) of the vector collinear to $(-1,1)$ is:

$$\begin{pmatrix} -\Pi_{1s}^- \\ \Pi_{2s}^+ \end{pmatrix} \longrightarrow \mu \frac{R_u + R_d}{2} \begin{pmatrix} -\Pi_{1s}^- \\ \Pi_{2s}^+ \end{pmatrix} \quad (1.70)$$

Applying Bode and Nyquist theory, an amplification (i.e. instability) occurs at a frequency if the both following conditions are obtained:

- the gain is superior to the unity, that is:

$$\left| \mu \frac{R_u + R_d}{2} \right| > 1 \quad (1.71)$$

- the phase delay of the gain is an integer number of 2π : the returning wave is in phase with the generated one, that is:

$$phase \left(\mu \frac{R_u + R_d}{2} \right) = 0 \quad (1.72)$$

Unsatisfactory results have been obtained. The configuration used is the same as described in the previous section (same reflection coefficients). The example described in the following is obtained for $M_0 = 1.01 \cdot 10^{-2}$, but four different flow velocities and two different configurations have been tested. Whistling is observed, as illustrated in Fig. 1.55, at 1776 Hz in the example described. The model

predicts no whistling, as the magnitude of the gain (Fig. 1.58) is under the unity.

However, some results are obtained: the assumptions of the model on the shape of the scattering matrix S'_e are verified (Fig. 1.56), the phase of the gain vanishes around 1820 Hz (Fig. 1.57) and the magnitude of the gain is maximum at a value of 0.6 in the range 1550-1750 Hz. The unsatisfactory result of this model may be due to inaccuracies when adopting the approximate expression of the scattering matrix S'_e . The magnitude of the gain may be sensitive to this approximation. However, this model is based on this approximation, so that no improvement of the model is proposed.

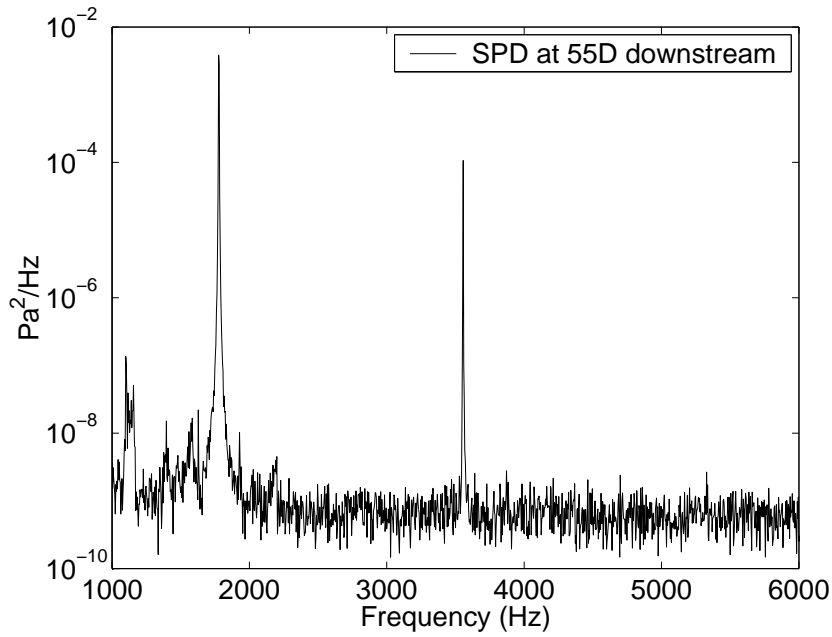


Figure 1.55: Presentation of the case presented: the configuration used is described in the previous section, using, from both sides of the orifice, an expansion chamber and an open pipe end termination to create acoustic reflections, and a flow of $M_0 = 1.01 \cdot 10^{-2}$. The spectrum observed shows a whistling frequency of 1776 Hz.

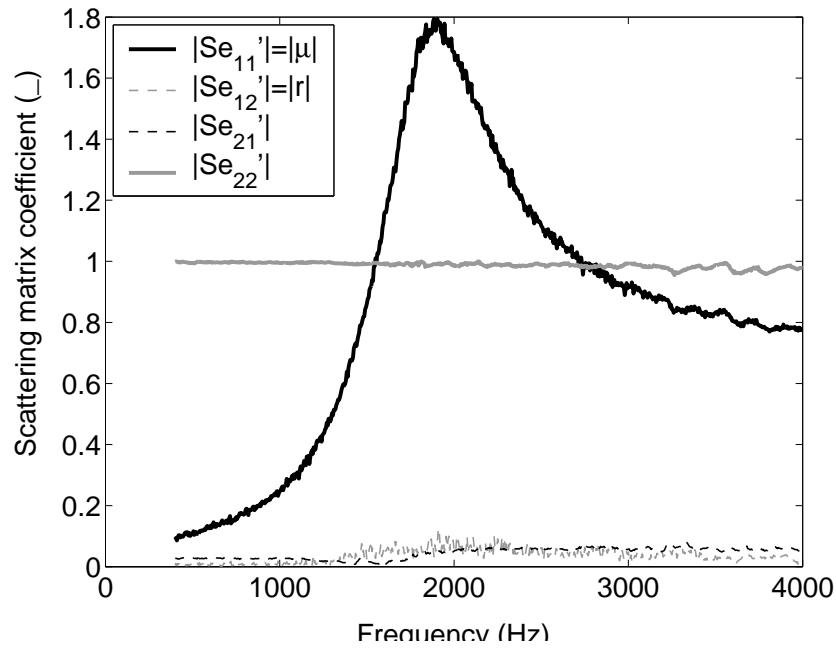


Figure 1.56: Scattering matrix S'_e written in the new basis of vectors $(-1,1);(1,1)$. The assumption of the Bode-Nyquist model that the extra-diagonal coefficients of the experimental scattering matrix are negligible seems correct, as well as the assumption that Se'_{22} equals the unity - $M_0 = 1.01 \cdot 10^{-2}$.

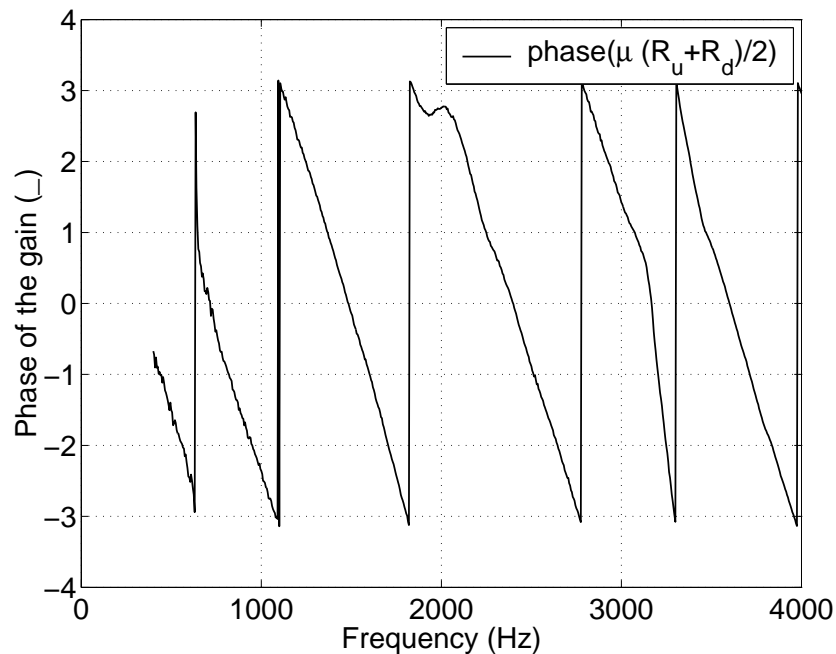


Figure 1.57: Phase of the gain. The application of the Bode-Nyquist model asks for a value of the phase equalling 0 $[2\pi]$. Such a condition is found around 1820 Hz, close to the observed whistling frequency (1776 Hz).

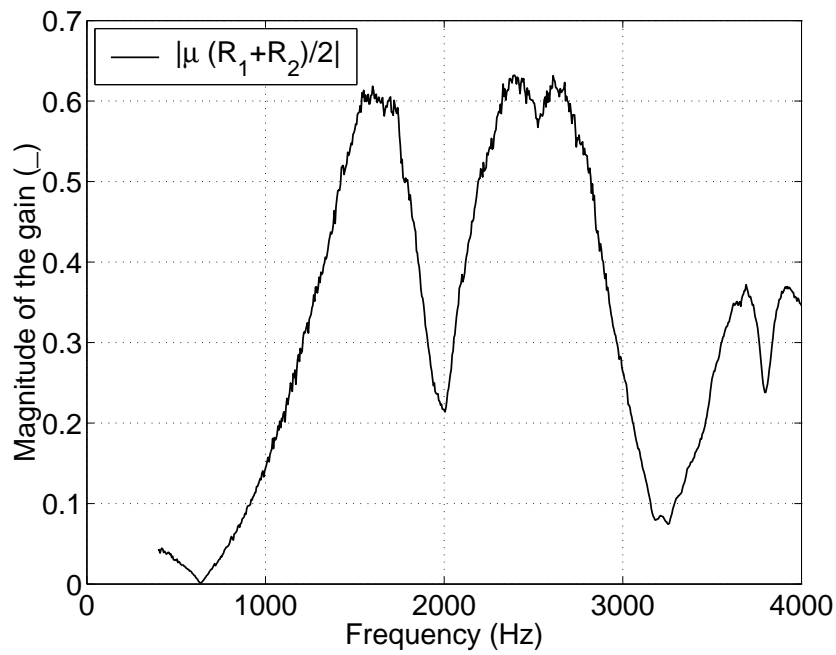


Figure 1.58: Magnitude of the gain. The application of the Bode-Nyquist model asks for a value of magnitude over the unity, to predict whistling frequencies. No such condition is found around the observed whistling frequency 1776 Hz. However, a maximum value around 0.6 is obtained in the range 1550-1750 Hz.

1.8 Broadband noise

Broadband spectra are presented in complements of the previous sections. The objective is to study the effect of the potentially whistling frequencies on the spectra obtained in real conditions, that is without exterior source and in presence of acoustic reflections from both sides of the orifice.

1.8.1 Broadband spectra

Measurements are done in ‘Frequency Response’ mode: no source is used, only turbulence noise is measured. Acoustic terminations are the same as for scattering matrix measurements (with a reflection of about 6% of the acoustic energy in one round trip).

Spectra as PSD (Power Spectral Densities) are obtained at the 8 transducers. Only the spectrum at microphone d4 is presented here. This microphone is placed at $55D$ downstream of the orifice, so that this observation point is far away from the source region.

A typical result for orifice $t = 5$ mm, $d = 15$ mm is given in Fig. 1.59:

- the hump form around 5500 Hz seems to correspond to the amplification due to the first transverse mode. This frequency is relatively far from the cut-off frequency of the pipe at 6700 Hz without flow, but we observe experimentally that this hump does not vary with the Mach number;
- the first hump form corresponds to potentially whistling frequencies. This is confirmed by the representation in Strouhal number given in Fig. 1.60. Data collapse very well in the x-coordinates with the Strouhal representation. Also, data collapse well in magnitude by dividing the PSD with the square of the estimated pressure drop across the orifice (the vena contracta coefficient is taken equal to 0.70) with a classical quasi-stationary model (see Hofmans (1998)).

1.8.2 Lighthill scaling laws

Investigations have been lead to verify Lighthill scaling laws: a dipole noise would follow a law in M_d^4 (M_d is the Mach number at the orifice), while a turbulence noise would follow a law in M_d^6 (Nelson and Morfey, 1981).

Results are shown in Fig. 1.61 and 1.62 with 1/3 band octave spectra. As a result, it seems that the behaviour of the orifice is more complex than those simple scaling laws.

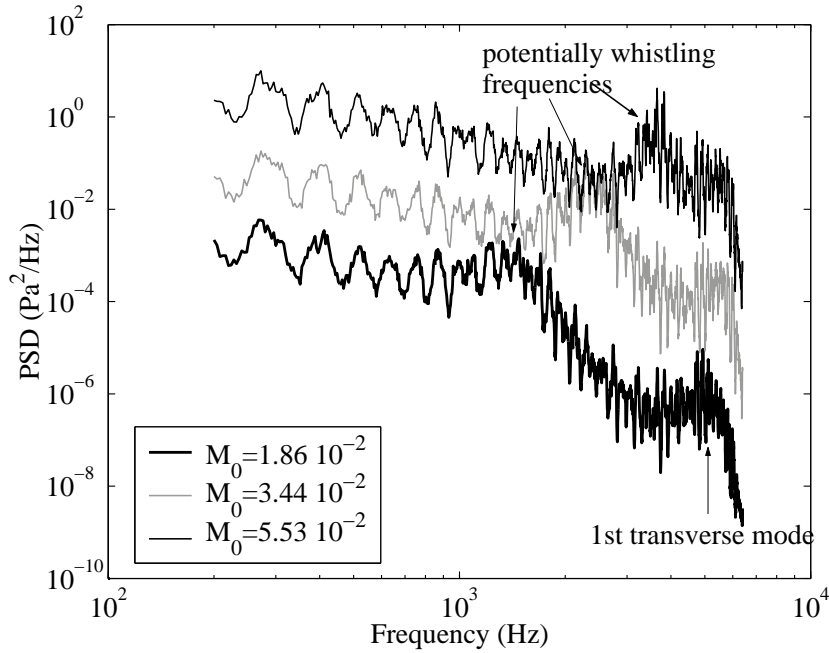


Figure 1.59: Typical broadband noise spectra obtained far downstream ($55D$) of the orifice: appearance of a hump of production of acoustic energy, corresponding to the potentially whistling frequencies - orifice $t = 5$ mm, $d = 15$ mm with various Mach numbers.

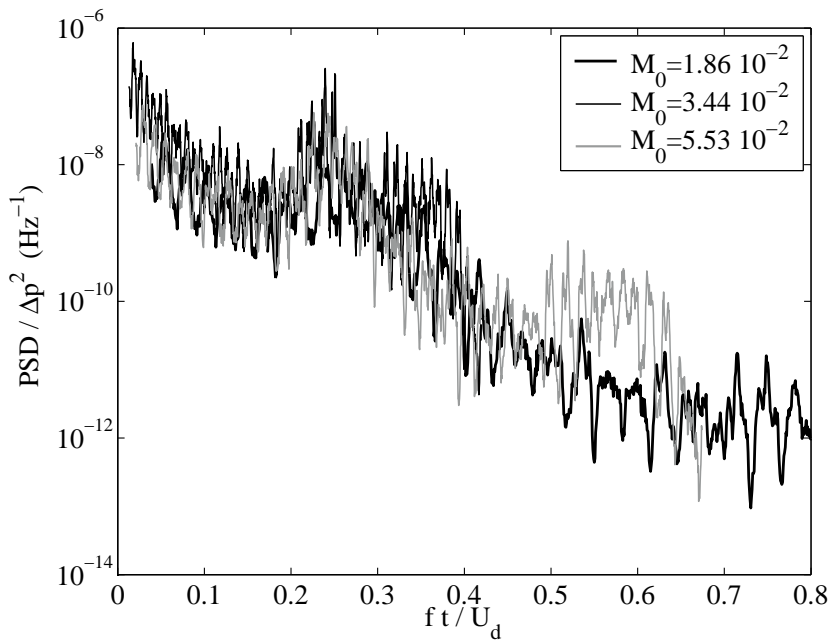


Figure 1.60: Non-dimensional broadband noise spectra obtained far downstream ($55D$) of the orifice: the hump form of production of acoustic energy corresponds to the potentially whistling Strouhal numbers (here around 0.2 -0.3) - orifice $t = 5$ mm, $d = 15$ mm with various Mach numbers.

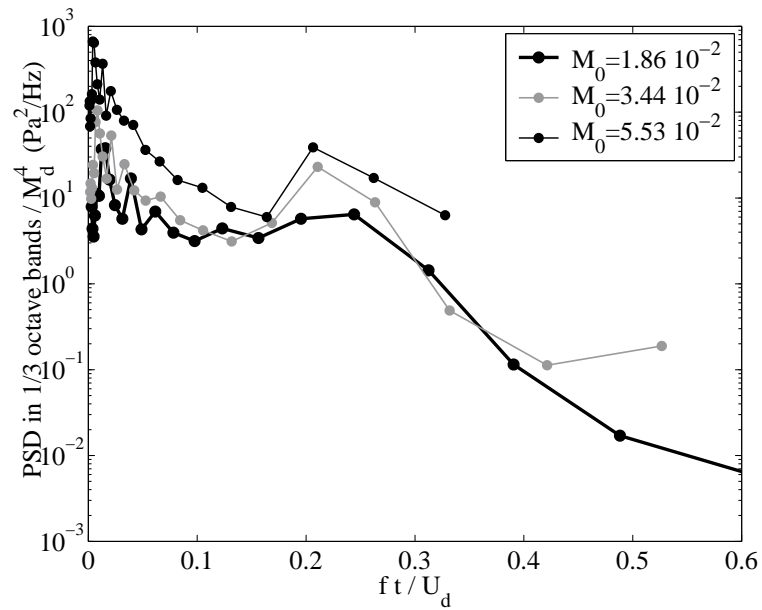


Figure 1.61: Evaluation of the non-dimensional noise representation using the Lighthill scaling law in M_d^4 when assuming a dipole noise: this representation is not satisfactory for the hump form corresponding to an assumed dipole type source of sound - orifice $t = 5$ mm, $d = 15$ mm.

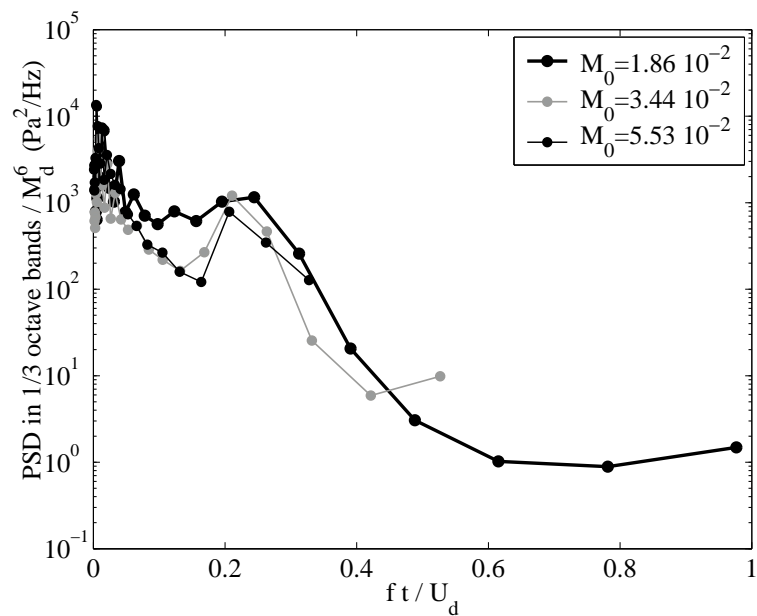


Figure 1.62: Evaluation of the non-dimensional noise representation using the Lighthill scaling law in M_d^6 when assuming a turbulence noise: this representation is not satisfactory for the broadband spectrum outside the hump form - orifice $t = 5$ mm, $d = 15$ mm.

1.9 Conclusion

This chapter is an experimental study of a whistling criterion of singularities under constant air flow in a straight pipe. The singularities tested are mainly a range of thin circular-centred single-hole orifices, with various thickness and diameter. The tested air flow conditions are typical of nuclear power plant: high Reynolds number (of the order of 10^4 - 10^5), and low Mach number (of the order of 10^{-2} in air). The whistling criterion into account is a simple acoustic energy balance, in our case limited to a plane-wave propagation, applied to a region enclosing the vortex shedding and the orifice. The idea is to assimilate the whistling with an acoustic power production (physically, some energy of the flow is transferred to acoustic energy), and to link this acoustic balance with the scattering matrix of the orifice under this flow.

Our experimental results validate the whistling criterion:

- on the one hand, using this criterion, ranges of potentially whistling frequencies are systematically found (section 1.5.3), whatever the orifice tested and the flow imposed (as long as the orifice has no beaver on its upstream edge, and that the flow is non-vanishing). These frequencies correspond to the frequencies of instability, of type Kelvin-Helmholtz, of the shear layer formed at the separation point on the upstream edge of the orifice;
- on the other hand, our measurements in actual whistling conditions, that is, when there are acoustic reflecting conditions from both sides of the orifice (for instance, using an expansion chamber and an open pipe end termination), show that the whistling frequencies are close to the potentially whistling frequencies (section 1.7). This indicates that the non-linear process of saturation of the self-sustained oscillation does not modify much the frequency of instability from which it starts. A close study on the level of correspondence of these two frequencies has not been made;
- Additionally, the study of the broadband noise, when only turbulent noise is present because the acoustic reflecting conditions are too low, confirms that an acoustic production occurs at these instability frequencies, which gives a direct confirmation of the validity of the whistling criterion (section 1.8).

A deep study has been made on the potentially whistling or instability frequencies. Literature data have been confirmed and quantitatively established:

- a Strouhal number corresponding to these instability frequencies has been studied extensively on single-hole circular-centred orifices without bevel (section 1.5.3). Various scaling variables have been tested to define this Strouhal number, but the most satisfactory ones have proven to be the orifice thickness, and the orifice velocity.

The values obtained are quite constant, between 0.2 and 0.3, concerning the first hydrodynamic mode and a fully turbulent pipe flow (pipe Reynolds number above $5 \cdot 10^3$). This range of values is in close coherence with literature data from Anderson. The Strouhal number is shown to decrease slightly with the Reynolds number, and to vary slightly with the orifice thickness and diameter. Higher order hydrodynamic modes (up to mode three) are present in our data, but have not been particularly studied.

Additionally, it has been observed that, for a flow close to the laminar-turbulent transition (pipe Reynolds number under $5 \cdot 10^3$), Strouhal numbers increase significantly. It is attributed to the fact that the flow in this case is of a different kind;

- the study of other singularities (section 1.6), that is, curved slits, has shown similar results: potentially whistling ranges of frequency and similar Strouhal number values. This seems to confirm that the whistling criterion can be applied on any kind of discontinuity;
- the influence of a bevel on an edge of the orifice has been studied (section 1.6.1). Particularly, a bevel on the upstream edge of the orifice is shown to be critical for whistling: it reduces much the potentiality of whistling. This result is in accordance with literature data, and with our actual whistling observations;
- the incident wave conditions allowing the instability have been clarified (section 1.5.5). The maximum of production of acoustic energy correspond to an excitation of the shear layer with a maximum of acoustic velocity (a minimum acoustic pressure). In other terms, whistling occurs when the incident pressure waves from both sides of the orifice are equal in magnitude and in phase opposition. Complementarily, no energy exchange occurs between the acoustic field and the main flow when the incident waves are in phase (velocity node). Those results are in agreement with qualitative descriptions in literature;
- a dimensionless representation of the amplitude of the eigenvalues from the whistling criterion, representing an acoustic power ratio, has been proposed and is shown to be quite constant with the Mach number (section 1.5.6), for a given orifice. However, when varying the orifice thickness and diameter, strong discrepancies are found: hence more study is needed to find a satisfactory dimensionless representation.

In actual whistling configurations, that is without any exterior sources and acoustic reflections from both sides of the orifice, the following results are obtained:

- an understanding of the whistling configurations is obtained (section 1.7.1). The whistling occurs if there is enough acoustic reflection (upstream and/or downstream of the orifice) in the test rig;
- a model is proposed (section 1.7.4) to predict the whistling frequency, given the scattering matrix of the orifice under the flow, and the two (upstream and downstream) acoustic reflection coefficients. The model gives satisfactory results but would need more data to be considered as validated.

In perspective, numerous studies would worth being made to complement this first study on this whistling criterion:

- to confirm this validation work, other singularities would be worth testing, such as types of orifices (multi-hole orifices, thick orifices), valves, and the assembly of successive singularities. The difficulty when using other geometries is that higher order acoustic mode may propagate. In that case, the criterion can be applied, but the mathematical formalism is more complicated;

- more study is needed to understand the amplitudes obtained in the energy transfer ratio of the criterion. A complete non-dimensional representation lacks. This topic can be a very interesting one, as this amplitude is very related to the phenomenon of whistling, and no saturation is into account in this process.
- it would be interesting to compare the theoretical formulas from theory (Michalke for instance) to predict the instability frequencies. If such formulas are found, then the potentiality of whistling of a configuration is known without the need of determining experimentally its scattering matrix coefficients. This would be very interesting from an experimental point of view.
- more study is needed to understand why the model inspired by Bode-Nyquist method fails (section 1.7.5). New measurements should be made, taking a particular care to the measure of the reflection coefficients of the test rig. They were only approximate in our measurement;
- to obtain a definitely dimensionless Strouhal number, measurements have to be made with different speed of sound and static pressure in the pipe. For instance, measurements should be made in water.

Additionally, the dimensionless representation of the broadband noise spectra, when the orifice is not whistling, is not satisfactory, when following the simple Lighthill scaling laws. The behaviour seems to be adapted between a dipole sound and a quadrupole source. This seems in fact not surprising, as turbulence and amplified unstable frequencies are present, but further study would be needed on this topic.

Finally, this whistling criterion represents a useful tool to design nuclear power plants ducts and prevent from whistling. Its major advantage is its simplicity, both in its idea (for instance, we do not need vortex sound theory, but only a simple energy balance) and in its application. It ‘only’ needs the measurement of the scattering matrix of the orifice under flow, which can be done in any test rig because this matrix does not depend on the acoustic conditions of the test rig.

Bibliography

- M. Abom, S. Allam, S. Boij, Aero- Acoustics of Flow Duct Singularities at Low Mach Numbers, 12th AIAA/CEAS Aeroacoustics Conference, AIAA-2006-2687.
- G. Ajello, Mesures acoustiques dans les guides d'ondes en présence d'écoulement: mise au point d'un banc de mesure, application à des discontinuités, Thèse de doctorat de l'Université du Maine, Académie de Nantes, 1997
- S. Allam, M. Abom, Investigation of damping and radiation using full plane wave decomposition in ducts, *Journal of Sound and Vibration*, 292: 519-534, 2006
- A. B. C. Anderson, Dependence of Pfeifenton (pipe tone) frequency on pipe length, orifice diameter, and gas discharge pressure, *Journal of the Acoustical Society of America*, 24: 675-681, 1952.
- A. B. C. Anderson, Dependence of the primary Pfeifenton (pipe tone) frequency on pipe-orifice geometry, *Journal of the Acoustical Society of America*, 25: 541-545, 1953^a.
- A. B. C. Anderson, A circular-orifice number describing dependency of primary Pfeifenton frequency on differential pressure, gas density and orifice geometry, *Journal of the Acoustical Society of America*, 4: 626-631, 1953^b.
- A. B. C. Anderson, A jet-tone orifice number for orifices of small thickness-diameter ratio, *Journal of the Acoustical Society of America* 26(1): 21-25, 1954.
- A. B. C. Anderson, Metastable jet-tone states of jets from sharp-edged, circular, pipe-like orifices, *Journal of the Acoustical Society of America*, 27: 13-21, 1955^a.
- A. B. C. Anderson, Structure and velocity of the periodic vortex-ring flow pattern of a primary Pfeifenton (pipe tone) jet, *Journal of the Acoustical Society of America*, 27: 1048-1053, 1955^b.
- A. B. C. Anderson, Vortex ring structure-transition in a jet emitting discrete acoustic frequencies, *Journal of the Acoustical Society of America*, 28: 914-921, 1956.
- Angot, A, *Compléments de mathématiques*, 6th Ed., Masson et Cie Ed., Paris, 1972.
- Y. Aurégan, A. Maurel, V. Pagneux, J.-F. Pinton, Sound-Flow Interactions, Lecture Notes in Physics, Springer Ed., 2002.
- Y. Aurégan, R. Starobinsky, Determination of acoustic energy dissipation/production potentiality from the acoustic transfer functions of a multiport, *Acustica*, 85: 788-792, 1999.

- Y. Aurégan, M. Leroux. Failures in the discrete models for flow duct with perforations: an experimental investigation, *Journal of Sound and Vibration*, 265(1): 109-121, 2003.
- A. Billon, Étude expérimentale de sons auto-entretenus produits par un jet d'un conduit et heurtant une plaque fendue, Thèse, Université de La Rochelle, 2003.
- W. K. Blake, A. Powell, *The development of contemporary views of flow-tone generation*, Vol I., Academic Press, Orlando, 1986.
- W. K. Blake, *Mechanics of Flow-Induced Sound and Vibration*, Vol. I & II., Academic Press.
- R. Blevins, *Applied Fluid dynamics handbook*, Krieger Ed., ISBN 0-89464-717-2, 1984.
- H. Boden, M. Abom, Influence of errors on the two-microphone method for acoustic properties in ducts, *Journal of the Acoustical Society of America*, 79(2): 541-549, 1986.
- P. O. A. L. Davies Practical flow duct acoustics. *Journal of Sound and Vibration*, 124 (1): 91-115, 1988.
- P. E. Doak. Fluctuating total enthalpy as a generalized field. *Acoustica Physics*, 44: 677-685, 1995.
- P. G. Drazin, W. H. Reid. Hydrodynamic instability. Cambridge University Press, 1981.
- P. Durrieu, G. Hofmans, G. Ajello, R. Boot, Y. Aurégan, A. Hirschberg, M.C.A.M. Peters. Quasisteady aero-acoustic response of orifices. *Journal of the Acoustical Society of America*, 110(4): 1859-1872, 2001.
- A. Hirschberg, J. C. Bruggeman, A. P. J. Wijnands, N. Smits. The Whistler Nozzle and Horn as Aero-Acoustic Sound Sources in Pipe Systems. *Acustica* 68: 157-160, 1989
- A. Hirschberg, C. Schram. *A primitive approach to aerocoustics*. Lecture Notes in Physics, Springer Berlin / Heidelberg Publisher, ISSN: 1616-6361, Volume 586, 2002.
- C. M. Ho, N. S. Nossier. Dynamics of an impinging jet, part 1: the feedback phenomenon. *Journal of Fluid Mechanics*, 105, p. 443-473.
- G. C. J. Hofmans. *Vortex sound in confined flows*. PhD Thesis, Technische Universiteit Eindhoven, The Netherlands, 1998.
- G. Hofmans, R. Boot, P. Durrieu, Y. Aurégan, A. Hirschberg. Aeroacoustic response of a slit-shaped diaphragm in a pipe at low Helmholtz number, 1: quasi-steady results. *Journal of Sound and Vibration*, Volume 244, Issue 1, 28 June 2001, Pages 35-56.
- K. Hourigan, M. C. Welsh, M. C. Thompson, A. N. Stokes. Aerodynamic sources of acoustic resonance in a duct with baffles. *Journal of Fluids and Structures*, 4: 345-370, 1990.
- M. S. Howe. Contributions to the theory of aerodynamic sound, with application to excess jet noise and the theory of the flute. *Journal of Fluid Mechanics*, 71: 625-673, 1975.
- I. E. Idel'cik, *Memento des pertes de charge* (in French), Eyrolles Ed., Paris, 1969.

- L. V. King, On the electrical and acoustic conductivities of cylindrical tubes bounded by infinite flanges, *Philosophical Magazine*, 21(7): 128-144, 1936.
- S. Lang, *Algèbre*, Dunod Ed., ISBN 2100079808, 2004.
- H. Levine, J. Schwinger, On the radiation of sound from an unflanged circular pipe, *Physical Review*, 73: 383-406, 1948.
- J. Lighthill, On sound generated aerodynamically , *Proceedings of the Royal Society of London*, Series A211: 564-587, 1952.
- C. L. Morfey, Sound transmission and generation in ducts with flow, *Journal of Sound and Vibration*, 14: 37-55, 1971.
- P. A. Nelson, C. L. Morfey, Aerodynamic sound production in low speed flow ducts, *Journal of Sound and Vibration* 79(2): 263-289, 1981.
- S. Nygard, Modelling of low frequency sound in duct networks, Licentiate Thesis, KTH, Stockholm, Sweeden, 2000.
- M.C.A.M. Peters, A. Hirschberg, A.J. Reijnen, A.P.J. Wijnands, Damping and reflection coefficient measurements for an open pipe at low Mach and low Helmholtz numbers, *Journal of Fluid Mechanics*, 256: 499-534, 1993.
- A. D. Pierce, *Acoustics: An Introduction to Its Physical Principles and Applications*, McGraw-Hill Book Company, New York, 1981.
- A. Powell, Theory of vortex sound, *Journal of the Acoustical Society of America*, 36, 1964.
- S. W. Rienstra, A. Hirschberg, *An Introduction to Acoustics*, Eindhoven University of Technology, The Netherlands, 2003.
- D. Rockwell, Oscillations of impinging shear layers, *AIAA Journal*, 21: 645-664, 1983.
- T. Sarpkaya, A critical review of the intrinsic nature of vortex-induced vibrations, *Journal of Fluids and Structures*, 19: 389-447, 2004.
- T. A. Wilson, G. S. Beavers, M. A. De Coster, D. K. Holger, D. Regenfuss, Experiments on the fluid mechanics of whistling, *Journal of the Acoustical Society of America*, 50: 366-372, 1971.
- G. S. K. Wong, Speed of sound in standard air, *Journal of Acoustical society of America*, 77 (5): 1359-1366, 1985.

Chapter 2

Aeroacoustical behaviour of a single expansion with the multimodal method

2.1 Introduction

A numerical method, called the multimodal method, is introduced in this chapter, and applied it to study of the aeroacoustical behaviour of a single expansion. The objective is to obtain the acoustic fields and the acoustic scattering matrix of the configuration, and compare them to literature data, in order to estimate the validity of this calculation method on this configuration.

This method is a simple calculation method, already used at the LAUM for different configurations (Bi et al., 2006; Leroux et al., 2003). It neglects viscous-thermal effects and consists of the resolution of the linearized Euler equations under a sheared flow profile in established harmonic regime, using a finite difference scheme in the transverse direction, whereas the evolution in the longitudinal direction is simply obtained by propagating the solutions. The flow profile imposed is incompressible, with a shape close to the power flow profile typical of turbulent pipe flow. It is invariable in the longitudinal direction, so that we neglect the expansion of this main flow in the scattering matrix coefficient.

With applying rigidity condition of the wall pipe, the solutions obtained are called modes. The study of the wave numbers of those modes separate them into three types: acoustic modes, propagating (approximately as there is the influence of the main flow) at the speed of sound, hydrodynamic modes, convected approximately at the speed of the flow, and evanescent modes, with varying wave numbers. Among the hydrodynamic modes, one of them, concentrated near a virtual inflexion point of the flow profile, appears to be unstable for certain conditions of the parameters (frequency, flow profile, Mach number): the real part of its wave number is non-vanishing and makes an exponential amplification of the response of this mode.

The connection of the modes using conditions of continuity of the acoustical variables at the location of the single expansion gives the acoustic scattering matrix of the single expansion. The coefficients obtained are compared to experimental data from Ronneberger and some analytical models for behaviour at limit.

2.2 Analytical problem

2.2.1 Problem to solve

The propagation of a sound wave, at a pulsation frequency ω , encountering a single expansion in a 2D-duct with a sheared mean flow profile, is considered.

The problem to solve is to find the acoustical reflection and transmission coefficients of this singularity, and to obtain the acoustical fields when applying an excitation wave.

2.2.2 Geometry and flow hypothesis

The single expansion is a discontinuity of duct cross-section. It is made by a succession of two ducts (see Fig. 2.1):

- duct I: radius a^* (in meter), dimensionless radius 1;
- duct II: radius $b^* > a^*$, dimensionless radius b .

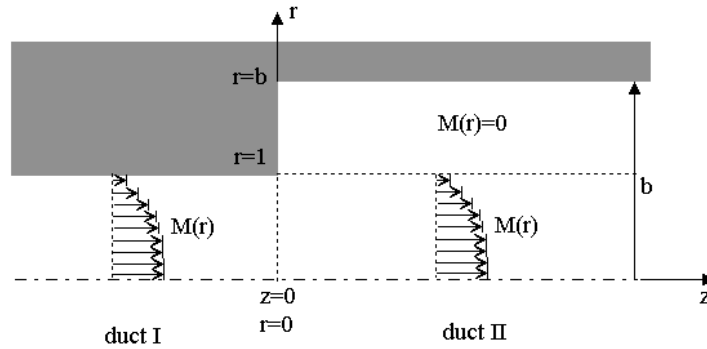


Figure 2.1: Geometry of the problem (in dimensionless cylindrical variables)

Ducts studied are two-dimensional, and can have either a rectangular or a circular section:

- in 2D Cartesians (rectangular duct): the coordinate system is (x, y) , the x-axis being the direction of the flow, the y-axis the longitudinal dimension;
- in 2D axisymmetric (circular duct): the coordinate system is (z, r) , the z-axis being the direction of the flow, the r-axis the longitudinal dimension.

For reasons of symmetry, only half of the expansion is studied: $r = 0$ ($y = 0$) refers to the centre of the pipe.

2.2.3 Assumption of non-expansion of the main flow

An incompressible sheared flow profile is imposed in duct I, of Mach number $M(r)\mathbf{e}_z$, where $M(r) = U(r)/c_0$ (c_0 is the speed of sound in the fluid; $c_0=343 \text{ m.s}^{-1}$ at $T=293 \text{ K}$ in air). This flow profile goes

into duct II unchanged: there is no expansion of the flow in the downstream duct, hence the region $1 \leq r \leq b$ in duct II is without flow.

Thus we assume that the physics of the phenomenon is concentrated at the sudden enlargement: this is where acoustic reflections is supposed to mainly occur, because the acoustic field is very sensitive to discontinuities of sections, and not so much to the evolution of the flow in a pipe of constant section.

Quantitatively, this assumption of non-expansion of the main flow is evaluated in Boij and Nilsson (2005). It is shown that the expansion of the flow does not influence significantly the scattering matrix coefficients of the expansion, which indicates a good validity of this assumption.

Finally, the close agreement between our calculations and experimental data, for which the flow expands in the downstream duct, shows *a posteriori* clearly the good validity of such an approximation.

2.2.4 Equations of the problem

2.2.4.1 Resolution in dimensionless variables

The dimensional variables are denoted with a '*'. They are made dimensionless using the scale variables of the speed of sound in the fluid c_0 ($c_0=343 \text{ m s}^{-1}$ at $T=293 \text{ K}$ in air), the density of the fluid ρ_0 ($\rho_0=1.1 \text{ kg m}^{-3}$ at $T=293 \text{ K}$ in air) and the the radius of duct I a^* :

$$z = \frac{z^*}{a^*}, \quad r = \frac{r^*}{a^*}, \quad p' = \frac{p'^*}{\rho_0 c_0^2}, \quad \rho' = \frac{\rho'^*}{\rho_0}, \quad (2.1)$$

$$v'_z = \frac{v'^*_z}{c_0}, \quad v'_r = \frac{v'^*_r}{c_0}, \quad t = \frac{t^* c_0}{a^*}, \quad \omega = \frac{\omega^* a^*}{c_0}. \quad (2.2)$$

The problem is solved in the dimensionless variables: $z, r, t, p', \rho', v'_r, v'_z, \omega$.

2.2.4.2 Resolution in established harmonic regime

Established harmonic regime is assumed: the calculation is done for a fixed dimensionless frequency ω . The convention used for the temporal dependency of the variables is in $e^{+j\omega t}$.

2.2.4.3 Equations of the problem

Simple assumptions are used:

- the effect of the viscosity is neglected: the fluid is considered as a perfect fluid;
- entropy variations (that is, thermal and viscous effects) are neglected: Hence the speed of sound in the fluid is: $c_0^2 = p'^*/\rho'^*$;
- at initial time, all variables (fluid density, entropy) are uniform.

The idea of these assumptions, together with the assumption of the incompressibility of the main flow, is that they are consistent with the Kelvin-Helmholtz type instabilities that we want to model, as those kinds of instabilities are produced in a non-viscous and incompressible flow.

In this two-dimensional geometry, and under those assumptions, the problem has four variables: p', ρ', v'_r, v'_z . They are determined by four equations: the equations of mass conservation, the equation of

momentum conservation (here linearized Euler equations as viscosity is ignored) in the two directions and the fluid constitutive law. The dimensionless equations to be solved are (see details in appendix C with all equations in dimensional variables), in 2D axisymmetric coordinates:

- mass conservation equation:

$$\frac{Dp'}{Dt} = -\left(\frac{v'_r}{r} + \frac{\partial v'_r}{\partial r} + \frac{\partial v'_z}{\partial z}\right), \quad (2.3)$$

where the convective derivative is: $\frac{D}{Dt} = j\omega + M(r)\frac{\partial}{\partial z}$;

- momentum conservation equations, respectively, in longitudinal and transversal directions:

$$\frac{Dv'_z}{Dt} + v'_r \frac{dM(r)}{dr} = -\frac{\partial p'}{\partial z}, \quad (2.4)$$

$$\frac{Dv'_r}{Dt} = -\frac{\partial p'}{\partial r}; \quad (2.5)$$

- the fluid constitutive law:

$$c_0^2 = \frac{p'}{\rho'}. \quad (2.6)$$

It should be noted that the 2D Cartesians and 2D axisymmetric cases are in fact very similar: they only differ (see appendix C) from the expression of the Laplacian: in the cylindrical case, the Laplacian gets one more term. As a consequence, up to here the four previous equations are identical in Cartesians geometry.

2.2.4.4 Acoustical boundary conditions

The boundary conditions are chosen as the most simple ones:

- the upward wall is considered as infinitely rigid. This gives the condition $v'_r = 0$, equivalent to $\frac{\partial p'}{\partial r} = 0$ using Eq. 2.5;
- the centre line of the duct is considered as a line of symmetry. This gives also the condition $v'_r = 0$.

2.2.5 Method of resolution

2.2.5.1 Resolution in p' and v'_r

The resolution of the previous four equations in the four variables can be reduced to the resolution of the two following equations in variables p' and v'_r :

$$j\omega v'_r + M(r)\frac{\partial v'_r}{\partial z} = -\frac{\partial p'}{\partial r}, \quad (2.7)$$

$$(1 - M(r)^2)\frac{\partial^2 p'}{\partial z^2} + \frac{\partial^2 p'}{\partial r^2} + \frac{1}{r}\frac{\partial p'}{\partial r} + \omega^2 p' = 2j\omega M(r)\frac{\partial p'}{\partial z} - 2\frac{dM(r)}{dr}\frac{\partial v'_r}{\partial z}, \quad (2.8)$$

while the other variables ρ' and v'_z are determined from p' and v'_r :

$$\rho' = \frac{p'}{c_0^2}, \quad (2.9)$$

$$\frac{\partial v'_z}{\partial z} = \frac{Dp'}{Dt} - \left(\frac{v'_r}{r} + \frac{\partial v'_r}{\partial r} \right). \quad (2.10)$$

The numerical calculation consists of the resolution of Eq. 2.7 and 2.8 associated with the acoustical boundary conditions.

2.2.5.2 Resolution in a matrix form

The resolution is made simple using a trick of organisation of the equations, in order to reduce the problem to the resolution of differential equation of first-order with constant coefficient.

If we put the variables in an appropriate column manner:

$$\mathbf{E} = \begin{bmatrix} p' \\ dp'/dz \\ v'_r \end{bmatrix}, \quad (2.11)$$

then it appears that the resolution of Eq. 2.7 and 2.8 comes to the resolution of a first order differential equation in a matrix form:

$$\frac{d\mathbf{E}}{dz} = \mathbf{A}\mathbf{E}, \quad (2.12)$$

with:

$$\mathbf{A} = \begin{bmatrix} 0 & 1 & 0 \\ \frac{2}{M} \frac{dM}{dr} \frac{\partial}{\partial r} - \frac{\frac{\partial^2}{\partial r^2} + \frac{1}{r} \frac{\partial}{\partial r} + \omega^2}{1-M^2} & \frac{2j\omega}{1-M^2} & \frac{2j\omega \frac{dM}{dr}}{M} \\ -\frac{1}{M} \frac{\partial}{\partial r} & 0 & -j \frac{\omega}{M} \end{bmatrix}. \quad (2.13)$$

What is essential to note is that the matrix \mathbf{A} is independent of z . Hence the solutions depend only on r and are thus known to be in the form:

$$E = \hat{E}(r) e^{-jk\omega z}, \quad (2.14)$$

where the dimensionless wave number k is a complex scalar (function of ω).

As a consequence, we have demonstrated that, assuming a frequency dependency in $e^{j\omega t}$, the solutions of our problem necessarily take the form $e^{j(\omega t - kz)}$.

2.2.6 Solutions: acoustic, evanescent and hydrodynamic modes

So as to understand the solutions obtained, we consider the solution obtained for the pressure p' . The merge of Eq. 2.7 and 2.8 gives the propagation equation in pressure (see appendix C). As demonstrated in the previous section, the solution is in the form:

$$p' = \hat{p}(r) e^{j(\omega t - kz)}. \quad (2.15)$$

The unknowns \hat{p} and k satisfy the propagation equation, also known as the Pridmore-Brown equation (convected equation of the modes in a duct with sheared flow):

$$(1 - kM) [(1 - kM)^2 + \Delta] \hat{p} + 2k \frac{dM}{dr} \frac{d\hat{p}}{dr} = 0, \quad (2.16)$$

and the boundary conditions (which constitutes the dispersion relation for k):

$$\frac{d\hat{p}}{dr} = 0 \text{ for } r = 0 \text{ and } r = 1. \quad (2.17)$$

There is no possible analytical resolution of unknowns \hat{p} and k with these two equations 2.16 and 2.17. However, we know from similarity with other type of acoustic equations (for instance, taking a vanishing flow), the solution in pressure is an infinite sum of modes. Incidentally, it is worth noting that this denomination of ‘modes’ is not the common one used in pipe systems: our modes are transverse ones, and do not correspond to any longitudinal conditions.

Assuming that the solutions are known, the following mathematical analysis can give some insight in the solutions obtained. The aim is to understand some properties of the solutions (we don’t demonstrate mathematically the existence of these solutions). When considering a solution of the problem, we can distinguish two cases (see Vilensky and Rienstra (2005); Félix (2002)):

- **the solution is such that $\mathbf{1} - \mathbf{kM}(r) \neq \mathbf{0}$, for any $r \in [0, 1]$:**

A denumerable (due to the boundary conditions) set of solutions may be obtained, satisfying the Pridmore-Brown equation:

$$\frac{d^2\hat{p}}{dr^2} + \left(\frac{1}{r} + \frac{2k \frac{dM}{dr}}{1 - kM} \right) \frac{d\hat{p}}{dr} + \omega^2 [(1 - kM)^2 - k^2] \hat{p} = 0. \quad (2.18)$$

Solutions are understood without flow, and we extend this understanding for the flow case:

- in the particular case $M(r) = 0$:

In the new variable $\tilde{r} = r/\sqrt{\omega^2(1 - k^2)}$, the previous equation reduces to:

$$\frac{d^2p}{d\tilde{r}^2} + \frac{1}{\tilde{r}} \frac{dp}{d\tilde{r}} + p = 0. \quad (2.19)$$

This is the well-known Bessel equation of order $m = 0$: $y'' + y'/r + (1 - m^2/x^2)y = 0$, of solutions $J_0^i(r)$, $i = 1, 2, \dots$, which are called acoustic solutions as they propagate at the speed of sound (this comes from the change of variable from r to \tilde{r}).

- in the general case $M(r) \neq 0$:

As a consequence of the non-flow case, solutions are supposed constituted by Bessel solutions slightly modified by the presence of the flow $M(r)$. Those solutions are called acoustic modes and evanescent modes, and we will see that we obtain them in our calculations. Below the cut-off frequency of the duct, the wave numbers obtained are purely real: those solutions are neither amplified nor attenuated (i. e., plane wave mode and transverse modes), and they are called acoustic modes. Beyond the cut-off frequency of the duct, the wave numbers obtained have an imaginary part and a varying real part: those solutions correspond to exponentially attenuated waves (i. e., transverse modes, also called evanescent modes), at a varying speed, and they are called evanescent modes.

- **the solution is such that it exists $r_1 \in [0, 1]$ such that $\mathbf{1} - \mathbf{kM}(r_1) = \mathbf{0}$:**

A continuous set of solutions may be obtained. Far away from $r = r_1$, solutions satisfy Pridmore-Brown equation. Around $r = r_1$, the Pridmore-Brown equation degenerates into:

$$k \frac{dM}{dr} \frac{d\hat{p}}{dr} = 0. \quad (2.20)$$

Hence around $r = r_1$, the pressure is extremum:

$$\hat{p}(r) = \text{constant}, \quad (2.21)$$

and, using Eq.2.7, the velocity takes the expression:

$$\hat{v}_r = \frac{\frac{1}{k} - 2M - k(1 - M^2)}{\frac{dM}{dr}} \frac{\omega}{2j} \hat{p}(r). \quad (2.22)$$

As $k = 1/M$, those waves propagate with the flow and travel downstream. They are called hydrodynamic modes. In duct I, where the flow profile has no inflexion point, it is observed that the wave numbers of those modes are purely real. In duct II, where there is a flow and a non-flow region, it is observed that either all wave numbers are purely real, either all wave numbers but two are purely real, the two complex wave numbers being complex conjugate. These two modes correspond to an exponentially attenuated hydrodynamic mode, and the other one to an exponentially amplified hydrodynamic mode. They suppose to appear as a consequence of the presence of a virtual inflexion point in the flow profile, at the separation between the flow and the non-flow regions, between the last discretization point when in the flow and the next discretization point when in no flow.

To sum up the preceding discussion and anticipating the results of the numerical resolution, the convected wave equation Eq.2.16 associated with the acoustic boundary conditions Eq.2.17 gives different modes:

- acoustic modes propagating approximately at the speed of sound (slightly modified by the convection of the main flow): they have purely real wave numbers. They represent the two plane wave modes (propagating upstream and downstream) and possibly the higher order transverse modes with frequencies below the cut-off frequency of the duct;
- evanescent modes: they have complex wave numbers: they are attenuated exponentially in the direction of their propagation;
- hydrodynamic modes propagating approximately at the flow velocity:
 - with purely real wave numbers: each one propagating at a velocity $M(r)$, r varying;
 - in certain conditions, with complex wave numbers: one is exponentially attenuated, the other one is exponentially amplified.

2.2.7 Determination of the scattering matrix

Once the modes are calculated in each duct segment, at $z = 0$ (the phase origin corresponding to the location of the expansion), the scattering matrix is deduced by linking these modes between each other by defining conditions of crossing the discontinuity at the expansion.

The conditions of crossing the discontinuity, for $z = 0$ and $0 \leq r \leq b$, are defined as the following:

- we demonstrate (see appendix D) that the linearized conservations of mass, momentum and energy for the total variables, give the continuity of $p', \partial p' / \partial z$ and v'_r at the crossing of the expansion. Hence, we apply:

$$p'_{\text{duct I}} = p'_{\text{duct II}}, \tag{2.23}$$

$$\frac{\partial p'_{\text{duct I}}}{\partial z} = \frac{\partial p'_{\text{duct II}}}{\partial z}, \tag{2.24}$$

$$v'_{r \text{ duct I}} = v'_{r \text{ duct II}}, \tag{2.25}$$

for $z = 0$ and $0 \leq r \leq 1$;

- for the upward vertical wall of duct II (at $z = 0$ and $1 \leq r \leq b$), a simple condition of infinite rigidity is imposed: $v'_z = 0$. In this region, there is no flow, hence $v'_r = 0$, so that this condition, using Eq. 2.4, is equivalent to:

$$\frac{\partial p'_{\text{duct II}}}{\partial z} = 0, \tag{2.26}$$

for $z = 0$ and $1 \leq r \leq b$.

2.3 The multimodal method

2.3.1 Imposed flow profile

The imposed flow profile is represented in Fig. 2.2. It takes the form ($r = 0$ is the centre of the duct, $r = 1$ is the upward wall):

$$\frac{M(r)}{M_0} = \alpha_m (1 - r^m) \quad m \geq 1, \tag{2.27}$$

where the coefficient α_m is a constant depending of m , defined so that the integral of the profile on the duct section gives the mean flow M_0 :

- in 2D axisymmetric, $\alpha_m = \frac{m+2}{m}$ so that $\int_{r=0}^{r=1} M(r)rdr = M_0$;
- in 2D Cartesians, $\alpha_m = \frac{m+1}{m}$ so that $\int_{y=0}^{y=1} M(y)dy = M_0$.

2.3.2 Schlichting turbulent pipe flow profile

We compare this flow profile with the one proposed by Schlichting (1968) for fully turbulent pipe flows in circular ducts:

$$\frac{M(r)}{M(r=0)} = (1 - r)^{1/a}, \tag{2.28}$$

where r is the dimensionless distance (the pipe radius is the scaling length) to the axe. Its mean flow is given by:

$$M_0 = \int_{r=0}^{r=1} M(r)rdr = M(r=0) \frac{a^2}{(1+a)(1+2a)}. \tag{2.29}$$

The parameter a depends on the pipe Reynolds number, as shown by Schlichting with a fit of experimental values in Tab. 2.3.2. For pipe Reynolds number around 10^4 , Schlichting indicates a value of $a = 7$.

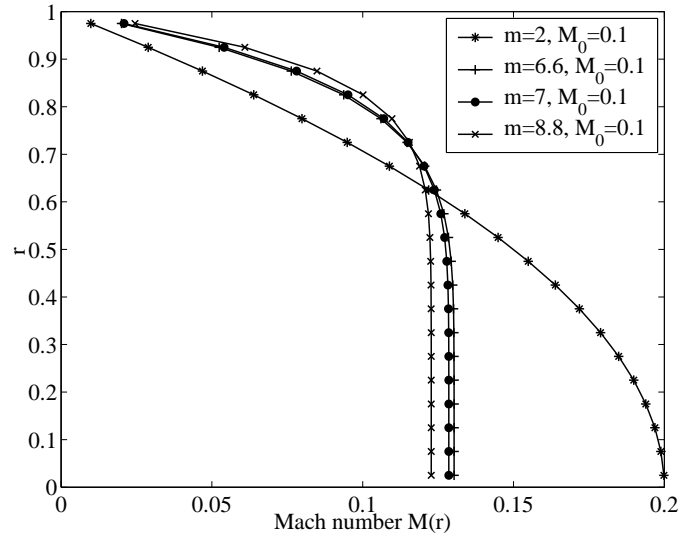


Figure 2.2: Effect of exponent m on the main flow profile in 2D axis-symmetric pipe.

Re	$2.3 \cdot 10^4$	$1.1 \cdot 10^5$	$1.1 \cdot 10^6$
a	6.6	7.0	8.8

Table 2.1: Schlichting parameter a for a power law flow profile.

2.3.3 Comparison of the two flow profiles

Our numerical profile and the Schlichting profile is illustrated in Fig. 2.3. The shape is similar, but the slope of the two profiles is quite different.

This seems however a sensible approximation to use this flow profile, because we do not know exactly the flow profile for the experimental data that we will compare to. The essential fact seems that the shape of the two profiles is similar.

The hypothesis is that the scattering matrix coefficients are not highly sensitive to the flow profile imposed, which seems physically reasonable.

Indeed, we have tested it and obtained that the calculated scattering matrix coefficients only display relative differences of 10^{-2} , when varying our flow profile parameter m from 0.2 to 8.8 (for $M_0 = 0.1$). Furthermore, as presented in the following, the satisfying comparison of our calculations using $m = 7$ to experimental data gives an indication *a posteriori* that the scattering matrix coefficients are not significantly dependent on our flow profile parameter m , and that our flow profile is a satisfying one.

2.3.4 Discretization of the variables

Fig. 2.4 illustrates the transverse discretization in the two ducts. One should note that the advantage of this transverse discretization is that we get a discrete number of hydrodynamic modes, and not an analytically denumerable set of hydrodynamic modes.

The discretization of the r -coordinates is regular with a constant step $h = 1/N$ between each point.

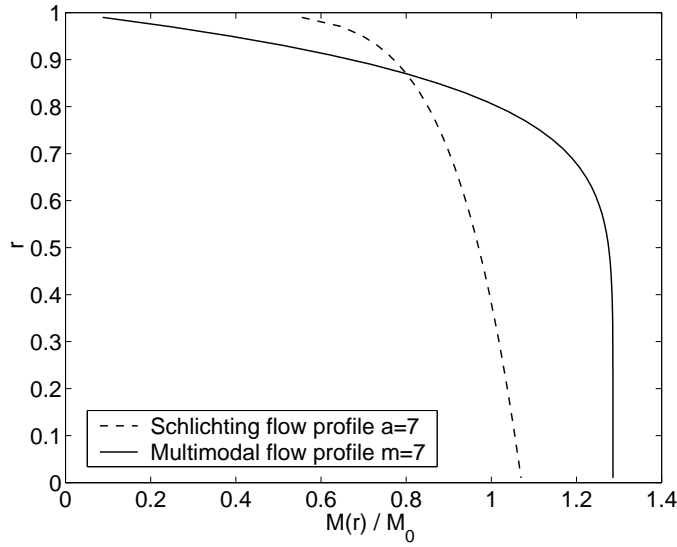


Figure 2.3: Shape of the flow profile and comparison with Schlichting flow profile - duct I, axisym., $N = 50$, $m = 7$, $\omega = 0.1$, $M_0 = 0.1$.

The number of points is N in duct I and M in duct II.

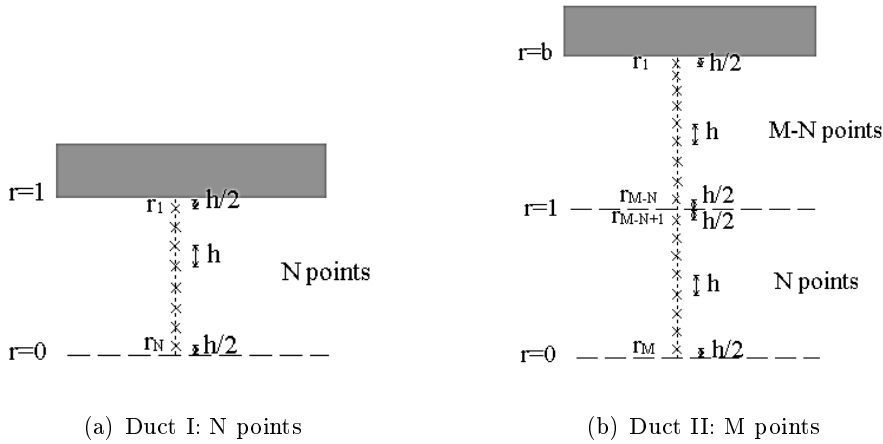


Figure 2.4: Discretization with a constant step in the ducts.

The discretized variables are noted in vector. For instance in duct I:

$$\mathbf{P} = \begin{pmatrix} P_1 \\ \vdots \\ P_N \end{pmatrix}, \quad \mathbf{V} = \begin{pmatrix} V_{r,1} \\ \vdots \\ V_{r,N} \end{pmatrix}, \quad \mathbf{M} = \begin{pmatrix} M_1 \\ \vdots \\ M_N \end{pmatrix}.$$

2.3.5 Derivatives expressions in the finite difference scheme

The discretization imposes to approximate the derivatives of the variables.

The derivative matrices of first order \mathbf{D}_1 and second order \mathbf{D}_2 are defined as (in cylindrical):

$$\mathbf{D}_1 \mathbf{P} = \frac{d\mathbf{P}}{dr}, \quad \mathbf{D}_2 \mathbf{P} = \frac{d^2 \mathbf{P}}{dr^2}. \quad (2.30)$$

The finite difference scheme used is a very classical one: centred scheme of the second order, that is giving an error of $\mathcal{O}(h^2)$. Hence for $2 \leq i \leq N-1$, the derivatives get the expression:

$$\mathbf{D}_1 \mathbf{P}|_i = \frac{P_{i+1} - P_{i-1}}{2h}, \quad (2.31)$$

$$\mathbf{D}_2 \mathbf{P}|_i = \frac{P_{i+1} - 2P_i + P_{i-1}}{h^2}. \quad (2.32)$$

For $i = 1$ and $i = N$, that is at the upward wall and at the centre of the duct, the evaluation of the derivative needs the use of a virtual point:

- P_0 is the image of P_1 in the upward wall: the derivative at $i = 1$ is $\mathbf{D}_1 \mathbf{P}|_{i=1} = \frac{P_2 - P_0}{2h}$. As the wall is rigid, $\frac{dP}{dr} = 0$, so that $P_0 = P_1$. Hence:

$$\mathbf{D}_1 \mathbf{P}|_{i=1} = \frac{P_2 - P_1}{2h}; \quad (2.33)$$

- P_{N+1} is the image of P_N in the centre of the duct: the derivative at $i = N$ is $\mathbf{D}_1 \mathbf{P}|_{i=N} = \frac{P_{N+1} - P_{N-1}}{2h}$. As the centre of the duct is an axe of symmetry, $\frac{dP}{dr} = 0$, so that $P_{N+1} = P_N$. Hence:

$$\mathbf{D}_1 \mathbf{P}|_{i=N} = \frac{P_N - P_{N-1}}{2h}. \quad (2.34)$$

As a result, the derivative matrices \mathbf{D}_1 and \mathbf{D}_2 , including the boundary conditions on their first and last line, are tri-diagonal matrices:

$$\mathbf{D}_1 = \frac{1}{2h} \begin{pmatrix} -1 & 1 & & & \\ -1 & 0 & 1 & & \\ & \ddots & \ddots & \ddots & \\ & & -1 & 0 & 1 \\ & & & -1 & 1 \end{pmatrix}, \quad (2.35)$$

$$\mathbf{D}_2 = \frac{1}{h^2} \begin{pmatrix} -1 & 1 & & & \\ 1 & -2 & 1 & & \\ & \ddots & \ddots & \ddots & \\ & & 1 & -2 & 1 \\ & & & 1 & -1 \end{pmatrix}. \quad (2.36)$$

2.3.6 Discretized equations

The calculation of the modes in duct I and duct II is made at $z = 0$ as origin of the phases.

The equations to solve in unknowns \mathbf{P} and \mathbf{V} are put in vector formalization:

$$j\omega \mathbf{V} + \mathbf{M} \frac{d\mathbf{V}}{dz} = -\mathbf{D}_1 \mathbf{P} \quad (2.37)$$

$$(1 - \mathbf{M}^2) \frac{d^2 \mathbf{P}}{dz^2} + \mathbf{D}_2 \mathbf{P} + \mathbf{D}_1^{cyl} \mathbf{P} + \omega^2 \mathbf{P} = 2j\omega \mathbf{M} \frac{d\mathbf{P}}{dz} - 2\mathbf{M}' \frac{d\mathbf{V}}{dz}. \quad (2.38)$$

where \mathbf{D}_1^c appears for cylindrical geometry:

$$\mathbf{D}_1^{cyl} \mathbf{X}|_i = \frac{1}{r_i} \mathbf{D}_1 \mathbf{X}|_i. \quad (2.39)$$

Putting conveniently the variables into a vector:

$$\mathbf{X} = \begin{pmatrix} \mathbf{P} \\ \mathbf{Q} \\ \mathbf{V} \end{pmatrix}, \quad (2.40)$$

where $\mathbf{Q} = \frac{d\mathbf{P}}{dz}$, solving the previous equations comes to solve a first-order differential equation in matrix form:

$$\mathbf{A} \frac{d\mathbf{X}}{dz} = \mathbf{B} \mathbf{X}. \quad (2.41)$$

with \mathbf{A} and \mathbf{B} being given in the following section, for duct I and duct II.

The resolution of the system is hence a diagonalization problem. As a result, eigenvalues and eigenvectors are found, in number equal to the dimension of the resolution vector \mathbf{X} .

Solutions are of the form: $\mathbf{X}_n = \hat{\mathbf{X}}_n e^{\lambda_n z}$, where λ_n are the eigenvalues and $\hat{\mathbf{X}}_n$ the eigenvectors such that: $\lambda_n \mathbf{A} \hat{\mathbf{X}}_n = \mathbf{B} \hat{\mathbf{X}}_n$.

From the calculated eigenvalues, the physical wave numbers K_n of the modes written in the convention $e^{-jK_n \omega x}$ are determined:

$$K_n = j\lambda_n / \omega. \quad (2.42)$$

2.3.7 Modes determination in duct I

In duct I, the vector of resolution has the form:

$$\mathbf{X} = \begin{pmatrix} \mathbf{P} \\ \mathbf{Q} \\ \mathbf{V} \end{pmatrix} \quad \begin{array}{l} \updownarrow N \text{ points} \\ \updownarrow N \text{ points} \\ \updownarrow N \text{ points} \end{array}. \quad (2.43)$$

The matrices get the expression (in 2D cylindrical):

$$\mathbf{A} = \begin{pmatrix} \mathbf{I}_{N,N} & \mathbf{0}_{N,N} & \mathbf{0}_{N,N} \\ \mathbf{0}_{N,N} & \mathbf{I}_{N,N} - \mathbf{M}^2 & 2 \frac{d\mathbf{M}}{dr} \\ \mathbf{0}_{N,N} & \mathbf{0}_{N,N} & \mathbf{M} \end{pmatrix}, \quad (2.44)$$

$$\mathbf{B} = \begin{pmatrix} \mathbf{0}_{N,N} & \mathbf{I}_{N,N} & \mathbf{0}_{N,N} \\ -\mathbf{D}_2 - \mathbf{D}_1^{cyl} - \omega^2 \mathbf{I}_{N,N} & 2j\omega \mathbf{M} & \mathbf{0}_{N,N} \\ -\mathbf{D}_1 & \mathbf{0}_{N,N} & -j\omega \mathbf{I}_{N,N} \end{pmatrix}. \quad (2.45)$$

Those expressions are identical in 2D Cartesians, except that the term \mathbf{D}_1^{cyl} is not present.

As \mathbf{X} is a vector of $3N$ lines, the resolution in duct I gives $3N$ eigenvalues K_n with $3N$ associated eigenvectors of size $3N$ denoted Ψ_n :

$$\psi_{\mathbf{n}} = \begin{pmatrix} \mathbf{P}_n \\ \mathbf{Q}_n \\ \mathbf{V}_n \end{pmatrix} \begin{array}{l} \updownarrow N \text{ points} \\ \updownarrow N \text{ points} \\ \updownarrow N \text{ points} \end{array} . \quad (2.46)$$

Modes are sorted (see section 2.3.9) in function of their wave numbers. We note, in respect to their direction of propagation, upstream propagating modes by subscript 'u', and downstream propagating modes by subscript 'd'. As a result, we note the $3N$ eigenvalues in a column vector:

$$\begin{pmatrix} \vdots \\ K_n^I \\ \vdots \end{pmatrix} = \begin{pmatrix} \mathbf{K}_d^I \\ \mathbf{K}_u^I \end{pmatrix} \begin{array}{l} \updownarrow 2N \text{ points} \\ \updownarrow N \text{ points} \end{array} . \quad (2.47)$$

Similarly, we note the $3N$ eigenvectors in a matrix:

$$\begin{pmatrix} \dots & \Psi_{\mathbf{n}}^I & \dots \end{pmatrix} = \begin{pmatrix} \Psi_d^I & \Psi_u^I \end{pmatrix} = \begin{pmatrix} \Psi_{d,1}^I & \Psi_{u,1}^I \\ \Psi_{d,2}^I & \Psi_{u,2}^I \end{pmatrix} \begin{array}{l} \updownarrow 2N \text{ points} \\ \updownarrow N \text{ points} \end{array} \quad (2.48)$$

where Ψ_d is $3N \times 2N$ and Ψ_u is $3N \times N$.

To obtain the resulting acoustic fields after imposing an excitation wave, and hence to visualize the acoustic fields, the solution obtained in duct I is a summation of these modes:

$$p'(\mathbf{r}, z, t) = e^{j\omega t} \mathbf{P}^I, \quad \frac{dp'}{dz}(\mathbf{r}, z, t) = e^{j\omega t} \mathbf{Q}^I, \quad v'_r(\mathbf{r}, z, t) = e^{j\omega t} \mathbf{V}^I, \quad (2.49)$$

with:

$$\begin{pmatrix} \mathbf{P}^I \\ \mathbf{Q}^I \\ \mathbf{V}^I \end{pmatrix} = \begin{pmatrix} \Psi_d^I & \Psi_u^I \end{pmatrix} \begin{pmatrix} \vdots \\ \alpha_n^I e^{-jK_n^I z} \\ \vdots \end{pmatrix}, \quad (2.50)$$

where the α_n^I are the amplitudes of the modes determined by the multiplication of the calculated scattering matrix of the configuration (see in the following) by the imposed excitation wave.

2.3.8 Modes determination in duct II

The difference from duct II to duct I is that there is a non-flow region in $r \geq 1$, hence the vector \mathbf{V} is zero in this region: it is no more a variable in this region, hence the new variable to be considered is $\mathbf{V}_|$, restriction of \mathbf{V} to the flow region ($r = M - N + 1$ to M).

In duct II, the vector of resolution has the form:

$$\mathbf{X} = \begin{pmatrix} \mathbf{P} \\ \frac{d\mathbf{P}}{dx} \\ \mathbf{V}_| \end{pmatrix} \begin{array}{l} \updownarrow M \text{ points} \\ \updownarrow M \text{ points} \\ \updownarrow N \text{ points} \end{array} \quad (2.51)$$

The matrices get the expression (in 2D cylindrical):

$$\mathbf{A} = \begin{pmatrix} \mathbf{I}_{M,M} & \mathbf{0}_{M,M} & \mathbf{0}_{M,N} \\ \mathbf{0}_{M,M} & \mathbf{I}_{M,M} - \mathbf{M}^2 & 2\frac{d\mathbf{M}|_{M,N}}{dr} \\ \mathbf{0}_{N,M} & \mathbf{0}_{N,M} & \mathbf{M}|_{N,N} \end{pmatrix}, \quad (2.52)$$

$$\mathbf{B} = \begin{pmatrix} \mathbf{0}_{M,M} & \mathbf{I}_{M,M} & \mathbf{0}_{M,M} \\ -\mathbf{D}_2 - \mathbf{D}_1^{cyl} - \omega^2 \mathbf{I}_{M,M} & 2j\omega \mathbf{M} & \mathbf{0}_{M,N} \\ -\mathbf{D}_1|_{N,M} & \mathbf{0}_{N,M} & -j\omega \mathbf{I}_{N,N} \end{pmatrix}. \quad (2.53)$$

As \mathbf{X} is a vector of $2M + N$ lines, the resolution in duct II gives $2M + N$ eigenvalues K_n with $2M + N$ associated eigenvectors of size $2M + N$ denoted Ψ_n :

$$\psi_n = \begin{pmatrix} \mathbf{P}_n \\ \mathbf{Q}_n \\ \mathbf{V}_n \end{pmatrix} \begin{array}{l} \updownarrow M \text{ points} \\ \updownarrow M \text{ points} \\ \updownarrow N \text{ points} \end{array}. \quad (2.54)$$

Modes are sorted, similarly than in duct I:

$$\begin{pmatrix} \vdots \\ K_n^{II} \\ \vdots \end{pmatrix} = \begin{pmatrix} \mathbf{K}_d^{II} \\ \mathbf{K}_u^{II} \end{pmatrix} \begin{array}{l} \updownarrow N+M \text{ points} \\ \updownarrow N \text{ points} \end{array} \quad (2.55)$$

$$\begin{pmatrix} \dots & \Psi_n^{II} & \dots \end{pmatrix} = \begin{pmatrix} \Psi_d^{II} & \Psi_u^{II} \end{pmatrix} = \begin{pmatrix} \Psi_{d,1}^{II} & \Psi_{u,1}^{II} \\ \Psi_{d,2}^{II} & \Psi_{u,2}^{II} \end{pmatrix} \begin{array}{l} \updownarrow N+M \text{ points} \\ \updownarrow N \text{ points} \end{array}, \quad (2.56)$$

where Ψ_d is $(2M+N) \times (M+N)$ and Ψ_u is $(2M+N) \times N$.

To visualize the solution after an excitation wave, the solution obtained in duct II is calculated from (similarly as in duct I):

$$p'(\mathbf{r}, z, t) = e^{j\omega t} \mathbf{P}^{II}, \quad \frac{dp'}{dz}(\mathbf{r}, z, t) = e^{j\omega t} \mathbf{Q}^{II}, \quad v'_r(\mathbf{r}, z, t) = e^{j\omega t} \mathbf{V}^{II}, \quad (2.57)$$

with:

$$\begin{pmatrix} \mathbf{P}^{II} \\ \mathbf{Q}^{II} \\ \mathbf{V}^{II} \end{pmatrix} = \begin{pmatrix} \Psi_d^{II} & \Psi_u^{II} \end{pmatrix} \begin{pmatrix} \vdots \\ \alpha_n^{II} e^{-jK_n^{II} z} \\ \vdots \end{pmatrix}, \quad (2.58)$$

where the α_n^{II} are the amplitudes of the $2M + N$ modes given by the scattering matrix of the single expansion applied to the excitation wave.

2.3.9 Numerical classification of the modes

The eigenvalues obtained by the resolution are sorted in order to differentiate the modes. The modes are classified as the following into hydrodynamic, acoustic and evanescent modes:

2.3.9.1 Hydrodynamic modes

Those modes corresponds to $1 - K_n M(r_n) = 0$. We get N modes in duct I, and also N in duct II (as the flow does not expand).

They are called hydrodynamic modes, as they are convected at the flow velocity. Their wave number is purely real, for all of them, except 2. These two ones have a non-vanishing imaginary part, which are complex conjugates, and represent an exponential attenuation and an exponential amplification.

They are numerically identified with two conditions:

- their wave number is such that $1/M_{max} \leq \Re(K_n) \leq 1/M_{min}$. This is sufficient to give the stable hydrodynamic modes, but not the two unstable ones that have an imaginary wave number;
- In practice, we don't know the value of the imaginary part of the unstable hydrodynamic mode, so that we use a purely artificial criterion, consisting of a parabola, of expression $\Im(K_n)^2 = A [\Re(K_n)^2 - x_0^2]$, with fitting parameters $x_0 \approx 0.8/\max(M_0)$ and $A \approx 5$, that we change if need be, that is, if the number of modes obtained with this algorithm is not N .

This use of the parabola has given good satisfaction in practice, and little difficulties (see section 2.4.4.1 when difficulties appear). One should note that physical criterions exist (Crighton-Leppington or Briggs-Bers). They could have been implemented in this calculation to make really no ambiguity and difficulty when identifying the unstable hydrodynamic mode.

2.3.9.2 Acoustic and evanescent modes

The non-hydrodynamic modes are distinguished into acoustic and evanescent modes:

- propagating acoustic modes, that is, plane wave modes and possibly higher order modes propagating for frequency below the cut-off frequency of the duct. They propagate nearly at the speed of sound (slightly modified y the main flow), and their wave numbers are purely real. They are numerically identified with the condition of having $\Im(K_n) = 0$ and of not being an hydrodynamic modes.
- what we call evanescent modes, as their wave number have a non-vanishing imaginary part. They are numerically identified without condition, that is, they represent the remaining modes not classified as hydrodynamic and acoustic.

2.3.9.3 Upstream or downstream propagation

The sense of propagation of the mode whether upstream or downstream is given by:

- for hydrodynamic and acoustic modes, the real part of their wave number, as they are propagating;
- for evanescent modes, the imaginary part of their wave number, in order to attenuate those modes.

As a result, we obtain in duct I N (N in duct II) hydrodynamic modes convected downstream, N (M in duct II) acoustic and evanescent mode propagating downstream and N (M in duct II) acoustic and evanescent mode propagating upstream.

2.3.10 Scattering matrix determination

The amplitudes α^{I} of the $3N$ modes in duct I are linked with the amplitudes α^{II} of the $2M + N$ modes in duct II applying the conditions of crossing the discontinuity of section at the expansion. The matrix determining this link is called the scattering matrix \mathbf{S} of size $(2N + M, 2N + M)$ defined as :

$$\mathbf{S} = \begin{pmatrix} \mathbf{T}^+ & \mathbf{R}^- \\ \mathbf{R}^+ & \mathbf{T}^- \end{pmatrix}, \quad (2.59)$$

with

$$\begin{pmatrix} \alpha_{\text{d}}^{\text{II}} \\ \alpha_{\text{u}}^{\text{I}} \end{pmatrix} = \mathbf{S} \begin{pmatrix} \alpha_{\text{d}}^{\text{I}} \\ \alpha_{\text{u}}^{\text{II}} \end{pmatrix}, \quad (2.60)$$

with ‘u’ referring to upstream propagating modes, ‘d’ to downstream propagating modes, ‘I’ to duct I and ‘II’ to duct II.

The scattering matrix is determined with the $2N + M$ equations coming from the application of the conditions of crossing the discontinuity defined previously (section 2.2.7):

- continuity of the variables at the interface ($3N$ equations):

$$\begin{pmatrix} \mathbf{P}^{\text{I}} \\ \mathbf{Q}^{\text{I}} \\ \mathbf{V}^{\text{I}} \end{pmatrix} = \begin{pmatrix} \mathbf{P}^{\text{II}}| \\ \mathbf{Q}^{\text{II}}| \\ \mathbf{V}^{\text{II}} \end{pmatrix}, \quad (2.61)$$

where $\mathbf{P}^{\text{II}}|$ and $\mathbf{Q}^{\text{II}}|$ (with $\mathbf{Q} = \frac{d\mathbf{P}}{dz}$) are the restriction of \mathbf{P}^{II} and \mathbf{Q}^{II} to the region with flow, corresponding to the interface between duct I and duct II.

- condition of rigidity of the vertical upward wall of duct II ($M - N$ equations):

$$\mathbf{Q}^{\text{II}}|_{\text{vertical wall}} = \mathbf{0}_{N-M,1} \quad (2.62)$$

The numerical implementation of these equations, Eq. 2.61 and 2.62, is given in the following. Equations are written in a matrix form with sub-matrices:

$$\begin{pmatrix} \Psi_{\text{d},1}^{\text{I}} & \Psi_{\text{u},1}^{\text{I}} \\ \chi_1^{\text{I}} & \chi_2^{\text{I}} \end{pmatrix} \begin{pmatrix} \alpha_{\text{d}}^{\text{I}} \\ \alpha_{\text{u}}^{\text{I}} \end{pmatrix} = \begin{pmatrix} \Psi_{\text{d},1}^{\text{II}} & \Psi_{\text{u},1}^{\text{II}} \\ \chi_1^{\text{II}} & \chi_2^{\text{II}} \end{pmatrix} \begin{pmatrix} \alpha_{\text{d}}^{\text{II}} \\ \alpha_{\text{u}}^{\text{II}} \end{pmatrix}, \quad (2.63)$$

where:

$$\chi_1^{\text{I}} = \begin{pmatrix} \Psi_{\text{d},2}^{\text{I}} \\ \mathbf{0}_{M-N,2N} \end{pmatrix}, \quad \chi_2^{\text{I}} = \begin{pmatrix} \Psi_{\text{u},2}^{\text{I}} \\ \mathbf{0}_{M-N,N} \end{pmatrix}, \quad (2.64)$$

$$\chi_1^{\text{II}} = \begin{pmatrix} \Psi_{\text{d},2}^{\text{II}} \\ \mathbf{K}_1 \end{pmatrix}, \quad \chi_2^{\text{II}} = \begin{pmatrix} \Psi_{\text{u},2}^{\text{II}} \\ \mathbf{K}_2 \end{pmatrix}, \quad (2.65)$$

$$\mathbf{K}_1 = \Psi_{\text{d}}^{\text{II}} : \begin{pmatrix} \mathbf{0}_{M,1} \\ \text{Id}_{M-N,1} \\ \mathbf{0}_{2N,1} \end{pmatrix}, \quad \mathbf{K}_2 = \Psi_{\text{u}}^{\text{II}} : \begin{pmatrix} \mathbf{0}_{M,1} \\ \text{Id}_{M-N,1} \\ \mathbf{0}_{2N,1} \end{pmatrix}. \quad (2.66)$$

Hence we find:

$$\mathbf{S} = \mathbf{S}_1^{-1} \mathbf{S}_2, \quad (2.67)$$

with:

$$\mathbf{S}_1 \begin{pmatrix} \alpha_d^{\text{II}} \\ \alpha_u^{\text{I}} \end{pmatrix} = \mathbf{S}_2 \begin{pmatrix} \alpha_d^{\text{I}} \\ \alpha_u^{\text{II}} \end{pmatrix}, \quad (2.68)$$

and:

$$\mathbf{S}_1 = \begin{pmatrix} \Psi_{d,1}^{\text{II}} & -\Psi_{u,1}^{\text{I}} \\ \chi_1^{\text{II}} & -\chi_2^{\text{I}} \end{pmatrix}, \quad \mathbf{S}_2 = \begin{pmatrix} \Psi_{d,1}^{\text{I}} & -\Psi_{u,1}^{\text{II}} \\ \chi_1^{\text{I}} & -\chi_2^{\text{II}} \end{pmatrix}. \quad (2.69)$$

2.4 Single expansion calculations

We present in this section intermediate results obtained in the calculations, as a first step validation of the method before comparing results with experimental data. We present the shapes of the modes obtained, the convergence of the calculations, the visualization of the acoustic fields and the difficulties typical of the calculations.

2.4.1 Modes obtained in duct I and duct II

2.4.1.1 Wavenumbers obtained in duct I and duct II

The resolution of the system gives the eigenvalues in the notation $\exp[j(\omega t - \omega K_n x)]$. The eigenvalues K_n obtained are sorted in function of their real and imaginary part.

Wavenumbers obtained in duct I are illustrated in Fig. 2.5, with a very low number $N = 3$ points of discretization to help understand the classification. One should note particularly the position of acoustic modes on the x-axis: close to 1 and -1, they correspond to 2 plane waves acoustic modes propagating upstream and downstream.

Numerical investigations show that we obtain other acoustic modes than plane wave modes in close agreement with analytical formulae in the vanishing flow case: the first transverse modes appear for the dimensionless $\omega = 3.83, 7.01, \dots$, corresponding to the first analytical zeros of the derivative of the Bessel function J_0 of order 0.

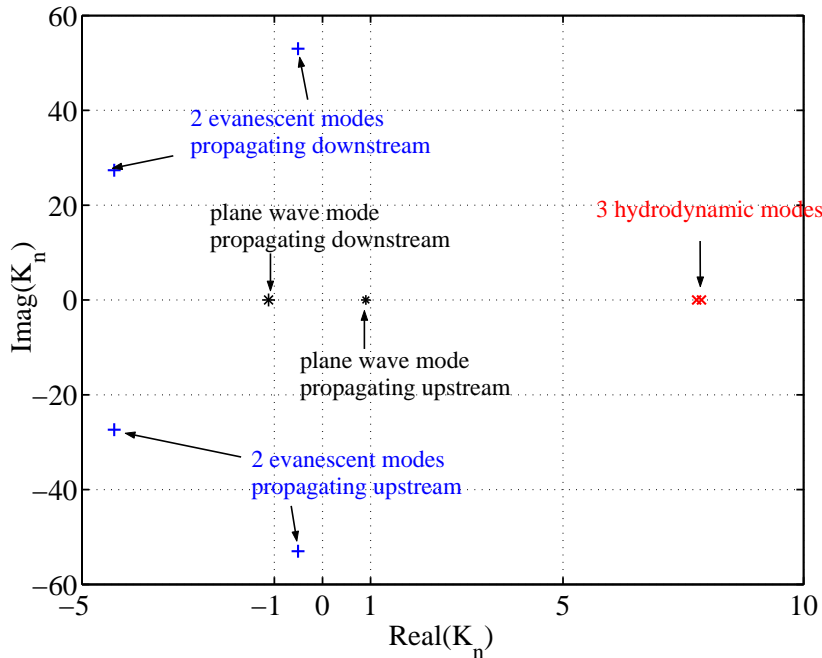


Figure 2.5: Classification of the modes from their wave numbers in duct I (axisym., $N = 3$, $m = 7$, $\omega = 0.1$, $M_0 = 0.1$): N hydrodynamic modes propagating downstream, N acoustic and evanescent modes propagating downstream and N acoustic and evanescent modes propagating upstream.

Wavenumbers obtained more typically in duct I, that is with a large number of modes, are illustrated in Fig. 2.6.

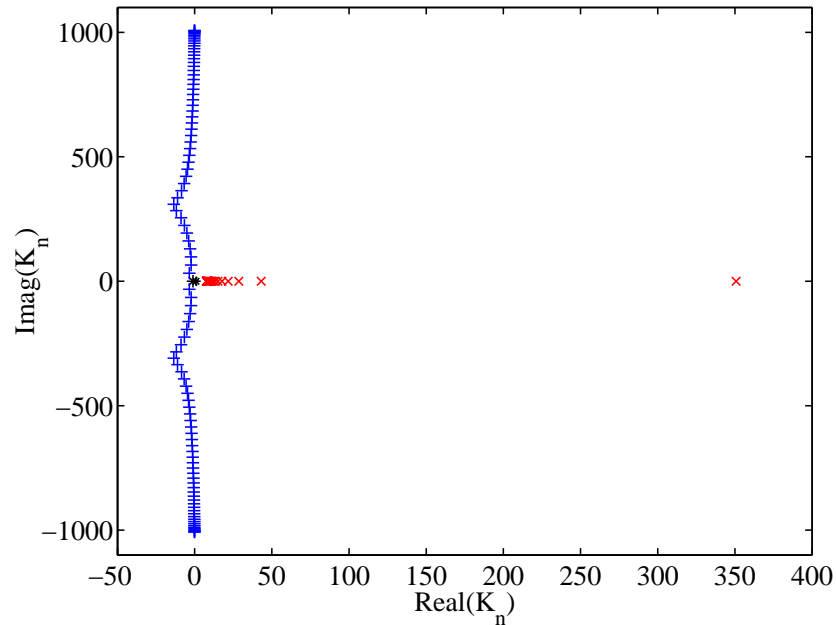


Figure 2.6: Wavenumbers obtained typically in duct I (axisym., $N = 50$, $m = 7$, $\omega = 0.1$, $M_0 = 0.1$): 'x' for N hydrodynamic modes propagating downstream, '*' for acoustic modes and '+' for evanescent modes, with N acoustic and evanescent modes propagating downstream and N acoustic and evanescent modes propagating upstream.

In duct II, similar profiles of wave numbers are obtained and are illustrated in Fig.2.7 for a low number a modes. There is a strong difference with duct I as an unstable hydrodynamic mode can appear. That is why the artificial parabola is used: to distinct this unstable hydrodynamic mode from an evanescent mode.

Wavenumbers obtained more typically in duct II, that is with a large number of modes, are illustrated in Fig. 2.8.

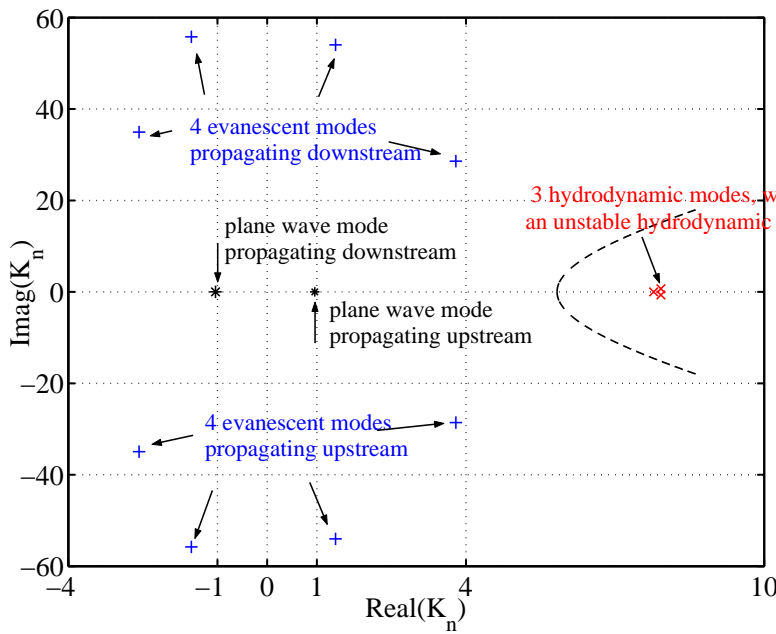


Figure 2.7: Classification of the modes from their wave numbers in duct II (axisym., $N = 3$, $b = 1.5$ hence $M = 5$, $m = 7$, $\omega = 0.1$, $M_0 = 0.1$): N hydrodynamic modes propagating downstream, M acoustic and evanescent modes propagating downstream and M acoustic and evanescent modes propagating upstream. The parabola is a purely artificial means to distinct the unstable hydrodynamic mode from the evanescent mode.

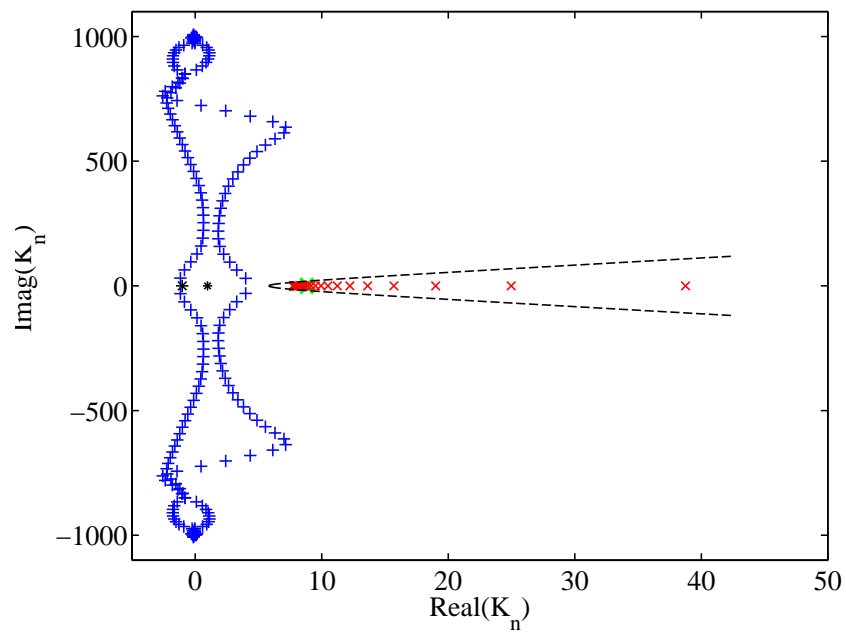


Figure 2.8: Wavenumbers obtained typically in duct II (axisym., $N = 50$, $b = 2$ hence $M = 100$, $m = 7$, $\omega = 0.1$, $M_0 = 0.1$): 'x' for N hydrodynamic modes propagating downstream, '*' for acoustic modes and '+' for evanescent modes, with M acoustic and evanescent modes propagating downstream and M acoustic and evanescent modes propagating upstream. The parabola is a purely artificial means to distinct the unstable hydrodynamic mode from the evanescent mode.

2.4.1.2 Mode shapes (eigenvectors)

In this section, we give visualizations of the shapes of the modes obtained. The shapes seem satisfying the boundary conditions imposed, and differentiate the acoustic and the hydrodynamic modes.

The shape of the modes is given by the eigenvector associated with the eigenvalue (the wave number). This eigenvector is constituted by the pressure P , the derivative of the pressure dP/dz and the transversal velocity V_r . It is made dimensionless by dividing with the average of the pressure.

The first acoustic mode is a plane-wave mode, with a quasi-constant pressure as illustrated in Fig. 2.9. Higher order acoustic modes have a Bessel shape satisfying the boundary conditions, as illustrated in Fig. 2.10 and 2.11.

Hydrodynamic modes are extremum at a varying given point $r = r_1$, as illustrated in Fig. 2.12 and 2.13. This is coherent with the mathematical discussion presented in section 2.2.6, .

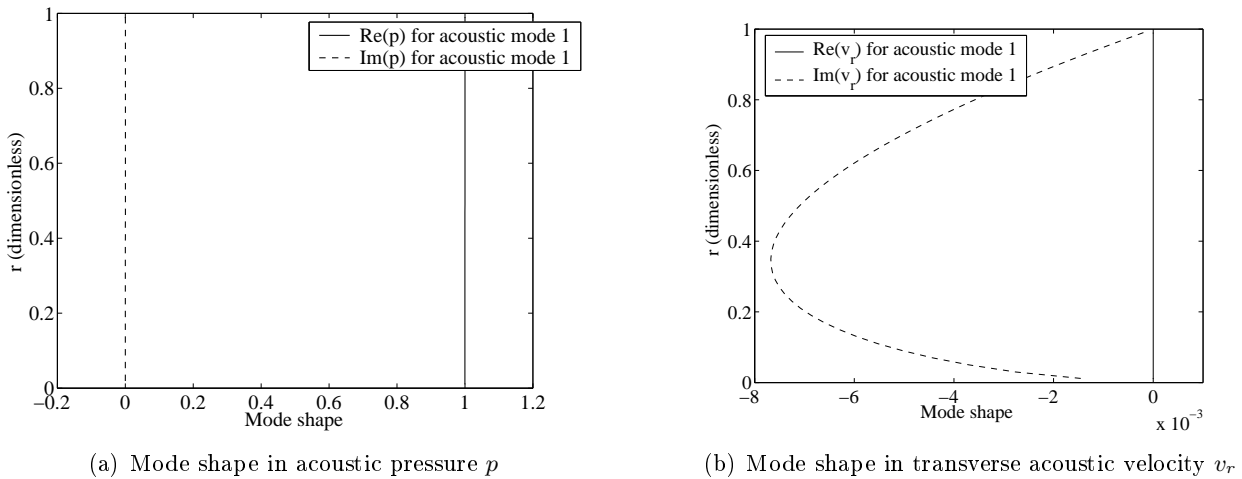


Figure 2.9: Shape of the first acoustic mode corresponding to a quasi-plane wave mode in duct I (axisym., $N = 50$, $m = 7$, $\omega = 0.1$, $M_0 = 0.1$).

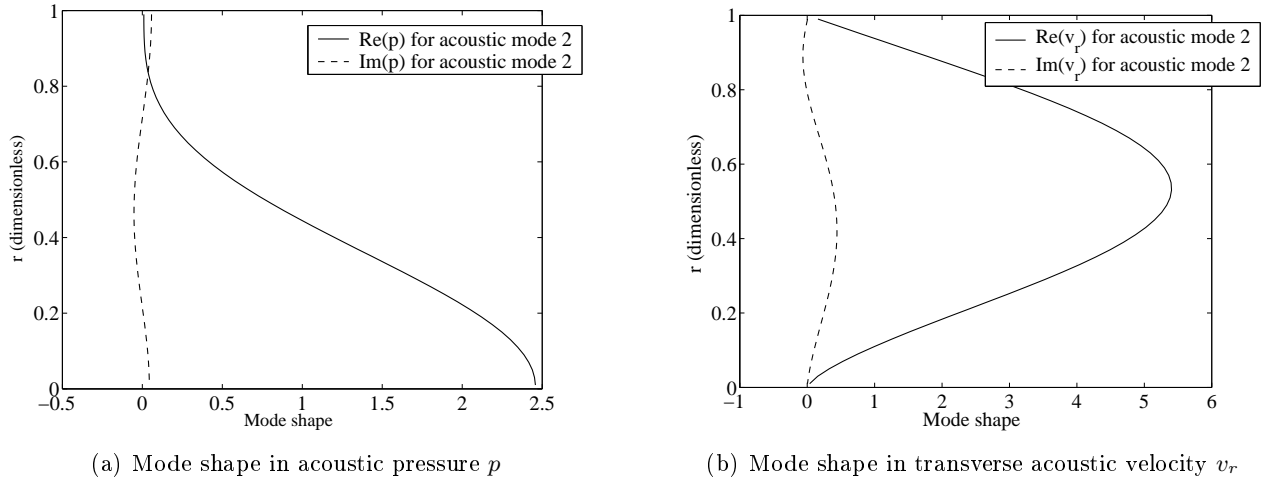


Figure 2.10: Shape of the second acoustic mode in duct I (axisym., $N = 50$, $m = 7$, $\omega = 0.1$, $M_0 = 0.1$).

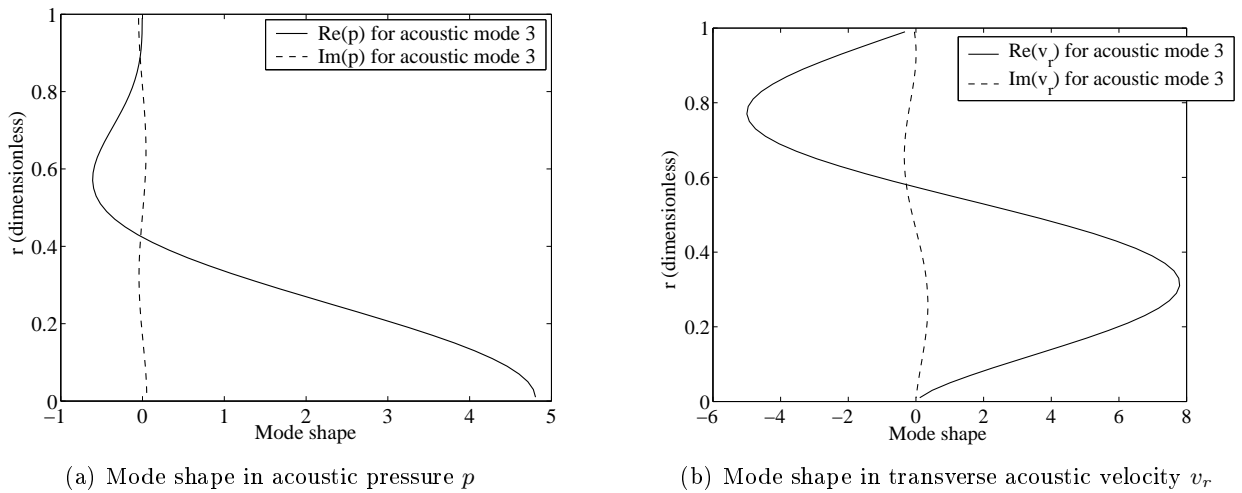
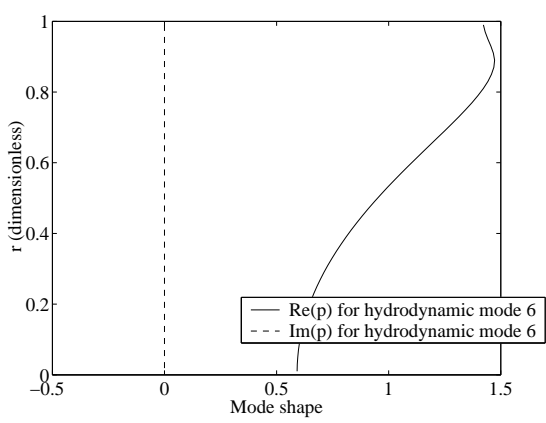
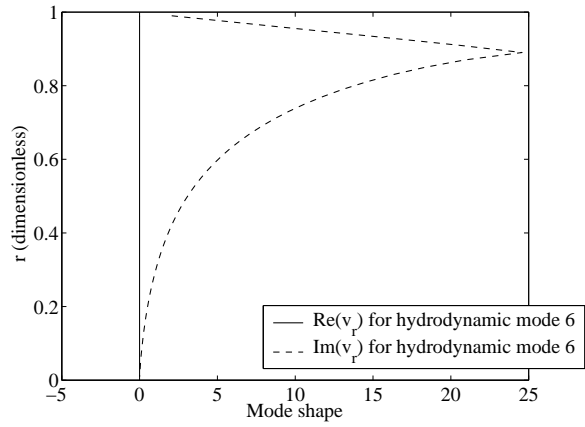


Figure 2.11: Shape of the third acoustic mode in duct I (axisym., $N = 50$, $m = 7$, $\omega = 0.1$, $M_0 = 0.1$).

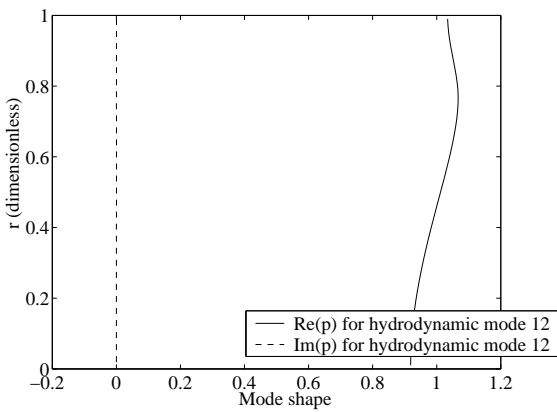


(a) Mode shape in acoustic pressure p

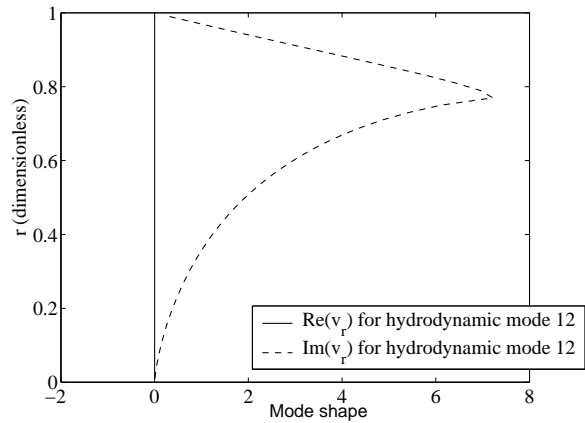


(b) Mode shape in transverse acoustic velocity v_r

Figure 2.12: Shape of the 6th hydrodynamic mode in duct II (axisym., $N = 50$, $b = 1.5$, $m = 7$, $\omega = 0.1$, $M_0 = 0.1$).



(a) Mode shape in acoustic pressure p



(b) Mode shape in transverse acoustic velocity v_r

Figure 2.13: Shape of the 12th hydrodynamic mode in duct II (axisym., $N = 50$, $b = 1.5$, $m = 7$, $\omega = 0.1$, $M_0 = 0.1$).

2.4.2 Convergence results

Convergence of the 4 scattering matrix coefficients is studied, in magnitude and in phase. In order to evaluate convergence, an estimation of the error between a reference calculation (with a high number of points N) and the current calculation is made:

$$E(X, N, N_{ref}) = \frac{|X(N) - X(N_{ref})|}{|X(N_{ref})|}, \quad (2.70)$$

where X is the quantity of interest (i.e. $|R^+|$ or $\text{phase}(R^+)$).

Illustration is given in Fig. 2.14 and 2.15. It is found a convergence slope in log-log representation of 1.19 for the illustrated case.

Convergence results show that $N = 150$ corresponds to an approximate error of the order of 10^{-3} between a calculation for $N = 400$ points. We have chosen to employ $N = 150$ to compare those coefficients with experimental data.

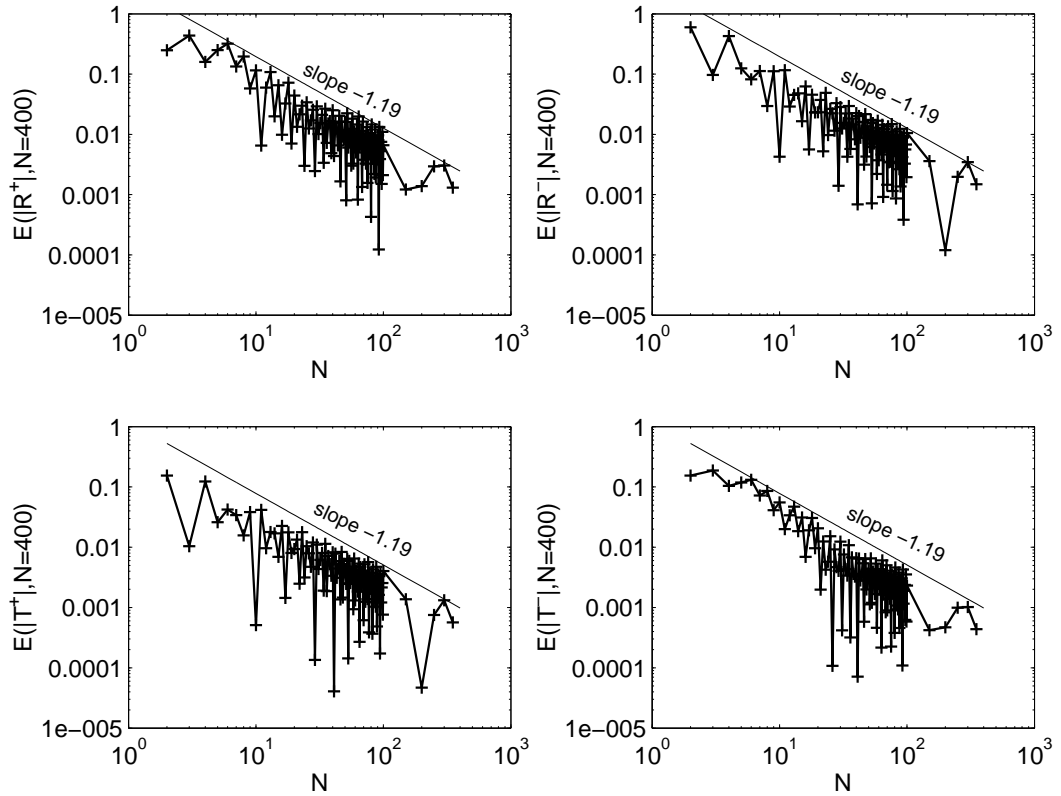


Figure 2.14: Example of convergence for the magnitude of the coefficients of the scattering matrix for a single expansion (axisym., $\omega=1$ ($f=2164$ Hz), $M_0 = 0.3$, $m = 10$, $b = \sqrt{2}$).

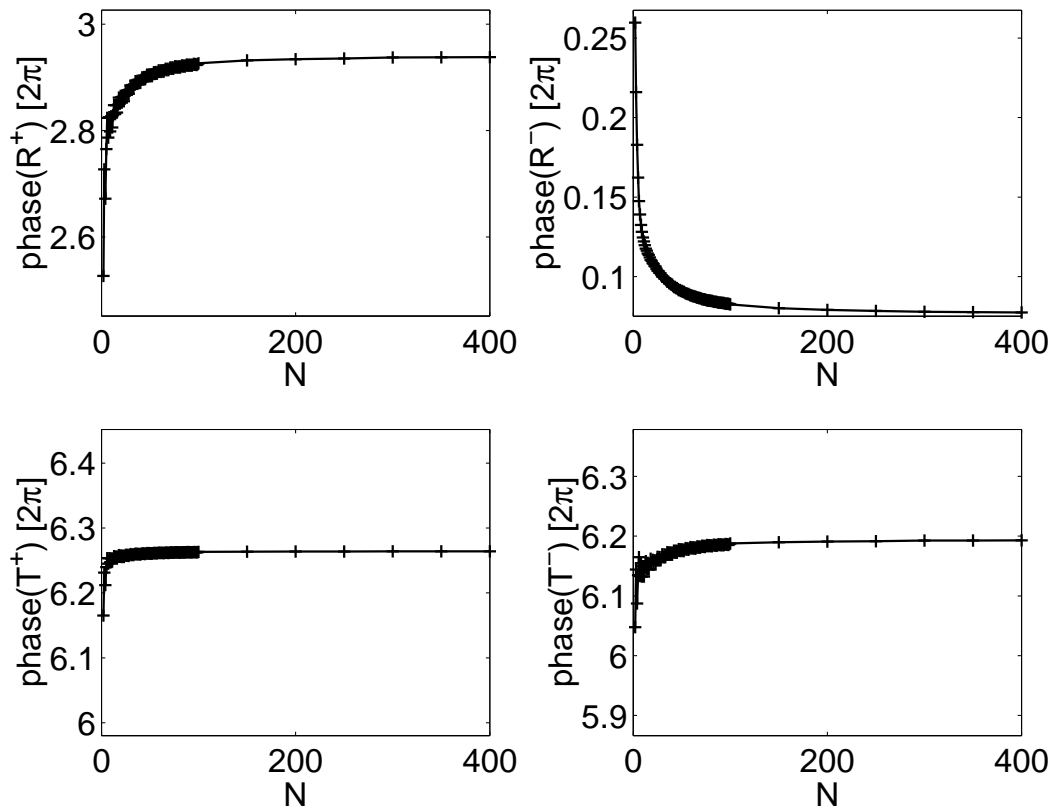


Figure 2.15: Example of convergence for the phase of the coefficients of the scattering matrix for a single expansion (axisym., $\omega=1$ ($f=2164$ Hz), $M_0=0.3$, $m=10$, $b=\sqrt{2}$).

2.4.3 Visualization of the excited fields

2.4.3.1 Excitation with a plane-wave

The response of the modes is determined by imposing an excitation vector on the calculated scattering matrix:

$$\begin{pmatrix} \alpha_{\mathbf{d}}^{\text{II}} \\ \alpha_{\mathbf{u}}^{\text{I}} \end{pmatrix} = \begin{pmatrix} \mathbf{T}^+ & \mathbf{R}^- \\ \mathbf{R}^+ & \mathbf{T}^- \end{pmatrix} \begin{pmatrix} \alpha_{\mathbf{d}}^{\text{I exc}} \\ \alpha_{\mathbf{u}}^{\text{II exc}} \end{pmatrix}. \quad (2.71)$$

The excitation is made of a plane-wave in duct I, of amplitude $\alpha = 1$, coming from upstream and propagating downstream, so that the excitation vector is:

$$\alpha_{\mathbf{d}}^{\text{I exc}} = \begin{pmatrix} 1 \\ 0 \\ \vdots \\ 0 \end{pmatrix}, \quad \alpha_{\mathbf{u}}^{\text{II exc}} = \begin{pmatrix} 0 \\ \vdots \\ 0 \end{pmatrix}. \quad (2.72)$$

The visualizations of the total fields are given in the following, discerning from the presence or not of an unstable hydrodynamic mode.

2.4.3.2 The resulting acoustic fields when the hydrodynamic modes are all stable

An example of visualization of the acoustic fields is shown in this section, when sending a plane-wave, in the case where the hydrodynamic modes are all stable.

The excitation in downstream plane-wave and the matching of the modes result in getting a response composed, mainly, by excitation of the other plane-waves: in duct I, mainly the other plane-wave mode (propagating upward) (see Fig.2.16), and in duct II, mainly the plane-wave mode propagating downward (see Fig.2.17). Thus, it appears that the higher order acoustic modes, and the hydrodynamic modes, are not, or very negligibly excited.

The corresponding visualizations are given, for the acoustic pressure in Fig. 2.18. One observes that the acoustic pressure field is a superposition of the two plane-waves (the excitation one and the reflected one) in duct I, and the transmitted one in duct II. The acoustic velocity field shows a vanishing value, except in the region between the two regions of flow and non-flow. A narrower x-axis scale shows, for the acoustic pressure in Fig. 2.19, and for the acoustic transverse velocity in Fig. 2.20, that those fluctuations correspond to the excitation of the first hydrodynamic mode, which is stable in this calculation.

In this case where hydrodynamic modes are all stable, we find that the resulting acoustic field is mainly composed of plane-waves (the excitation plane-wave, and the reflected and transmitted ones). The excited hydrodynamic modes seem negligible in the solution.

2.4.3.3 The resulting acoustic fields when unstable hydrodynamic modes are present

An example of visualization of the acoustic fields is shown in this section, when sending a plane-wave, in the case where there is an unstable hydrodynamic modes. We use the same parameters as for the stable case, but changing $\omega = 0.50$ to $\omega = 0.45$.

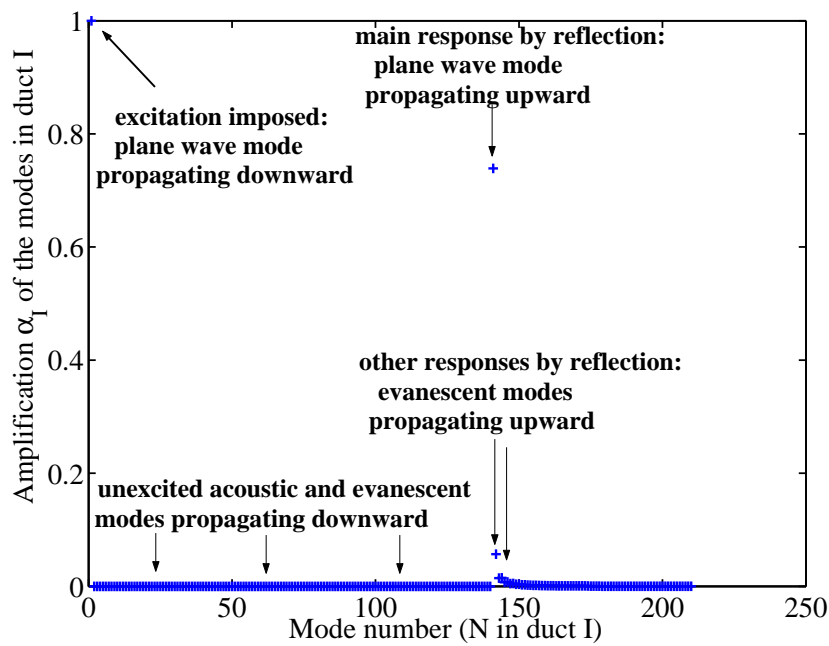


Figure 2.16: Response of the modes in duct I when applying an excitation in plane wave propagating downstream in duct I. We see that the acoustic reflection at the single expansion occurs, giving an amplification to the plane wave mode propagating upstream and secondary responses from evanescent modes propagating upstream ($N = 70$, $m = 3.5$, $\omega = 0.5$, $M_0 = 0.1$, $b = 2$).

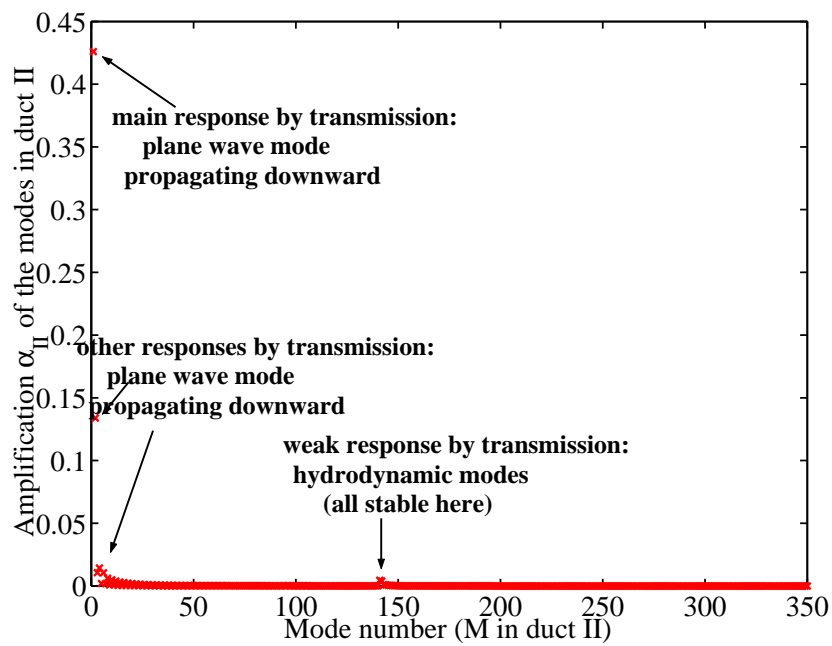


Figure 2.17: Response of the modes in duct II when applying an excitation in plane wave propagating downstream in duct I and when all hydrodynamic modes are stable in duct II. We see that the acoustic transmission at the single expansion occurs, giving an amplification to the plane wave mode propagating downstream and secondary responses from evanescent modes propagating downstream, and a weak excitation of hydrodynamic modes ($N = 70$, $m = 3.5$, $\omega = 0.5$, $M_0 = 0.1$, $b = 2$).

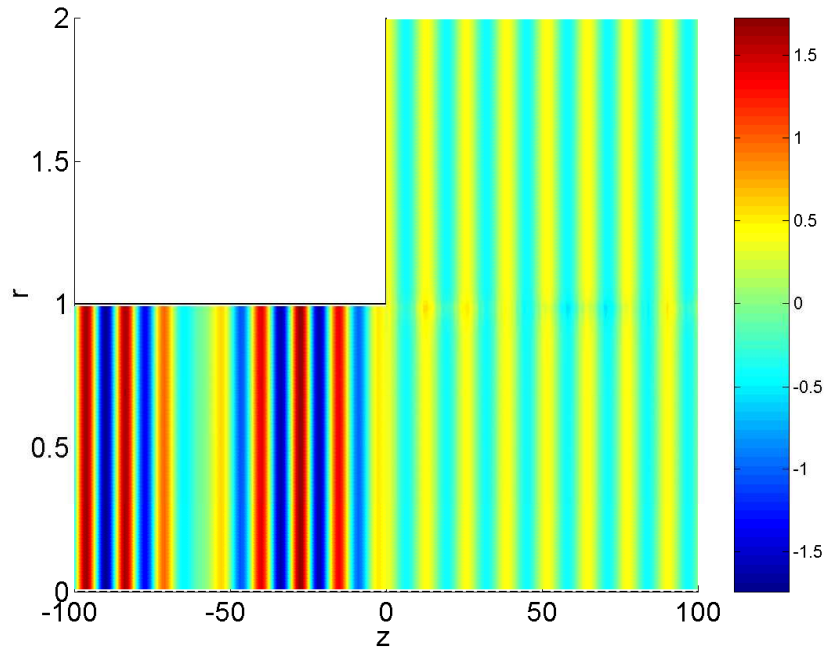


Figure 2.18: Real part of the pressure p' sending a plane wave excitation upstream P_1^+ of amplitude $\alpha = 1$ when no unstable hydrodynamic modes are present ($N = 70$, $m = 7$, $\omega = 0.5$, $M_0 = 0.1$, $b = 2$).

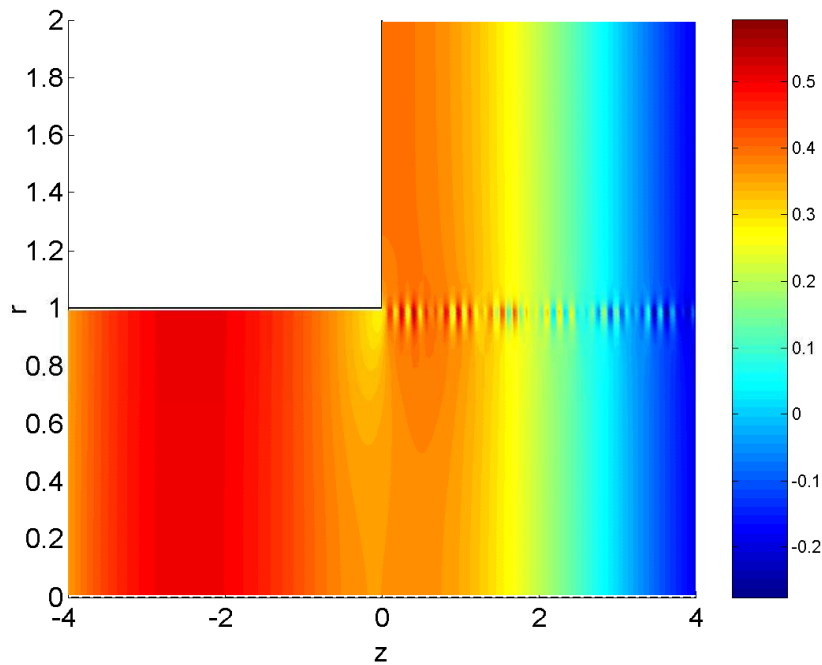


Figure 2.19: Zoom of the real part of the pressure p' sending a plane wave excitation upstream P_1^+ of amplitude $\alpha = 1$ when no unstable hydrodynamic modes are excited ($N = 70$, $m = 3.5$, $\omega = 0.5$, $M_0 = 0.1$, $b = 2$).

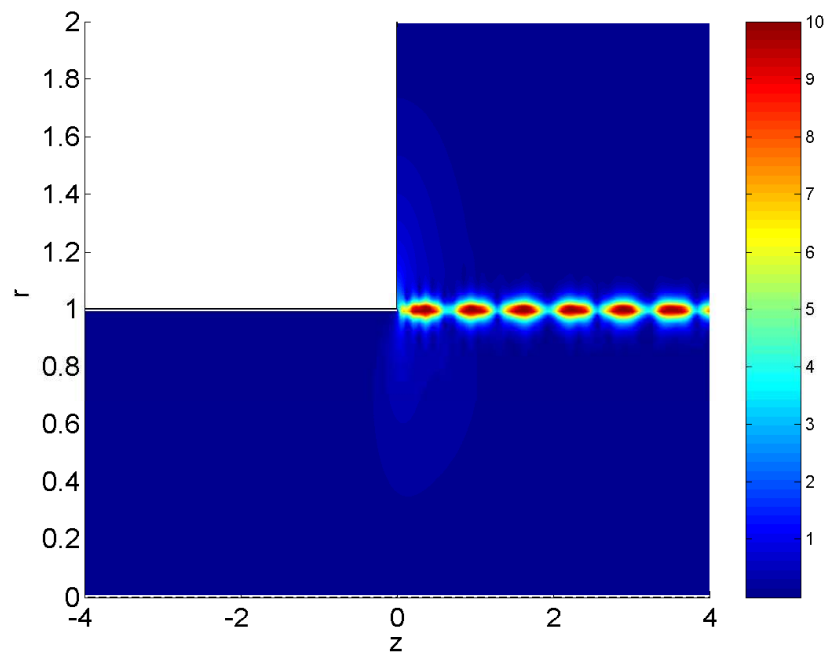


Figure 2.20: Zoom of the real part of the transversal velocity v'_r sending a plane wave excitation upstream P_1^+ of amplitude $\alpha = 1$ when no unstable hydrodynamic modes are present ($N = 70$, $m = 3.5$, $\omega = 0.5$, $M_0 = 0.1$, $b = 2$). We see clearly the response of a stable hydrodynamic mode excited at the edge of the expansion.

The excitation results in getting a response composed, as previously, by plane-waves reflected in duct I (similar as for the previous stable case), but above all here, by the transmitted unstable amplified hydrodynamic mode in duct II. In fact, the amplification is very similar to the previous case (see Fig.2.22), as we have only change ω from 0.50 to $\omega = 0.45$. The difference is that the hydrodynamic mode excited is the unstable one. His amplitude is small, but non-vanishing, and will become very large rapidly, as it is amplified exponentially by propagation.

The acoustic field is exponentially amplified by this mode. Hence it is needed to saturate the influence of this mode, in order to make the visualization possible all the same. On the figures, the visualization is made using a saturation level of 10 (the excitation plane-wave has a value of 1) at which all quantities are put if they exceed this level.

Visualizations are given, for the acoustic pressure in Fig. 2.21. The influence of the unstable hydrodynamic mode is clear: the saturation expands till all the region of propagation. The visualization is very difficult in this case, as high accuracy is needed to locate very close to the transition from stability to instability, in order that the imaginary part of the unstable wave number would not be too high. Close to the transition (at 10^{-4}), we can see more clearly, as shown in Fig. 2.22, the influence of the unstable hydrodynamic mode on the response downstream of the expansion.

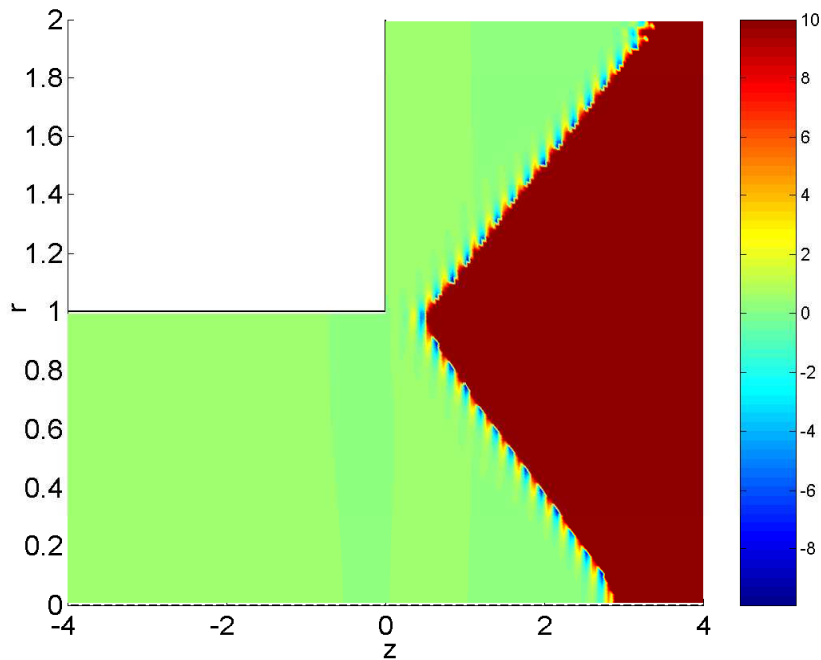


Figure 2.21: Zoom of the real part of the pressure p' sending a plane wave excitation upstream P_1^+ of amplitude $\alpha = 1$ when an unstable hydrodynamic mode is excited ($N = 70$, $m = 3.5$, $\omega = 0.45$, $M_0 = 0.1$, $b = 2$).

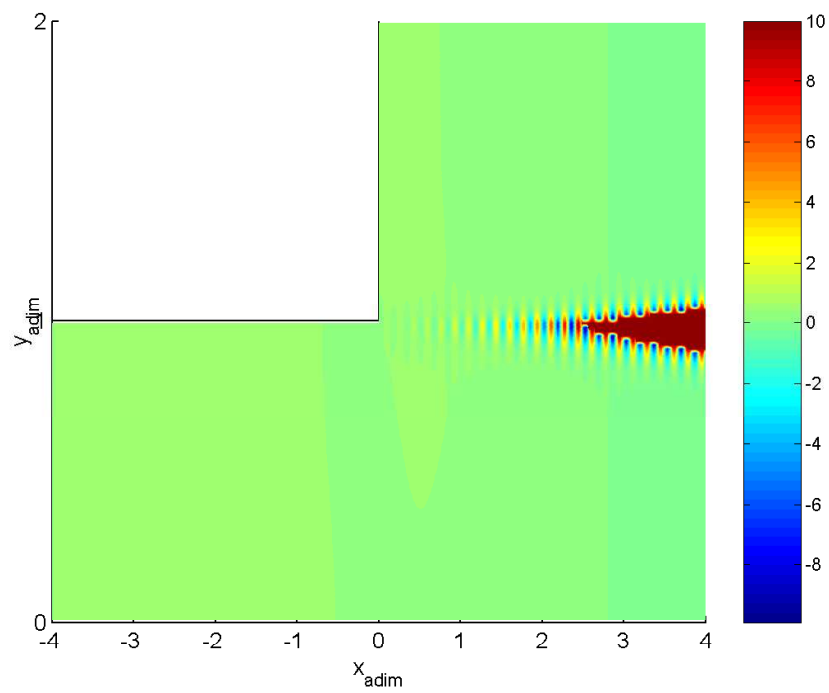


Figure 2.22: Real part of the pressure p' sending a plane wave excitation upstream P_1^+ of amplitude $\alpha = 1$ when an unstable hydrodynamic mode is excited ($N = 70$, $m = 3.5$, $\omega = 0.4911$, $M_0 = 0.1$, $b = 2$).

2.4.4 Difficulties in the calculation

2.4.4.1 Adjusting the coefficients of the parabola

The correct identification of the hydrodynamic modes is made by the knowing that N modes have to be found and using the purely artificial parabola:

$$Im(K)^2 = A(Real(K)^2 - x_0^2), \tag{2.73}$$

The parameters A and x_0 have to be fitted. Evanescent modes can wrongly be identified as unstable hydrodynamic modes, as illustrated in Fig.2.23. In this case, the calculation identifies the mistake, as the number of hydrodynamic modes exceeds the theoretical number.

The solution is to adjust the coefficients of the parabola A and x_0 . Good determination is mostly obtained for A between 1 and 15 and x_0 between $0.6/\max(M_0)$ and $0.9/\max(M_0)$. In fact, such problem in the parabola parameters occurs rarely, taking for example $A = 5$ and $x_0 = 0.8$.

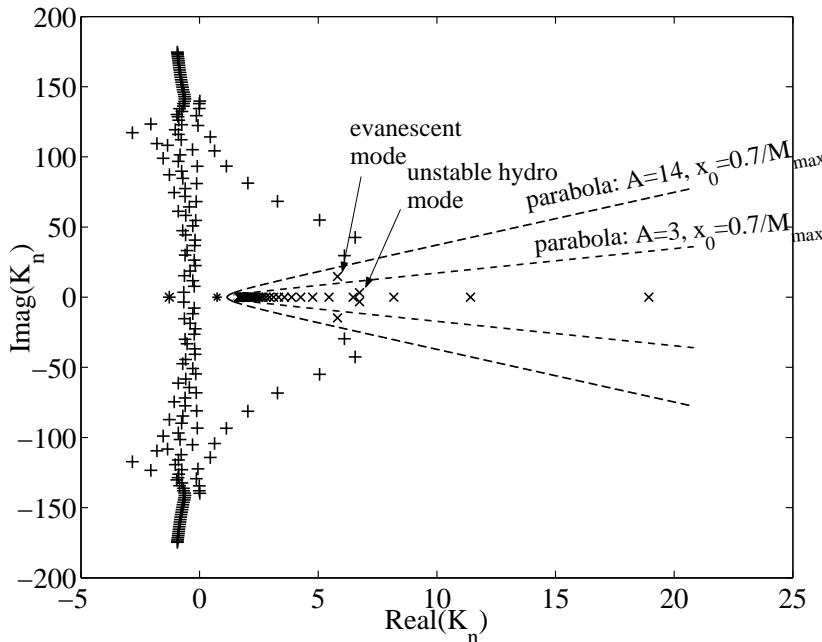


Figure 2.23: Adjustment of the parabola parameters to identify the right number of hydrodynamic modes - cylindrical coordinates, $N = 70$, $m = 4$, $\omega = 1$, $M_0 = 0.4$, $b=1.2$.

The use of a causality criterion (Crighton-Leppington or Briggs-Bers) is the most satisfying method to discern acoustic and hydrodynamic modes. It has not been implemented in this work.

2.4.4.2 In some low frequency cases

When the frequency ω is very low, the first evanescent modes upstream and downstream goes numerically on the X-axis, as illustrated in Fig.2.24. In this case, four propagating acoustic modes are found, with one travelling downstream and three upstream: the calculation is wrong (also, no transverse mode should propagate for $\omega < 3.83$).

The reason for this problem is not identified. However the solution is found: one should increase sufficiently the number of points N . At some value the calculation will give good determination of the modes.

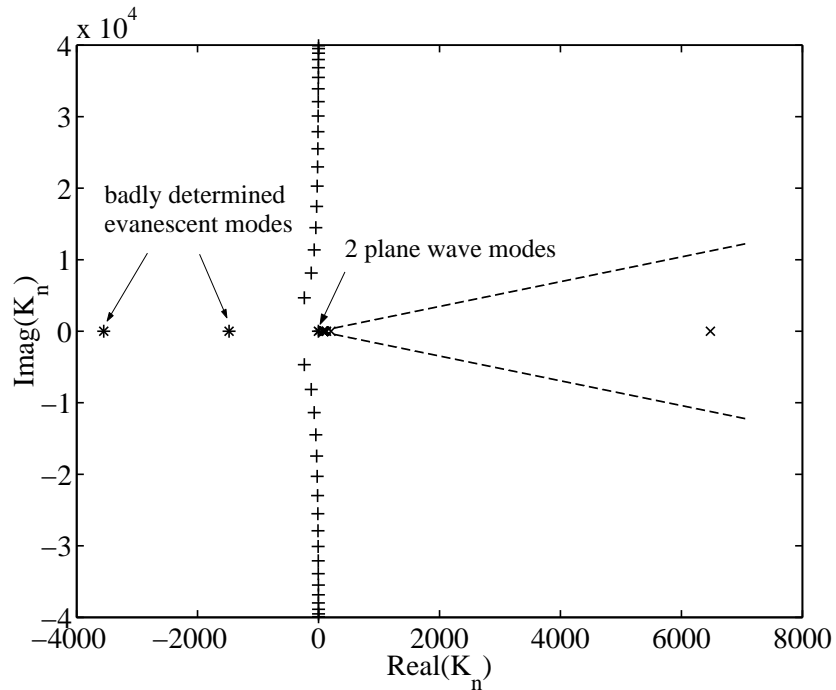


Figure 2.24: Jump of the first evanescent modes on the X-axis - cylindrical coordinates, $N = 20$, $m = 10$, $\omega = 0.001$, $M_0 = 0.01$, $b = 1.5$ -. A good determination is obtained for $N = 30$.

2.5 Single expansion results

2.5.1 Results without flow: comparison with a model

Without flow, and in the limit of vanishing frequency, a quasi-stationary model is studied: the linearized mass conservation and the linearized Bernoulli equation are applied to a single expansion (see Fig. 2.25). As in the limit of vanishing frequency, the end correction vanishes, one obtains:

$$S_1 \rho_0 u'_1 = S_2 \rho_0 u'_2, \quad (2.74)$$

$$p'_1 = p'_2. \quad (2.75)$$

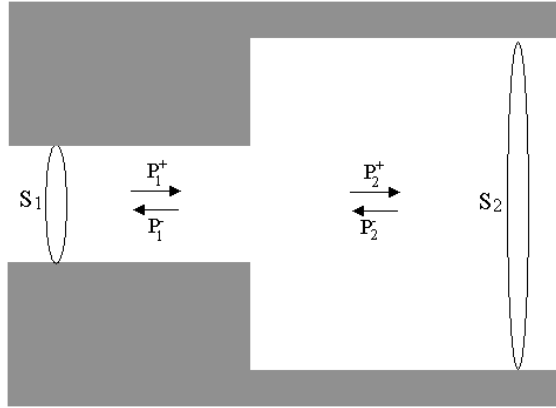


Figure 2.25: Single expansion.

The scattering matrix of the single expansion for this model is obtained:

$$R^+ = \frac{1 - \alpha}{1 + \alpha}, \quad R^- = \frac{-1 + \alpha}{1 + \alpha}, \quad (2.76)$$

$$T^+ = \frac{2}{1 + \alpha}, \quad T^- = \frac{2\alpha}{1 + \alpha}, \quad (2.77)$$

where $\alpha = S_2/S_1$ is the ratio of the duct section.

The comparison to this model is very satisfying for very low frequencies and very low Mach numbers, as illustrated in Fig. 2.26 and 2.27.

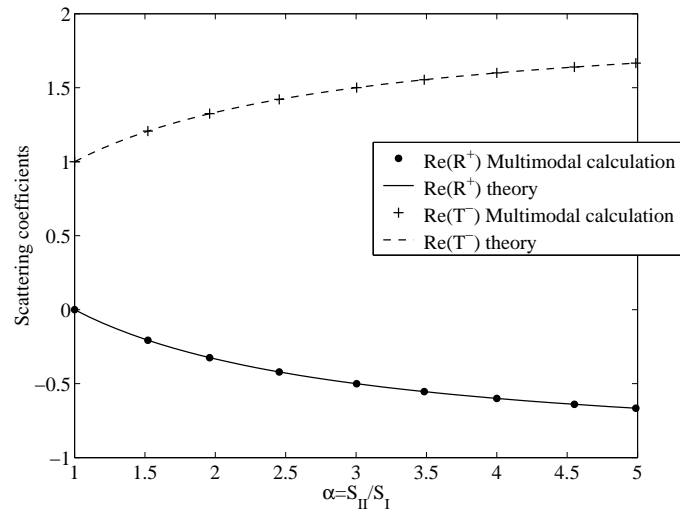


Figure 2.26: Comparison of single expansion calculations $\Re(R^+)$ and $\Re(T^-)$, as function of the expansion ratio of sections, with an analytical model in the limit of no flow and stationary regime ($f = 0.1$ Hz, $M_0 = 10^{-4}$, $N = 30$, $m = 7$).

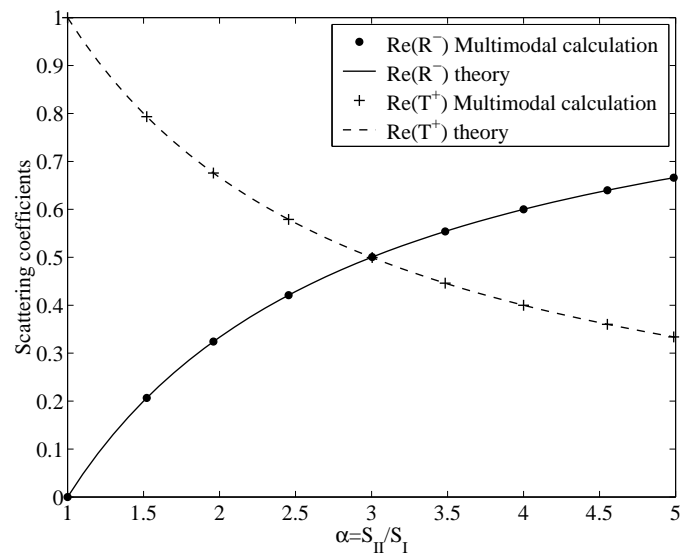


Figure 2.27: Comparison of single expansion calculations $\Re(R^-)$ and $\Re(T^+)$, as function of the expansion ratio of sections, with an analytical model in the limit of no flow and stationary regime ($f = 0.1$ Hz, $M_0 = 10^{-4}$, $N = 30$, $m = 7$).

2.5.2 Results with flow: comparison with experimental data

2.5.2.1 Principal result: good correlation with experimental data

Calculations with flow are compared with experimental data from Ronneberger (1989), for $|R^+|$ and $\text{phase}(R^+)$. The parameter $m = 7$ is used in calculations to compare with a fully turbulent flow as in those experimental data.

The effect of the flow profile is relatively weak, as illustrated in Fig. 2.28 and 2.29. For instance, a difference of around 10^{-2} is obtained between $m = 7$ and $m = 9$.

In most of the cases, multimodal calculations are close to experimental data, for the magnitude and phase of R^+ , as illustrated in Fig. 2.28, 2.29, 2.30, 2.31, 2.32.

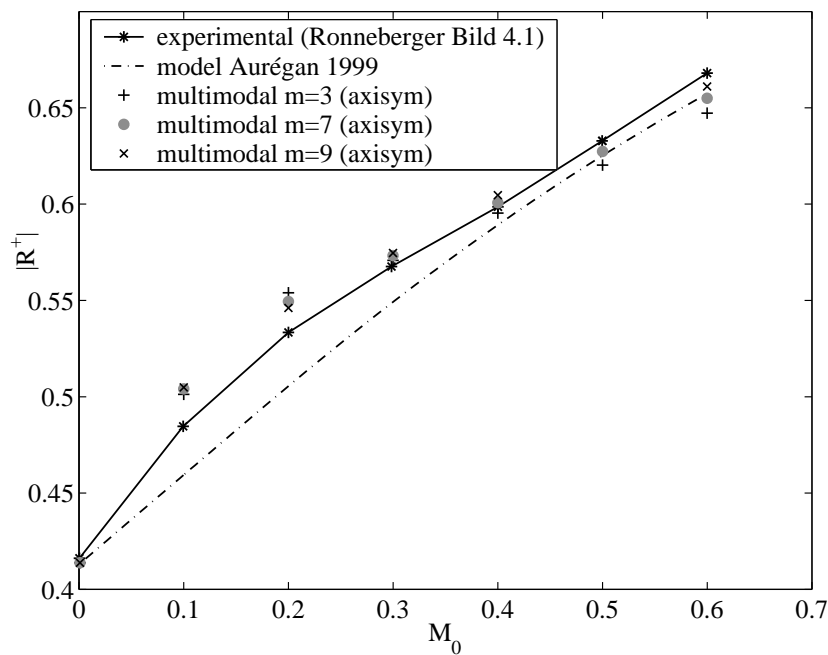


Figure 2.28: Comparison of single expansion calculation $|R^+|$, as function of the mean Mach number in the duct, with experimental literature data from Ronneberger (Bild 4.1, $\eta = S_I/S_{II} = 0.419$, $f=900$ Hz, $m = 7, N=150$).

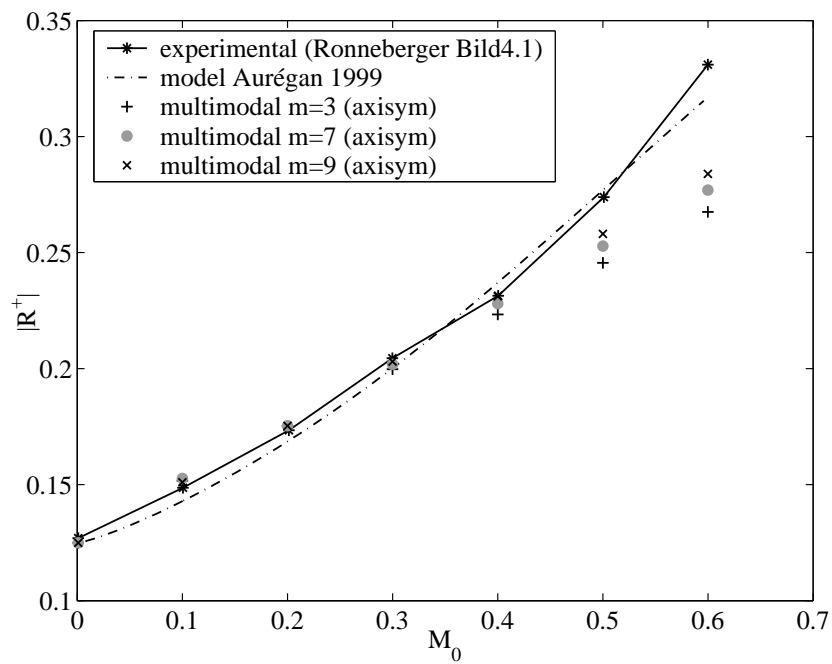


Figure 2.29: Comparison of single expansion calculation $|R^+|$, as function of the mean Mach number in the duct, with experimental literature data from Ronneberger (Bild 4.1, $\eta = 0.779$, $f=900$ Hz, $m = 7, N=150$.)

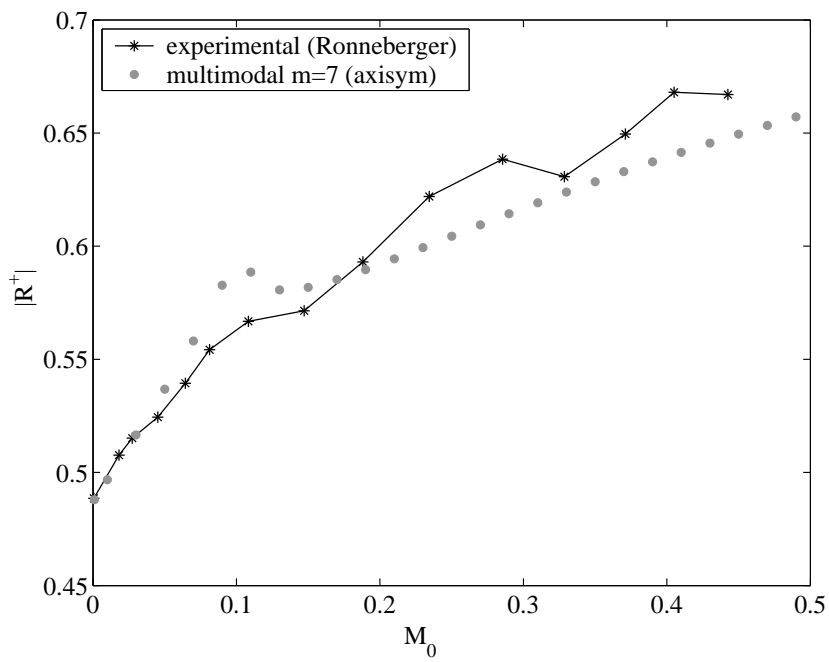


Figure 2.30: Comparison of single expansion calculation $|R^+|$, as function of the mean Mach number in the duct, with experimental literature data from Ronneberger (Bild 4.1, $\eta = 0.346$, $f=500$ Hz, $m = 7, N=150$.)

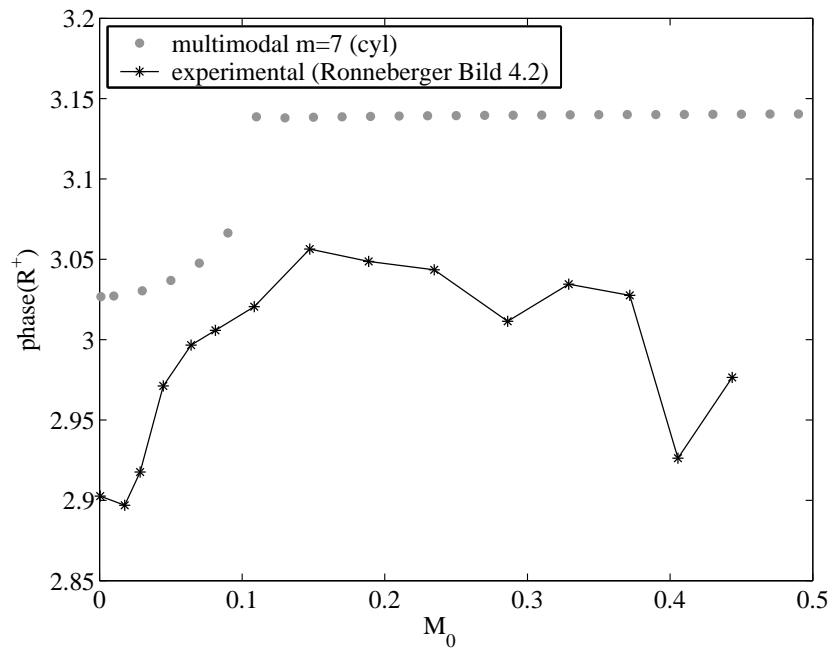


Figure 2.31: Comparison of single expansion calculation $phase(R^+)$, as function of the mean Mach number in the duct, with experimental literature data from Ronneberger (Bild 4.1, $\eta = 0.346$, $f=500$ Hz, $m = 7, N=150$.)

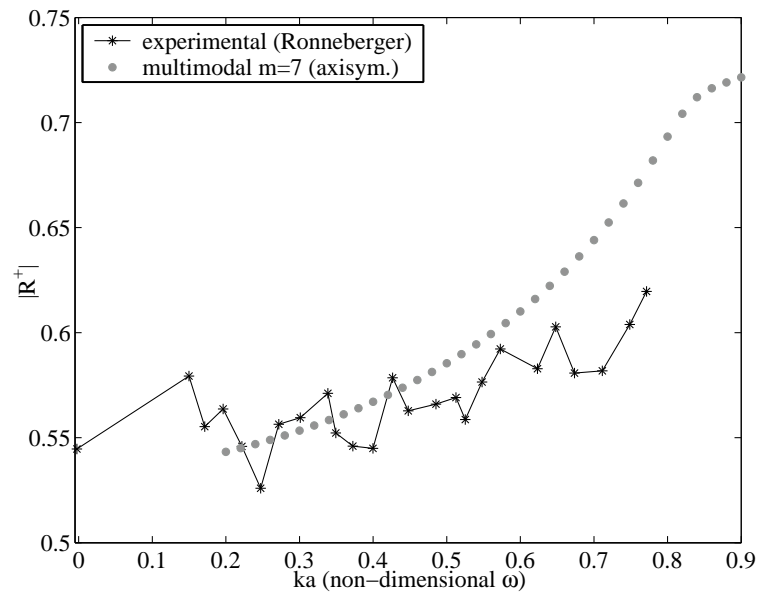


Figure 2.32: Comparison of single expansion calculation $|R^+|$, as function of the mean Mach number in the duct, with experimental literature data from Ronneberger (Bild 4.1, $\eta = 0.42$, $M_0=0.3$, $m = 7$, $N=150$).

2.5.2.2 Comparison with another numerical method and Kutta condition

The works of Boij and Nilsson (2003 and 2005) represents another numerical method to determine the acoustical properties of a single expansion. The particularity of this method is that a Kutta condition can be implemented or not. It is employed exclusively on a rectangular duct.

We have tried to compare our results with this numerical method. In order to do so, The variable He^* is proposed by Boij and Nilsson (2003) to scale cylindrical and rectangular configurations. The idea is to get a dimensionless frequency corresponding to the same distance from the frequency of study to the cut-off frequency of the duct. This gives:

$$He^* = \frac{kb}{kb_{cut-off}}, \quad (2.78)$$

where $kb_{cut-off} = 3.832$ for a circular duct, and $kb_{cut-off} = \pi$ for a square duct. Hence:

$$He^* = \frac{1}{\eta} \frac{\omega_{rect}}{\pi} = \frac{1}{\sqrt{\eta}} \frac{\omega_{cyl}}{3.832}, \quad (2.79)$$

where $\eta = S_1/S_2$.

An example of result is given in Fig. 2.33. As already observed, our calculations are close to Ronneberger's results. The limits are particularly well obtained. Also, as already observed and indicated, the parameter of the flow profile is not critical for calculations, which is very satisfying, as the same results are obtained within a relative error of less than 2% when using the range $m = 3$ and $m = 15$ of flow profile parameter. The main difference of level is obtained at a hump, for $He^*/M_0 \approx 1.1$. This difference is expected to be due to the amplification of the unstable hydrodynamic mode, but should be clarified in further study.

Comparison with Boij's results indicates that the Kutta condition is obtained for low He^*/M_0 .

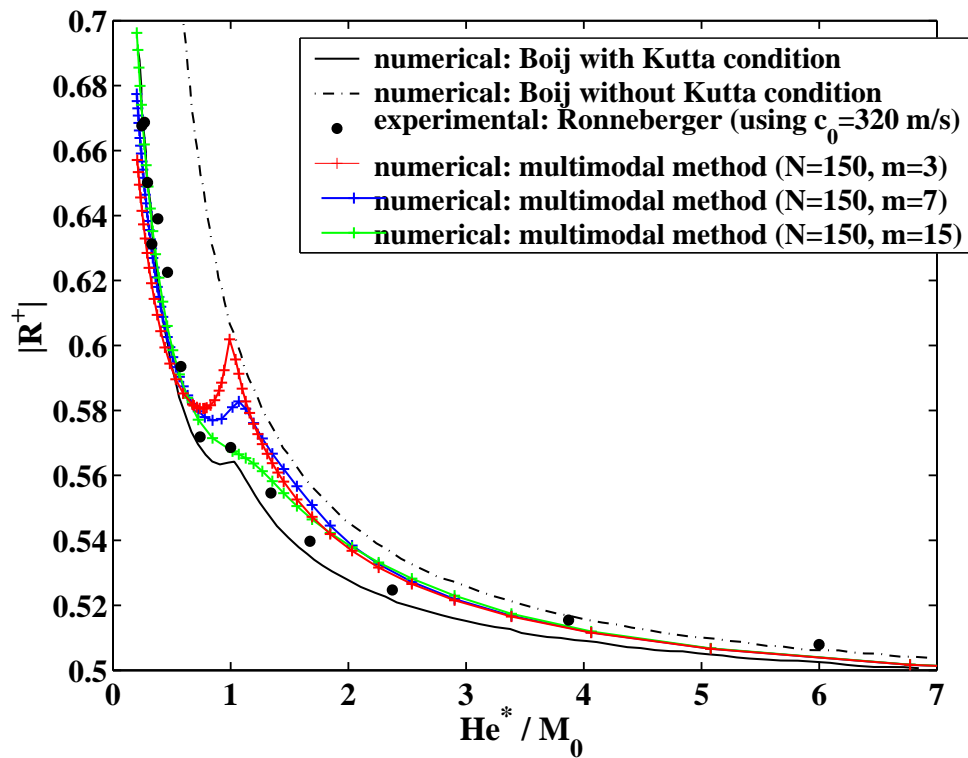


Figure 2.33: Comparison of single expansion calculation $|R^+|$, as function of the dimensionless Helmholtz number, with experimental literature data from Ronneberger and numerical method from Boij ($\eta = 0.346$, $f^*=500\text{Hz}$).

2.5.2.3 Problematic results: bad correlation for certain cases when $\omega > 0.7$

Strong difference is found for R^+ between numerical and experimental data, for ω above 0.6-0.7 and for a high Mach number. It is illustrated in Fig. 2.34. One should note that this range of parameters is quite extreme.

This discrepancy with experimental data has not been clarified. We have checked that the phase of R^+ is well calculated, as shown in Fig. 2.35. Also, the convergence of the results has been checked carefully. Finally, it would be quite surprising that our calculations abruptly give such bad correlation with experiments. Consequently, it seems that the first question is to know the discrepancies in the experimental data, as they correspond to a quite delicate measure in this extreme range of frequency.

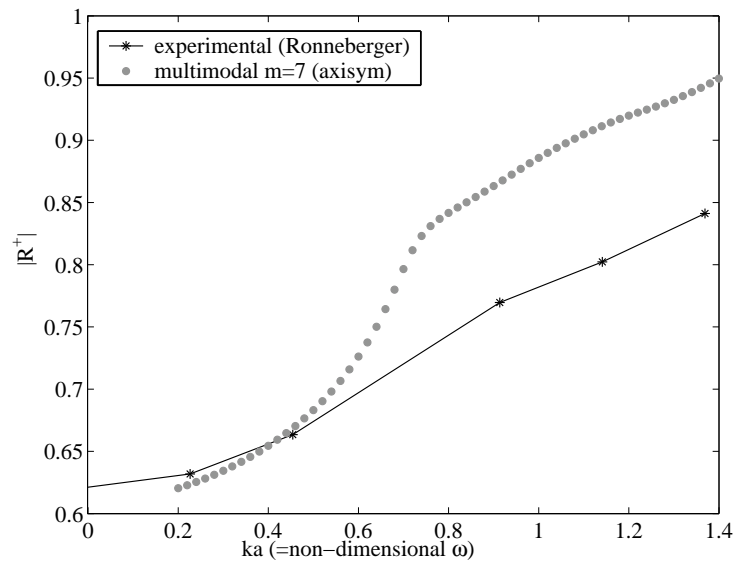


Figure 2.34: Comparison with literature (Ronneberger Bild 4.3) for the magnitude ($\eta = 0.35$, $M_0=0.3$, $N=150$).

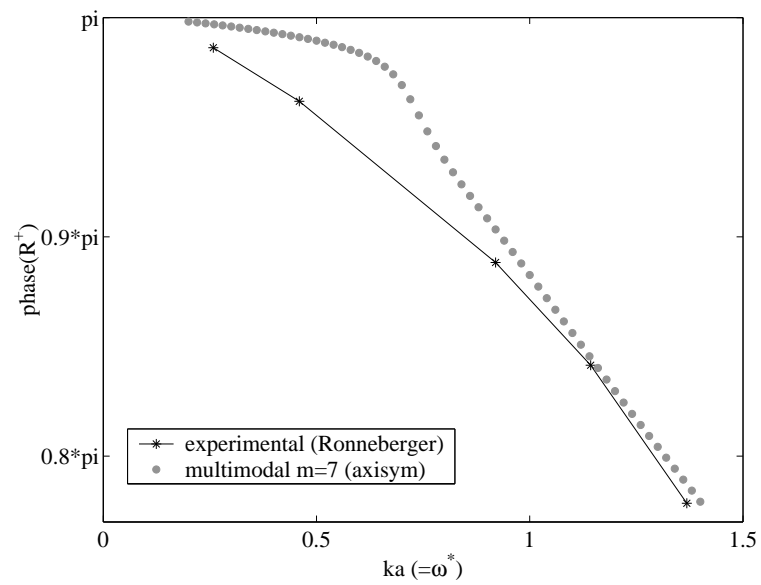


Figure 2.35: Comparison with literature (Ronneberger Bild 4.3) for the phase ($\eta = 0.35$, $M_0=0.3$, $N=150$).

2.5.3 Transition to unstable hydrodynamic mode

The transition from stable to unstable hydrodynamic mode is illustrated in Fig. 2.36. We use the momentum thickness of the wall boundary layer δ :

$$\delta = \int_{r=r_1}^{r=1} M(r)(1 - M(r))dr, \quad (2.80)$$

where r_1 is determined so that for $r \leq r_1$, $M(r) \geq 0.99M_0$. δ is dimensionless with the radius a of duct I. We find a critical value of $\omega\theta/M_0 = k^*\theta^*/M_0$ ('*' denotes dimensional variables) around 0.25 in the limit of infinitely shear layers.

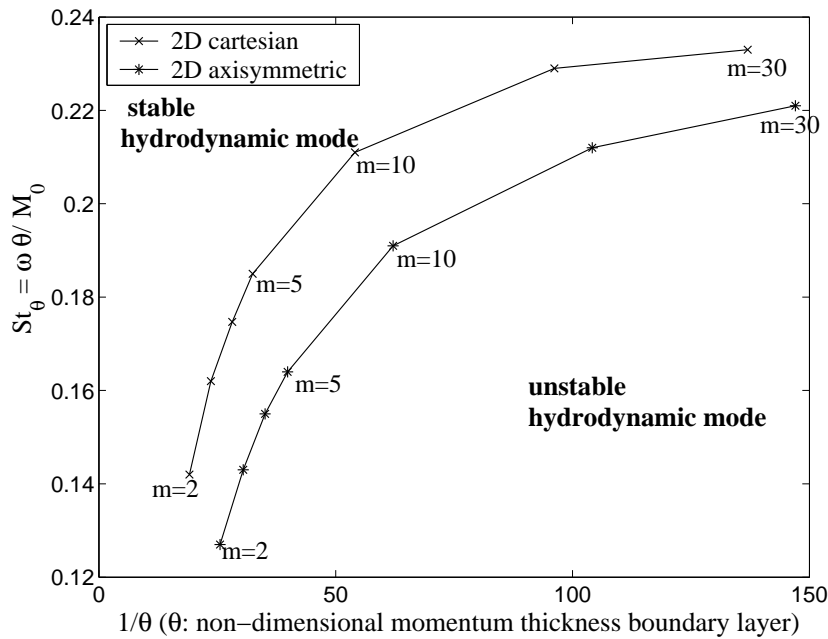


Figure 2.36: Determination with the multimodal method of the Strouhal number for the hydrodynamic instability transition, as function of the flow profile parameter m linked with the momentum thickness δ of the boundary layer.

The Strouhal number for the transition is given in Michalke (1965), indicating a value of $k^*\theta^*/M_0 = 0.25$ (also mentioned in Boij and Nilsson (2003); the value has to be divided by two, as it corresponds to a pipe diameter) for infinitely thin shear layers and dimensional variables. This is in good agreement with our numerical values.

2.5.4 Comparison between circular and rectangular duct

2.5.4.1 A satisfying dimensionless frequency

The comparison between a circular and a rectangular duct gives different results, see Fig. 2.37. Hence, to make the results dimensionless in frequency, the proposition from Boij and Nilsson (2003) is studied. The idea is to use a frequency made dimensionless with the distance to the cut-off frequency: the dimensionless Helmholtz number He^* is defined, as presented in section 2.5.2.2.

Results for this dimensionless frequency representation are given in Fig. 2.38. The collapse is satisfying, especially for low Helmholtz number $He^* \lesssim 0.25$.

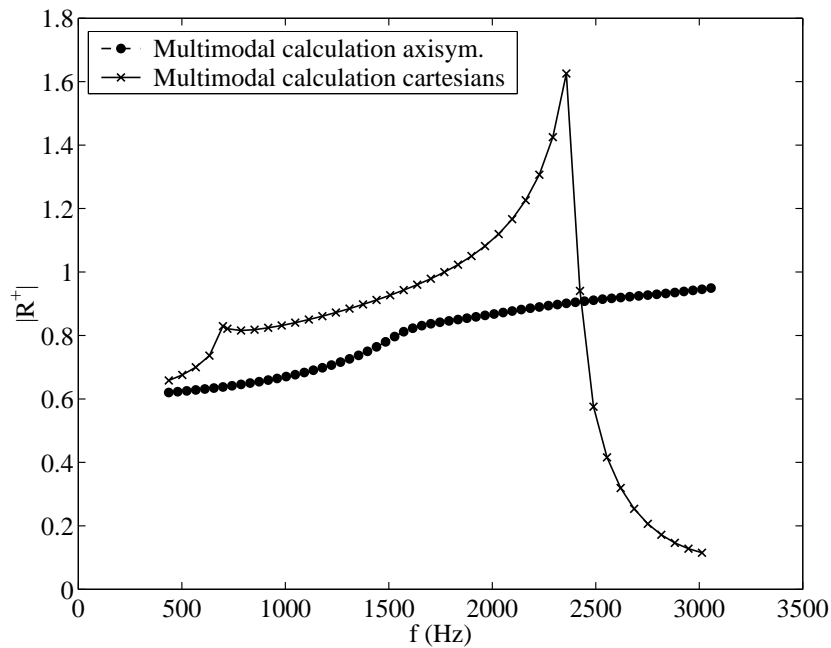


Figure 2.37: Comparison on $|R^+|$ between a circular and a rectangular duct, using a similar ratio of sections ($M_0 = 0.3$, $m = 7$, $\eta = 0.35$, $N = 150$).

2.5.4.2 Investigation of a hump form on scattering matrix coefficients

A local hump form is sometimes found, as the one visible in Fig. 2.30 around $M_0 = 0.11$. It appears in our calculations, and also clearly on the previous works of Boij & Nilsson (without explanation). Moreover, on this figure, it is clear that it exists also in experimental data, in a more smooth form. We have tried to investigate this phenomenon on our calculation in the case presented in Fig. 2.30.

First, it is clear that this phenomenon is not linked to the transition from stable to unstable hydrodynamic modes, as this one in this case appears around $M_0 = 0.045$.

It seems, as observed in Fig. 2.39, that this hump corresponds to a minimum distance between the unstable hydrodynamic mode and the smallest (or closest) evanescent mode. This is however not obvious. The influence of such proximity on the scattering matrix coefficient is not understood. A

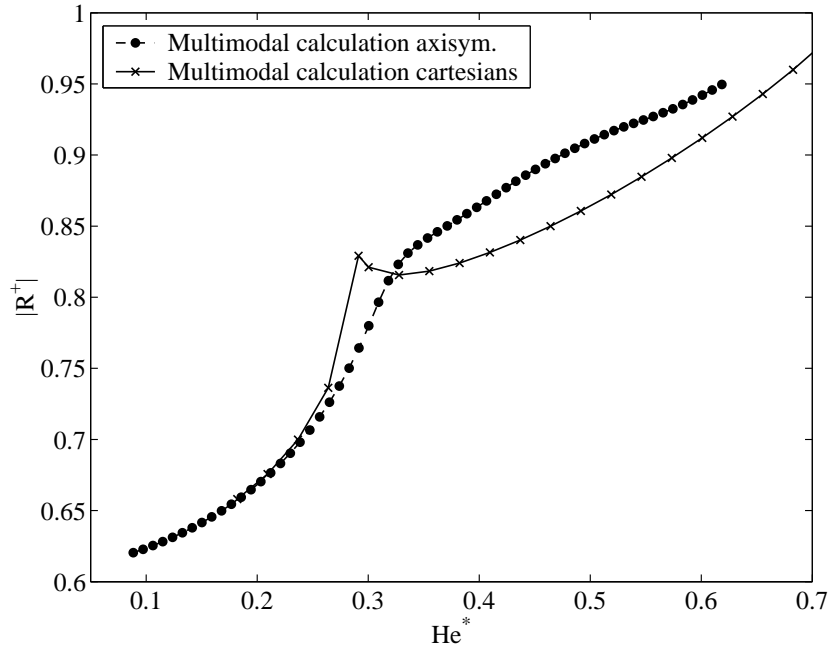


Figure 2.38: Dimensionless representation of $|R^+|$ for a circular and a rectangular duct, using a similar ratio of sections ($M_0 = 0.3$, $m = 7$, $\eta = 0.35$, $N = 150$).

physical explanation for the existence of this hump form lacks also. Hence further study would be needed on this subject to understand what really happens.

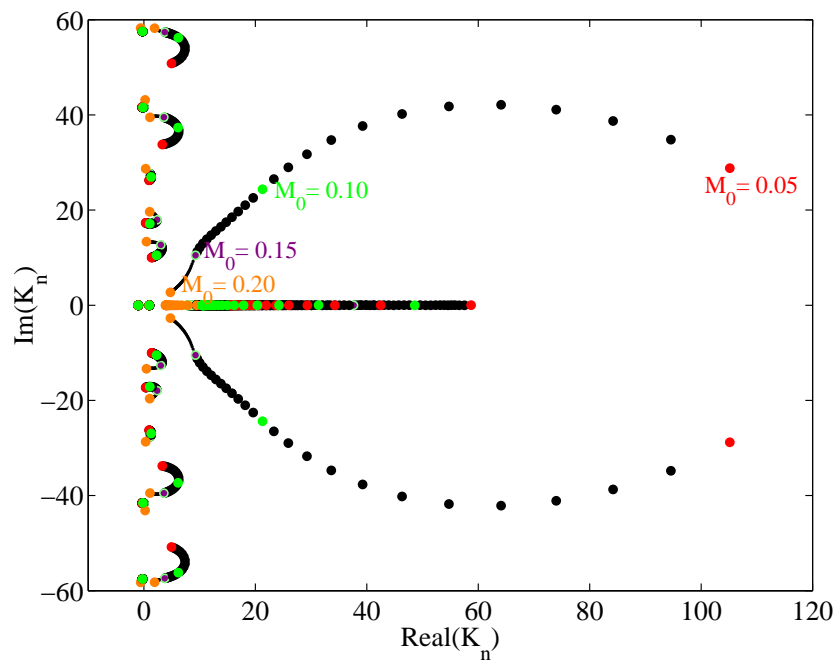


Figure 2.39: Evolution of the modes around the hump form observed around $M_0 = 0.11$ on the reflection coefficient in Fig. 2.30 ($\eta = 0.346$, $f = 500$ Hz, $N=50$; the wave numbers depend weakly on N when N is sufficiently high, above 20).

2.6 Conclusion

A numerical calculation has been used to determine the acoustical properties of a single expansion under a shear flow profile. The scattering matrix and the resulting acoustical fields when sending excitation waves have been calculated. The multimodal method used is a simple finite difference resolution in established harmonic regime of the linearized Euler equations under incompressible shear mean flow. Only the transverse direction is solved, then fields are deduced on the longitudinal direction simply by propagation at the imposed frequency. Visco-thermal effects are neglected and, the flow is assumed not to expand after going through the expansion. The resolution gives acoustic modes, propagating at the speed of sound, hydrodynamic modes, convected by the mean flow, and evanescent modes, with varying speed between each other. The calculation of these modes is made in the two ducts, and the x-axis location corresponding to the location of the expansion, and the matching of these modes at that point by conditions of continuity of the acoustic variables gives the acoustic scattering matrix of the configuration. In this chapter, the objective was to validate this method, particularly by comparing with experimental results.

As a result, the calculations give good satisfaction. A large number of comparisons has been made on a large range of the parameters (frequency, Mach number, height of the expansion), both with a vanishing shear flow, and with a shear flow, and a large number of comparisons have been made with theory and experimental data:

- an unstable hydrodynamic mode is sometimes present in the duct II. Its existence is supposed to be linked with the virtual inflexion point of the flow profile at the separation between the flow and the non-flow region. The transition from stable to unstable hydrodynamic modes is in close agreement with literature (section 2.5.3). This result has been confirmed by the study of G. Koojman on the same method (PhD, TU/e Eindhoven);
- the method calculates very satisfyingly the scattering matrix coefficients of the single expansion. Comparison with simple models is very good for limit cases (no flow, quasi-stationary), and above all comparisons are in general very satisfying with all experimental data found in Ronneberger concerning the magnitude and the phase of the reflection coefficient R^+ (sections 2.5.1 and 2.5.2.1);
- the method, as it allows both rectangular and cylindrical calculations, has confirmed a satisfying dimensionless Helmholtz number, proposed in literature (Boij and Nilsson, 2005) to plot data for these two geometries (section 2.5.4). This confirms that the ratio of the frequency compared to the cut-off frequency of the pipe is a good dimensionless frequency in those problems.

However, some problems have been pointed out and would need more study:

- for some extreme range of parameters (high frequency and high Mach number), comparison with experimental data is bad (section 2.5.2.3). We have no clear understanding of this phenomenon. This is not a problem of convergence of our calculations, as it has been checked. But one should note that it may be due to inaccuracies in the experimental data, as for this extreme range of parameter, measurements are difficult to handle;

- a local hump form, in the evolution of the magnitude of a reflection coefficient, is sometimes found, but its signification is not understood (section 2.5.4.2). This phenomenon appears in the experimental data. We have understood that it corresponds approximately to a close distance, in the real part and imaginary part of the wave numbers representation, between an evanescent mode and the unstable hydrodynamic mode. However, the physics of the phenomenon is not understood, and this study would need further study.

As a conclusion, we have considered this method as been validated by this single expansion configuration, and we have decided to apply it to a more complex, potentially whistling, configuration: a double expansion, that is, two successive single expansions (chapter 3).

In perspective, more study should be however be made to clarify the unsolved problems, and also to use more efficiently its advantages:

- the comparison between cylindrical and rectangular ducts is possible with this method. We have begun this study, but not deepened it particularly in terms of understanding. It would be interesting to do more study on this topic, as it is hardly covered in literature;
- a larger understanding of this method would be given by a deeper understanding of the evanescent modes found in our calculations. As the wave numbers of those modes do not clarify if they are propagated or convected, we do not know in this study whether they are compressible modes (that is, acoustic modes) or incompressible modes (that is, incompressible-type modes, meaning that we would obtain them in an incompressible modelling). To this purpose, an incompressible calculation should be done in the same manner of this method to clarify whether the evanescent modes are incompressible or compressible.

One should note finally that this method could not be applied to any flow configuration, and to any geometry: the price of its simplicity is that it has a quite restrained field of application: the flow entering the expansion must be horizontal, and non-expanding.

Bibliography

- Y. Aurégan, Comportement aéroacoustique d'une expansion sifflante, Congrès CFA, Tours, 2006.
- Y. Aurégan, Comportement aéro-acoustique basse-fréquence d'une expansion, 14e Congrès Français de Mécanique, Toulouse, 1999.
- C. Bailly, Modélisation du rayonnement acoustique des écoulements turbulents libres subsoniques et supersoniques, thèse, HP 63/94/068, EDF-DER Clamart, 1994.
- W.P. Bi, V. Pagneux, D. Lafarge and Y. Aurégan, Modelling of sound propagation in a non-uniform lined duct using a Multi-Modal Propagation Method, *Journal of Sound and Vibration*, 289 (4-5): 1091-1111, 2006.
- S. Boij, B. Nilsson, Scattering and absorption of sound at flow duct expansions, *Journal of Sound and Vibration*, 289 (3): 577-594 , 2006.
- S. Boij, B. Nilsson, Reflection of sound at area expansions in a flow duct, *Journal of Sound and Vibration*, 260(3): 477-498, 2003.
- S. Félix, V. Pagneux, Fonction de Green dans un écoulement cisailé, 16e Congrès Français de Mécanique, Nice, 2003.
- Félix, S, Propagation acoustique dans les guides d'ondes courbes & problème avec source dans un écoulement cisailé, Thèse, École doctorale de l'Université du Maine, Le Mans, France, 2002.
- M. Leroux, S. Job, Y. Aurégan, V. Pagneux, Acoustical propagation in lined duct with flow, *Numerical simulations and measurements*. 10th ICSV, Stockholm, July 2003.
- A. Michalke, On spatially growing disturbances in an inviscid shear layer, *Journal of Fluid Mechanics*, 23: 521-544, 1965.
- D. Ronneberger, Theoretische und experimentelle Untersuchung der Schallausbreitung durch Querschnittsprünge und Lochplatten in Strömungskanälen, DFG-Abschlussbericht. Drittes Physikalisches Institut der Universität Göttingen, 1987.
- H. Schlichting, *Boundary Layer Theory*, McGraw-Hill, 6th Ed., 1968.
- G. Vilenski, S. Rienstra, Acoustic Modes in a ducted shear flow, 11th AIAA/CEAS Aeroacoustics Conference, Montana, CA, USA, 2005.

Chapter 3

Aeroacoustical behaviour of a whistling expansion

3.1 Introduction

This chapter is an experimental and numerical study of the aeroacoustical behaviour of a whistling expansion. The objective is to study the potentially whistling frequency of this configuration, by applying the whistling criterion (introduced in chapter 1), and then, to obtain some local understanding of the behaviour of the acoustic fields in this configuration.

The multimodal method (introduced in chapter 2) is used to calculate the scattering matrix of this configuration. Numerical results are compared to our experimental data.

3.2 Configuration studied

The geometry considered is an orifice with a double expansion (see Fig. 3.1) constituted by:

- upstream, a constriction, composed by an orifice with a bevel upstream. The idea to use a bevel upstream is that the jet formed at the exit of this constriction will be horizontal, hence allowing numerical calculations on this configuration;
- downstream, a double expansion, composed by an orifice with no bevel and a larger diameter. The idea is that this second orifice of length L will create a feedback and make this configuration potentially whistling, compared to an orifice with a single expansion (as presented in chapter 1).

This configuration is the simplest whistling one on which we can apply the multimodal method. Indeed, in order to use the multimodal method, the flow has to be stabilized so that it forms a jet at the entrance of the expansion. Consequently, the calculation of a simple circular centred orifice was not possible, and the configuration of an orifice with only a bevel upstream is not interesting, as it is not a potentially whistling configuration.

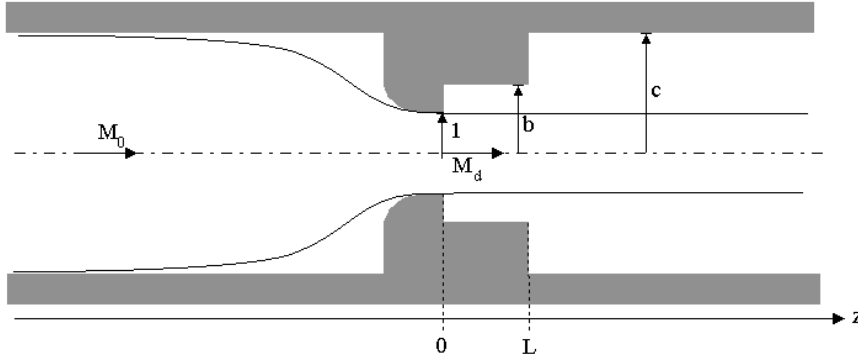


Figure 3.1: Geometry of the configuration studied: a constriction, forming a jet at $x = 0$, followed by a double expansion. The lengths are made non-dimensional with the height of the constriction a^* ('1' on the figure). M_d is the Mach number at the constriction ($z = 0^-$).

3.3 Experimental results: the configuration is potentially whistling

Experiments show that this configuration is a potentially whistling one, applying the whistling criterion presented in chapter 1, as illustrated in Fig. 3.2 (the other results on this configuration are reported in appendix B).

The potentially whistling frequencies are made non-dimensional in a similar manner as for single orifices (see chapter one). The Strouhal number is based on the length L of the expansion, and the velocity U_d at the entrance of the expansion ($z = 0^-$):

$$St = \frac{fL}{U_d}. \quad (3.1)$$

The first mode (first peak of the potentially whistling frequencies) is obtained around 0.2-0.3, as visible in Fig. 3.3 and in appendix B. This is coherent with the values obtained for the single orifices presented in chapter 1.

One exception is constituted by the case $M_0 = 0.56 \times 10^{-2}$, because the Strouhal number is quite high compared to 0.2-0.3. This corresponds to a known phenomenon. This measurement corresponds to a low Reynolds number $Re_D = U_0 D / \nu = 3.8 \times 10^3$ (using $\nu_{air} = 1.51 \times 10^{-5} \text{ m}^2 \text{ s}^{-1}$, $c_0 = 343 \text{ m s}^{-1}$), near the laminar-turbulent transition. We have already reported this behaviour in chapter 1 of significant increase of the Strouhal number at pipe Reynolds number under 5×10^3 .

3.4 Description of the numerical calculation method

The numerical calculation of the scattering matrix of this configuration is made as the following. The total scattering matrix is seen as a combination of the scattering matrix of the constriction with the scattering matrix of the double expansion.

The scattering matrix of the constriction is obtained at once by using a simple and classic acoustic model, which is presented in the following section.

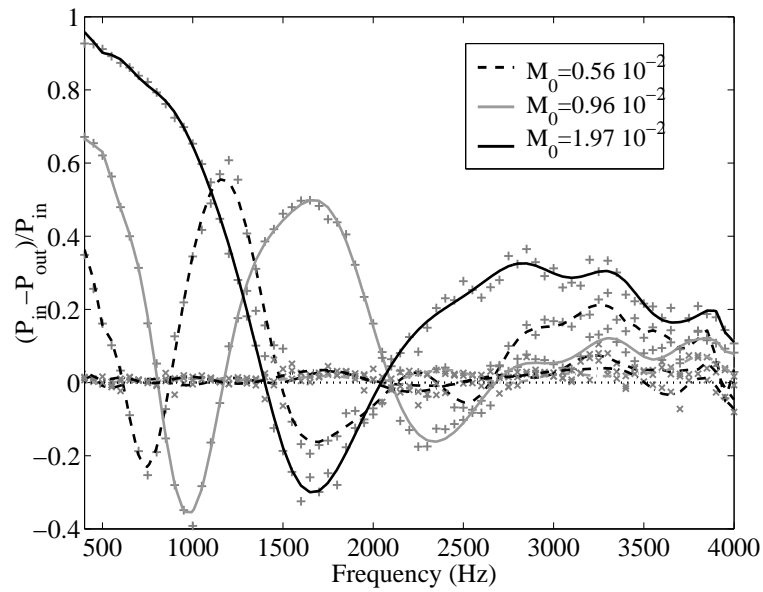


Figure 3.2: Eigenvalues of the acoustic power ratio from the whistling criterion for configuration: $b = 1.5$, $c = 3$, $L = 2$ (CCb6+CC19) for three Mach numbers: it appears that this configuration is potentially whistling.

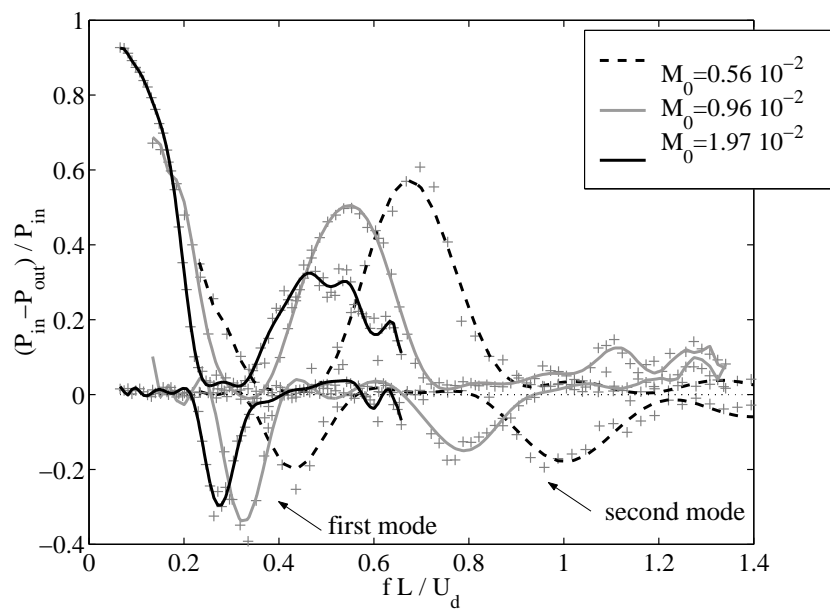


Figure 3.3: Strouhal number of the potentially whistling eigenvalues from the whistling criterion for configuration: $b = 1.5$, $c = 3$, $L = 2$ (CCb6+CC19) for three Mach numbers: the configuration is potentially whistling, exhibiting two successive modes here.

The difficulty of the calculation is represented by the calculation of the scattering matrix coefficients of the double expansion. This calculation is done using the multimodal method introduced in chapter 2, and is detailed in the following.

The combination of the two scattering matrices gives the scattering matrix of the whole configuration (presented in the following).

3.4.1 Scattering matrix of the constriction

The geometry of the constriction is shown in Fig. 3.4. A simple incompressible model is used to determine the scattering matrix of this constriction. We discern the cases with flow and without flow, as it appears that the effective length is critical to well model the non-flow case.

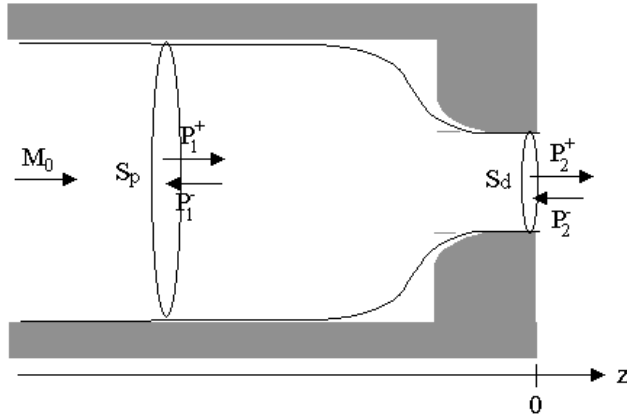


Figure 3.4: The constriction: notations used in models to determine the scattering matrix of the constriction, in the plane-wave and incompressible approximations.

3.4.1.1 Scattering matrix of the constriction with flow

Assuming the flow to be incompressible, without viscosity and stationary, Bernoulli equation indicates that the following quantity is constant on a streamline:

$$h + \frac{1}{2}\mathbf{u}^2 + \frac{\partial\phi}{\partial t} = \text{cste}, \quad (3.2)$$

where $h = p/\rho$ is the enthalpy and ϕ the velocity potential such that $\mathbf{u} = \nabla\phi$.

We linearize at first order this expression to obtain acoustical quantities. As the flow is considered incompressible, $h' = p'/\rho_0$ (where ρ_0 is the volume density of air). We obtain:

$$\frac{p'}{\rho_0} + \mathbf{u}'\mathbf{U}_0 = \text{cste}, \quad (3.3)$$

neglecting the effect of ϕ' (which leads to an end correction purely imaginary).

This general expression is applied from far upstream of the constriction (denoted by 1, of section S_p) to the constriction (denoted by 2, of section S_d), which gives the first equation:

$$\frac{p'_1}{\rho_0} + u'_1 U_0 = \frac{p'_2}{\rho_0} + u'_2 U_0. \quad (3.4)$$

The second equation of the model is the mass conservation equation linearized at the first order:

$$S_p(\rho_1 u'_1 + \rho'_1 U_1) = S_d u'_2(\rho_2 u'_2 + \rho'_2 U_2). \quad (3.5)$$

To obtain the scattering matrix coefficients corresponding to this model, we use the relations (neglecting the effect of the flow in the propagating upstream and downstream wave numbers):

$$p' = P^+ + P^-, \quad u' = \frac{P^+ - P^-}{\rho_0 c_0}, \quad \rho' = \frac{p'}{c_0^2}, \quad (3.6)$$

where c_0 is the speed of sound in air ($c_0 = 343 \text{ m}\cdot\text{s}^{-1}$ at $T=293 \text{ K}$.)

The scattering matrix coefficients of this simple model of constriction with flow are, using $\eta = S_d/S_p$:

$$R^+ = \frac{1 - \eta}{1 + \eta} \cdot \frac{1 + M_0}{1 - M_0}, \quad T^+ = \frac{2}{1 + \eta} \cdot \frac{1 + M_0}{1 + \frac{M_0}{\eta}}, \quad (3.7)$$

$$R^- = \frac{-1 + \eta}{1 + \eta} \cdot \frac{1 - \frac{M_0}{\eta}}{1 + \frac{M_0}{\eta}}, \quad T^- = \frac{2\eta}{1 + \eta} \cdot \frac{1 - \frac{M_0}{\eta}}{1 - M_0}. \quad (3.8)$$

They are illustrated as function of the Mach number M_0 in Fig. 3.5.

3.4.1.2 Scattering matrix of the constriction without flow

Without flow, the same previous model is considered, except that we take into account the end correction term, so that:

$$\frac{p'_1}{\rho_0} = \frac{p'_2}{\rho_0} + j\omega\alpha L_{eff} u'_2, \quad (3.9)$$

where $\eta = S_d/S_p$ and L_{eff} is an effective length.

The scattering matrix coefficients of this model of constriction without flow are:

$$R^+ = \frac{1 - \eta + jA}{1 + \eta + jA}, \quad T^+ = \frac{2}{1 + \eta + jA}, \quad (3.10)$$

$$R^- = \frac{-1 + \eta + jA}{1 + \eta + jA}, \quad T^- = \frac{2\eta}{1 + \eta + jA}, \quad (3.11)$$

where $A = \omega\eta L_{eff}/c_0$.

The scattering matrix coefficients obtained with this model are illustrated in Fig. 3.6.

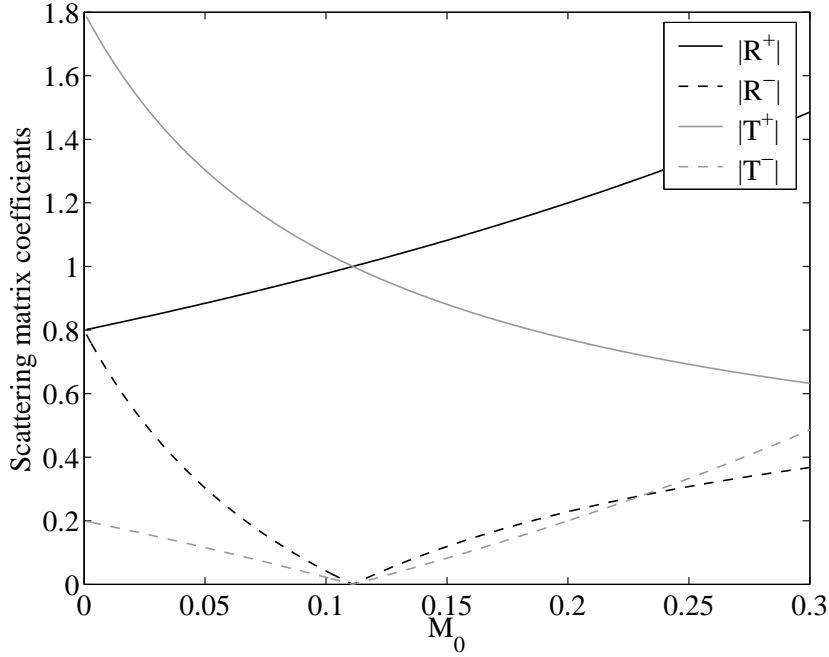


Figure 3.5: Scattering matrix of the constriction with flow: application of the incompressible plane-wave model, for $\eta = 1/9$ ($\eta = S_d/S_p$), $c_0 = 343 \text{ m.s}^{-1}$, $\rho_0 = 1.1 \text{ kg.m}^{-3}$.

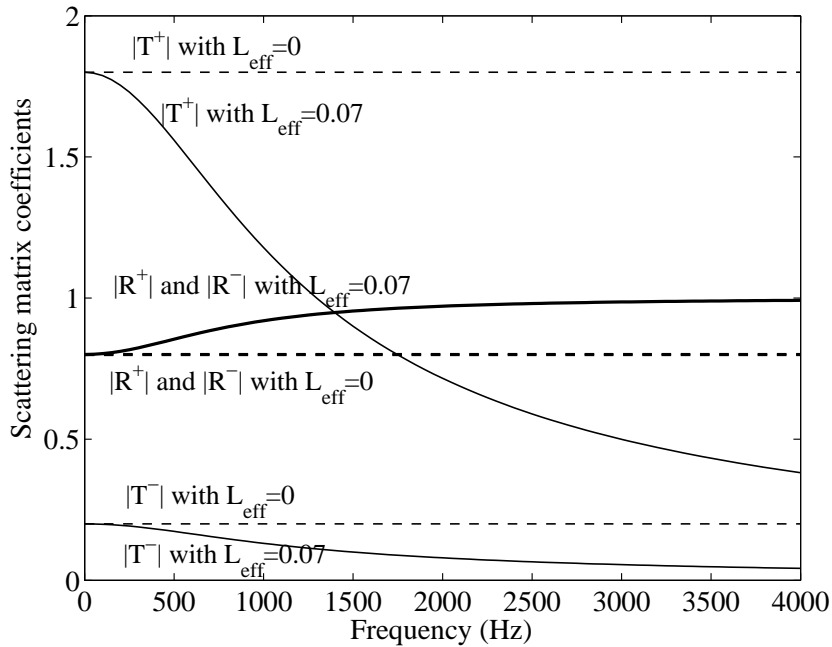


Figure 3.6: Scattering matrix of the constriction without flow: application of the incompressible plane-wave model, for $\eta = 1/9$ ($\eta = S_d/S_p$), $c_0 = 343 \text{ m.s}^{-1}$, $\rho_0 = 1.1 \text{ kg.m}^{-3}$. The coefficients depend strongly on the value of the effective length L_{eff} .

3.4.2 Scattering matrix of the double expansion with the multimodal method

The multimodal method is used to obtain the scattering matrix and the acoustic fields of the double expansion.

The geometry of the double expansion is shown in Fig. 3.7. The number of discretization points is N in duct I, M in duct II and P in duct III (see chapter 2 for more details about the method).

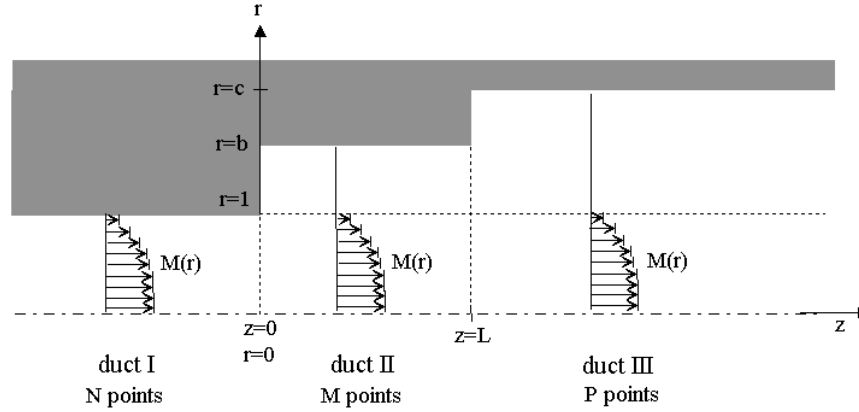


Figure 3.7: Double expansion calculation with the multimodal method: the injected flow in duct I does not expand at its crossing in duct II and duct III. There is no flow in the regions of duct II and III corresponding to $r > 1$. The length of duct II is noted L .

Modes are calculated in duct I, duct II and duct III in the same manner as for the single expansion case presented in chapter 2.

The scattering matrix of the double expansion is then determined: the amplitudes α^{I} of the $3N$ modes in duct I are linked with the amplitudes α^{III} of the $2P + N$ modes in duct III. The scattering matrix \mathbf{S} of the double expansion is then:

$$\begin{pmatrix} \alpha_{\text{d}}^{\text{II}} \\ \alpha_{\text{u}}^{\text{I}} \end{pmatrix} = \mathbf{S} \begin{pmatrix} \alpha_{\text{d}}^{\text{I}} \\ \alpha_{\text{u}}^{\text{II}} \end{pmatrix}. \quad (3.12)$$

It is a squared matrix of size $(2N + M, 2N + M)$.

Two methods can be used to calculate this scattering matrix of the double expansion, and are presented in the following. Both have been implemented, so as to validate calculations.

3.4.3 Scattering matrix of the double expansion: method by assemblage of successive matrices

The scattering matrices of the single expansions between duct I / duct II and duct II / duct III are calculated, in the same manner as for a single expansion. Then, the assemblage of these two successive matrices gives the scattering matrix of the double expansion.

The scattering matrix \mathbf{A} of the single expansion between duct I / duct II gives the following coefficients, corresponding at the location $z = 0$:

$$\mathbf{A} = \begin{pmatrix} R_A^+(0) & T_A^-(0) \\ T_A^+(0) & R_A^-(0) \end{pmatrix}. \quad (3.13)$$

The scattering matrix \mathbf{B} of the single expansion between duct II / duct III gives the following coefficients, corresponding at the location $z = L$:

$$\mathbf{B} = \begin{pmatrix} R_B^+(L) & T_B^-(L) \\ T_B^+(L) & R_B^-(L) \end{pmatrix}. \quad (3.14)$$

Before assembling the two matrices, one should include the propagation in the duct II of length L . In other terms, the coefficients in the two matrices should be expressed at the same location point. The choice of the location point should be done numerically with care, as exponentials terms appear and may lead to divergence problems. In this prospect, a good choice of variables is the following: $R^+(0), T^-(L), T^+(0), R^-(L)$. Thus scattering matrices are arranged in the following manner

$$\mathbf{A}_{\text{arranged}} = \begin{pmatrix} R_A^+(0) & T_A^-(0) \exp(j\mathbf{K}_u^{\text{II}}\omega) \\ T_A^+(0) & R_A^-(0) \exp(j\mathbf{K}_d^{\text{II}}\omega) \end{pmatrix}. \quad (3.15)$$

and:

$$\mathbf{B}_{\text{arranged}} = \begin{pmatrix} R_B^+(L) \exp(-j\mathbf{K}_d^{\text{II}}\omega) & T_B^-(L) \\ T_B^+(L) \exp(-j\mathbf{K}_u^{\text{II}}\omega) & R_B^-(L) \end{pmatrix}, \quad (3.16)$$

where \mathbf{K}_u^{II} are the wave numbers corresponding to upstream propagating mode in duct II, and \mathbf{K}_d^{II} he wave numbers corresponding to downstream propagating modes in duct II. One should note that the length L is critical but is not visible in these expression of exponentials as the pulsation frequency ω is made dimensionless with respect with L .

From now on, the assemblage of the two matrices can be done, because they express the four coefficients at the same points. The formula of assemblage is given for a general expression in the following.

Let \mathbf{A} be the first scattering matrix and \mathbf{B} the second scattering matrix (see illustration in Fig. 3.8), and \mathbf{C} he scattering matrix of the whole:

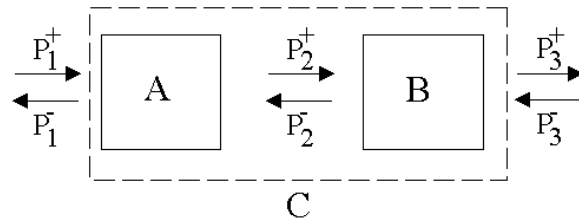


Figure 3.8: Assemblage of two scattering matrices: notations used, in plane-wave propagation.

$$\mathbf{A} = \begin{pmatrix} A_{11} & A_{12} \\ A_{21} & A_{22} \end{pmatrix}, \quad \mathbf{B} = \begin{pmatrix} B_{11} & B_{12} \\ B_{21} & B_{22} \end{pmatrix}, \quad \mathbf{C} = \begin{pmatrix} C_{11} & C_{12} \\ C_{21} & C_{22} \end{pmatrix}, \quad (3.17)$$

written in our formalism ('11' for R^+ , '12' for T^- , '21' for T^+ , '22' for R^-). After calculations, \mathbf{C} is given by the following expressions (Furnell and Bies, 1989; Bi et al., 2006):

$$C_{11} = \frac{A_{11} + B_{11}(A_{21}A_{12} - A_{11}A_{22})}{1 - A_{22}B_{11}}, \quad C_{12} = \frac{A_{12}B_{12}}{1 - A_{22}B_{11}}, \quad (3.18)$$

$$C_{21} = \frac{A_{21}B_{21}}{1 - A_{22}B_{11}}, \quad C_{22} = \frac{B_{22} + A_{22}(A_{21}A_{12} - B_{11}B_{22})}{1 - A_{22}B_{11}}. \quad (3.19)$$

This assemblage is applied, taking \mathbf{A} as matrix $\mathbf{A}_{\text{arranged}}$ and \mathbf{B} as matrix $\mathbf{B}_{\text{arranged}}$. The obtained scattering matrix of the whole \mathbf{C} is noted $\mathbf{C}_{\text{arranged}}$:

$$\mathbf{C}_{\text{arranged}} = \begin{pmatrix} R_C^+(0) & T_C^-(L) \\ T_C^+(0) & R_C^-(L) \end{pmatrix}. \quad (3.20)$$

The scattering matrix of the double configuration $\mathbf{C}_{\text{final}}$, expressed at $x = 0$, is given by:

$$\mathbf{C}_{\text{final}} = \begin{pmatrix} R_C^+(0) & T_C^-(L) \exp(-j\mathbf{K}_u^{\text{II}}\omega) \\ T_C^+(0) \exp(j\mathbf{K}_d^{\text{II}}\omega) & R_C^-(L) \exp(j(\mathbf{K}_d^{\text{II}} - \mathbf{K}_u^{\text{II}})\omega) \end{pmatrix}. \quad (3.21)$$

3.4.4 Scattering matrix of the double expansion: method by direct calculation

Another method is to calculate directly the scattering matrix of the whole configuration (the intermediate single expansion matrices are not calculated), by calculating the modes in the three ducts and applying the relations of passage at the two expansions.

$$\begin{pmatrix} \alpha_d^{\text{III}} \\ \alpha_u^{\text{I}} \end{pmatrix} = \mathbf{S} \begin{pmatrix} \alpha_d^{\text{I}} \\ \alpha_u^{\text{III}} \end{pmatrix} \quad \text{with} \quad \mathbf{S} = \begin{pmatrix} \mathbf{T}^+ & \mathbf{R}^- \\ \mathbf{R}^+ & \mathbf{T}^- \end{pmatrix}. \quad (3.22)$$

Denoting $\mathbf{S}^* = \mathbf{S}_1^{-1} \cdot \mathbf{S}_2$ the whole scattering matrix, we obtain the coefficients of the scattering matrix \mathbf{S} :

$$\mathbf{R}^+ = \mathbf{S}^*_{|(1:N,1:2N)}, \quad (3.23)$$

$$\mathbf{R}^- = \exp(j\mathbf{K}_d^{\text{III}}\omega) \cdot \mathbf{S}^*_{|(N+1:2N+P,2N+1:2N+P)} \cdot \exp(-j\mathbf{K}_u^{\text{III}}\omega), \quad (3.24)$$

$$\mathbf{T}^+ = \exp(j\mathbf{K}_d^{\text{III}}\omega) \cdot \mathbf{S}^*_{|(N+1:2N+P,1:2N)}, \quad (3.25)$$

$$\mathbf{T}^- = \mathbf{S}^*_{|(1:N,2N+1:2N+P)} \cdot \exp(-j\mathbf{K}_u^{\text{III}}\omega). \quad (3.26)$$

and denoting $\mathbf{X}_{\mathbf{N}_1, \mathbf{N}_2}$ a matrix of N_1 lines and N_2 columns, $\mathbf{X}_{|\mathbf{N}_1: \mathbf{N}_2}$ the constriction of the vector \mathbf{X} from the line N_1 to the line N_2 , the intermediate matrices are calculated from:

$$\mathbf{S}_1 \begin{pmatrix} \alpha_u^{\text{I}} \\ \alpha_d^{\text{III,L}} \\ \alpha_d^{\text{II}} \\ \alpha_d^{\text{II,L}} \\ \alpha_u^{\text{II,L}} \end{pmatrix} = \mathbf{S}_2 \begin{pmatrix} \alpha_d^{\text{I}} \\ \alpha_u^{\text{III,L}} \end{pmatrix}. \quad (3.27)$$

It is important to use those intermediate phase references: $\alpha_u^{II,L}$ and $\alpha_d^{III,L}$, so that the exponentials coming from the propagation across the expansion $\exp(j\mathbf{K}_u^{II}L)$ and $\exp(-j\mathbf{K}_d^{II}L)$ are attenuated (except for the unstable hydrodynamic mode in $\exp(-j\mathbf{K}_d^{II}L)$):

$$\mathbf{S}_1 = \begin{pmatrix} \psi_u^I & 0_{3N,N+P} & -\psi_{d,\text{rest1}}^{II} & -\psi_{u,\text{rest1}}^{II} \cdot \exp(j\mathbf{K}_u^{II}L) \\ 0_{M-N,N} & 0_{M-N,N+P} & \psi_{d,\text{rest2}}^{II} & \psi_{u,\text{rest2}}^{II} \cdot \exp(j\mathbf{K}_u^{II}L) \\ 0_{3N,N} & -\psi_{d,\text{rest1}}^{III} & \psi_{d,\text{rest1}}^{II} \cdot \exp(-j\mathbf{K}_d^{II}L) & \psi_{u,\text{rest1}}^{II} \\ 0_{P-M,N} & \psi_{d,\text{rest2}}^{III} & 0_{P-M,M+N} & 0_{P-M,M} \\ 0_{2M-2N,N} & \psi_{d,\text{rest3}}^{III} & -\psi_{d,\text{rest3}}^{II} \cdot \exp(-j\mathbf{K}_d^{II}L) & -\psi_{u,\text{rest3}}^{II} \end{pmatrix} \quad (3.28)$$

$$\mathbf{S}_2 = \begin{pmatrix} -\psi_d^I & 0_{3N,P} \\ 0_{M-N,2N} & 0_{M-N,N+P} \\ 0_{3N,2N} & \psi_{u,\text{rest1}}^{III} \\ 0_{P-M,2N} & -\psi_{u,\text{rest2}}^{III} \\ 0_{2M-2N,2N} & -\psi_{u,\text{rest3}}^{III} \end{pmatrix}, \quad (3.29)$$

with:

$$\psi_{d,\text{rest1}}^{II} = \begin{pmatrix} \psi_d^{II} |_{M-N+1:M} \\ \psi_d^{II} |_{2M-N+1:2M+N} \end{pmatrix}, \quad \psi_{u,\text{rest1}}^{II} = \begin{pmatrix} \psi_u^{II} |_{M-N+1:M} \\ \psi_u^{II} |_{2M-N+1:2M+N} \end{pmatrix}, \quad (3.30)$$

$$\psi_{d,\text{rest2}}^{II} = \psi_d^{II} |_{P+1:2P-M}, \quad \psi_{u,\text{rest2}}^{II} = \psi_u^{II} |_{P+1:2P-M}, \quad (3.31)$$

$$\psi_{d,\text{rest3}}^{III} = \psi_d^{III} |_{1:M-N} \psi_d^{III} |_{M+1:2M-N}, \quad \psi_{u,\text{rest3}}^{III} = \psi_u^{III} |_{1:M-N} \psi_u^{III} |_{M+1:2M-N}. \quad (3.32)$$

3.5 Validation of the calculations

3.5.1 Comparison with experimental data - without flow

We compare the numerical estimation of the scattering matrix of the whole configuration to our experimental data without flow. This is a first validation step, in order to apply next the method with a flow.

The scattering matrix coefficient are given in Figs. 3.9 and 3.10. It appears that the effective length is a very important parameter for the model without flow and has to be taken into account. Hence, there are strong effects of transverse acoustic modes in this case, and a model without acoustic length correction is quite bad.

Calculations fit well experimental data using the effective length of $L_{eff} = 0.07$ as a fit variable. The qualitative and quantitative evolution of the scattering matrix coefficients are very well represented when taking this value.

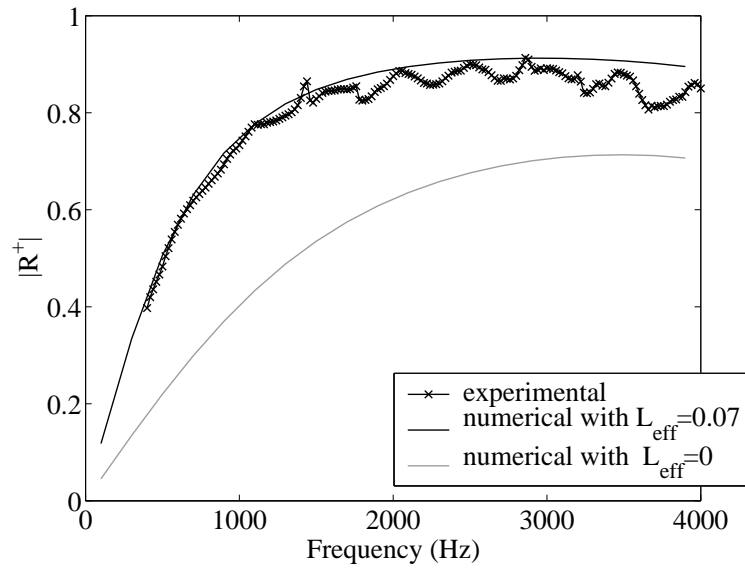


Figure 3.9: Reflection coefficient $|R^+|$ for the configuration studied (constriction and double expansion) in the case of no flow: the calculations are closed to the experimental data, when using a well fitted effective length L_{eff} . The numerical calculations are made with $a^*=5$ mm, $b = 2$, $c = 3$, $L = 3.6$, $N=20$, $M_d = 0$; the reported experimental data concern the configuration CCb6+CC18+CC9 without flow.

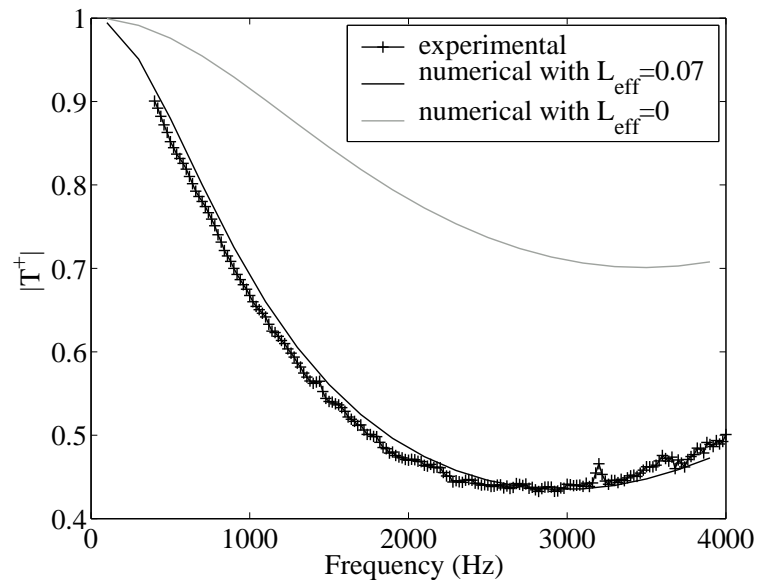


Figure 3.10: Transmission coefficient $|T^+|$ for the configuration studied (constriction and double expansion) in the case of no flow: the calculations are closed to the experimental data, when using a well fitted effective length L_{eff} . The numerical calculations are made with $a^*=5$ mm, $b = 2$, $c = 3$, $L = 3.6$, $N=20$, $M_d = 0$; the reported experimental data concern the configuration CCb6+CC18+CC9 without flow.

3.5.2 Comparison with experimental data - with flow

We compare the numerical estimation of the scattering matrix to our experimental data with flow.

The scattering matrix coefficients are given in Fig. 3.11 for $|R^+|$, Fig.3.12 for $|R^-|$, Fig.3.13 for $|T^+|$ and Fig.3.14 for $|T^-|$ and are discussed in the following.

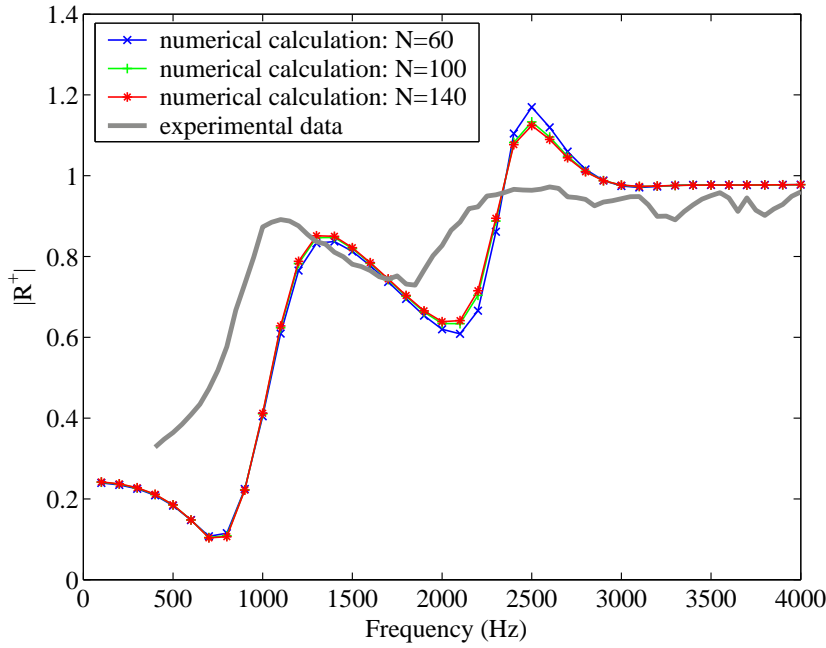


Figure 3.11: Reflection coefficient $|R^+|$ for the configuration studied (constriction and double expansion) in the case of flow: a good convergence is obtained for $N \geq 100$. The numerical calculations are made with $a^*=5$ mm, $b = 1.5$, $c = 3$, $L = 2$, $M_d = 8.67 \cdot 10^{-2}$; the reported experimental data concern the configuration CCB6+CC19 with $M_0 = 9.6 \cdot 10^{-3}$.

Firstly, convergence is reached for $N \geq 100$ with a relative discrepancy of 10^{-2} . We use then in the following sections $N = 100$ as a satisfactory number of points for the calculations.

The qualitative evolution of the scattering matrix coefficients is satisfactory, exhibiting several peaks (modes), as in experiments. The position of the Strouhal modes is close to the experimental values (see the following section for more details).

The levels obtained at the limits of the scattering matrix coefficients are well obtained: the low frequency limit of the four scattering matrix coefficients is very well obtained; the high frequency limit of the four scattering matrix coefficients is very well obtained, except for T^+ for which the calculated limit is bad: it goes to zero, whereas the experimental limit is around 0.3.

But the quantitative level of the scattering matrix coefficients is entirely satisfactory. The level of the coefficients is globally under-estimated for the reflection coefficients, and over-estimated for the transmission coefficients. More study of this phenomenon is made in section 3.5.3.

One should note however that those results seem quite sufficient to obtain correct whistling frequencies, as will be presented in the following, and which represents our objective. The problem of determination of the magnitudes of the scattering matrix coefficients is not critical to our needs,

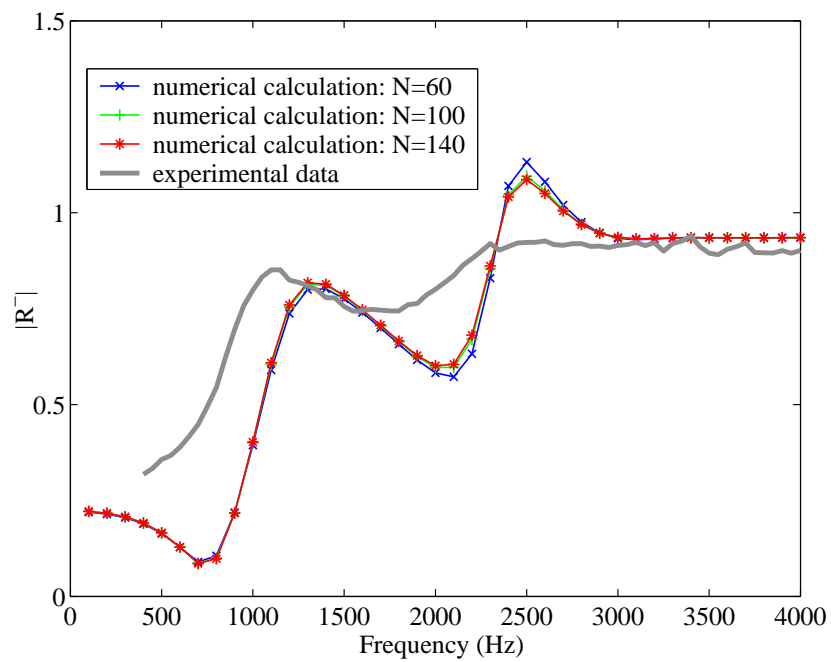


Figure 3.12: Reflection coefficient $|R^-|$ for the configuration studied (constriction and double expansion) in the case of flow: a good convergence is obtained for $N \geq 100$. The numerical calculations are made with $a^*=5$ mm, $b = 1.5$, $c = 3$, $L = 2$, $M_d = 8.67 \cdot 10^{-2}$; the reported experimental data concern the configuration CCb6+CC19 with $M_0 = 9.6 \cdot 10^{-3}$.

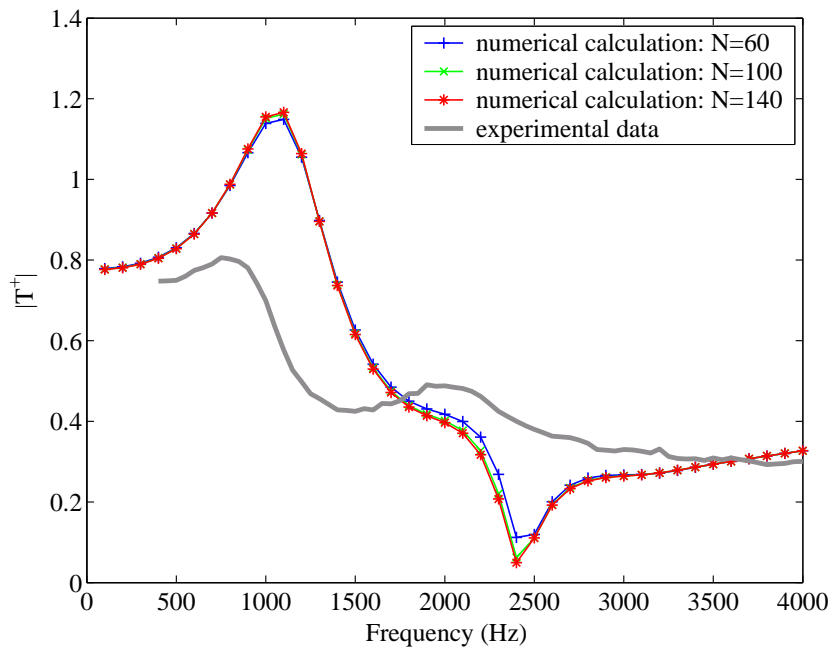


Figure 3.13: Transmission coefficient $|T^+|$ for the configuration studied (constriction and double expansion) in the case of flow: a good convergence is obtained for $N \geq 100$. The numerical calculations are made with $a^*=5$ mm, $b = 1.5$, $c = 3$, $L = 2$, $M_d = 8.67 \cdot 10^{-2}$; the reported experimental data concern the configuration CCB6+CC19 with $M_0 = 9.6 \cdot 10^{-3}$.

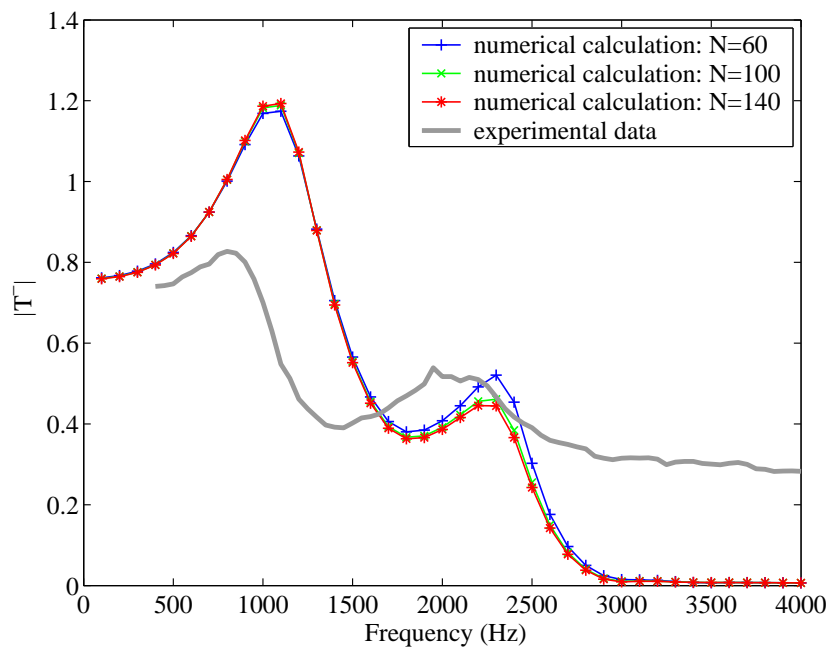


Figure 3.14: Transmission coefficient $|T^-|$ for the configuration studied (constriction and double expansion) in the case of flow: a good convergence is obtained for $N \geq 100$, but the limit for the high frequency is not well obtained. The numerical calculations are made with $a^*=5$ mm, $b = 1.5$, $c = 3$, $L = 2$, $M_d = 8.67 \cdot 10^{-2}$; the reported experimental data concern the configuration CCb6+CC19 with $M_0 = 9.6 \cdot 10^{-3}$.

and the discrepancy we obtained is acceptable, considering the simplicity of the approach used: simple model for the behaviour of the constriction, and simple assumptions for the multimodal method. The main objective is then presented in section 3.6, while a closer look at the meaning of this discrepancy is given in the following section.

3.5.3 Effect of the saturation of the unstable hydrodynamic mode

A problem in the calculations is that the peak values of the potentially whistling eigenvalues are not well correlated with experimental data. We assume this is due to the influence of the unstable hydrodynamic mode in our calculations.

In the calculation of the scattering matrix of the double expansion, exponentials terms are present (see Eq. 3.28). The term in the exponential $\exp(-j\mathbf{K}_d^{\text{II}}\omega)$ for the unstable hydrodynamic mode is exponentially amplified, whereas the other terms of this exponential are in magnitude below the unity. In the illustration case of previous section (Fig. 3.17), the value of the exponential for this unstable mode is 5.6.

In order to test the influence of this term, we have saturated it in the calculation (this is not aimed to represent any physical phenomenon). The exponential term in $\exp(-j\mathbf{K}_d^{\text{II}}\omega)$ for this unstable hydrodynamic is put to an arbitrary saturation value. A weak saturation is a saturation level of 5 (in magnitude), as it is close to the value 5.6 of the exponential. A strong saturation is a saturation level of 2, which is close to the value of the other terms of the exponentials (near and below the unity).

Results are illustrated in Fig. 3.15 and 3.16. The hypothesis is validated: it appears that the magnitude of the scattering matrix coefficients, and also the potentially whistling eigenvalues, depend strongly on the saturation used, at least for potentially whistling frequencies. Hence the amplification due to the unstable hydrodynamic mode is critical to determine the amplitudes of the scattering matrix coefficients and the potentially whistling eigenvalues. In this case, a saturation at 2 would give the best comparison with experimental results.

The improvement of the determination of this amplification is problematic. In our calculations, this amplification is obtained by the multiplication of the imaginary part of the wave number of the unstable hydrodynamic mode with the length L of the double expansion. The value of the imaginary part of the wave number depends on the flow profile imposed, and the exponential amplification is hence critically dependent on this value. For instance, using a flow parameter $m = 3$, $m = 7$ and $m = 15$ respectively, the imaginary part of the unstable wave number equals 1.9, 4.4 and 5.3 respectively (made in duct II with $M_0 = 0.1$, $b = 2$, $\omega = 0.1$, $N = 50$). Hence it is problematic to find a more precise prediction of this amplification in our model, unless knowing very precisely the experimental flow profile. This result is rather coherent physically. It is not a surprise that the shape of the boundary layer of the flow profile is important to determine the aeroacoustical response of the system, as this is in this region that the main phenomenon, the presence of an unstable hydrodynamic mode, occurs.

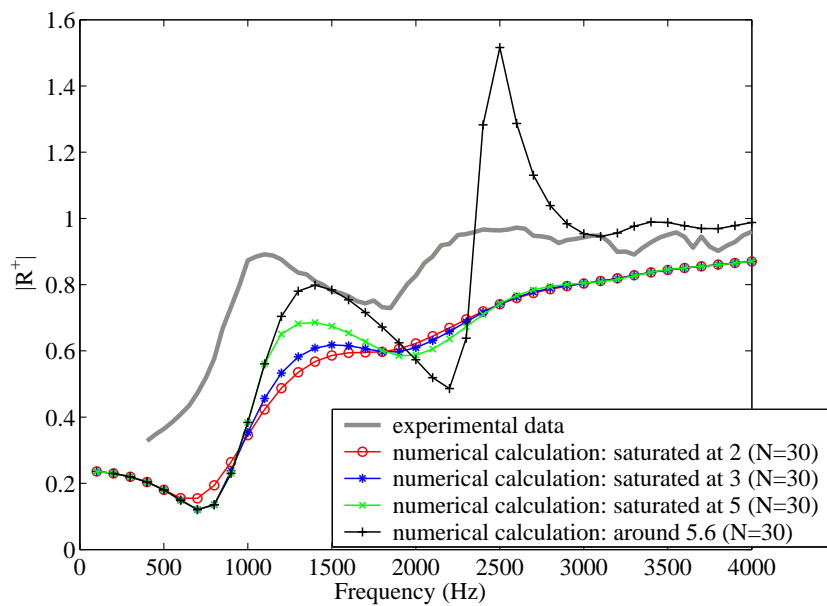


Figure 3.15: Variations of $|R^+|$ when saturating numerically to a truncated value the unstable amplified hydrodynamic mode in the scattering matrix calculation of the double expansion. The numerical calculations are made with $a^*=5$ mm, $b = 1.5$, $c = 3$, $L = 2$, $N=20$, $M_d = 8.67 \cdot 10^{-2}$; the reported experimental data concern the configuration CCb6+CC19 with $M_0 = 9.6 \cdot 10^{-3}$.

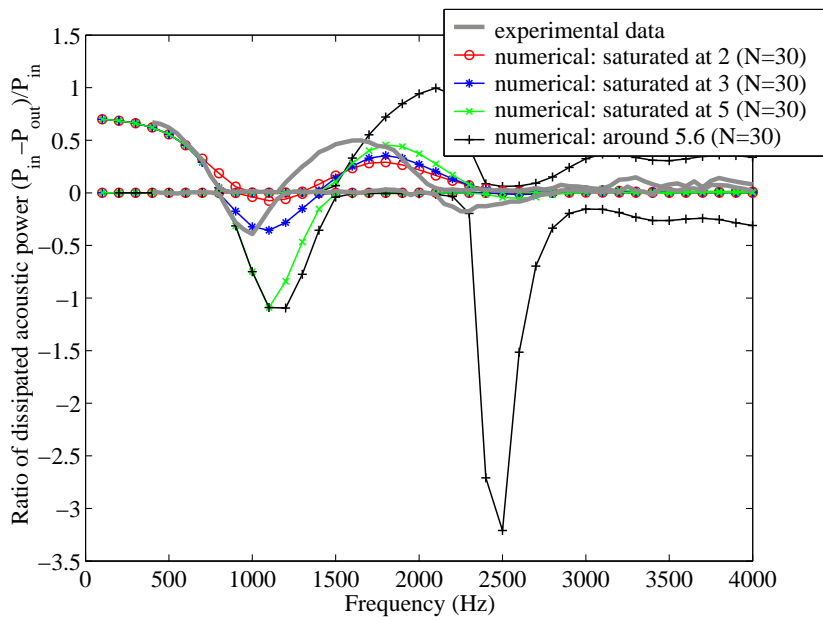


Figure 3.16: Variations of the potentially whistling eigenvalues when saturating numerically to a truncated value the unstable amplified hydrodynamic mode in the scattering matrix calculation of the double expansion. The numerical calculations are made with $a^*=5$ mm, $b = 1.5$, $c = 3$, $L = 2$, $N=30$, $M_d = 8.67 \cdot 10^{-2}$; the reported experimental data concern the configuration Ccb6+CC19 with $M_0 = 9.6 \cdot 10^{-3}$.

3.6 Whistling ability of the configuration

In this section, we apply the whistling criterion presented in chapter 1 to the numerical results with flow presented in the previous section and compare them to experimental data.

3.6.1 Whistling ability of the configuration

The potentially whistling eigenvalues deduced from the scattering matrix coefficients previously presented are illustrated in Fig. 3.17. The same conclusions come, than those obtained on the scattering matrix coefficients: a good qualitative evolution is found, the limit behaviour at very low and very high frequency is correct, There is however a slight shift in frequency: the experimental Strouhal number, corresponding to the first peak, is $f_{peak1}L/U_d = 0.34$ (with $f_{peak1} = 1000Hz$), while the numerical Strouhal number is $f_{peak1}L/U_d = 0.37$ (with $f_{peak1} = 1100Hz$). As the model used for the constriction is a simple one, this shift does not seem critical;

The potentially whistling eigenvalues deduced from those coefficients are illustrated in Fig. 3.17.

- it appears that the qualitative evolution of the eigenvalues is satisfactory, exhibiting two peaks (modes), and potentially whistling frequencies, as in experiments. The corresponding Strouhal number is close to experiments: this calculation provides satisfactory Strouhal number for potentially whistling frequencies.

We note however a slight shift in frequency: for example for the first peak, in experiments $f_{peak1}L/U_d = 0.34$ ($f_{peak1} = 1000Hz$), while in calculations $f_{peak1}L/U_d = 0.37$ ($f_{peak1} = 1100Hz$), which corresponds to a 8% relative discrepancy. As the model used for the constriction is a simple one, this shift does not seem critical (no study has been made to reduce it);

- the amplitudes of the peaks are wrong. For example, the peak of the first mode is over-estimated with a ratio of three. . . This issue is under study in the following section.

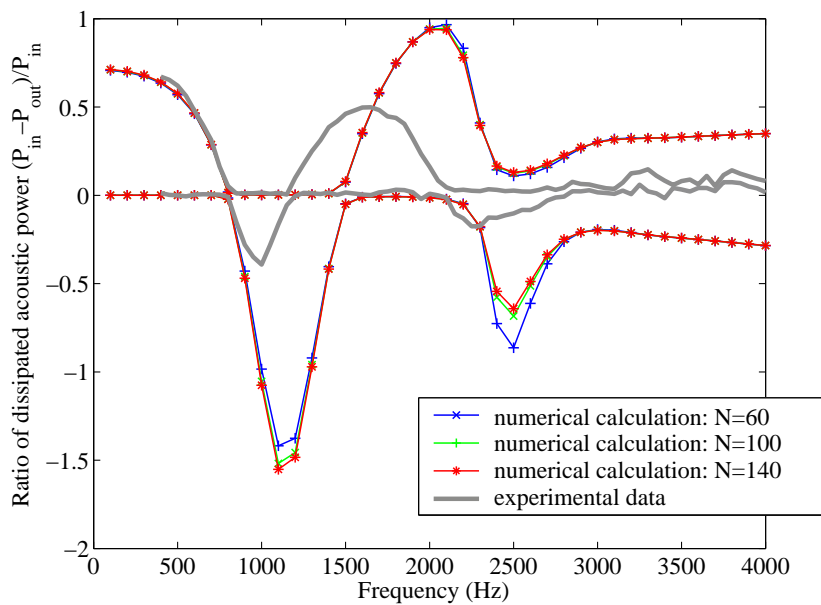


Figure 3.17: Whistling criterion applied numerically for the configuration studied (constriction and double expansion) in the case of flow: a good convergence is obtained for $N \geq 100$, and the potentially whistling frequencies are obtained satisfactorily, for the two whistling modes, but not the amplitude of the eigenvalues. The numerical calculations are made with $a^*=5$ mm, $b = 1.5$, $c = 3$, $L = 2$, $M_d = 8.67 \cdot 10^{-2}$; the reported experimental data concern the configuration CCb6+CC19 with $M_0 = 9.6 \cdot 10^{-3}$.

3.6.2 Comparison with the whistling ability of a single expansion configuration

It is particularly interesting to compare the whistling ability of the configuration with a similar configuration without the second expansion zone of length L (see Fig.3.18). In fact, this corresponds to an orifice with a bevel upstream, configuration that has already been studied in chapter 1 as a typical non-whistling one. We compare these experimental data with numerical calculations, using the scattering matrix of the constriction as presented in this chapter and the scattering matrix of a single expansion. Results are given in Fig.3.19. The calculations give a good estimation for the magnitude, with a discrepancy which is not critical: the main result is that numerical calculations predict the correct behaviour of the configuration, that is a non-whistling ability.

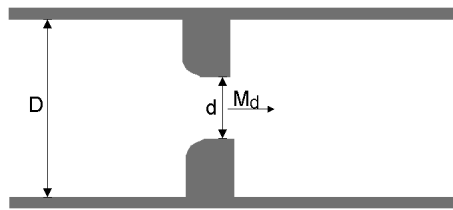


Figure 3.18: Configuration studied without a double expansion.

This non-whistling ability shows clearly, with experimental and numerical results, that the presence of the second expansion is a necessary condition to allow whistling. In fact, there is a length of synchronisation on this second expansion, corresponding to an acoustic and/or hydrodynamic feedback (immediate as the main flow is incompressible) toward the separation point of the jet.

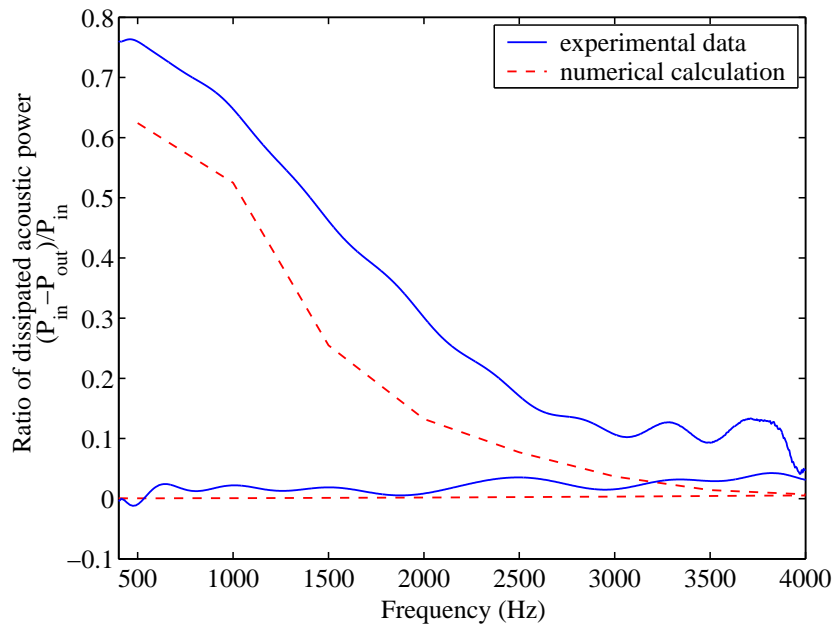


Figure 3.19: Whistling ability of the configuration without a double expansion, from experimental and numerical calculations. The calculations give a satisfactory result that this configuration is not a potentially whistling one. (The numerical calculations are made with $a^*=5$ mm, $b=3$, $M_d = 8.67 \cdot 10^{-2}$; the reported experimental data concern the configuration CCb2 with a bevel $r_{bevel}/t = 0.2$ downstream with flow $M_d = 8.67 \cdot 10^{-2}$).

3.6.3 Parametric study on the Strouhal number

A parametric study is done on the whistling configuration, in order to estimate the variations of the Strouhal number of the potentially whistling frequency peak with the variations of the geometrical parameters of the configuration. The aim is to get better understanding of the aeroacoustical behaviour of the configuration in function of the parameters of the problem, and particularly the second expansion.

3.6.3.1 The flow parameters influence weakly the Strouhal number

Weak variations of the Strouhal number are found on the Strouhal number, when varying the flow parameters:

- the flow profile parameter m , as shown in Fig. 3.20. This is coherent with the single expansion results, where we showed that calculations are weakly sensitive on the flow profile we impose. Also, it seems a coherent result: as far as the flow profile is typical of a turbulent flow (that is, the flow is not laminar), small variations of its shape are not expected to influence greatly the instability frequency;
- the radius of the jet a , as illustrated in Fig. 3.21. In this illustration, L has values superior to unity. The same result is obtained for values of L inferior to unity. The weak variation obtained seems coherent with the fact the the diameter of the jet is not representative of any characteristic length for the instability;
- the Mach number M_d , as illustrated in Fig. 3.22. This result is coherent with experimental data presented in chapter 1 (see Fig1.23), where we found a decrease of the Strouhal number as function of the flow velocity. Of course, the weak variation obtained is coherent with the definition of the Strouhal number as a number made dimensionless using the Mach number of the flow.

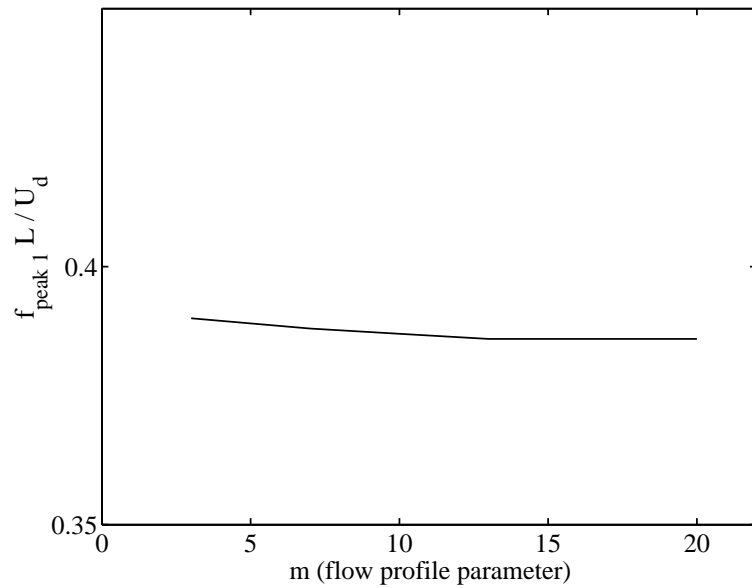


Figure 3.20: Very weak variations with the flow profile parameter m of the numerical Strouhal number $f_{peak}L/U_a$, corresponding to the most potentially whistling frequency of the first mode of the configuration studied (constriction with double expansion). The calculations made with $M_d = 8.67 \cdot 10^{-2}$, $L/a = 2$, $b/a = 1.5$, $c/a = 3$ (length variables on the figure are in meters).

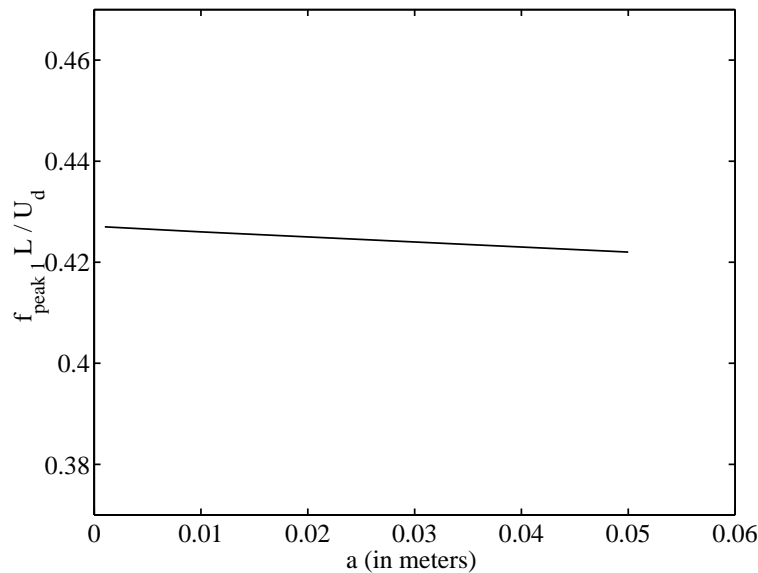


Figure 3.21: Weak variations with the jet radius a on the numerical Strouhal number $f_{peak}L/U_a$, corresponding to the most potentially whistling frequency of the first mode of the configuration studied (constriction with double expansion). The calculations are made with $M_d = 0.1$, $m = 10$, $L/a = 2$, $b/a = 1.5$, $c/a = 3$ (length variables on the figure are in meters).

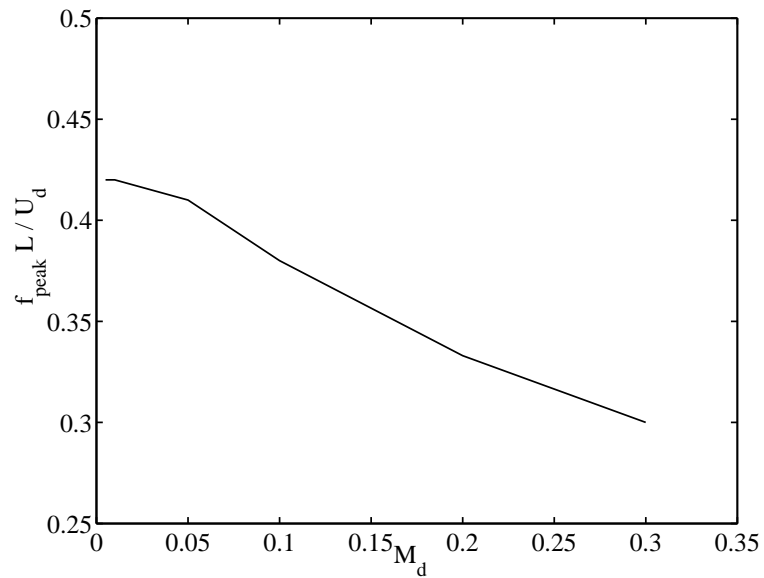


Figure 3.22: Moderate variations with the Mach number at the constriction M_d on the numerical Strouhal number $f_{peak}L/U_a$, corresponding to the most potentially whistling frequency of the first mode of the configuration studied (constriction with double expansion). The calculations are made with $m = 10$, $L/a = 2$, $b/a = 1.5$, $c/a = 3$, $a = 5 \cdot 10^{-3}m$ (length variables on the figure are in meters).

3.6.3.2 The geometry of the second expansion influences strongly the Strouhal number

Strong variations of the Strouhal number are found when varying the characteristics of the zone constituted by the second expansion. Typically, values for the Strouhal number are obtained between 0.2 and 0.5, when varying:

- the height b of the first expansion, as illustrated in Fig. 3.23. This result points out the significant influence of the distance of the hydrodynamic mode to the walls in the amplification zone. This is a well-known result in literature. However, this is difficult to take into account in a very simple model, that is, the Strouhal number dimensionless frequency proves not to be constant, when varying the height of the amplification zone;
- the length L of the double expansion, as illustrated in Fig. 3.24. This parameter is particularly sensitive. A doubling of it can correspond to a doubling of the Strouhal number. Comparable result in tendency has been obtained with the experiments on the right-angle edged orifices: in Fig. 3.26, we have obtained a strong experimental variation of the Strouhal number when varying the thickness of the orifice, the diameter and the Reynolds number being constant (approximately).

Another spectacular illustration of the strong dependency with the length of the second expansion is given in Fig. 3.25.

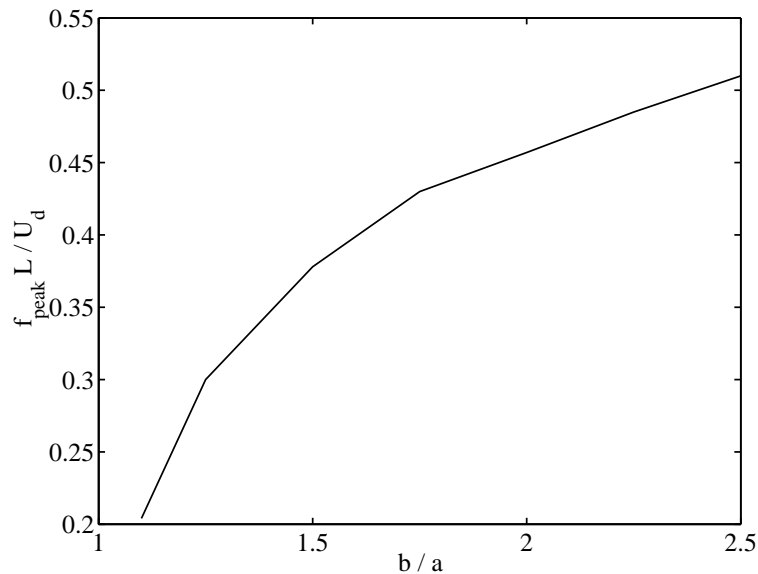


Figure 3.23: Strong variations with the intermediate expansion radius b on the numerical Strouhal number $f_{peak}L/U_a$, corresponding to the most potentially whistling frequency of the first mode of the configuration studied (constriction with double expansion). The calculations are made with $M_0 = 0.1$, $m = 10$, $L/a = 2$, $c/a = 3$, $a = 5 \cdot 10^{-3}m$ (length variables on the figure are in meters).

Hence the instability frequency varies much with the geometry of the second expansion. This result is in agreement with the previous observation that this configuration is whistling, as there exists this

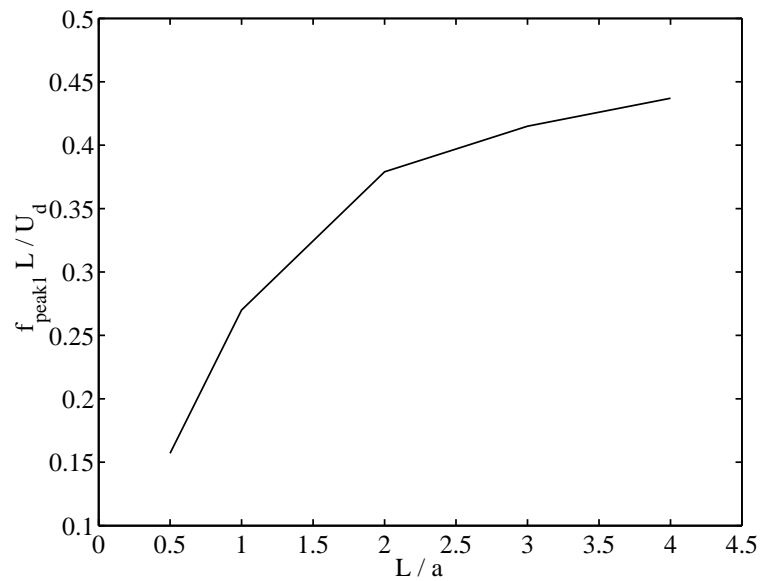


Figure 3.24: Strong variations with the length L of the double expansion on the numerical Strouhal number $f_{peak}L/U_a$, corresponding to the most potentially whistling frequency of the first mode of the configuration studied (constriction with double expansion). The calculations are made with $m = 10$, $L/a = 2$, $b/a = 1.5$, $c/a = 3$, $a = 5 \cdot 10^{-3}m$ (length variables on the figure are in meters).

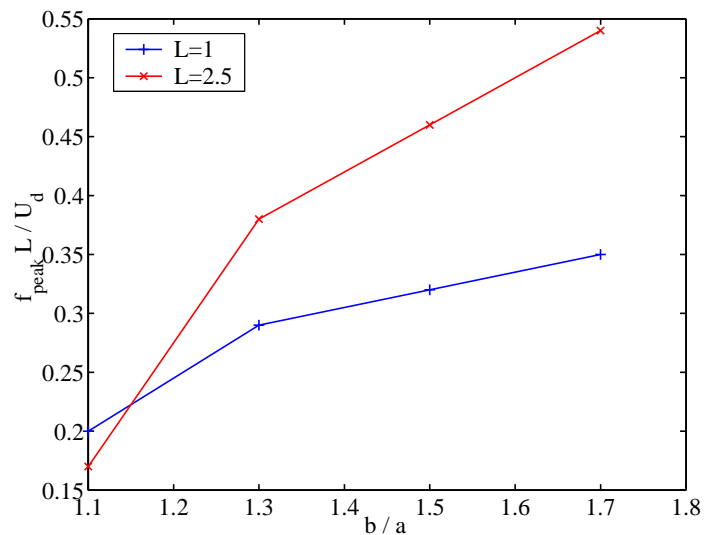


Figure 3.25: Example of strong variations when varying the length L of the double expansion on the numerical Strouhal number $f_{peak}L/U_a$. The calculations are made with $m = 10$, $c/a = 3$, $a = 5 \cdot 10^{-3}m$ (length variables on the figure are in meters).

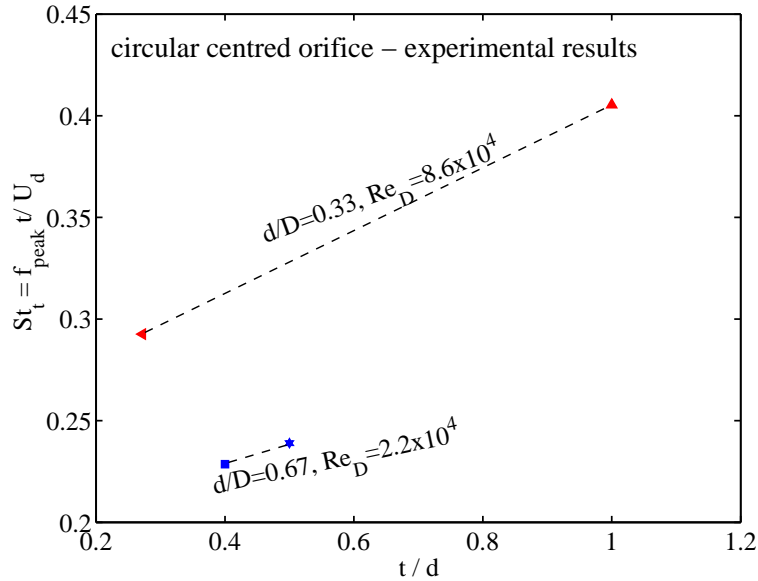


Figure 3.26: Experimental variations of the Strouhal number with the variation of the thickness of right-angled orifice, the diameter and the Reynolds number being approximately constant. Data correspond to the one reported in chapter 1 for circular centred orifices without bevels.

second expansion. Also, this result has already been pointed out in Aurégan and Testud (2006), using a similar multimodal method, but a simplified one with six modes, and applied on the same configuration. Moreover, one should note that, in chapter 1, we showed that the Strouhal number obtained for circular centred orifices depends on the thickness of the orifice. This thickness is a kind of second expansion zone, and is comparable to the model investigated in this chapter. This confirms our results on this simple configuration.

As a result, the Strouhal number can not be considered as a constant for such a configuration, and consequently no simple model can be found to describe the phenomenon of whistling on this configuration.

3.7 Conclusion

A potentially whistling configuration has been studied in this chapter, constituted by a constriction followed by a double expansion. The multimodal method has been used to calculate the scattering matrix of the double expansion, and simple incompressible acoustic models have been used to obtain the scattering matrix of a constriction. The potential whistling ability of this configuration has been investigated, using the whistling criterion presented in chapter 1.

The objective of the work has been reached: the potentially whistling frequencies are numerically predicted, in good agreement with experimental data, both without flow (section 3.5.1) and with a mean shear flow (section 3.5.2). In this latter case, the discrepancy is of the order of about 8%, and should be improvable, by using more elaborated models for the constriction, and by refining the measurements. It has not been looked for particularly.

The comparison with a single expansion configuration then gives the strong result that the presence of the second expansion is essential to create whistling potentiality. Parametric studies on the potentially whistling frequency confirm that this zone is critical to determine the Strouhal number. We show also that the parameters of the flow do not influence strongly the Strouhal number, which seems in agreement with the physics of the phenomena. Those results are in agreement with the experimental results obtained in chapter 1 for right orifices, where the instability frequency depends on the thickness of the orifice, which corresponds to a kind of second expansion.

Bibliography

- Y. Aurégan, P. Testud, Comportement aéroacoustique d'une expansion sifflante, Congrès Français d'Acoustique, Tours, 2006.
- Y. Aurégan, Comportement aéro-acoustique basse-fréquence d'une expansion, 14e Congrès Français de Mécanique, Toulouse, 1999.
- W. P. Bi, V. Pagneux, D. Lafarge, Y. Aurégan, Modelling of sound propagation in a non-uniform lined duct using a Multi-Modal Propagation Method, *Journal of Sound and Vibration*, 286: 1091-1111, 2006.
- G.D. Furnell, D.A. Bies, Matrix analysis of acoustic wave propagation within curved ducting system, *Journal of Sound and Vibration*, 132: 245-263, 1989.

Chapter 4

Noise generated by cavitating single-hole and multi-hole orifices in a water pipe

P. Testud, P. Moussou, A. Hirschberg, Y. Aurégan
published in *Journal of Fluid and Structures* (2006)

4.1 Introduction

4.1.1 Motivations

In industrial processes, cavitating flows are known to sometimes generate significant levels of noise and high vibrations of structures. Some papers have been published in the last years on this topic: Au-Yang (2001); Weaver et al. (2000); Moussou et al. (2004).

In particular, fatigue issues have been reported recently for the configurations of a cavitating valve (Moussou et al., 2001) and a cavitating orifice (Moussou et al., 2003). The examination of the noise generated by a cavitating device, in this study a cavitating orifice, is typically an industrial issue. It provides information which is a basis for a safer design in terms of pipe vibrations.

4.1.2 Literature

In single-phase flow, an orifice generates a free jet surrounded by a dead water pressure region of uniform pressure, cf. Fig. 4.1. The static pressure reaches its minimum value P_j in the jet region, also called the *vena contracta*, and large eddies are generated in the shear layer separating the jet from the dead water region.

Two-phase flow transition occurs when the lowest static pressure in the fluid falls below the vapor pressure (Brennen, 1995). The level of cavitation is usually correlated with the help of a so-called cavitation number. Different definitions exist of the cavitation number for cavitation in a flowing stream (also called hydrodynamic cavitation). They correspond to different cavitation configurations, and are usually chosen for convenience, so that they can easily be determined in practice:

- for wake cavitation, that is cavitation round a body (i. e. an hydrofoil) or generated by a slit, the cavitation number is commonly defined as function of the upstream conditions (Young, 1999;

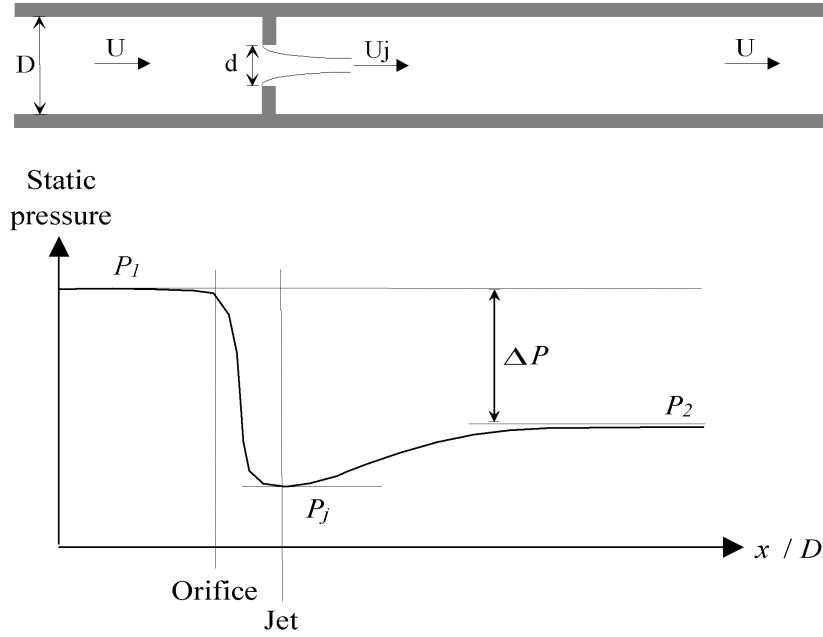


Figure 4.1: Flow through an orifice and corresponding evolution of the static pressure.

(Brennen, 1995; Franc et al., 1995; Lecoffre, 1994):

$$\sigma = \frac{P_0 - P_v}{\frac{1}{2}\rho_L U_0^2}, \quad (4.1)$$

where U_0 is the infinite upstream flow velocity, P_0 the ambient static pressure, P_v the vapor pressure of the liquid and ρ_L the density of the liquid.

- for mixing cavitation, that is cavitation formed in a jet (i. e. in pumps, valves, orifices), a similar cavitation number, as in the wake cavitation, can be used (Young, 1999; Brennen, 1995):

$$\sigma = \frac{P_{\text{ref}} - P_v}{\frac{1}{2}\rho_L U_0^2}, \quad (4.2)$$

where P_{ref} is very often defined as the downstream static pressure.

We prefer to use the cavitation number, based on the pressure drop across the singularity generating the jet:

$$\sigma = \frac{P_2 - P_v}{\Delta P}, \quad (4.3)$$

where $\Delta P = P_1 - P_2$ is the pressure drop across the orifice, with P_1 the static pressure upstream of the orifice and P_2 the downstream static pressure far away from the orifice. In this choice, we follow common practice in industry (Tullis, 1989; Franc et al., 1995; Lecoffre, 1994).

One should note that both those cavitation numbers lead to very similar classifications as they are related to each other by the pressure drop coefficient of the singularity.

When the pressure P_j has a sufficiently low value, intermittent tiny cavitation bubbles are produced in the heart of the turbulent eddies along the shear layer of the jet. This flow regime transition is called cavitation inception, and it appears at a cavitation number of the order of 1 (when $d/D = 0.30$) according to the data of Tullis (1989). Other references (Numachi et al., 1960; Tullis et al., 1973; Ball et al., 1989; Yan and Thorpe, 1990; Kugou et al., 1996; Sato and Saito, 2001; Pan et al., 2001) are in good agreement with the values and scale effects given by Tullis (1989). Some differences result from the influence of the variation in the dissolved gas content and in the viscosity (Keller, 1994).

As the jet pressure decreases further, more bubbles with larger radii are generated, forming a white cloud. The pressure fluctuations increase and a characteristic shot noise can be heard. A further decrease in jet pressure induces the formation of a large vapor pocket just downstream of the orifice, surrounding the liquid jet. The regime occurring after this transition is called super cavitation and it exhibits the largest noise and vibration levels. In the super cavitation regime, noise is known, see, for example, VanWijngaarden (1972), to be mainly generated in a shock transition between the cavitation region and the pipe flow, at some distance downstream of the orifice. Downstream of the shock, some residual gas (air) bubbles can persist but pure vapor bubbles have disappeared.

Cavitation indicators are used to predict the occurrence of cavitation regimes. The use of two of them has seemed relevant, in view of our experimental results. First, a so-called incipient cavitation indicator, noted σ_i , which predicts the transition from a noncavitating flow to a moderately cavitating flow, that is called developed cavitation regime. Second, a so-called choked cavitation indicator, noted σ_{ch} , which predicts the transition from a moderately cavitating flow to a super cavitating flow, with the formation and continuous presence of a vapor pocket downstream of the orifice around the liquid jet. To calculate both those incipient and the choked cavitation indicators, scaling laws are given by Tullis (1989). They take into account the various pressure effects and size scale effects, by means of extensive experiments on single-hole orifices in water pipe-flow. For multi-hole orifices, as mentioned in the same work, less data are available but identical values are expected to hold.

Only a few studies provide downstream noise spectra generated by cavitating orifices (Yan et al., 1988; Bistafa et al., 1989; Kim et al., 1997; Pan et al., 2001). A few complementary studies give the noise spectra created by cavitating valves (Hassis, 1999; Martin et al., 1981). In fact, it appears that far more research has been developed on submerged water jets (Jorgensen, 1961; Esipov and Naugol'nykh, 1975; Franklin and McMillan, 1984; Brennen, 1995; Latorre, 1997). A comprehensive overview of the state of the art in this domain is given in Brennen (1995).

Nomenclature			
c	speed of sound measured downstream of the orifice (in m.s^{-1})	S_j	cross section of the jet (in m^2)
c_w	speed of sound in pure water (in m.s^{-1})	St	Strouhal number for the whistling frequency
c_{\min}	minimum speed of sound (in m.s^{-1})	t	orifice thickness ($t = 14 \times 10^{-3}$ m)
d	diameter of the single-hole orifice ($d = 2.2 \times 10^{-2}$ m)	t_p	pipe wall thickness ($t_p = 8 \times 10^{-3}$ m)
d_{eq}	single-hole equivalent diameter of the multi-hole orifice ($d_{\text{eq}} = 2.1 \times 10^{-2}$ m)	U	volume flux divided by pipe cross-sectional area (in m.s^{-1})
d_{multi}	diameter of the holes of the multi-hole orifice ($d_{\text{multi}} = 3 \times 10^{-3}$ m)	U_d	volume flux divided by orifice cross-sectional area (in m.s^{-1})
f_0	whistling frequency (in Hz)	U_j	volume flux divided by orifice jet cross-sectional area (in m.s^{-1})
D	pipe diameter ($D = 7.4 \times 10^{-2}$ m)	β	volume fraction of gas in the water
G_{pp}	Power Spectrum Density of the pressure (in Pa^2/Hz)	ΔP	static pressure difference across the orifice (in Pa)
N_{holes}	number of holes for the multi-hole orifice ($N_{\text{holes}} = 47$)	ν_{water}	kinematic viscosity of water [$\nu_{\text{water}}(310 \text{ K}) = 7.2 \times 10^{-7} \text{ m}^2 \text{ s}^{-1}$ (Idel'cik, 1969)]
p^+ , p^-	forward, backward propagating plane wave spectra (in $\text{Pa}/\sqrt{\text{Hz}}$)	ρ_w	density of water ($\rho_w(310 \text{ K}) = 994 \text{ kg m}^{-3}$)
P_1 , P_2	static pressure respectively upstream and far downstream of the orifice	σ	cavitation number
P_j	static pressure at the jet (vena contracta)	σ_i	incipient cavitation number
P_v	vapor pressure ($P_v(310 \text{ K}) = 5.65 \times 10^3 \text{ Pa}$ (Tullis, 1989))	σ_{ch}	choked cavitation number
S	cross-section of the pipe (in m^2)		

4.2 Experimental set-up

4.2.1 Tested orifices

In the piping system of French nuclear power plants, a basic configuration to obtain a pressure discharge can be realized with a single-hole orifice. The maximum flow velocity can reach about 10 m.s^{-1} and the pressure drop 100 bar across the orifice. This can induce high vibration levels. The orifices used are chosen in order to reduce the pipe vibration to acceptable levels (Caillaud et al., 2006).

In our study, two orifices have been tested (see Fig. 4.2), as follows.

- A single-hole orifice, circular, centered, with right angles and sharp edges. It has a thickness of $t = 14$ mm ($t/d = 0.64$) and a diameter of $d = 22$ mm ($d/D = 0.30$), for a pipe diameter of $D = 74$ mm. It is considered as a 'thin' orifice as $t/d \lesssim 2$ (Idel'cik, 1969). In a sharp edged orifice flow, separation occurs at the upstream inlet edge. In a thin orifice, there is no reattachment of the flow within the orifice.
- A multi-hole orifice, with $N_{\text{holes}} = 47$ circular right-angled and sharp-edged perforations of diameter $d_{\text{multi}} = 3$ mm. Its total open surface is practically identical to the single-hole orifice one, as it has an equivalent $d_{\text{eq}}/D = 0.28$ ratio. This multi-hole orifice also has the same thickness of $t = 14$ mm ($t/d_{\text{multi}} = 4.67$). It behaves as a thick orifice $t/d \gtrsim 2$. The flow reattaches to the wall within the orifice.

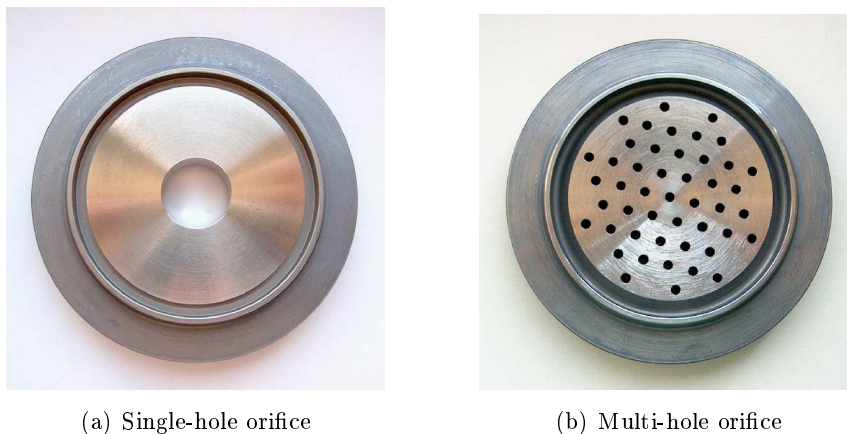


Figure 4.2: Front views of the tested orifices.

4.2.2 Test rig

The test-section, as shown in Fig. 4.3, consists out of an open loop with a hydraulically smooth steel pipe of inner diameter $D = 74$ mm and wall thickness $t_p = 8$ mm. The orifices are placed between straight pipe sections with lengths respectively equal to 42 diameters upstream and 70 diameters downstream.

The water is injected from a tank located 17 m upstream from the orifice. The nitrogen pressure in the tank above the water is controlled by a feedback system to maintain a constant main flow velocity. The water is released at atmospheric pressure 20 m downstream of the orifice. The temperature is kept equal to 310 K (± 1 K) during all experiments.

The flow velocity U is measured $26D$ upstream of the orifice, and the static pressures P_1 and P_2 are determined respectively by a transducer $11D$ upstream and another $40D$ downstream of the orifice. The fluctuating pressures are monitored by means of a combination of Kistler 701A piezo-electrical transducers and Kistler charge amplifiers. The location of the dynamical pressure transducers is given in Fig. 4.4. Upstream, the transducers 1 to 3 are positioned, at respectively $11D$, $8D$ and $5D$ from the

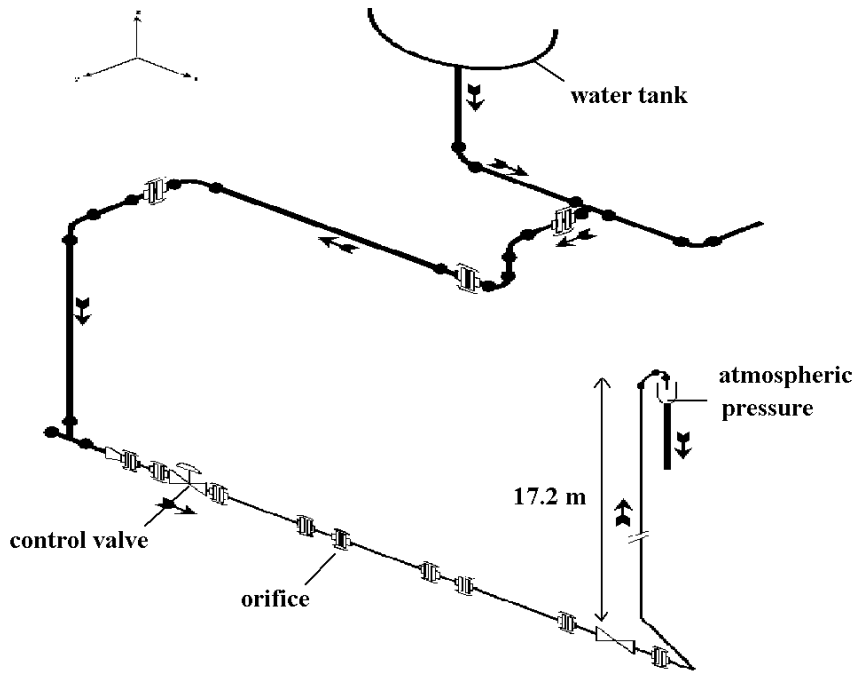


Figure 4.3: Scale scheme of the test rig.

orifice (0.25 m between consecutive transducers). Downstream, the transducers 4 to 10 are regularly positioned, from $7D$ to $39D$ (0.4 m between consecutive transducers).

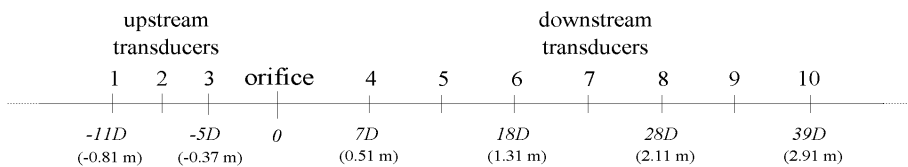


Figure 4.4: Location of the dynamical pressure transducers upstream and downstream of the orifice.

4.2.3 Experimental conditions

4.2.3.1 Water quality

The water used is tap water, demineralized, with pH 9 and weak conductivity. It is not degassed, hence it is expected to be saturated with dissolved air. The volume fraction of dissolved gas (denoted by β) is high compared to other cavitation studies. This gas content has not been measured, but an estimation, assuming saturation condition under a temperature of $T = 310$ K or $T = 273$ K, gives for the volume fraction an order of magnitude around, respectively, 10^{-2} or 10^{-3} .

It should be pointed out that the presence of dissolved gas in the water does not mean a presence of

gas bubbles in the water. Thus, the measured upstream speed of sound does not reveal any presence of gas bubbles as it is close to the one in pure water flow.

Correcting the compressibility of the water for the influence of the elasticity of the pipe (diameter $D=7.4 \times 10^{-2}$ m, wall thickness $e=8 \times 10^{-3}$ m, Young's modulus $E=2 \times 10^{11}$ N m $^{-2}$, Poisson ratio $\zeta=0.3$), the speed of sound c_{th} in pure water in the pipe is given in function of the speed of sound in pure water c_w (Lighthill, 1978):

$$c_{th} = c_w \left(1 + \rho_w c_w^2 \frac{D(1 - \zeta^2)}{eE} \right)^{-0.5}. \quad (4.4)$$

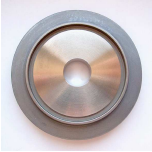
This predicts a speed of sound of $c_{th}=1454$ m.s $^{-1}$ using $c_w=1523$ m.s $^{-1}$. The measured speed of sound upstream of the orifice is 1420 ± 10 m.s $^{-1}$.

4.2.3.2 Experimental flow conditions

Experiments are carried out at a constant flow by controlling the static pressure upstream of the orifice. The downstream pressure P_2 is imposed by the hydraulic static head of the 17.2 m high vertical pipe downstream of the orifice. Each experiment lasts about 90 seconds. Pressures and volume flows are provided in Table 4.1 for the six experiments on the single-hole orifice, and in Table 4.2 for the six experiments on the multi-hole orifice.

The Reynolds number $Re = UD/\nu_{\text{water}}$ based on the pipe diameter and the water viscosity varies from 2×10^5 to 5×10^5 ; turbulence is fully developed, as usual in industrial pipes.

Table 4.1: Flow conditions for the single-hole orifice experiments (with standard deviations).

		Developed cavitation			Super cavitation		
	U (m.s $^{-1}$)	1.91	2.38	2.90	3.75	4.08	4.42
	st. deviation (m.s $^{-1}$)	0.06	0.04	0.04	0.03	0.03	0.05
	P_1 (10^5 Pa)	6.3	9.2	13.3	21.4	25.0	29.5
	st. deviation (10^5 Pa)	0.3	0.3	0.6	1.4	0.7	0.8
	P_2 (10^5 Pa)	2.7	2.7	2.7	2.8	2.8	2.8
	st. deviation (10^5 Pa)	0.0	0.0	0.0	2.0	0.2	1.5
	σ	0.74	0.41	0.25	0.15	0.12	0.10

Higher flow regimes have been tested, but the pressure transducers downstream delivered no signal, as they were located in a vapor pocket characteristic of the super cavitation regime. As a consequence, no acoustic data are available in these conditions, and the corresponding hydraulic conditions are not reported in Tables 4.1 and 4.2.

4.2.4 Distinction of two cavitation regimes

The application of Tullis' formulas to our experiments gives the cavitation indicators: σ_i for the developed cavitation and σ_{ch} for the super cavitation. Compared to our observations, those cavitation

Table 4.2: Flow conditions for the multi-hole orifice experiments (with standard deviations).



	Developed cavitation				Super cavitation	
U (m.s ⁻¹)	2.08	2.45	2.94	3.65	4.18	4.43
st. deviation (m.s ⁻¹)	0.02	0.04	0.04	0.02	0.02	0.04
P_1 (10 ⁵ Pa)	6.5	6.9	12.9	19.8	26.0	28.3
st. deviation (10 ⁵ Pa)	0.1	0.3	0.4	1.2	0.3	0.6
P_2 (10 ⁵ Pa)	2.7	2.8	2.8	2.9	3.0	0.9
st. deviation (10 ⁵ Pa)	0.0	0.1	0.1	0.3	1.2	2.1
σ	0.74	0.45	0.28	0.17	0.13	0.03

regime indicators are in good agreement.

- For the single-hole orifice: $\sigma_i \geq 0.93$, $\sigma_{ch} = 0.25$. The observations, based on listening and on the measured downstream speed of sound, indicate that all experiments (i.e., $\sigma < 0.74$) are cavitating. Furthermore, the downstream acoustic properties and particularly the shape of the downstream noise spectra indicate that the last three experiments (i.e., $\sigma < 0.25$) are in super cavitation regime.
- For the multi-hole orifice: $\sigma_i \geq 0.87$, $\sigma_{ch} = 0.20$. The observations in this case indicate that all experiments (i.e., $\sigma < 0.74$) are cavitating. The super cavitation regime is observed for the last two experiments (i.e., $\sigma < 0.17$).

4.2.5 Acoustic analysis method

In the frequency range of the study, only acoustic plane waves propagate. The issue is to determine the spectra p^+ and p^- representing, respectively, the upstream and downstream traveling plane waves and for which Fourier-like analysis holds.

From each experiment, time fluctuating-pressure signals are obtained. These data are truncated to a time interval where the acoustic properties do not evolve significantly, i.e., on a duration of about 10 s. With the help of a reference pressure p_{ref} , we compute the cross-spectral densities $G_{pp_{\text{ref}}}(f)$, which are defined as the Fourier Transform of the time correlation (Bendat and Piersol, 1986). It is worth recalling that, for a small frequency bandwidth Δf , the mean-square value of the pressure in the frequency range $[f, f + \Delta f]$ is given by $G_{pp}(f) \Delta f$. These cross-spectra are expressed in Pa²/Hz. In order to get a spectral expression linear with the pressure, we choose to use the following expression, in Pa/Hz^{1/2} (see Appendix E for more details):

$$p_n(f) = \frac{G_{p_n(t)p_{\text{ref}}(t)}(f)}{\sqrt{G_{p_{\text{ref}}(t)p_{\text{ref}}(t)}(f)}}, \quad (1 \leq n \leq 10). \quad (4.5)$$

For upstream observations, transducer 1 is chosen as reference and for downstream observations, transducer 10 is chosen as reference.

As plane waves propagate, the acoustic pressure at one point is the summation of the forward (in the direction of the flow) traveling wave p^+ and of the backward traveling wave p^- . We assume the speed of sound to be identical in the forward and in the backward directions, because the Mach number is low (of the order of 10^{-3}). The identification at each transducer of the local speed of sound and of the acoustic plane waves is carried out according to standard intensimetry techniques (Davies et al., 1980; Bodén and Abom, 1986; Hassis, 1999).

The final spectra represent an average of about 20 spectra, determined with a time signal of 10 s duration. Each intermediate spectrum is determined with a window of 1 s duration, and the successive windows have an overlapping ratio of 0.5 (between 0 and 1). This average is made in order to reduce the random errors.

The use of a single reference microphone may give uncertainties for determining standing waves if there is a pressure node at a microphone. This happens when the reflection coefficient is close to unity. At low frequencies (below 500 Hz), this is the case for developed cavitation (see Fig. 4.6). However, as shown in Fig. 4.19, the microphones are not close to the pressure nodes of the standing wave patterns. At higher frequencies, and for super cavitation, the reflection coefficient is so low that we do not expect a problem (see Figs. 4.6 and 4.7).

4.2.6 Acoustic boundary conditions on both sides of the orifice

4.2.6.1 Acoustic boundary conditions upstream of the orifice

The acoustic conditions imposed by the test rig upstream of the orifice are quite reflecting, as illustrated in Fig. 4.5 by the upstream reflection coefficient $R = p^-/p^+$, defined as the ratio between the forward and the backward propagating plane waves. These reflecting characteristics are due to multiple partial reflections of the acoustic waves on various elements present on the upstream part of the test rig as an open valve, a few bends and section restrictions. Those elements have not been modified in the course of the experiments, so that these reflecting conditions not vary much from one experiment to another.

4.2.6.2 Acoustic boundary conditions downstream of the orifice

The downstream acoustic boundary condition depends on the cavitation regime, developed cavitation regime or super cavitation regime.

In developed cavitation regime (see Fig. 4.6), the downstream reflection coefficient has a magnitude close to 1 up to 600 Hz, which indicates a strong reflecting condition. As the phase is a linear function of the frequency, the reflection point is determined: it corresponds to the location of an open valve (at $53D$ downstream of the orifice). The cavity of this valve is hence filled with a very compressible fluid, i. e. air, imposing an acoustic pressure node $p' = 0$.

The reflection coefficient shows values above unity in Figs. 4.5 and 4.6. This may be due to measurement inaccuracies. Also the presence of a noise source outside the main source region is possible and would give values above unity.

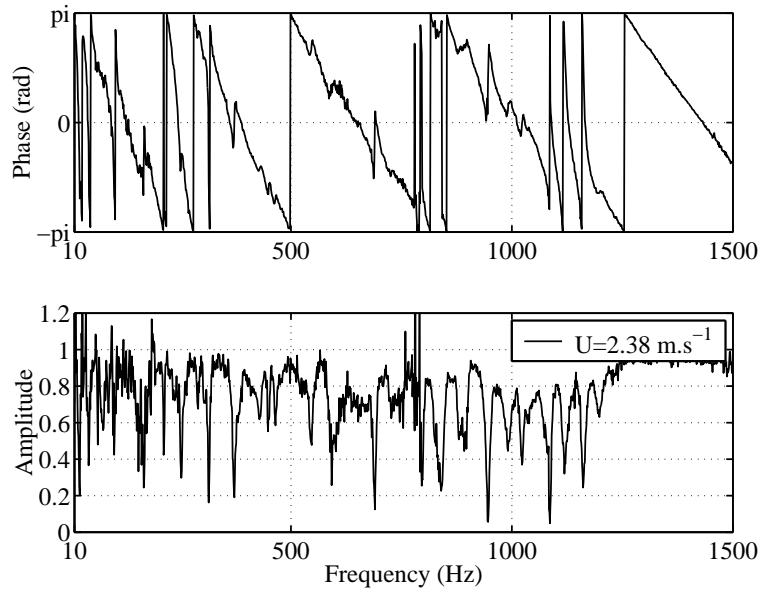


Figure 4.5: Typical acoustic reflection coefficient $R = \frac{p^+}{p^-}$ upstream of the orifice (calculated at transducer 1).

In super cavitation regime (see Fig. 4.7), the downstream reflection coefficient falls down below the value of 0.5. As a first approximation, the pipe termination is then almost anechoic. This difference of behavior between the developed cavitation regime and the super cavitation regime is not analysed in the framework of the present study.

This variation of the downstream acoustic boundary conditions is specific of the test rig. It has some impact on the levels of the downstream spectra. This will be taken into account further in the study of the downstream noise spectra.

It should be pointed out that, for some frequencies, the determination of the acoustical spectra is inaccurate. But coherence values are still good enough, as illustrated in Fig 4.8, to allow a satisfactory fit of the spectra to determine the speed of sound, as illustrated in Fig 4.9.

4.3 Cavitation regimes

4.3.1 Hydraulic model for the pressure drop ΔP across the single-hole orifice

A simple model of the hydraulics of the single-hole orifice is proposed. The hydraulic conditions (pressure and Mach number) at the jet of the orifice are estimated, hence giving some insight for a physical interpretation of the different cavitation regimes.

This hydraulic model is a simple classical Borda-Carnot model, see, for example Durrieu et al. (2001). It assumes an incompressible stationary single-phase flow, that is, no effect of cavitation on the hydraulics. Also, the ratio S_j/S between the free jet cross-section and the pipe cross-section S is considered as fixed.

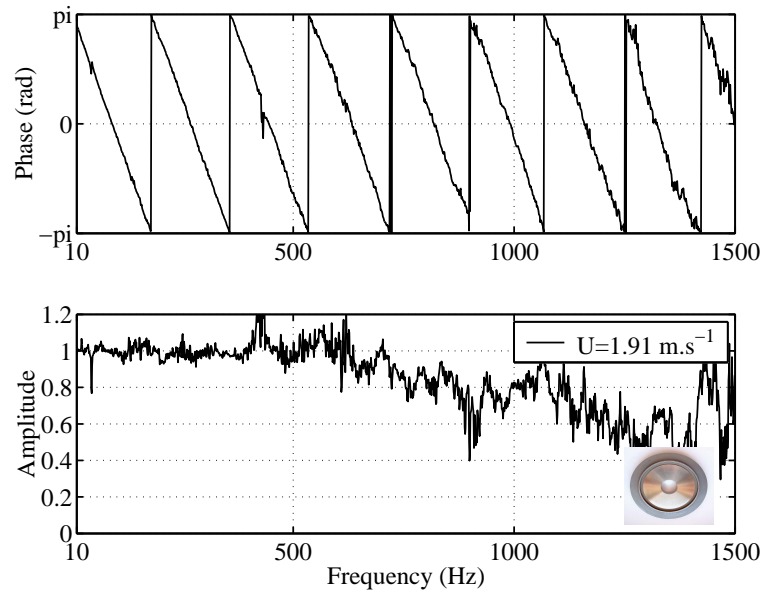


Figure 4.6: Typical acoustic reflection coefficient $R = \frac{p_-}{p_+}$ downstream of the orifice (calculated at transducer 8) in developed cavitation regime.

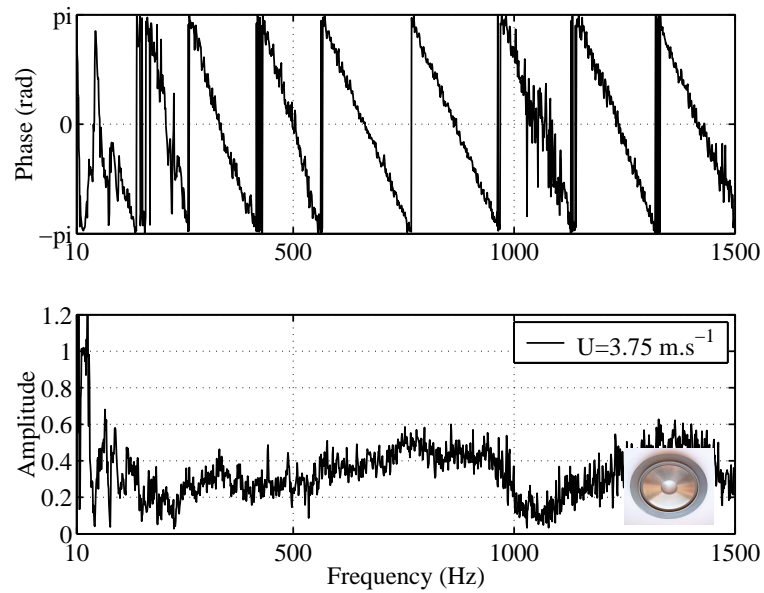


Figure 4.7: Typical acoustic reflection coefficient $R = \frac{p_-}{p_+}$ downstream of the orifice (calculated at transducer 8) in super cavitation regime.

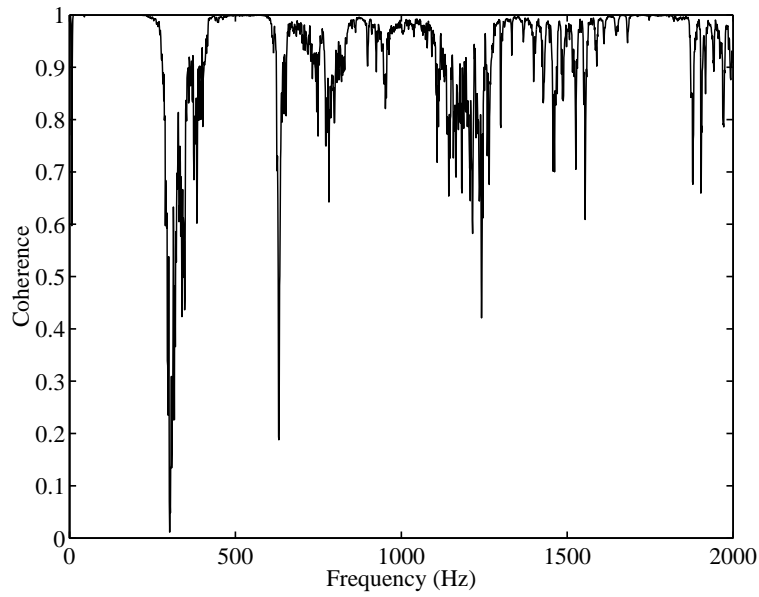


Figure 4.8: Example of the coherence function between 2 successive transducers (single-hole orifice, $U=2.38 \text{ m.s}^{-1}$, between transducers 7 and 8).

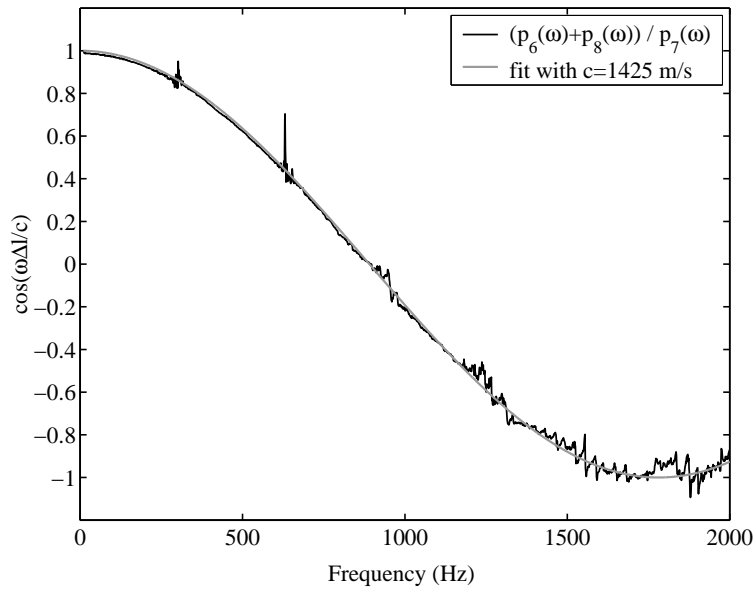


Figure 4.9: Example of the determination of the speed of sound using a fit on the spectra for 3 successive transducers (single-hole orifice, $U=2.38 \text{ m.s}^{-1}$, middle transducer: 7).

Firstly, mass conservation demands

$$S_j U_j = S U. \quad (4.6)$$

Secondly, the flow upstream of the jet is assumed to be an inviscid steady potential flow, so that

$$P_1 + \frac{1}{2} \rho_w U^2 = P_j + \frac{1}{2} \rho_w U_j^2. \quad (4.7)$$

Downstream of the jet, a turbulent mixing region is followed by a uniform flow of velocity U . Neglecting friction at the walls, and assuming a thin ($t/d \lesssim 2$) orifice (with no re-attachment of the flow inside the hole of the orifice), one obtains (S_d is the cross-section of the orifice)

$$S P_j + \rho_w U_j^2 S_j = S P_2 + \rho_w U^2 S. \quad (4.8)$$

The pressure P_j and the velocity U_j at the jet are deduced from Eqs. (4.6)-(4.8). The measured pressure drop, denoted by $\Delta P_{\text{measured}}$, is in this case equal to the pressure drop across the orifice: $\Delta P_{\text{measured}} = P_1 - P_2$. Hence, denoting by α the contraction coefficient ($\alpha = S_j/S_d$), this developed cavitation model gives

$$\frac{\Delta P_{\text{measured}}}{\frac{1}{2} \rho_w U^2} = \left[\left(\frac{S}{S_j} \right)^2 - 1 \right] + \left[2 - 2 \frac{S}{S_j} \right], \quad (4.9)$$

the first part representing the enthalpy variation from upstream to the jet, and the second part the dissipation from the jet to downstream.

Finally, after simplifications, we find

$$\frac{\Delta P_{\text{measured}}}{\frac{1}{2} \rho_w U^2} = \left[\left(\frac{D}{d} \right)^2 \frac{1}{\alpha} - 1 \right]^2. \quad (4.10)$$

In super cavitation, the downstream static sensor is in the jet region, measuring P_j . The pressure drop measured represents the dissipation from upstream to the jet (the first part of the preceding expression):

$$\frac{\Delta P_{\text{measured}}}{\frac{1}{2} \rho_w U^2} = \frac{1}{\alpha^2} \left(\frac{D}{d} \right)^4 - 1. \quad (4.11)$$

Figure 4.10 compares the two models using a contraction coefficient $\alpha = 0.65$ with experimental results (additional experimental results in super cavitation, not shown in Table 4.1, are plotted), as follows.

- In the developed cavitation regime ($U < 3.5 \text{ m.s}^{-1}$), theory agrees qualitatively well with experiments, predicting ΔP within 15 %.
- In the super cavitation regime ($U > 3.5 \text{ m.s}^{-1}$), experimental data agree remarkably well with the model, predicting ΔP within 1 %. Incidentally, we observe that super cavitation does not induce a strong slope variation in the ΔP versus U curve. This is mentioned in Tullis (1989) for orifices of low d/D ratio (approximately under 0.5, which is the case here).

As a result, the model is validated as a satisfying broad estimation of the hydraulics, taking a contraction coefficient of 0.65. This value is reasonable, as it is close to 0.61 which is the theoretical value for sharp-edged orifices with a jet from a gas to a free space exit (Gilbarg, 1960) and it is less

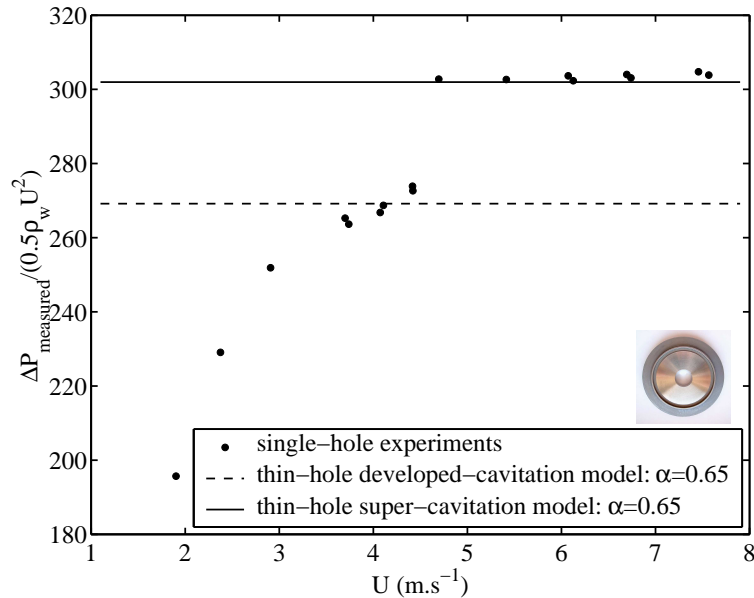


Figure 4.10: Comparison between the Borda-Carnot model with different contraction coefficients α and the single-hole orifice measurements.

than 0.70, which indicates (Blevins, 1984) that the real radius of curvature of the upstream edge of the orifice is less than 1% of the pipe diameter (this confirms that this edge is a neat sharp angle edge).

Using this model, the pressure and the velocity at the jet are estimated, see Table 4.3, as follows.

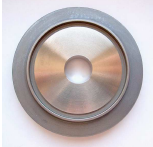
- The pressure in the jet P_j is very close to the vapor pressure of the liquid ($P_v=5.65 \times 10^3$ Pa) in super cavitation regime. This is coherent with the stationary presence of a vapor pocket in this region. Hence, it may be an indicator of the transition to super cavitation regime.
- The velocity U_j is compared to c_{\min} , an evaluation of the lowest speed of sound in the two-phase region of the jet. An estimation of it can be obtained, see VanWijngaarden (1972): the minimum speed of sound is obtained for a vapor volume fraction in the jet of $\beta = 0.5$, giving $c_{\min} = \sqrt{4\gamma P_j / \rho_w}$. We find (see Table 4.3) very low values: this is coherent, as there is much vapor in this region. Comparing those values with the velocity of the jet flow U_j , it appears from this crude model that the flow can be 'supersonic' in the jet region. This seems relevant in all cavitation regimes, hence this supersonic transition may be characteristic of the transition between a non-cavitating and a cavitating flow: it could be an indicator of incipient cavitation. Further research is needed to confirm this idea.

4.3.2 Hydraulic model for the pressure drop ΔP across the multi-hole orifice

Similarly to the single-hole orifice, a simple model of the hydraulics of the multi-hole orifice is proposed.

Contrary to the single-hole orifice, the multi-hole orifice has a ratio t/d_{eq} over 2 ($t/d_{\text{eq}} = 4.7$), so that each orifice is considered as thick. In that case, for noncavitating flows, there is re-attachment of

Table 4.3: Conditions at the jet using the Borda-Carnot model for the single-hole orifice.



	Developed cavitation			Super cavitation		
	1.91	2.38	2.90	3.75	4.08	4.42
U (m.s ⁻¹)	1.91	2.38	2.90	3.75	4.08	4.42
U_j (m.s ⁻¹)	33	41	50	65	71	76
c_{min} (m.s ⁻¹)	28	30	34	13	—	—
P_j (10 ⁵ Pa)	1.4	1.6	2.0	0.3	—	—

the flow within the orifices, followed by a turbulent mixing region, which corresponds to a first energy loss. A second energy loss is imposed by the sudden enlargement at the exit of the hole.

Following this description, and using similar equations as for the single-hole case, the pressure drop measured across the orifice $\Delta P_{\text{measured}} = P_1 - P_2$ for the developed cavitation regime is composed of a first part representing the dissipation from upstream to the jet (within the orifice), and a second part representing the dissipation after the jet (S_d is the cross-section of the orifice):

$$\frac{\Delta P_{\text{measured}}}{\frac{1}{2}\rho_w U^2} = \left[\left(\frac{S}{S_j} \right)^2 - 1 \right] + \left[2 \left(1 - \frac{S}{S_d} \right) + 2 \left(\frac{S}{S_d} \right)^2 \left(1 - \frac{S_d}{S_j} \right) \right]. \quad (4.12)$$

The total expression is hence the following:

$$\frac{\Delta P_{\text{measured}}}{\frac{1}{2}\rho_w U^2} = 1 - 2 \left(\frac{D}{d} \right)^2 + 2 \left(\frac{D}{d} \right)^4 \left(1 - \frac{1}{\alpha} + \frac{1}{2\alpha^2} \right). \quad (4.13)$$

In the super cavitation regime, we assume that there is no reattachment within the orifice. The downstream static pressure transducer is located intermediately between the two pressure losses, so that the measured pressure loss is given by $\Delta P_{\text{measured}} = P_1 - P_j$. We should again apply Eq. (4.11) to determine it. As the two orifices have the same open surface, we find the same expression as the developed cavitation model for the single-hole orifice.

Figure 4.11 shows comparison of this hydraulic model with experiments, as follows.

- In the developed cavitation regime, the correlation is not good for $\alpha = 0.65$. The pressure drop ΔP is underestimated by about 30 %. The thin orifice equation (Eq. (4.10)), however, performs better, indicating that there is not a full reattachment within the orifice. We observe a reduction of losses for the multi-hole measurements, which is coherent as a two-step dissipation induces less pressure losses than a single step.
- In the super cavitation regime, the correlation is again excellent, with a prediction of ΔP within 1 %.

Conditions at the jet are estimated. We use Eq. (4.10) with $\alpha = 0.65$ as the most satisfactory for this estimation in developed cavitation. Results are given in Table 4.4: in the developed cavitation regime, we get the same results as in the single-hole case: the flow is 'supersonic' in the sense that

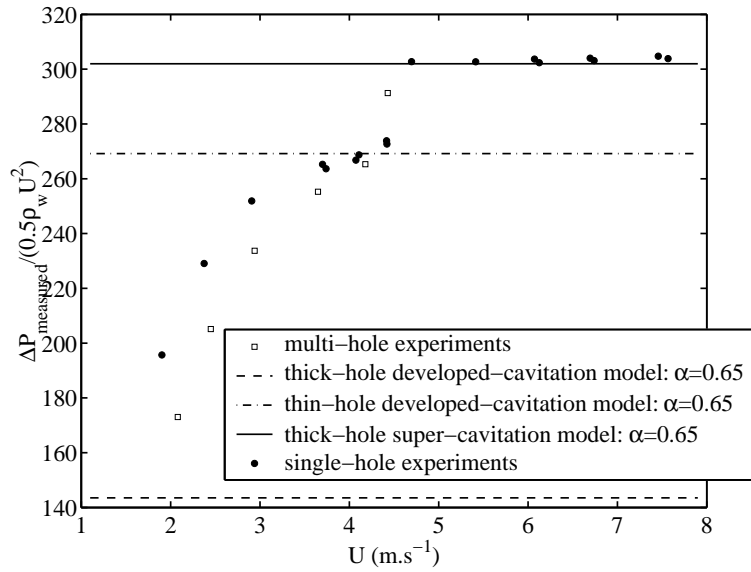


Figure 4.11: Evaluation of the multi-hole orifice model and comparison between the single-hole orifice measurements.

the jet flow velocity is higher than the minimum speed of sound in the region; in the super cavitation regime, the estimated pressure at the jet is at the vapor pressure. This also confirms the result obtained for the single-hole case.

Table 4.4: Conditions at the jet using the Borda-Carnot model for the multi-hole orifice.



	Developed cavitation			Super cavitation		
U (m.s ⁻¹)	2.08	2.45	2.94	3.65	4.18	4.43
U_j (m.s ⁻¹)	36	43	51	63	73	77
c_{min} (m.s ⁻¹)	20	—	27	—	—	—
P_j (10 ⁵ Pa)	0.7	—	1.3	—	—	—

4.3.3 Developed cavitation visualization and time signal

In the developed cavitation regime, bubbles are created intermittently, as illustrated in Fig. 4.12.

The typical time fluctuating pressure signals obtained are difficult to distinguish from a noncavitating flow (see Fig. 4.13). The fluctuations display a symmetric signal around the mean pressure, with hardly any distinguishable bursts coming from the implosion of the bubbles. Those bursts are discussed later for super cavitation.

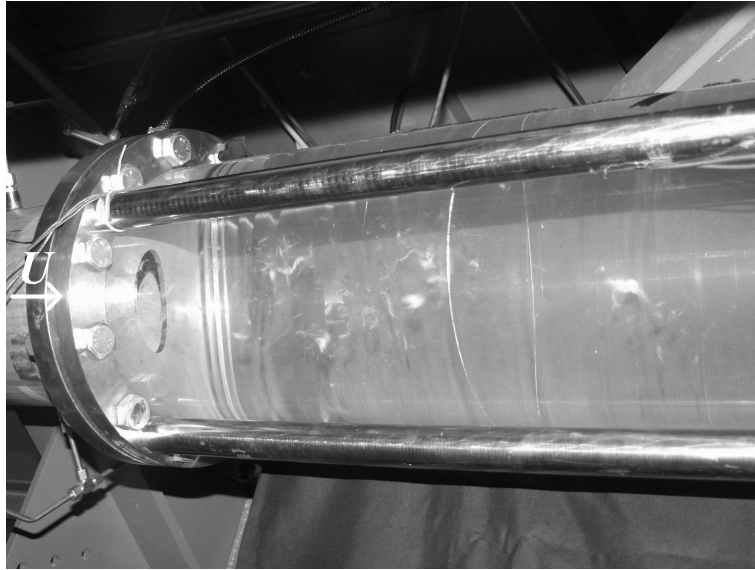


Figure 4.12: From other experiments at EDF (Archer et al., 2002), visualization of the developed cavitation regime for a single-hole orifice ($d/D = 0.30$, $t/d = 0.10$, $D = 2.66 \times 10^{-1}$ m) with $\sigma = 0.49$ and $U = 1.50$ m.s $^{-1}$ ($\Delta P = 3.1 \times 10^5$ Pa, $P_1 = 4.6 \times 10^5$ Pa). White bubble clouds are observed around the jet formed at the orifice.

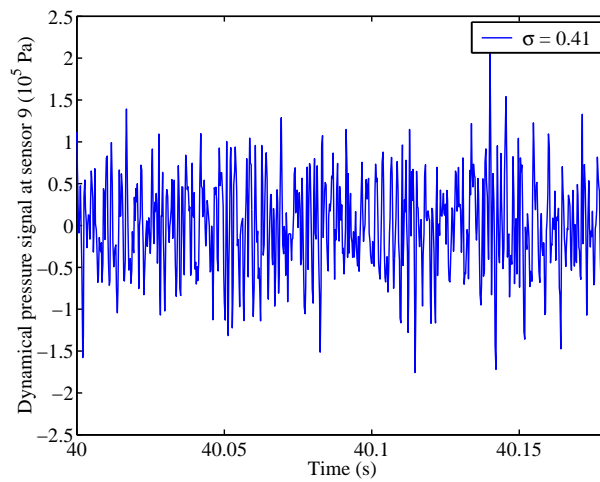


Figure 4.13: Typical dynamical time pressure signal from a downstream transducer for the developed cavitation regime (here for the single-hole orifice at $\sigma = 0.41$).

4.3.4 Whistling phenomenon in developed cavitation

Whistling is present in every developed cavitation regime of single-hole orifice experiments (it is never observed for multi-hole orifice experiments). Evidence of whistling is particularly given on the upstream acoustical spectra, by the sharpness of the fundamental frequency peak f_0 and the existence of several harmonics at exact multiples of f_0 (see an example in Fig. 4.14). The higher harmonics are typical of steady whistling stabilized by a nonlinear feedback effect as for all self-sustained oscillations (Fletcher, 1979; Rockwell and Naudascher, 1979).

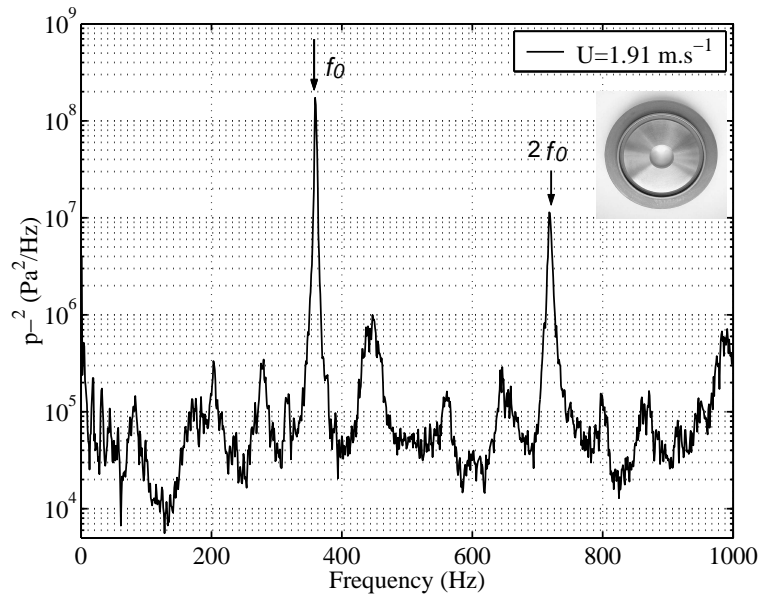


Figure 4.14: Detection of whistling frequency f_0 with harmonics on upstream plane wave spectra p^- (here for the single-hole orifice at $U = 1.91 \text{ m s}^{-1}$, $f_0 = 359 \text{ Hz}$ and the first harmonics at 718 Hz).

Scant literature has been found on whistling of cavitating orifices in pipes. A vortex shedding phenomenon in presence of cavitation has been investigated by Sato and Saito (2001), but in the particular case of thick orifices ($t/d \gtrsim 2$). On thin orifices, some visualizations (Moussou et al., 2003) made on other EDF experiments have shown the possibility of the presence of vortex-shedding in cavitation regime, as can be seen in Fig. 4.15, from Archer et al. (2002).

The whistling frequencies are given in Table 4.5. They do not increase continuously with the flow velocity, as one would expect for a hydrodynamic oscillation edge-tone like (Blake and Powell, 1983). The stable frequency is typical of an acoustic feedback which creates and maintains the acoustic oscillation close to a resonance frequency. This is also revealed by the locking of the phase of the time pressure signals on successive sensors, which indicates a standing wave pattern.

Upstream of the orifice, the level of whistling is higher than downstream: hence the acoustic feedback is suspected to happen predominantly upstream. The upstream reflection coefficient, see Fig. 4.5, is high but irregular: no clear acoustic reflection point can be identified (as it can be for the cavity of a valve downstream, see Section 4.2.6.2). This irregular shape is due to the intricacy of the upstream rig design, with a succession of elbows, slight restrictions of sections and some open valves.

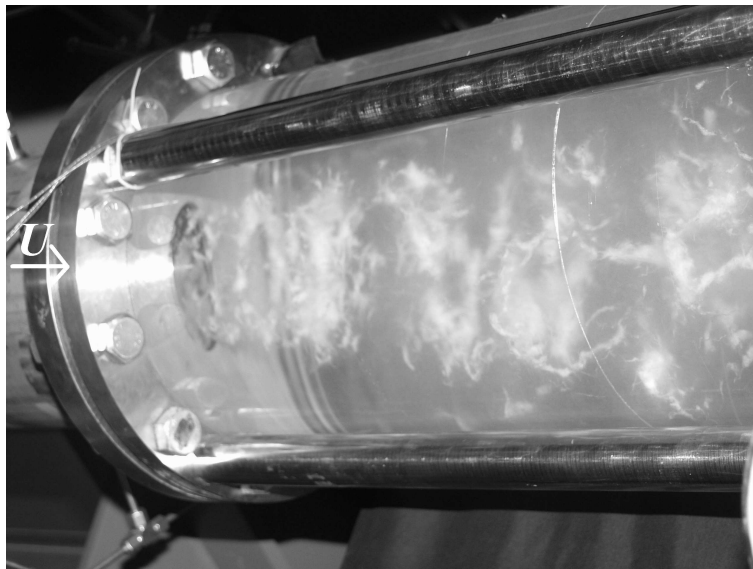


Figure 4.15: From other experiments at EDF (Archer et al., 2002), visualization of a cavitating and whistling single-hole orifice ($d/D = 0.30$, $t/d = 0.10$, $D = 2.6 \times 10^{-1}$ m) with $\sigma = 0.35$ and $U = 1.97$ m.s $^{-1}$ ($\Delta P = 5.3 \times 10^5$ Pa, $P_1 = 7.2 \times 10^5$ Pa).

It is also worth mentioning that the whistling frequency does not coincide with any downstream natural acoustic frequency. This is coherent with the acoustic uncoupling observed from both sides of the orifice.

The single-hole orifice has a ratio $t/d = 0.6$, inferior to 2, so that it is considered as a thin orifice. We assume that the whistling phenomenon is influenced by the thickness of the orifice t , rather than its diameter. It is also natural to use the velocity at the orifice U_d as a relevant scaling velocity. Hence the Strouhal number is defined as

$$\text{St} = \frac{f_0 t}{U_d}, \quad (4.14)$$

and values are reported in Table 4.5.

Table 4.5: Strouhal number $\text{St} = \frac{f_0 t}{U_d}$ of the whistling frequency f_0 (only observed in the single-hole orifice case).



U (m s $^{-1}$)	1.91	1.91	2.38	2.38	2.90	2.90
c (m s $^{-1}$)	1390	1200	660	1420	1130	1420
f_0 (Hz)	359	397	421	436	427	434
St	0.23	0.26	0.22	0.23	0.18	0.19

The Strouhal number is obtained in the range 0.18-0.26. These values are close to data on orifices: Anderson (1953) finds a Strouhal number around 0.2 for whistling orifices in air with a free air exit.

In Anderson's experiments, the orifices were a bit thinner (with $0.2 \leq t/D \leq 0.5$, whereas here $t/D = 0.19$) and the Reynolds numbers smaller ($U_d t/\nu_{\text{air}} \sim 10^3$ with ν_{air} the kinematic viscosity of air, whereas here $U_d t/\nu_{\text{water}} \sim 10^5$).

The multi-hole orifice is a thick one, as $t/d_{\text{multi}} = 4.7$. Hence it is no surprise that it does not whistle. The flow re-attaches itself inside each hole, which stabilizes the shear layers of the jet and hence prevents whistling in the same manner as observed for the single-hole orifice.

4.3.5 Super cavitation visualization and typical time signal

In the super cavitation regime, a vapor pocket is created in the jet region, as illustrated in Fig. 4.16.



Figure 4.16: From other experiments at EDF, visualization of the super cavitation regime for a single-hole orifice.

When the vapor pocket expands and reaches the downstream transducers, those transducers no longer deliver any acoustical signal. This constitutes an evidence for the existence of the vapor pocket.

It appears that the length of the vapor pocket increases quickly with flow velocity. The length of the vapor pocket increases from about $7D$ at $U_0 = 3.8 \text{ m.s}^{-1}$ to $18D$ at $U_0 = 4.4 \text{ m.s}^{-1}$ and is larger than $38D$ at $U_0 = 4.7 \text{ m.s}^{-1}$ for the single-hole orifice. For the multi-hole orifice, the length of the vapor pocket increases from around $7D$ at $U_0 = 4.2 \text{ m.s}^{-1}$ to larger than $38D$ at $U_0 = 4.5 \text{ m.s}^{-1}$.

The typical time-fluctuating pressure signals obtained are very different from those in the developed cavitation regime (see Fig. 4.17). They are asymmetric around the mean pressure, exhibiting very large positive spikes, up to 20 bars, linked to the collapse of bubbles.

Focusing on time signals (see an illustration in Fig. 4.18), it is seen that the phenomenon of bubble

implosion is characterized first by a decrease in negative values of the fluctuating pressure with a characteristic duration of a tens of milliseconds, followed by an abrupt increase of the pressure, a 'spike', with a characteristic duration of one millisecond. By modeling this bubble volume evolution with a monopole source, which is a common and satisfactory simple model; see, for instance, Brennen (1995), the first decrease is linked with a decrease of the bubble size from its initial size to a value close to zero; the second part of the signal is linked with a pressure shock wave originating from the abrupt collision of the water particles. However, extremely high amplitudes are observed in comparison to Brennen (1995) (cf. his Fig 3.19). This can be due either to the large size of our bubbles, either to the effect of confinement.

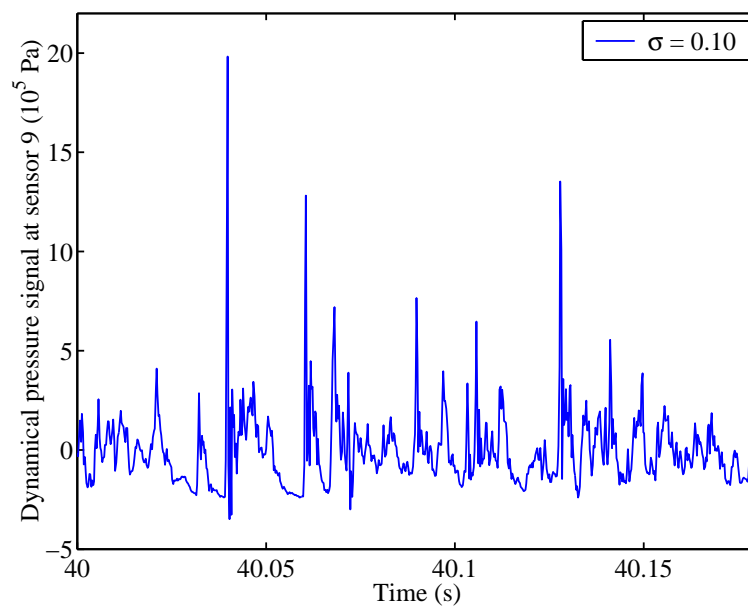


Figure 4.17: Spurious pressure pulses (spikes) from collapsing bubbles on dynamical time pressure signal from a downstream transducer in super cavitation regime (here for the single-hole orifice at $\sigma = 0.10$).

4.4 Results in the developed cavitation regime

The single-hole and the multi-hole orifice developed cavitation regimes are presented together, as they show similar acoustical behavior. Firstly, results on the acoustic features of this cavitation regime are introduced: the observed variations of the downstream speed of sound and the presence of resonance frequencies in downstream spectra. Then the downstream spectra, depending on those acoustical features, are presented and discussed.

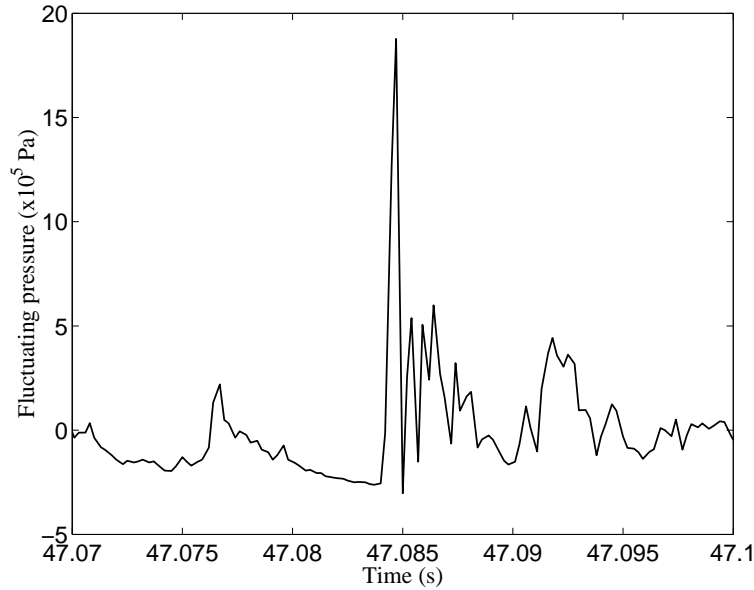


Figure 4.18: Cavitation peak in super cavitation regime (single-hole orifice at $\sigma=0.10$)

4.4.1 Acoustic features

4.4.1.1 Spontaneous variations of the downstream speed of sound

For a fixed set of hydraulic conditions in the developed cavitation regime, the downstream speed of sound may spontaneously evolve. For instance, the single-hole orifice experiment at $U = 2.38 \text{ m.s}^{-1}$ shows the downstream speed of sound evolving from 660 m.s^{-1} (during the first 20 s) to 1420 m.s^{-1} (till the end of the experiment: 90 s).

This variation of the speed of sound indicates that air bubbles are present, in varying quantity, in the water far downstream of the orifice. For instance, a value of 660 m.s^{-1} indicates a volume gas fraction in the water between 10^{-3} and 10^{-4} , assuming the static pressure being between P_j and P_2 [we use a classic formula; see, for example, VanWijngaarden (1972)]. On the contrary, a value of 1420 m.s^{-1} indicates a negligible content of air in the water, as it is close to the speed of sound in pure water (which equals to 1454 m.s^{-1} when correcting for pipe elasticity, as presented in section 4.2.3.1).

Cavitation bubbles, when they are formed, are originally mainly constituted of vapor. During their lifetime, they are gradually filled with air, due to the diffusion of the dissolved gas present in the water surrounding them. As they drift downstream, moving away from their region of creation, they reach regions where the pressure recovers higher levels. Pure vapor bubbles cannot persist, those bubbles remaining far downstream of the orifice are mainly filled with air (see for example Fig. 4.12). Consequently, the observed variation of the quantity of air bubbles is suspected to be due to an inhomogeneity of the dissolved gas content in the injected water. This inhomogeneity may be related to temperature variations in the experimental installations. This hypothesis is all the more plausible as the water used has not received any degassing treatment, hence having a fluctuating and high dissolved gas content, not measured but estimated around 10^{-2} or 10^{-3} (values at saturation conditions for $T = 273 \text{ K}$ and $T = 310 \text{ K}$ respectively). In some experiments, the change in residual air bubble content

occurs after the water from the pipe segment between the orifice and the tank has been evacuated and 'fresh' tank water has started to flow through the orifice.

These variations of the downstream speed of sound during each experiment have some influence on the acoustical behavior downstream of the orifice: the values of the natural frequencies, appearing downstream, are altered proportionally with the speed of sound.

The propagating waves are subjected to two-phase flow damping, as already mentioned by Hassis (1999). As regards this last effect, no significant variation of the propagating wave amplitude could be measured along the downstream sensors, but the downstream acoustical reflection coefficient appears to vary significantly with the downstream speed of sound.

4.4.1.2 Acoustical uncoupling from both sides of the orifice

An acoustical uncoupling is observed between acoustical spectra upstream and downstream of the orifice: the natural frequencies present downstream are strongly attenuated on upstream spectra; the whistling, when present, is visible on upstream spectra, but hardly on downstream spectra; and, furthermore, the background noise on downstream spectra is higher than the one on upstream spectra, approximately from a factor 2 (for $U = 1.91 \text{ m.s}^{-1}$) up to 7 (for $U = 2.90 \text{ m.s}^{-1}$) for the single-hole orifice, and much more significantly for the multi-hole orifice, with an approximately constant factor of about 10.

This acoustical uncoupling is an effect of cavitation as there is choking (indicated in Table 4.3).

4.4.1.3 Presence of natural modes downstream

In this developed cavitation regime, resonance frequencies are systematically observed in acoustical spectra downstream of the orifice (both for the single-hole and the multi-hole).

The acoustic boundary conditions are of a similar type, as the frequencies are of the form: $f_n = n f_1$, f_1 being the first resonance frequency. More precisely, these acoustic boundary conditions can be identified by extrapolating the standing wave patterns at those resonance frequencies. This extrapolation is made possible as a series of transducers (7 in number) is present downstream of the orifice. As a result, we find two acoustic pressure nodes $p' = 0$ (see Fig. 4.19), discussed above.

- One acoustic pressure node is found far downstream of the orifice, at $52D (\pm 1D)$. It is the result of the influence of a cavity of an open valve filled with air. The reflection coefficient imposed by such a cavity has been presented in Fig 4.6. The magnitude of the reflection coefficient $|R|$ is close to 1, which confirms the acoustic influence of this cavity;
- Another is found just downstream of the orifice, at $4D (\pm 1D)$. It is likely to be caused by a cavitation cloud.

4.4.2 Noise spectra generated downstream

Noise spectra generated in the pipe downstream of the orifice for the developed cavitation regime are presented in this section.

The downstream transducers give a far-field measurement, as they are not located in the source region mainly constituted of bubble implosions located just downstream of the orifice. The acoustical

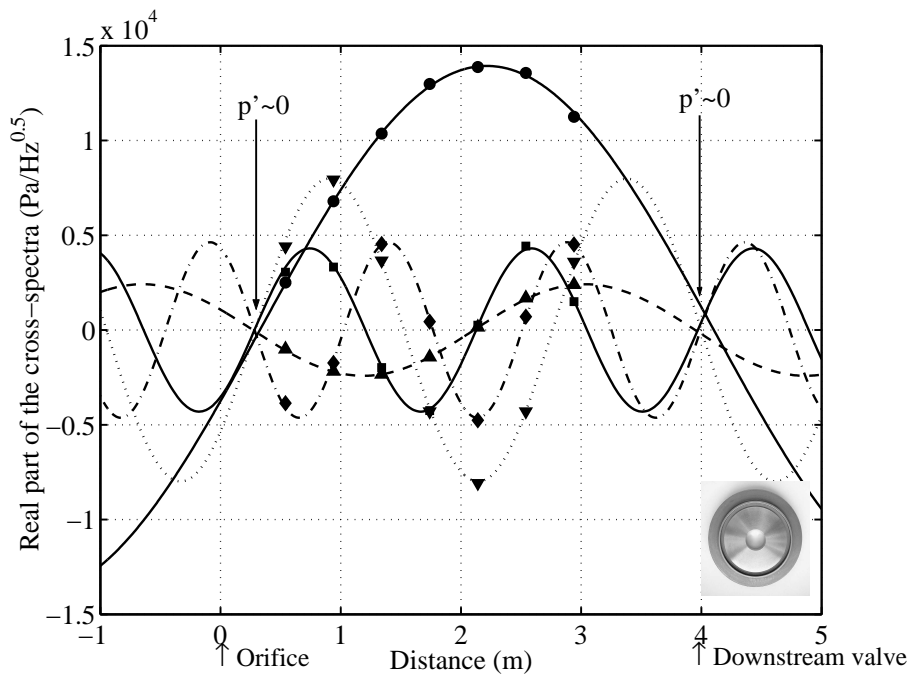


Figure 4.19: In the developed cavitation regime, two acoustic boundary conditions $p' \simeq 0$ are found downstream of the orifice, hence natural frequencies appear, pointed out by the interpolation of the values of the cross-spectra at those first natural frequencies (here for the single-hole orifice at $U = 2.38 \text{ m.s}^{-1}$, $c=1420 \text{ m.s}^{-1}$ and 5 natural frequencies: \bullet 188 Hz, \blacktriangle 386 Hz, \blacktriangledown 574 Hz, \blacksquare 770 Hz, \blacklozenge 957 Hz).

power measured at downstream transducers represents the noise generated in the pipe. Under the assumptions of plane-wave propagation and no influence of the flow (the Mach number is around 10^{-3}), the acoustical power takes the expression: $S(p^{+2} - p^{-2})/(\rho_w c_w)$ (Morfey, 1971).

It is furthermore assumed that the backward propagating wave spectrum of p^- is small enough to be neglected. Even if acoustical reflection is observed to occur downstream, this estimation of the source of noise is considered satisfactory enough as an order of magnitude (this is all the more relevant as logarithmic representation is used). Thus it comes to the source power being represented by the quantity $S p^{+2}/(\rho_w c_w)$.

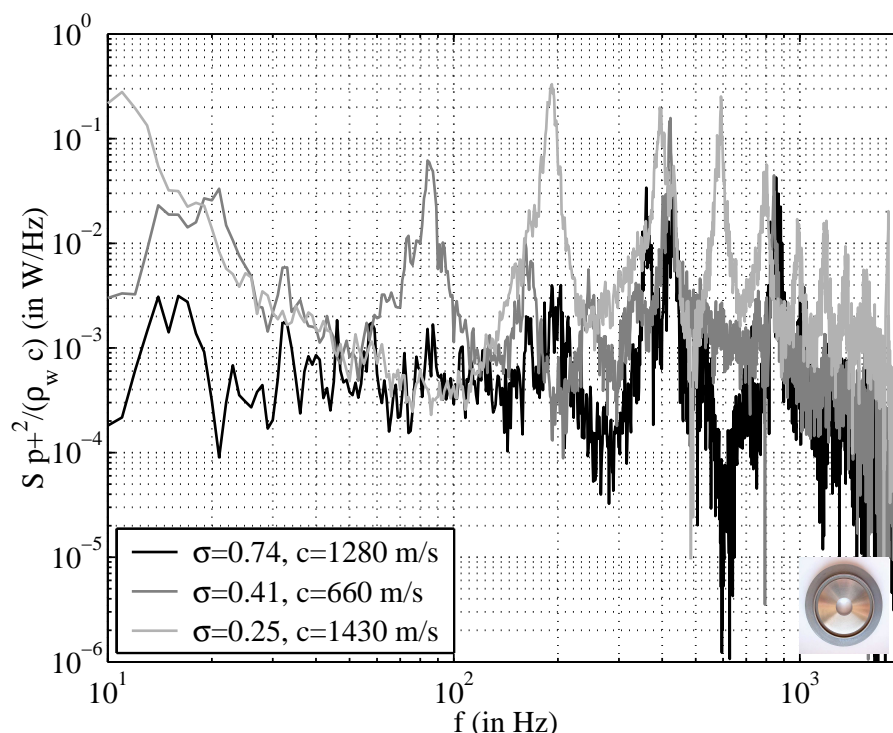


Figure 4.20: Acoustical power spectra in developed cavitation (single-hole orifice).

Of course, this representation is no more valid for the discrete frequencies which are whistling harmonics and resonance frequencies, as the backward propagating wave has great influence in those cases.

The acoustical power spectra obtained downstream of the orifice for the developed cavitation regime are given in Fig. 4.20 for the single-hole orifice and in Fig. 4.21 for the multi-hole orifice. The rejection frequency corresponding to a wavelength of half of the distance between two successive transducers and depending on the measured speed of sound has been excluded from those results. The following observations are made on those spectra:

- spectra exhibit a hump form in the upper frequency range (above 200 Hz); this hump form is typical of cavitation noise (Martin et al., 1981; Brennen, 1995);
- the single-hole orifice generates remarkably much more noise (by a factor of about 10^2 in the

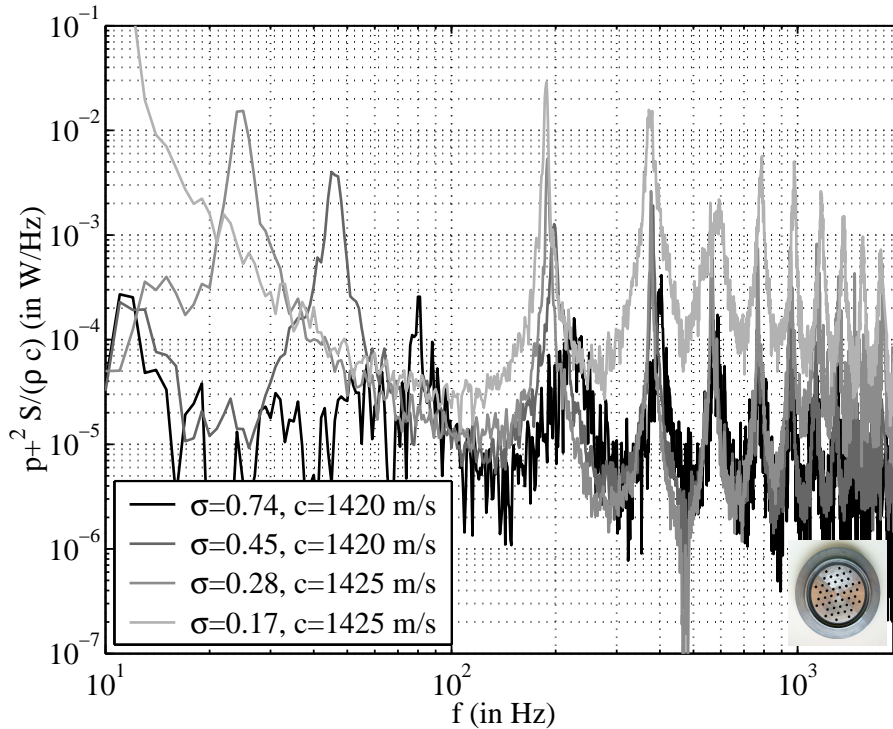


Figure 4.21: Acoustical power spectra in developed cavitation (multi-hole orifice).

acoustical power) than the multi-hole orifice.

4.4.3 Nondimensional analysis and representation

4.4.3.1 Choice of the scaling variables for the noise spectra

Scaling is proposed in order to obtain a dimensionless representation of the acoustical source power.

Cavitation noise from the implosions of bubbles is assumed to be predominant in order to scale the noise spectra. Hence, broadband turbulence noise from the mixing region downstream, whistling and resonance frequencies are not taken into account to choose the scaling variables. This assumption of predominance of cavitation noise is globally valid, but seems to fail at low frequencies (in this work, below 200-300 Hz approximately). Also, it is assumed that whistling does not alter cavitation noise, generalizing the hypothesis that broadband noise is not affected by whistling [as shown in Verge (1995) for a flue organ pipe].

Following Blake (1986), the amplitude of noise produced by cavitation should be made dimensionless by dividing with the downstream pressure, and not the pressure drop, when using a Rayleigh-Plesset bubble dynamic model for a spherical isolated free bubble. However, ring vortices generated by an orifice are not isolated bubbles in free space, so that this scaling should not hold in the case of the present study, as it also does not for sheet cavitation on airfoils (Keller, 1994).

As we lack a precise model, the scaling data are chosen for the sake of simplicity: the basic idea, as shown in Fig. 4.22, relies on the fact that, in the developed cavitation regime, the bubbles are created

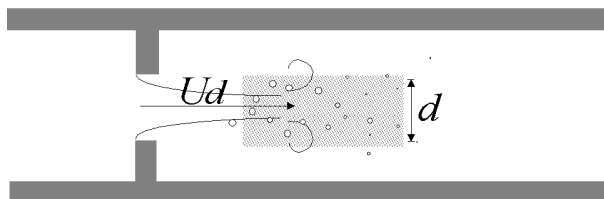


Figure 4.22: Choice of the variables d and U_d for the scaling of the noise spectra in the developed cavitation regime for the single-hole orifice.

in the mixing high-shear region of the jet.

For the single-hole orifice experiments, the velocity U_d and the orifice diameter d are representative of the conditions in this region, hence those quantities are used in order to scale the noise spectra in this regime. Furthermore, the scaling pressure is defined as the pressure drop ΔP across the orifice, which is a measure of the kinetic energy density in the jet. Hence for the single-hole orifice in developed cavitation, fd/U_d is the nondimensional frequency and $p^{+2}U_d/(\Delta P^2 d)$ is the nondimensional magnitude.

For the multi-hole orifice experiments, we assume the noise issuing from incoherent N_{holes} sources.

Each source represents the radiation of one hole. It radiates on a characteristic surface of S/N_{holes} . The strength of each source is assumed to be independent of the environment of the source. This assumption is natural, as we have previously supposed (see previous section) that the noise generated by the single-hole orifice does not depend on the diameter of the pipe. However, it should be pointed out that this assumption is wrong when whistling occurs.

In this model, the total acoustic power P measured downstream is a summation of the acoustic power $P_{\text{each source}}$ emitted by each source [the key element is that sources are supposed to be incoherent between each other, see Pierce (1981)]:

$$P = N_{\text{holes}} P_{\text{each source}}. \quad (4.15)$$

The acoustic power of each source $P_{\text{each source}}$ is, by definition, the total acoustic intensity flux I multiplied the surface of this source:

$$P_{\text{each source}} = I S/N_{\text{holes}}. \quad (4.16)$$

Hence the total acoustic power is

$$P = S I. \quad (4.17)$$

The total acoustic power is consequently independent of the number of holes. As previously, we ignore any downstream reflections, so that $I = p^{+2}/(\rho c)$.

This argumentation based on energy considerations can also be conducted in terms of forces: if the source is represented as a force acting on the orifice, taking the form $S p^+$, the total force imposed on the multi-hole orifice is due to the contribution of the forces imposed by N_{holes} equivalent single-hole orifices with open surface S/N_{holes} . Those forces are supposed to be uncorrelated with each other. Thus the total force squared equals N_{holes} times the force squared due to one hole. As the force

squared of one hole is $(p^+S/N_{\text{holes}})^2$, the total force squared is expressed as: $N_{\text{holes}}(p^+S/N_{\text{holes}})^2$, or by simplifying: $(p^+S)^2/N_{\text{holes}}$.

The scaling of the acoustic power is based on each source of surface S/N_{holes} . The scaling velocity is the velocity at the orifice, which is taken equal to the velocity of the single-hole orifice U_d , as the open surface of the two orifices are very similar, and the scaling length is the diameter of one hole d_{multi} . In conclusion for the multi-hole orifice in developed cavitation: fd_{multi}/U_d is the nondimensional frequency, and $p^{+2}U_d/(\Delta P^2 d_{\text{multi}})$ is the nondimensional magnitude.

4.4.3.2 Nondimensional noise spectra generated downstream

The dimensionless acoustical power spectra obtained downstream of the orifice for the developed cavitation regime are given in Fig. 4.23 for the single-hole orifice and in Fig. 4.24 for the multi-hole orifice. The following observations are worth noting.

- The scaling for the single-hole orifice and the multi-hole orifice is efficient as the nondimensional noise spectra collapse for each orifice. This is illustrated in Fig. 4.23 for the single-hole orifice and Fig. 4.24 for the multi-hole orifice. Hence it is found that these spectra do not depend significantly on the cavitation number or on the downstream speed of sound. However, the dispersion of the scaling variables is weak, so that additional data should be added to confirm this result.
- The different scaling used for the single-hole and the multi-hole orifice is rather efficient as it makes the levels of the two types of orifices closer to each other. However, the nondimensional level of noise of the single-hole orifice is still higher, with a ratio of 10, than the one of the multi-hole orifice experiments; see Figs. 4.23 and 4.24.
- We compare the cavitation noise with a standard turbulence noise from a noncavitating orifice in the low frequency range. Indeed, in this range of frequency, the level of noise is expected to be mainly determined by turbulence noise (Martin et al., 1981). We use a nondimensional turbulence noise level proposed by Moussou (2005). In this model, the scaling is based on empirical data obtained with simple singularities (single-hole orifice, valve) in water-pipe flow: the level of noise is assumed to depend only on a Strouhal number based on the pipe diameter and the pipe flow velocity. We apply this model with the values of the pipe diameter D and a pipe flow velocity of 2.20 m.s^{-1} and compare it to the single-hole orifice nondimensional noise, see Fig. 4.23. As expected, the turbulence level fits rather well the cavitation noise at low frequencies, with a good estimation of the slope; the cavitation noise is much stronger than the turbulence noise above the low-frequency range, which is a well-known result (Brennen, 1995).

4.5 Results in the super cavitation regime

4.5.1 Acoustic features

The super cavitation experiments exhibit two main differences compared to the developed cavitation experiments, as follows.

- The downstream speed of sound appears to be quite constant during each experiment.

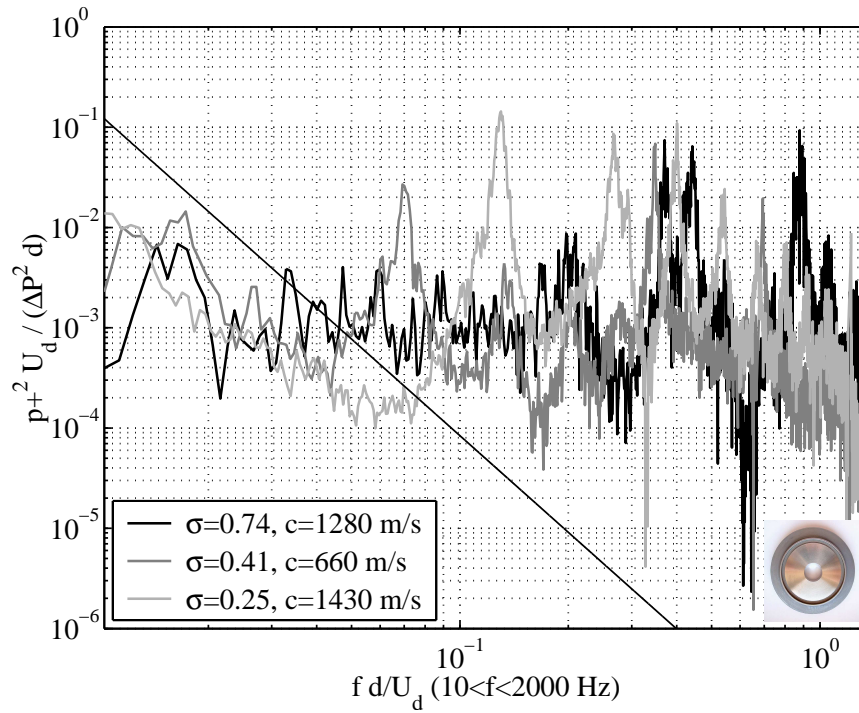


Figure 4.23: Non-dimensional acoustical power spectra in developed cavitation (single-hole orifice). Straight line: dimensionless turbulence level estimation of Moussou (2005).

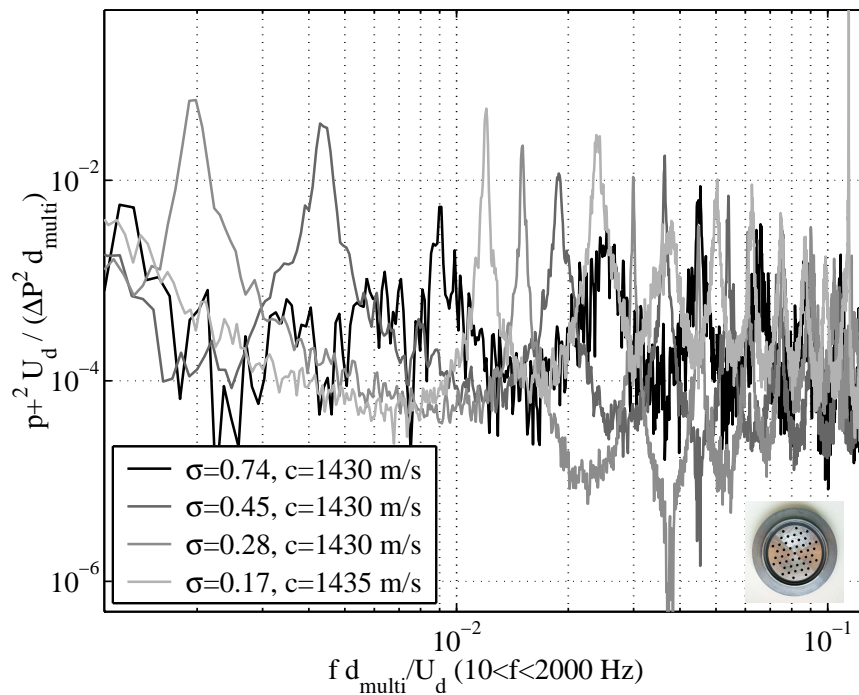


Figure 4.24: Non-dimensional acoustical power spectra in developed cavitation (multi-hole orifice).

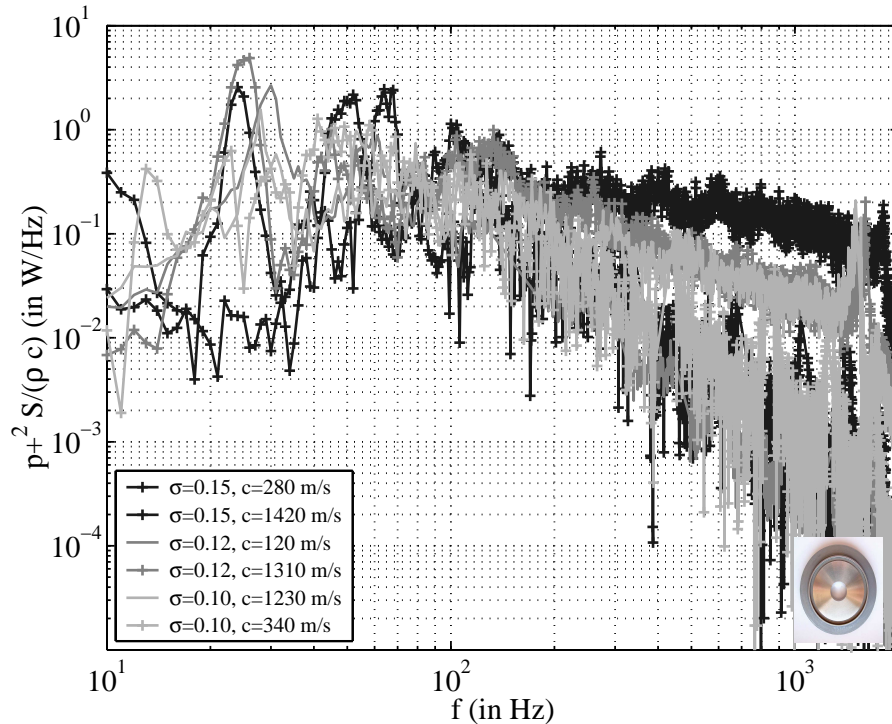


Figure 4.25: Acoustical power spectra in super cavitation (single-hole orifice).

- No resonance frequencies are found on downstream spectra. The downstream reflection coefficient is much lower than in the developed cavitation case (as previously shown in Fig. 4.7). In this case, the cavity of the downstream valve does not reflect the acoustic waves.

As for the developed cavitation case, strong acoustic uncoupling is observed from both sides of the orifice. The effect is much more obvious here, with an average ratio between downstream and upstream power spectra of about 2 to 30 for the single-hole orifice case, and about 10 to 50 for the multi-hole orifice case.

4.5.2 Noise spectra generated downstream

Noise spectra obtained downstream are given in Fig. 4.25 for the single-hole orifice and in Fig. 4.26 for the multi-hole orifice (as previously, the rejection frequencies being excluded). We note the following points.

- The typical cavitation hump form is observed, as in the developed cavitation case, but with much more evidence. The level of the hump is higher than for the developed cavitation regime; also, the frequency peak is smaller: those tendencies when the cavitation number increases confirm literature data (Brennen, 1995).
- Also, as in the developed cavitation case, the single-hole orifice is clearly more noisy (with an approximate factor of 10 on acoustical power spectra) than the multi-hole orifice.

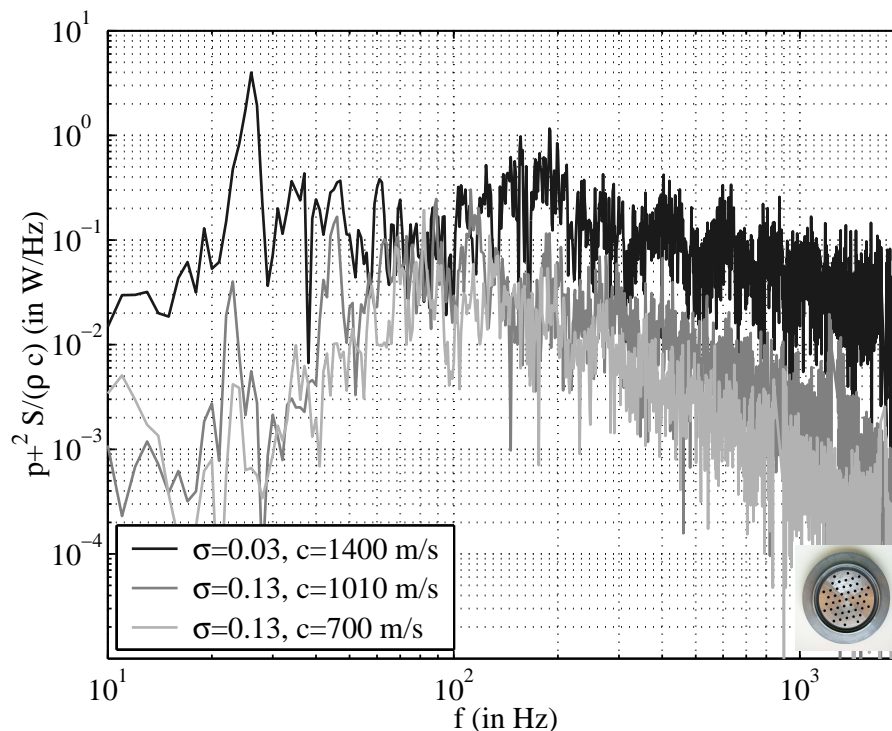


Figure 4.26: Acoustical power spectra in super cavitation (multi-hole orifice).

An important result is illustrated in Figs. 4.26 and 4.27: the part of the spectra succeeding the hump peak frequency depend strongly on the downstream speed of sound. Two-phase flow attenuations phenomena are supposed to be the cause of this observation.

4.6 Conclusion

A single-hole and a multi-hole cavitating orifice in a water pipe have been studied experimentally under industrial conditions, i.e., with a pressure drop varying from 3 to 30 bars and a cavitation number in the range $0.03 \leq \sigma \leq 0.74$.

In the regime of developed cavitation, whistling is observed for the single-hole orifice. This occurs at a Strouhal number based on the orifice thickness with a value close to 0.2.

Our results indicate that in the developed cavitation regime, a multi-hole orifice is much more silent than a single-hole orifice with the same total cross-sectional opening. This might be partially explained by the absence of correlation between the sound produced by different holes in the absence of whistling. No such difference is found in super cavitation. This is explained by the fact that, in the super cavitation regime, sound is produced far downstream of the orifice rather than in a near region downstream of the orifice.

A nondimensional noise source is proposed for the developed cavitation regime (cf. Section 4.4.3). The source model seems satisfactory for the developed cavitation case.

The results presented are certainly limited and call for further research. In particular, it could be

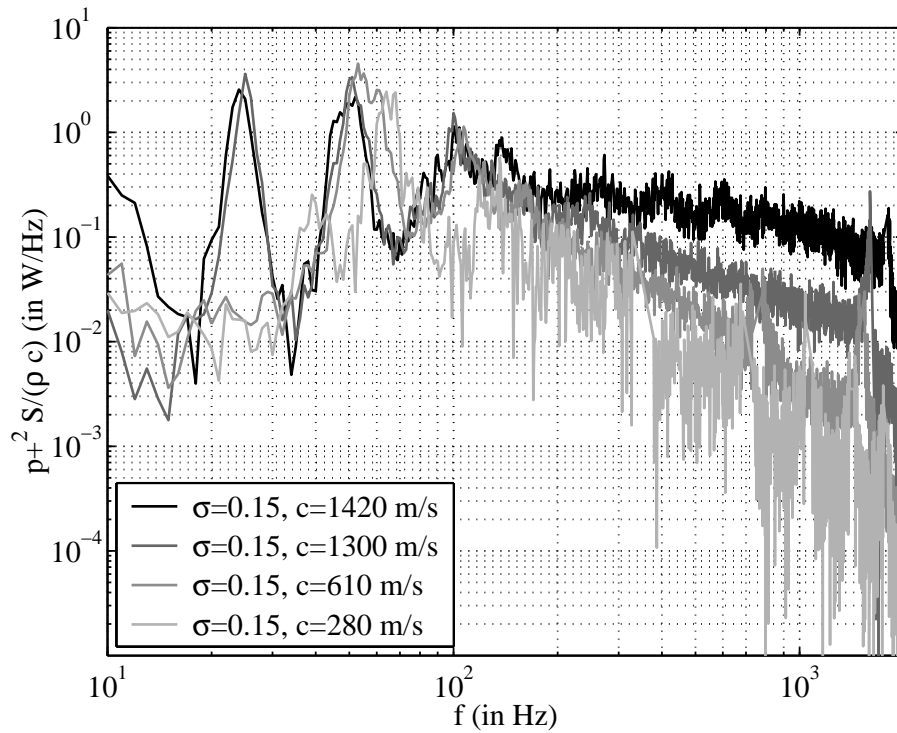


Figure 4.27: Supercavitation (single-hole orifice): influence of the speed of sound on the noise spectra.

interesting to vary the shape of the orifices and repeat the experiments with degassed water.

Bibliography

- Anderson, A. B. C., 1953. A circular-orifice number describing dependency of primary Pfeifenton frequency on differential pressure, gas density and orifice geometry. *Journal of the Acoustical Society of America*, 25, 626-631.
- Archer, A., Boyer, A., Nimanbeg, N., L'Exact, C., Lemerrier, S., 2002. Résultats des essais hydrauliques et hydroacoustiques du tronçon PTR 900 sur la boucle EPOCA (in French). EDF R&D, Technical Note HI-85/02/023/A, France.
- Au-Yang, M. K., 2001. *Flow-Induced Vibration of Power and Process Plant Components: a Practical Workbook*. ASME Press, New-York.
- Ball, J. W., Tullis, J. P., Stripling, T., 1975. Predicting cavitation in sudden enlargements. *ASCE Journal of the Hydraulics Division*, 101, 857-870.
- Bendat, J. S., Piersol, A. G., 1986. *Random Data - Analysis and Measurement Procedures* (2nd Edition). Wiley-Interscience Ed., ISBN 0-471-04000-2.
- Bistafa, S. R., Lauchle, G. C., Reethof, G., 1989. Noise generated by cavitation orifice plates. *ASME Journal of Fluids Engineering* 111, 278-289.
- Blake, W. K., 1986. *Mechanics of Flow-Induced Sound and Vibration* (Vol. II). Academic Press, Orlando.
- Blake, W. K., Powell, A., 1983. The development of contemporary views of flow-tone generation. In *Recent Advances in Aeroacoustics*, Springer-Verlag, New York.
- Blevins, R., 1984. *Applied Fluid dynamics handbook*. Krieger Ed., ISBN 0-89464-717-2.
- Bodén, H., Abom, M., 1986. Influence of errors on the two-microphone method for acoustic properties in ducts. *Journal of the Acoustical Society of America* 79 (2).
- Brennen, C. E., 1995. *Cavitation and bubble dynamics*. Oxford University Press.
- Caillaud, S., Gibert, J. R., Moussou, P., Cohen, J., Millet, F., 2006. Effect on pipe vibrations of cavitation in an orifice and in globe-style valves. In *ASME Pressure Vessels and Piping Division Conference, Proceedings PVP2006-ICPVT11-93882*, Vancouver, Canada.
- Davies, P. O. A. L., Bhattacharva, M., Bento Coelho, J. L., 1980. Measurement of plane wave acoustic fields in flow ducts. *Journal of Sound and Vibration* 72 (4), 539-542.

- Durrieu, P., Hofmans, G., Ajello, G., Boot, R., Aurégan, Y., Hirschberg, A., Peters, M. C. A. M., 2001. Quasisteady aero-acoustic response of orifices. *Journal of the Acoustical Society of America* 110 (4), 1859-1872.
- Esipov, I. B., Naugol'nykh, K. A., 1975. Cavitation noise in submerged jets. *Soviet Physics Acoustics* 21 (4), 404-405.
- Franklin, R. E. and McMillan, J., 1984. Noise generation in cavitating flows, the submerged jet. *ASME Journal of Fluids Engineering* 106, 336-341.
- Franc, J. P., Avellan, F., Belahadji, B., Billard, J. Y., Briançon-Marjollet, L., Fréchou, D., Fruman, D. H., Karimi, A., Kueny, J. L., Michel, J. M., 1999. *La cavitation* (in French). ISBN 2.7061.0605.0, Presses Universitaires de Grenoble.
- Fletcher, N. H., 1979. Excitation Mechanisms in Woodwind and Brass Instruments, *Acustica* 43 (1), 63-72.
- Gilbarg, G., 1960. Jets and cavities. In *Handbuch der Physik* (Vol. 9), Pflügge, S. (Ed.), Springer, 311-445.
- Hassis, H., 1999. Noise caused by cavitating butterfly and monovar valves. *Journal of Sound and Vibration* 225, 515-526.
- Idel'cik, I. E., 1969. *Memento des pertes de charge* (in French). Eyrolles Ed., Paris.
- Jorgensen, D. W., 1961. Noise from cavitating submerged water jets. *Journal of the Acoustical Society of America* 33 (10), 1334-1338.
- Keller, A. P., 1994. New Scaling Laws for Hydrodynamic Cavitation Inception. In 2nd Inter. Symp. On Cavitation (2), Tokyo, Japan, 327-334.
- Kim, B. C., Pak, B. C., Cho, C. H., Chi, D. S., Choi, H. M., Choi, Y. M., Park, K. A., Effects of cavitation and plate thickness on small diameter ratio orifice meters. *Flow Measurement and Instrumentation* 8, 85-92.
- Kugou, N., Matsuda, H., Izuchi, H., Miyamoto, H., Yamazaki, A., Ogasawara, M., 1996. Cavitation characteristics of restriction orifices, *ASME Fluids Engineering Division Conference, FED-Vol. 236* (1), San Diego, California, 457-462.
- Latorre, R., 1997. Bubble cavitation noise and the cavitation noise spectrum. *Acta Acustica* 83, 424-429.
- Lecoffre, Y., 1994. *La cavitation, traqueurs de bulles* (in French). Hermes Ed., Paris, ISBN 2-86601-409-X.
- Lighthill, J., 1978. *Waves in Fluids*. Cambridge University Press.
- Martin, C. S., Medlarz, H., Wiggert, D. C., Brennen, C. E., 1981. Cavitation inception in spool valves. *ASME Journal of Fluids Engineering* 103, 564-576.

- Morfeý, C. L., 1971. Acoustic energy in non-uniform flows. *J. Sound Vib.* 14 (2), 159-170.
- Moussou, P., Cambier, C., Lachene, D., Longarini, S., Paulhiac, L., Villouvier, V., 2001. Vibration investigation of a French PWR power plant piping system caused by cavitating butterfly valves. In PVP-Vol. 420-2, *Flow-Induced Vibration: Axial Flow, Piping Systems, Other Topics*, 99-106, ASME Press.
- Moussou, P., Caillaud, L., Villouvier, V., Archer, A., Boyer, A., Rechu, B., Benazet, S., 2003. Vortex-shedding of a multi-hole orifice synchronized to an acoustic cavity in a PWR piping system. In PVP-Vol. 465, *Flow-Induced Vibration PVP2003-2086*, 161-168, ASME Press.
- Moussou, P., Lafon, Ph., Potapov, S., Paulhiac, L., Tijsseling, A., 2004. Industrial cases of FSI due to internal flows. In 9th International conference on pressure surges, Chester (UK), Volume 1, 167-184, BHR Group Limited.
- Moussou, P., 2005. An attempt to scale the vibration of water pipes. Proceedings 71217 of PVP, ASME, Denver, Colorado, USA.
- Numachi, F., Yamabe, M., Oba, R., 1960. Cavitation effect on the discharge coefficient of the sharp-edged orifice plate. *ASME Journal of Basic Engineering*, 1-11.
- Pan, S. S., Xiang, T., Wu, B., 2001. Investigating to Cavitation Behavior of Orifice Tunnel. CAV2001, 4th Symposium on Cavitation, California Institute of Technology, Pasadena, USA (<http://cav2001.library.caltech.edu/222>).
- Pierce, A. D., 1981. *Acoustics: An Introduction to Its Physical Principles and Applications*. McGraw-Hill Book Company, Inc., New York.
- Rockwell, D., naudascher, E., 1979. Self-sustained oscillations of impinging free shear layers. *Annual Review of Fluid Mechanics* 11, 67-94.
- Sato, K., Saito, Y., 2001. Unstable Cavitation Behavior in a Circular-Cylindrical Orifice Flow. CAV2001, 4th Symposium on Cavitation, California Institute of Technology, Pasadena, USA (<http://cav2001.library.caltech.edu/318>).
- Tullis, J. P., Asce, M., Govindajaran, R., 1973. Cavitation and size scale effects for orifices. *ASCE Journal of the Hydraulics Division*, 417-430.
- Tullis, J. P., 1989. *Hydraulics of Pipelines: Pumps, Valves, Cavitation, Transients*. Wiley Interscience Ed., New York.
- Verge, M. P., 1995. *Aeroacoustics of confined jets*. Thesis, Technische Universiteit Eindhoven, the Netherlands, ISBN-90-386-0306-1.
- Van Wijngaarden, L., 1972. One-dimensional flow of liquids containing small gas bubbles. *Journal of Fluid Mechanics* 16, 369-396.

- Weaver, D. S., Ziada, S., Au-Yang, M. K., Chen S. S., Païdoussis, M. P., Petitgrew, M. J., 2000. Flow-Induced Vibration of Power and Process Plant Components: Progress and Prospects. ASME Journal of Pressure Vessel Technology, 122, 339-348.
- Yan, Y., Thorpe, R. B., Pandit, A. B., 1988. Cavitation noise and its suppression by air in orifice flow. In Symposium on Flow-Induced Noise, Chicago, Ill., Vol. 6, 25-39, ASME, New-York.
- Yan, Y., and Thorpe, R. B., 1990. Flow regime transitions due to cavitation in the flow through an orifice. Int. J. Multiphase Flow, 16 (6), 1023-1045.
- Young, F. R., 1999. Cavitation. Imperial College Press, London, ISBN 1-86094-198-2.

Chapter 5

End correction of single expansions and orifices

5.1 Introduction

This chapter is a preliminary investigation of the model of acoustic end correction, for single expansions and circular centred orifices.

Simple singularities (like expansions, restrictions and orifices) in duct without flow can be featured for their inertial acoustical effects at low frequency by a so-called end correction, using an incompressible and no dissipative model. The end correction represents the acoustic inertance of the orifice, that is, the real part of the acoustic inductance (the imaginary part, the acoustic reactance, represents the dissipation by viscosity, and is not studied in the model). We assume in this study that there is no reflection from both sides of the singularity considered. This represents a secondary correction to be taken into account, for example in industrial conditions.

Without flow, formulas exist in literature to estimate the end correction of single expansions, in a low frequency approximation. It is interesting to compare those formulas with our multimodal calculations for single expansions, and to compare them with our experimental results on orifices without flow.

With flow, very few results exist in literature. We present results obtained and try to understand them by use of the preceding non-flow models.

No clear understanding of the phenomena observed has been obtained in presence of flow, due to the complexity of the behaviour of the end correction. However, we have found interesting to report the most significant behaviours encountered. Consequently, this section of end correction with flow brings experimental observations.

5.2 End correction: single expansion without flow

5.2.1 Model of end correction: single expansion without flow

A single expansion is considered (illustrated in Fig 5.1). It is constituted by a first duct of radius a (section S_1), followed by a duct of radius $b > a$ (section S_2). We introduce the model of end correction for this single expansion, following Pierce (1981); Kergomard and Garcia (1986); Rienstra

and Hirschberg (2003).

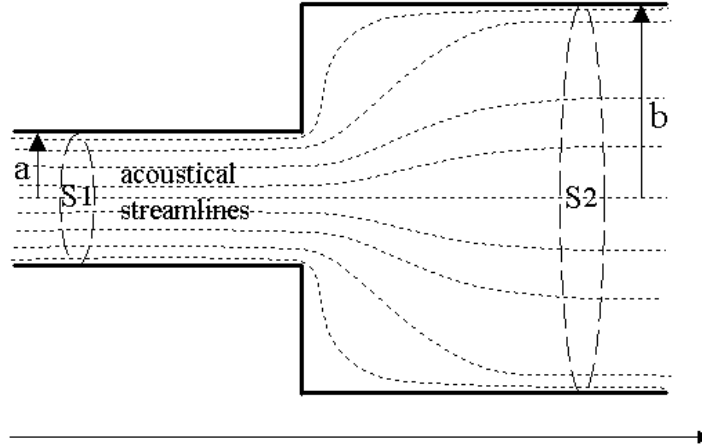


Figure 5.1: Single expansion in duct without flow.

The flow is assumed to be incompressible. Hence the equation of conservation of mass, at first order, is written:

$$S_1 u'_1 = S_2 u'_2 = Q. \quad (5.1)$$

As a simple model, the momentum conservation equation is written:

$$p'_1 = p'_2 + j\omega LQ, \quad (5.2)$$

where L is the acoustic inertance (real number) of the orifice, expressed in $kg\ m^{-2}$ (the quantity La/ρ_0 is non-dimensional). The acoustic inertance represents the effects due to inertia (that is, the non uniformity of the streamlines). The end correction Δl (real number expressed in m) is linked to the acoustic inertance with:

$$\Delta l = S_1 \frac{L}{\rho_0} \quad (5.3)$$

This model can be physically interpreted as the following (see illustration in Fig. 5.2): the acoustical air mass $m' = L S_1$ vibrates due to the pressure difference $p'_1 - p'_2$ across the orifice, while the fluid density and the acoustical flow rate are constant from both sides of the orifice. This acoustical air mass is localized at the discontinuity of sections: no phase shift is taken into account in this model, hence the singularity is considered as acoustically compact: this is a low frequency model.

5.2.2 Determination of the end correction from multimodal calculation: single expansion without flow

The end correction is calculated with the multimodal method on single expansion. The method to obtain the end correction from the calculations is explained in the following.

Plane-wave propagation in both ducts is assumed, so that:

$$p'_1 = P_1^+ + P_1^-, \quad p'_2 = P_2^+ + P_2^-, \quad (5.4)$$

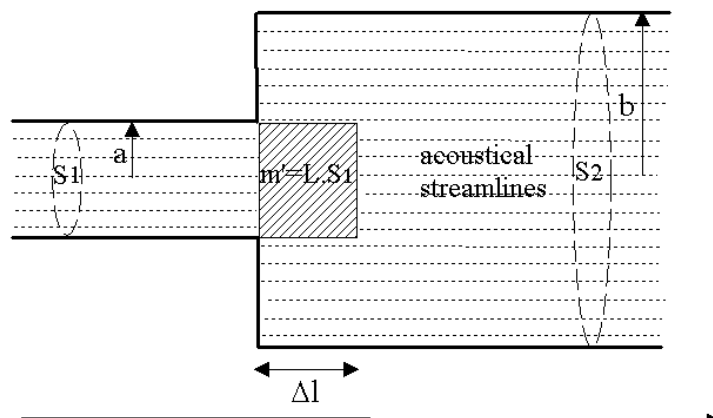


Figure 5.2: Model of end correction for a single expansion in duct.

$$u'_1 = \frac{P_1^+ - P_1^-}{\rho_0 c_0}, \quad u'_2 = \frac{P_2^+ - P_2^-}{\rho_0 c_0}, \quad (5.5)$$

with $\rho_0 = 1.1 \text{ kg m}^{-3}$ and $c_0 = 343 \text{ m s}^{-1}$ in air at $T = 293\text{K}$.

The end correction is determined from the scattering matrix coefficients using the following relations (the equations of the model, Eqs. 5.1 and 5.2, are combined with the previous equations, Eqs. 5.4 and 5.5):

$$\Delta l = \frac{-2c_0}{\gamma\omega} \Re\left(\frac{j}{T^+}\right) = \frac{-2c_0}{\omega} \Re\left(\frac{j}{T^-}\right), \quad (5.6)$$

$$= \frac{-2c_0}{\omega} \Re\left(\frac{j}{1-R^+}\right) = \frac{-2c_0}{\gamma\omega} \Re\left(\frac{j}{1-R^-}\right), \quad (5.7)$$

where $\Re(X)$ is the real part of X , and $\gamma = \frac{S_2}{S_1}$ is the ratio of sections. These four equations are four different means to determine the end correction. The model assumes them to be identical.

5.2.3 Literature data: single expansion without flow

Analytical formulas are known from literature, in the vanishing Helmholtz number limit:

- single expansion: $\alpha = a/b$

A modal decomposition method can be used to estimate the end correction analytically. A simplified decomposition method (with six modes) is presented in Aurégan et al. (2001), giving the formula:

$$\frac{\Delta l_{Auregan}}{a} = \sqrt{\frac{(1-\alpha)^2(1-\alpha^2)(15-2\alpha-\alpha^2)}{24}} \quad \text{when } ka \rightarrow 0. \quad (5.8)$$

This formula gives results close to those obtained from an exact decomposition method Kergomard and Garcia (1986);

- infinite downstream section: $\alpha \rightarrow 0$

This is called in literature duct with infinite baffle, or duct with a flanged opening. The model of Rayleigh gives an analytical formula for the end correction (Rayleigh, 1896; Pierce, 1981):

$$\frac{\Delta l_{Rayleigh}}{a} = 0.8282, \text{ when } ka \rightarrow 0. \quad (5.9)$$

5.2.4 Numerical results: single expansion without flow

In this section, we compare the calculations with these formulas.

Results are presented in Fig. 5.3 for very low frequency. Our calculations are converged with 20 modes, as the Mach number and the frequency are very low. Also, the determination from the four scattering matrix coefficients gives very similar results. Values obtained are in good agreement with the analytical formulas, with a slight under-estimation of the end correction compared to the exact and simplified decomposition method. The limit for $\alpha \rightarrow 0$ is well obtained in calculations.

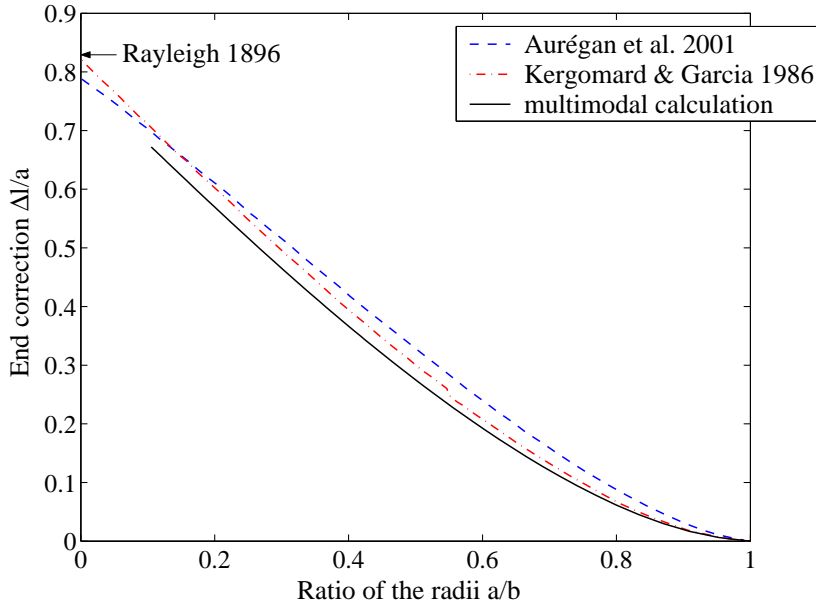


Figure 5.3: End correction for single expansion without flow, in the low frequency limit $ka \rightarrow 0$ - numerical calculations with $M_0 = 10^{-4}$, $ka = 10^{-4}$, $N = 20$.

Results are illustrated in Fig. 5.4 when varying the frequency. It appears that the end correction increases significantly, up to reach a maximum at the first cut-off frequency of the second duct.

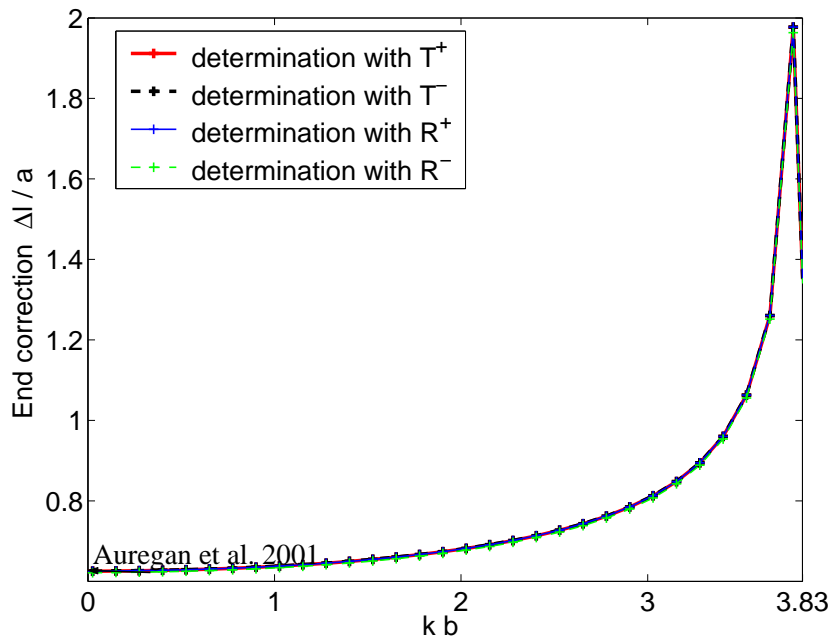


Figure 5.4: End correction for single expansion with flow - numerical calculation with $a/b = 0.18$, $M_0 = 10^{-4}$, $N = 15$.

5.3 End correction: orifice without flow

5.3.1 Determination of the end correction from measurements: orifice without flow

The end correction model is applied to orifices. Our experimental data on circular centred orifices are used. We recall that those results of the scattering matrix coefficients have been presented in chapter 1 and have been obtained with a sufficiently low excitation frequency so as it corresponds to a linear response of the orifice.

The orifice is seen as a succession of a restriction and an expansion. The model of end correction can be applied to a restriction without change, except the section ratio is inverse. Hence the end correction is determined using the equations used for a single expansion (Eqs. 5.6 and 5.7), taking $\gamma = 1$. The end correction hence obtained corresponds to an oscillating mass in the pipe section. To get an oscillating mass in the orifice section, we have to multiply the result by the ratio of the sections S_d/S_p (S_p is the pipe cross-section, S_d the orifice cross-section), so that:

$$\Delta l = = \frac{S_d - 2c_0}{S_p} \frac{1}{\omega} \Re \left(\frac{j}{T^+} \right) = \frac{S_d - 2c_0}{S_p} \frac{1}{\omega} \Re \left(\frac{j}{T^-} \right), \quad (5.10)$$

$$= \frac{S_d - 2c_0}{S_p} \frac{1}{\omega} \Re \left(\frac{j}{1 - R^+} \right) = \frac{S_d - 2c_0}{S_p} \frac{1}{\omega} \Re \left(\frac{j}{1 - R^-} \right). \quad (5.11)$$

5.3.2 Literature data and models: orifice without flow

Models have been proposed in literature, discerning if the orifice is thin or thick (using t/a as the thickness-to-radius ratio of the orifice):

- thin orifice: $t/a \ll 1$

In this configuration, Rayleigh has calculated the velocity potential and obtained the end correction using the principle of minimum kinetic energy to obtain the acoustic inertance and the end correction (Rayleigh, 1896; Pierce, 1981):

$$\frac{\Delta l_{thin}}{a} = \pi/2, \text{ when } ka \rightarrow 0. \quad (5.12)$$

- thick orifice: $t/a \gg 1$

In this configuration, the orifice can be seen (following Pierce (1981)) as a succession of a restriction, followed by a length, about the thickness t of the orifice, on which the velocity potential is uniform and an expansion. The end correction is the sum of three components. The components of the restriction and the expansion are taken as the same, and we use the formula of Aurégan et al. (2001). The end correction of the uniform velocity potential zone is approximately the thickness of the orifice t , hence we obtain:

$$\frac{\Delta l_{thick}}{a} = \frac{t + 2\Delta l_{Auregan}}{a}, \text{ when } ka \rightarrow 0. \quad (5.13)$$

5.3.3 Experimental results: orifice without flow

Results are presented for circular-centred right-angled orifices (with $t = 5$ mm in Figs. 5.5, 5.6, 5.7, and with $t = 10$ mm in Figs. 5.8, 5.9, 5.10) and for an orifice with a bevel (Fig. 5.11). They are plotted in function of the Helmholtz number at the orifice $f a / c_0$.

Firstly, it is observed that end corrections are quite small, of the order of the millimetre. Hence variations due to measurement inaccuracies are visible (whereas those measurements are precise, and difficult to improve significantly). Also, the determination with the four coefficients does not give similar values. Both observations are certainly related, indicating a high sensitivity of the model to measurements inaccuracies.

Secondly, the correlation with the model for thick orifices is good. It systematically gives a better agreement than the Rayleigh formula for a thin orifice, for orifices such that $0.4 \leq t/a \leq 1.33$. Also, data are all the more close to the thick orifice model as the orifice is thick in experiments.

The end correction obtained for an orifice with a small rounded bevel upstream is presented in Fig. 5.11. Surprisingly, the behaviour seems identical to the one obtained for an orifice without bevel: no difference can be made. This observation would need more data to be validated.

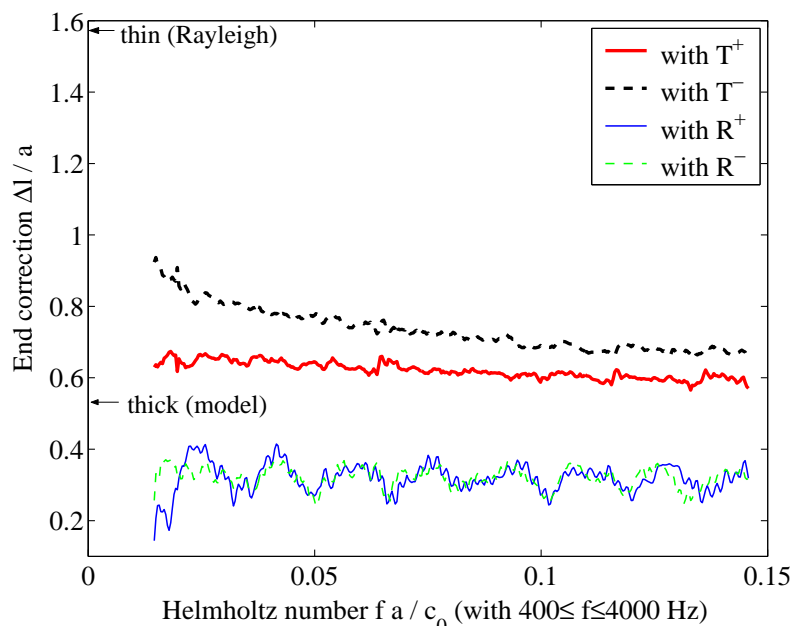


Figure 5.5: End correction for orifice without flow - experimental results with orifice $t = 5$ mm, $a = 12.5$ mm ($t/a = 0.40$).

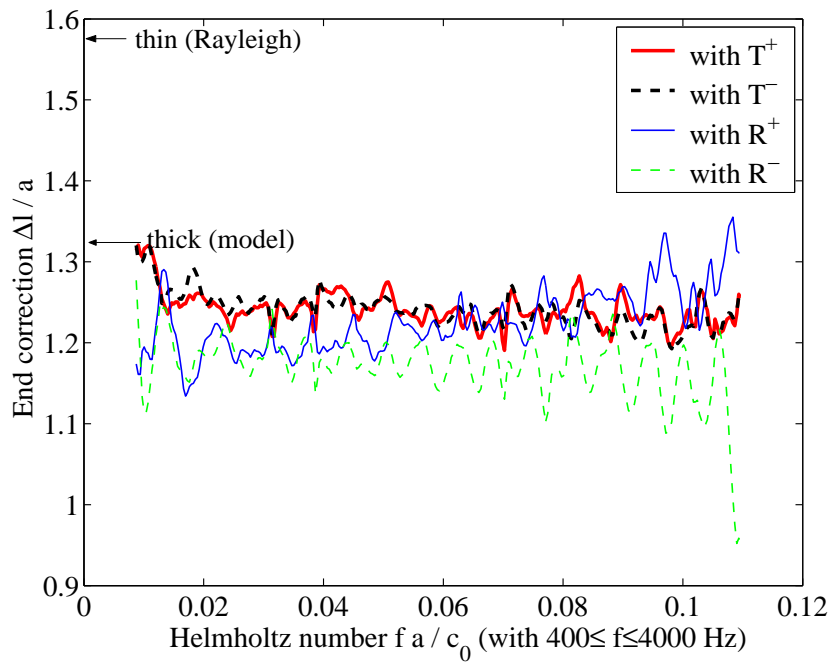


Figure 5.6: End correction for orifice without flow - experimental results with orifice $t = 5$ mm, $a = 7.5$ mm ($t/a = 0.66$).

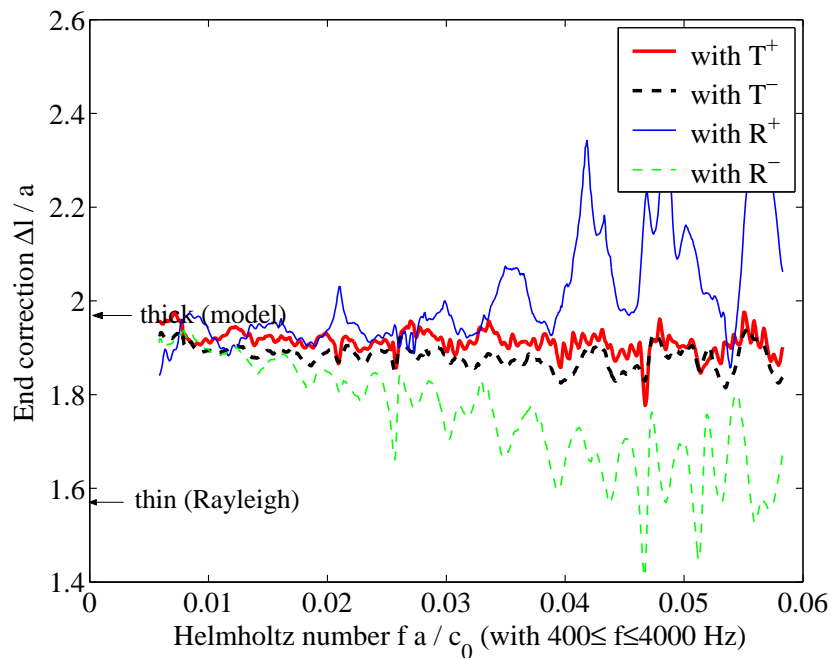


Figure 5.7: End correction for orifice without flow - experimental results with orifice $t = 5$ mm, $a = 5$ mm ($t/a = 1.00$).

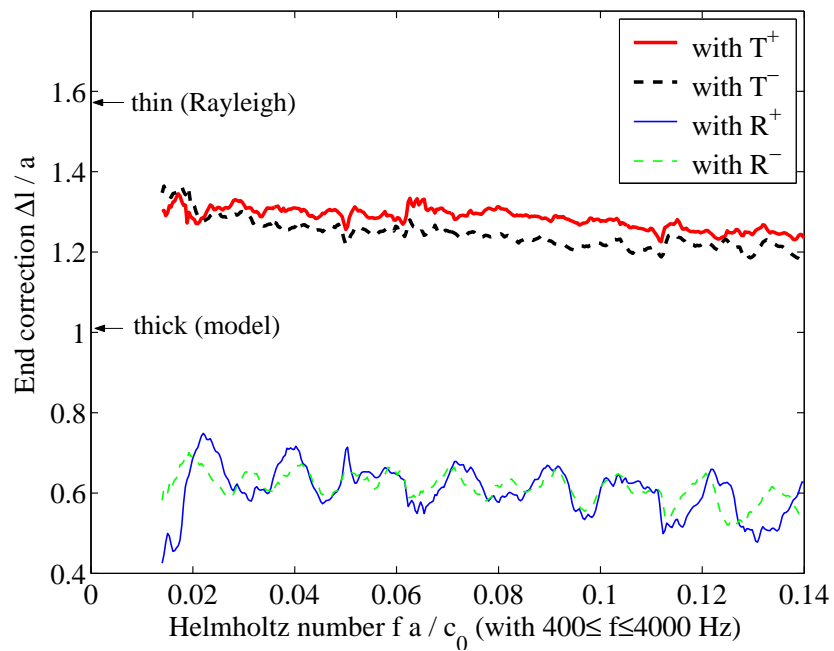


Figure 5.8: End correction for orifice without flow - experimental results with orifice $t = 10$ mm, $a = 12$ mm ($t/a = 0.84$).

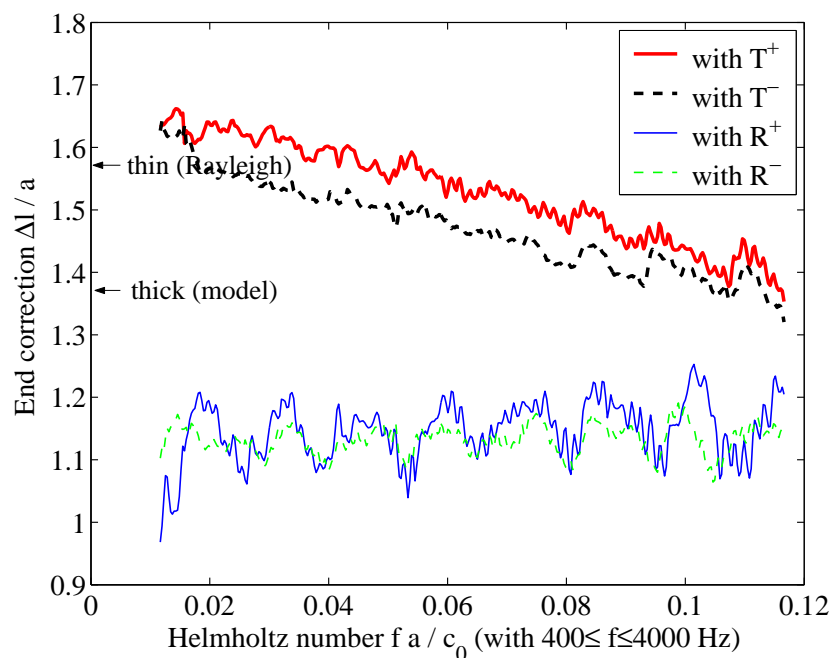


Figure 5.9: End correction for orifice without flow - experimental results with orifice $t = 10$ mm, $a = 10$ mm ($t/a = 1.00$).

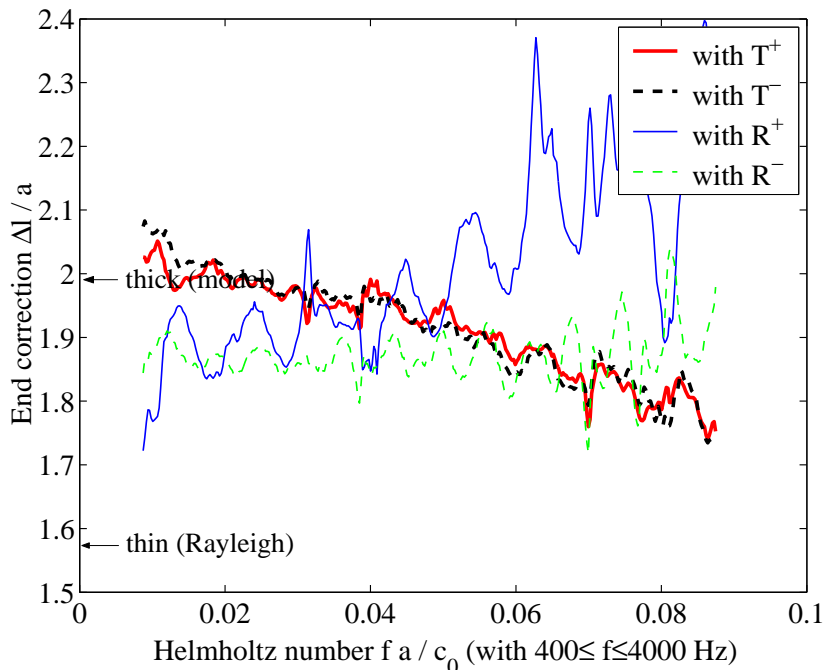


Figure 5.10: End correction for orifice without flow - experimental results with orifice $t = 10$ mm, $a = 7.5$ mm ($t/a = 1.33$).

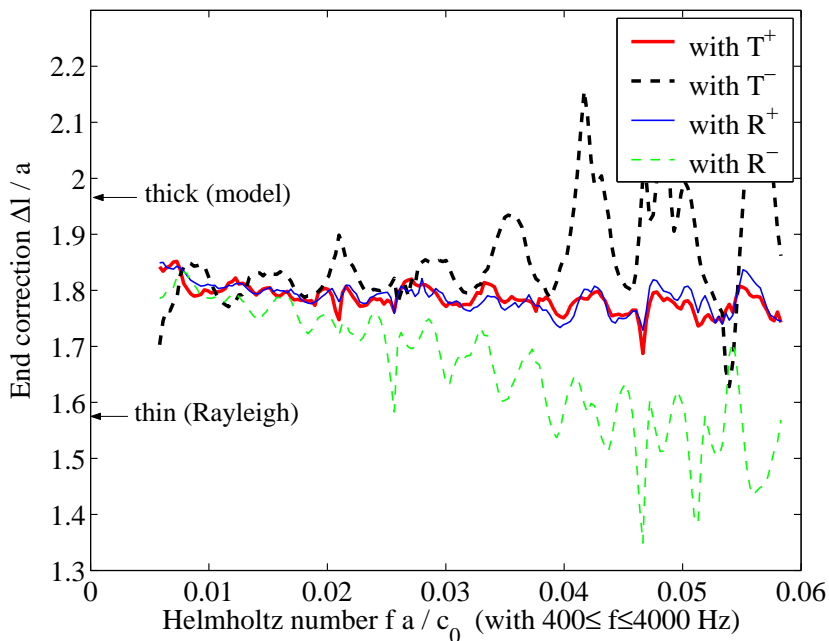


Figure 5.11: End correction for orifice without flow - experimental results with orifice with a small ($r = 1$ mm) rounded bevel upstream $t = 5$ mm, $a = 5$ mm ($t/a = 1$).

5.4 End correction: single expansion with flow

5.4.1 Model of end correction: single expansion with flow

The model of end correction is extended to a configuration with a constant mean flow M_0 . In this purpose, we use the ideas presented by Ajello (1997).

In presence of a mean flow, it is convenient to use the variables of the acoustical mass velocity m' and total acoustical enthalpy Π' (for more details, see section 1.3.2 in chapter one). One should note for example that, without flow, Π' corresponds to p'/ρ_0 and m' to $\rho_0 v'$. The extension of the model of end correction under constant mean flow is made with these new variables, as we define the equations to be:

$$m'_1 = m'_2, \quad (5.14)$$

$$\Pi'_1 = \Pi'_2 + j\omega L S_1 m'_1 / \rho_0^2, \quad (5.15)$$

where $m' = (\Pi^+ - \Pi^-)/c_0$ and $\Pi' = (\Pi^+ + \Pi^-)/\rho_0$ (with $\Pi^+ = (1 + M_0)P^+$, $\Pi^- = (1 - M_0)P^-$). These equations are identical to Eqs.5.1 and 5.2 when no flow is present. The end correction is defined as:

$$\Delta l = S_1 \frac{L}{\rho_0}. \quad (5.16)$$

5.4.2 Determination of the end correction from measurements: single expansion with flow

Using the above relations, the end correction Δl is determined from the four calculated scattering matrix coefficients. The expressions obtained are similar as for the non-flow case, except that the scattering matrix coefficients under mean flow are into account, so that:

$$\Delta l = = \frac{-2c_0}{\gamma\omega} \Re\left(\frac{j}{T_e^+}\right) = \frac{-2c_0}{\omega} \Re\left(\frac{j}{T_e^-}\right), \quad (5.17)$$

$$= \frac{-2c_0}{\omega} \Re\left(\frac{j}{1 - R_e^+}\right) = \frac{-2c_0}{\gamma\omega} \Re\left(\frac{j}{1 - R_e^-}\right), \quad (5.18)$$

where the scattering matrix coefficients under constant mean flow M_0 are defined as:

$$R_e^+ = \frac{1 + M_0}{1 - M_0} R^+, \quad R_e^- = \frac{1 - M_0}{1 + M_0} R^-, \quad (5.19)$$

$$T_e^+ = T^+, \quad T_e^- = T^-. \quad (5.20)$$

5.4.3 Literature data: single expansion with flow

For single expansion with flow, no literature theory has been found. We can only assume that in the high frequency limit $ka \rightarrow \infty$, the behaviour will follow the non-flow behaviour.

It should be pointed out however that for a different configuration, that is an exit of a duct with thin walls (flanged pipe termination), Rienstra (1983) has obtained a formula for the end correction in presence of flow, for small Mach numbers M_0 :

$$\frac{\Delta l_{Rienstra}}{a} = 0.2551 \sqrt{1 - M_0^2} \quad \text{when } ka \rightarrow 0 \text{ and } ka/M_0 \rightarrow 0. \quad (5.21)$$

5.4.4 Numerical results: single expansion with flow

Results obtained show a large dissimilarity of the four end corrections determined with the four scattering matrix coefficient, in the limit $ka/M_0 \rightarrow 0$. This work is in progress.

5.5 End correction: orifice with flow

5.5.1 Determination of the end correction from measurements: orifice with flow

The model of orifice end correction under constant mean flow is similar, in its ideas, to the model of the single expansion with flow.

The end correction for orifice under constant mean flow is obtained from measurements using:

$$\Delta l = = \frac{S_d - 2c_0}{S_p} \frac{1}{\omega} \Re \left(\frac{j}{T_e^+} \right) = \frac{S_d - 2c_0}{S_p} \frac{1}{\omega} \Re \left(\frac{j}{T_e^-} \right), \quad (5.22)$$

$$= \frac{S_d - 2c_0}{S_p} \frac{1}{\omega} \Re \left(\frac{j}{1 - R_e^+} \right) = \frac{S_d - 2c_0}{S_p} \frac{1}{\omega} \Re \left(\frac{j}{1 - R_e^-} \right). \quad (5.23)$$

5.5.2 Models using literature data: orifice with flow

No formulas are present in literature for end correction of orifice under constant flow. The difference with the non-flow case is that the flow forms a jet, which hence could change much the end correction compared to the non-flow case.

Even if no literature data are available on the subject, a physical analysis is proposed here to get simple formulas in the high and low Strouhal number limits. We separate the several contributions of the end correction: Δl_{up} is the end correction of the upstream part of the orifice, Δl_{down} of the downstream part. We use the variable of the Strouhal number at the orifice, fa/U_d (U_d is the orifice velocity), as it is demonstrated that, in presence of low, this variable should be preferred to the Helmholtz number ka (Rienstra, 1983):

- in the high Strouhal number limit: $ka/M_d \rightarrow \infty$

A behaviour similar to the non-flow case is expected: we use the formula corresponding to the limit $ka \rightarrow 0$, which gives $\Delta l_{up} = \Delta l_{down} = \Delta l_{Auregan}$, while the end correction within the orifice is approximately its thickness t , so that we assume:

$$\frac{\Delta l}{a} = \frac{\Delta l_{Auregan} + t + \Delta l_{Auregan}}{a}. \quad (5.24)$$

- in the low Strouhal number limit: $ka/M_d \rightarrow 0$

The effect of the upstream edge on the flow separation, and so on the end correction, is critical (Rienstra, 1983). Hence we differentiate the cases with the kind of the upstream edge of the orifice:

– **the upstream edge is a right angle**

The flow separates at the upstream edge. The end correction is assumed to be mainly due to the jet, hence $\Delta l_{up} = 0$, and the end correction due to the jet is assumed to follow Rienstra formula $\Delta l_{down} = \Delta l_{Rienstra}$ (which however does not correspond exactly to the

configuration). The thickness of the orifice has no effect on the end correction, as the flow is separated, and while there is no reattachment of the flow within the orifice. This is the case when the orifice is thin. When the orifice is thick, the reattachment of the flow is assumed to add an end correction approximately of the thickness of the orifice. Hence we assume:

$$\frac{\Delta l}{a} = \frac{\Delta l_{Rienstra}}{a}, \text{ thin orifice} \quad (5.25)$$

$$\frac{\Delta l}{a} = \frac{t + \Delta l_{Rienstra}}{a}, \text{ thick orifice} \quad (5.26)$$

– **the upstream edge is a bevel**

There is no flow separation at the upstream edge. The end correction upstream could be the same as a restriction without flow $\Delta l_{up} = \Delta l_{Auregan}$. The end correction downstream, where there is a jet, follows Rienstra formula $\Delta l_{down} = \Delta l_{Rienstra}$, and the end correction due to the orifice thickness is taken into account. Hence we assume:

$$\frac{\Delta l}{a} = \frac{\Delta l_{Auregan} + t + \Delta l_{Rienstra}}{a}. \quad (5.27)$$

5.5.3 Experimental results: orifice with flow

Comparison with our experimental data for circular-centred right-angled orifices with flow gives the following observations.

From data, we find that the evolution of the end correction is qualitatively the same for all orifices (Fig. 5.12 gives a typical example): in the low frequency limit, there is a threshold, followed by an increase of the end correction to attain a maximum, followed then by a decrease of the end correction to reach apparently a threshold limit.

For thin orifices (Fig. 5.12), the two limits proposed are satisfying. The high Strouhal number limit seems well obtained, but we lack higher frequency data to evaluate if the limit is really attained and draw definite conclusions. What is spectacular is how much the low Strouhal number limit is well obtained. This is spectacular, as the model proposed uses formula not corresponding to our configuration.

The effect of the thickness of the orifice is spectacular. It is illustrated in Fig. 5.13. When the orifice is thick, the end correction is much higher than for a thin orifice. Our model for thick orifice is systematically satisfying to fit well the data of thick orifices. As the difference is clear from the end correction value between a thin and a thick orifice, we can define experimentally thick orifices: they are found in the range $t/d \geq 2$, which is in agreement with literature (the flow re-attachment occurs for $t/d \geq 2$).

Similarly as in the non-flow case, results for orifices with a large diameter $d \geq 20$ mm give a discrepancy of the four values of the end correction determined by the four scattering matrix coefficients.

It is observed that for low Mach numbers, under $M_0 = 0.03$, the end correction shows systematically strong variations in the low Strouhal limit, as illustrated in Fig. 5.14.

Results for orifices with a bevel upstream show that our model in the low Strouhal limit is not well satisfied (Fig. 5.15). The correlation seems good when cancelling the upstream contribution of the end correction, that is with the end correction $\Delta l/a = (t + \Delta l_{Rienstra})/a$. However, this result needs further study, as few data are available (two orifices).

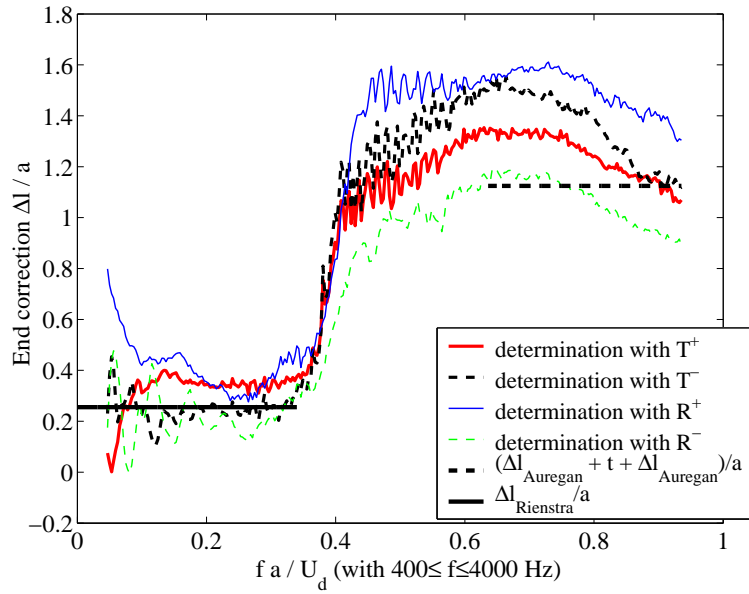


Figure 5.12: End correction with flow - thin orifice $t = 5$ mm, $a = 8.5$ mm ($t/a = 0.58$), $M_0 = 2.55 \cdot 10^{-2}$.

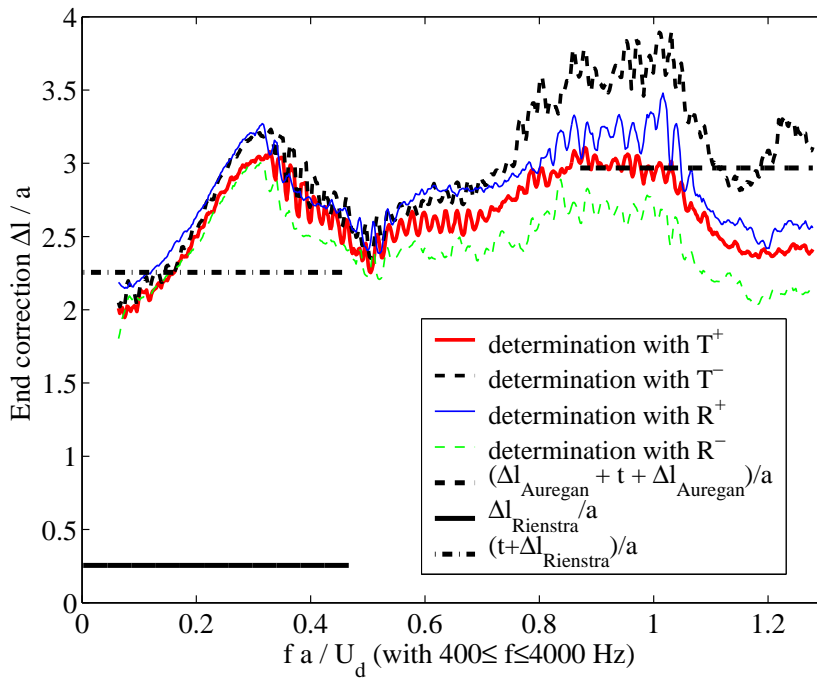


Figure 5.13: End correction with flow - thick orifice $t = 5$ mm, $a = 5$ mm ($t/a = 1$), $M_0 = 3.8 \cdot 10^{-3}$.

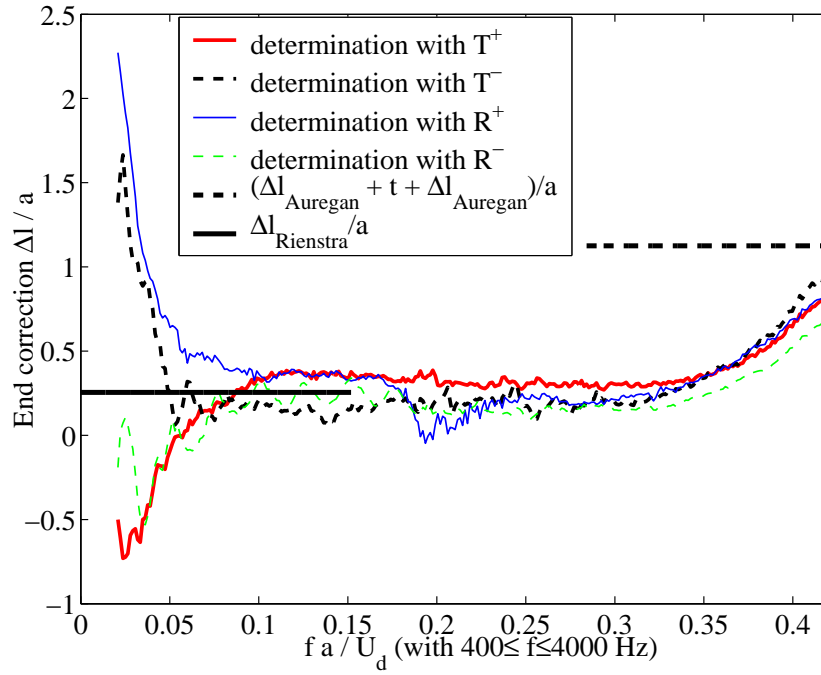


Figure 5.14: End correction with flow - thin orifice $t = 5$ mm, $a = 8.5$ mm ($t/a = 0.58$), $M_0 = 5.71 \cdot 10^{-2}$.

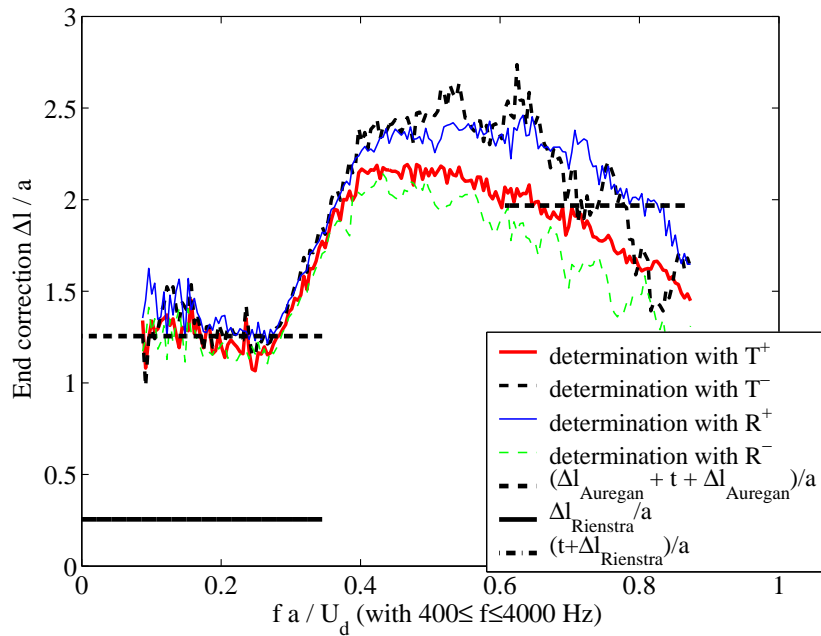


Figure 5.15: End correction with flow - thin orifice with bevel upstream (CCb2, $r_{bevel}/t = 0.2$) $t = 5$ mm, $a = 5$ mm, ($t/a = 1.00$), $M_0 = 7.4 \cdot 10^{-3}$.

As a result, we have reported those experimental observations on the end correction of orifices with flow. This is a difficult task, as the quantity of our data (around 60) showed that it is quite difficult to draw a common behaviour for all orifices, or to observe common behaviours between some of them. Indeed, the end correction with flow has a very complex behaviour, and it is difficult to understand the subtleties of such a model. Moreover, it is a simple model, developed without flow, so it is questionable whether it is sensible to understand it thoroughly in the case with flow.

5.6 Conclusion

The acoustic model of end correction is investigated for single expansions, using our numerical calculations, and for orifices, using our experimental data. We studied the non-flow case and the flow case.

Without flow, results are in good agreement with literature models both for orifices (experimental data) and single expansions (numerical calculations using the multimodal method).

In presence of a constant mean flow, experimental observations are reported for the end correction of circular centred orifices. In particular, good agreement is obtained with the literature models introduced, in the low and high Strouhal number limits, when differentiating the orifices into thin and thick ones. But for common frequencies, the behaviour of the end correction appears to be quite difficult to describe. It varies much from an orifice to another, and with the Mach number of the flow. Even if no clear understanding has been obtained, these experimental observations seem useful, as very scarce literature exist in this case with flow.

Bibliography

- G. Ajello. Mesures acoustiques dans les guides d'ondes en présence d'écoulement: mise au point d'un banc de mesure, application à des discontinuités. Thèse de doctorat de l'Université du Maine, Académie de Nantes, 1997 .
- Y. Aurégan, A. Debray, R. Starobinski. Low frequency sound propagation in a coaxial cylindrical duct : application to sudden area expansions and to dissipative silencers. *Journal of Sound and Vibration*, 243(3): 461-473, 2001.
- J. Kergomard, A. Garcia. Simple discontinuities in acoustic waveguides at low frequencies: critical analysis and formulae. *Journal of Sound and Vibration*, 114(3): 465-479, 1986.
- M.C.A.M. Peters, A. Hirschberg, A.J. Reijnen, A.P.J. Wijnands. Damping and reflection coefficient measurements for an open pipe at low Mach and low Helmholtz numbers. *Journal of Fluid Mechanics*, 256: 499-534, 1993.
- A. D. Pierce. *Acoustics: An Introduction to Its Physical Principles and Applications*. McGraw-Hill Book Company, New York, 1981.
- J. W. S. Rayleigh. *The theory of sound*. Vol. 2, 2nd Ed. Macmillan, 1986.
- S. W. Rienstra. A small Strouhal number analysis for acoustic wave-jet flow-pipe interaction. *Journal of Sound and Vibration*, 86: 539-556, 1983.
- S. W. Rienstra, A. Hirschberg. *An Introduction to Acoustics*, Eindhoven University of Technology, 2003.

Conclusion générale

Ce travail avait pour objectif de mieux comprendre les mécanismes de génération de bruit par les singularités d'écoulement en conduit, en régime fortement turbulent.

Nous nous sommes essentiellement intéressés au phénomène de sifflement, et partiellement au bruit de cavitation.

Résultats majeurs

Le résultat majeur de cette étude est constitué par la validation expérimentale d'un critère de sifflement de singularité en conduit sous écoulement. Ce critère utilise la mesure de la matrice de diffusion acoustique d'une singularité sous écoulement pour détecter les fréquences d'instabilité de cette configuration, dans l'hypothèse de propagation d'ondes planes dans les conduits. Nous avons testé en air sur la boucle du LAUM une large gamme (19) de diaphragmes circulaires centrés fins (avec un ratio d'épaisseur sur diamètre inférieur à 1.5). On montre qu'en conditions acoustiques réverbérantes dans le conduit, les fréquences de sifflement apparaissant sont ces fréquences d'instabilité prédites par le critère. Le grand intérêt de ce critère est sa simplicité théorique et sa relative facilité de mise en oeuvre industrielle.

Deux résultats importants ont été obtenus concernant la méthode numérique, appelée méthode multimodale, utilisée pour prédire le comportement aéroacoustique d'une configuration sifflante:

- le coefficient de réflexion R^+ d'un élargissement brusque sous écoulement est très bien prédit, en amplitude et en phase, par la méthode multimodale, par comparaison avec les données expérimentales existantes (Ronneberger). Comme les autres coefficients de la matrice de diffusion obtenus par cette méthode sont très proches de modèles analytiques simples dans la limite quasi-stationnaire, et dans la limite sans écoulement, on en déduit que cette méthode donne de façon satisfaisante la matrice de diffusion acoustique d'un élargissement brusque;
- les fréquences d'instabilité, obtenues par application du critère d'instabilité sur une configuration sifflante, constituée par une restriction continue de section suivie de deux élargissements brusques de section, sont bien prédites (<10% en erreur relative) par la méthode multimodale. La grande simplicité des modèles utilisés rend ce résultat intéressant. Les niveaux de ratio de puissance acoustique dissipée sont bien prédits dans les limites hautes et basses fréquences, et dans leur évolution qualitative.

Les analyses d'essais effectuées en eau, sur un diaphragme droit monotrou et un diaphragme droit multitrou, ont apporté un résultat important, du fait de la présence de sifflement détectée en régime de

faible cavitation pour le diaphragme droit monotrou. Les nombres Strouhal de sifflement observés sur cette boucle (en eau, diamètre du tuyau de 7.4 cm, pression statique aval de 2.7 bar) avec ceux obtenus sur la boucle du LAUM (en air, diamètre du tuyau 3 cm, pression statique aval 1 bar) sont similaires, entre 0.2 et 0.3 pour un nombre de Reynolds dans le tuyau supérieur à 10^4 . Cette comparaison indique que le nombre Strouhal ne varie pas sensiblement avec le diamètre du tuyau, la pression statique dans le tuyau et surtout la compressibilité du fluide. Ce sont ces paramètres qui n'ont pas été variés sur la boucle du LAUM.

Autres résultats

Nous détaillons dans la suite les résultats majeurs et nous présentons les autres résultats de ce travail.

Validation d'un critère de sifflement des singularités en conduit

Dans le premier chapitre, nous avons présenté l'étude expérimentale d'un critère de sifflement proposé par Aurégan and Starobinsky (1999) pour des singularités d'écoulement en conduit droit, en propagation d'ondes planes dans les tuyaux. Ce critère utilise la mesure de la matrice de diffusion acoustique de la singularité sous écoulement et consiste en un bilan acoustique de part et d'autre de la singularité, pour mettre en évidence les fréquences de production de puissance acoustique, nommées alors fréquences potentielles de sifflement ou fréquences d'instabilité. Cette étude a validé ce critère sur des diaphragmes droits circulaires centrés sans biseau, et aussi des diaphragmes avec biseau et quelques fentes décentrées.

Ce travail expérimental a mis en évidence, pour la première fois, des gammes de fréquence potentielle de sifflement (section 1.5.3). Ces fréquences potentielles de sifflement ont été systématiquement trouvées sur les diaphragmes droits, sauf à très faible écoulement et excepté les singularités connues pour être très peu sifflantes (diaphragmes avec biseaux à l'amont).

Des mesures de sifflement (section 1.7) ont permis de montrer que les fréquences de sifflement observées en configuration de type industrielle, c'est à dire sans source extérieure et avec des réflexions acoustiques de part et d'autre de la singularité, correspondent à ces fréquences d'instabilité. Dans une telle configuration, un modèle a été proposé (1.7.4), utilisant la mesure de la matrice de diffusion et la mesure des coefficients de réflexion amont et aval, permettant de prédire de façon satisfaisante l'existence de sifflement et la valeur de la fréquence de sifflement. Ce modèle nécessiterait toutefois une validation sur plus de données. Un autre modèle, inspirée du critère de Bode-Nyquist, ne donne pas de bons résultats, sans que nous en ayons bien compris la raison.

Nous avons montré que le nombre de Strouhal le plus satisfaisant pour adimensionnaliser les fréquences potentielles de sifflement est basé sur l'épaisseur du diaphragme et la vitesse d'écoulement au niveau de du diaphragme (section 1.5.3). Les valeurs obtenues sont remarquablement constantes pour les 19 diaphragmes fins testés (en variant l'épaisseur du diaphragme, son diamètre, et le nombre de Mach), lorsque l'écoulement est à turbulence pleinement développée (nombre de Reynolds supérieur à $5 \cdot 10^3$). Les nombres Strouhal de sifflement potentiel sont obtenus entre 0.2 et 0.3, ce qui est en très bon accord avec la littérature (mesures d'Anderson (1953)).

Nous montrons que la configuration géométrique du bord amont du diaphragme est très importante pour déterminer ou non son potentiel sifflant: si ce bord est biseauté, le diaphragme n'est plus sifflant.

Ce résultat est un accord avec la littérature existante sur ce sujet.

Nous montrons (section 1.5.5) que, pour créer l'instabilité, les ondes planes de pression incidentes sur la singularités doivent être de même amplitude et en opposition de phase. Cela correspond à une excitation en vitesse acoustique de la couche de cisaillement instable. Inversement, nous montrons qu'une excitation en ondes de pression en phase, correspondant à une excitation en pression acoustique au niveau de la couche de cisaillement du diaphragme, ne provoque ni production ni dissipation d'énergie acoustique. Ces résultats sont cohérents avec la littérature existante.

En conclusion de cette étude, une nouvelle méthodologie est applicable à EDF pour prédire les gammes de sifflement potentielles de singularité en conduit. Elle consiste à mesurer la matrice de diffusion de la singularité sous l'écoulement considéré, et à appliquer le critère de sifflement sur cette mesure (diagonalisation d'une matrice 2x2). L'avantage d'une telle méthode est sa simplicité, et le fait que la mesure de la matrice de diffusion soit indépendante des conditions aux limites de la boucle. Le résultat majeur est l'obtention de gammes de fréquences non-sifflantes, c'est à dire pour lesquelles la singularité ne sifflera jamais, quelles que soient les réflexions acoustiques dans le conduit. Si les conditions acoustiques dans le conduit sont connues, l'utilisation du modèle élémentaire de sifflement permet de prédire le sifflement ou le non-sifflement sur les gammes de fréquences de sifflement potentiel.

Validation d'une méthode de calcul pour prédire les fréquences potentielles de sifflement d'une expansion sifflante

Les chapitres 2 et 3 concernent la modélisation aéroacoustique d'élargissements brusques de section, par une méthode numérique appelée méthode multimodale.

Cette méthode de calcul numérique est une résolution modale des équations d'Euler linéarisées en régime harmonique établi, par un schéma aux différences finies (le plus simple). Les conditions de raccord des champs acoustiques permettent d'obtenir la matrice de diffusion de l'ensemble. La méthode donne les champs acoustiques en tous points et la matrice de diffusion acoustique de la configuration étudiée. On utilise des hypothèses simples: les pertes visqueuses et thermiques sont négligées, les parois du tuyau sont rigides. L'écoulement imposé est un jet cisailé incompressible, indépendant de la direction de propagation: il est supposé invariable dans sa propagation (il ne se recolle pas aux parois).

La méthode est validée sur un élargissement brusque (chapitre 2) et appliquée (chapitre 3) sur une expansion sifflante (biseau amont suivi d'un double élargissement brusque de section). L'objectif recherché de cette étude numérique a été atteint: les fréquences potentielles de sifflement de la configuration sifflante sont bien calculées, en comparaison avec les fréquences mesurées expérimentalement sur cette configuration.

Le chapitre 2 est la validation de la méthode multimodale sur un élargissement brusque. Nous montrons que la méthode donne des résultats très satisfaisants, comparés aux résultats expérimentaux (section 2.5.2.1), pour le coefficient de réflexion R^+ . Les modèles analytiques dans certaines limites de paramètres de fréquence et d'écoulement sont bien retrouvés également, pour tous les coefficients de la matrice de diffusion. Des points nécessiteraient des éclaircissements: la présence d'une forme de bosse sur certains résultats de coefficients de réflexion, la différence entre le calcul et la mesure pour des valeurs extrêmes des paramètres (haute fréquence et for nombre de Mach), et la différence entre un tuyau rectangulaire et un tuyau circulaire.

Le chapitre 3 est l'application de la méthode multimodale sur une expansion sifflante. Les

comparaisons avec les expériences effectuées montrent une prédiction satisfaisante des fréquences potentielles de sifflement de la configuration. Nous avons alors mené des études paramétriques sur l'influence des paramètres de l'écoulement et de la géométrie que le nombre de Strouhal instable. Nous montrons que le nombre de Strouhal de la configuration est peu variable avec les paramètres d'écoulement: le paramètre numérique imposé pour la forme du profil, le nombre de Mach de l'écoulement et le diamètre du jet. Par contre, le nombre Strouhal varie de façon importante avec les paramètres de la zone d'amplification de l'instabilité: la hauteur et la longueur du premier élargissement. Dans une telle configuration donc, nous montrons l'importance critique de cette zone, et en conséquence un modèle simple de description du phénomène de sifflement semble impossible, tant le nombre Strouhal varie avec ces paramètres géométriques.

En complément à cette étude sur la méthode multimodale, le travail effectué dans la thèse de Gerben Koojman à l'Université technique d'Eindhoven (Pays-Bas) devrait apporter des éclaircissements: étude sur un écoulement uniforme, et dans d'autres configurations.

Analyses de spectres de bruit de diaphragme monotrou et multitrou, en régime de cavitation et de sifflement

Le chapitre 4 présente une étude expérimentale de spectres de bruit typiques obtenus sur des diaphragmes monotrou et multitrou, en régime de cavitation et parfois de sifflement.

Une adimensionnalisation des spectres de cavitation est proposée, en distinguant deux régimes de cavitation (cavitation faible dite 'cavitation développée' et cavitation forte dite 'super cavitation'):

- en régime de faible cavitation, une bonne adimensionnalisation est obtenue. Une forme en bosse du spectre est mise en évidence, typique du régime de cavitation. Il s'agit d'un résultat cohérent avec la littérature, mais non quantifié jusque là en terme de bruit émis par un diaphragme monotrou. De plus, les sifflements observés correspondent à des nombres de Strouhal proches de ceux obtenus en air (nombre Strouhal autour de 0.2-0.3). L'observation de sifflement en concomitance avec de la cavitation est un résultat jamais reporté dans la littérature à notre connaissance;
- en régime de forte cavitation, il apparaît que la quantité d'air résiduelle dans l'eau en aval du diaphragme, après diffusion dans les bulles de cavitation de vapeur, affecte de façon spectaculaire les spectres, ce qui représente un résultat nouveau.

Ces résultats sont à vérifier en testant la répétabilité des essais analysés, et l'influence de la quantité de gaz dissous dans l'eau utilisée. En effet, ce paramètre pourrait être important, surtout pour le régime de faible cavitation, et il n'a pas été mesuré ni contrôlé pendant ces essais.

Résultats pour le modèle de correction de bout de diaphragme sous écoulement

Le chapitre 5 est l'étude expérimentale et numérique du modèle acoustique de correction de bout appliqué à des élargissements brusques et les diaphragmes:

- sans écoulement, les modèles analytiques simples proposés dans la littérature, pour la correction de longueur de diaphragme très fins et très épais, sont très satisfaisants en comparaison avec les

corrections de longueur expérimentales que nous avons obtenues expérimentalement au LAUM. De même, les corrections de longueur obtenues par la méthode multimodale sur un élargissement brusque donnent de bons résultats par comparaison avec la littérature.

- avec écoulement, très peu de littérature existe, c'est pourquoi les résultats expérimentaux présentés sur les diaphragmes sont intéressants. Cependant, il apparaît que le comportement de la correction de longueur est complexe, avec des variations en fonction de la fréquence, du nombre de Mach, et ceci d'un diaphragme à l'autre. Ces comportements sont particulièrement difficiles à synthétiser et à comprendre.

Perspectives

Critère de sifflement

En perspective, la continuation de l'étude du critère de sifflement est envisageable. Il serait intéressant de tester les autres singularités que l'on peut rencontrer en tuyau de centrale nucléaire: vannes, robinets, diaphragmes multitrou. A priori, le critère de sifflement devrait s'appliquer sur ces organes. L'intérêt serait de valider l'application industrielle un tel critère. Dans cette optique, il serait intéressant de vérifier les résultats trouvés en eau (reportés au chapitre 4), c'est à dire que le nombre de Strouhal ne varie pas sensiblement en changeant de compressibilité de fluide. L'intérêt serait alors que la mesure de la matrice de diffusion serait suffisante en air, ce qui évite d'utiliser une boucle en eau pour cette mesure.

Dans cette optique d'application industrielle, il serait intéressant de valider le modèle élémentaire de prédiction des fréquences de sifflement en conditions acoustiques réverbérantes sur de plus amples configurations (nous avons obtenu de bons résultats avec ce modèle, mais sur peu de mesures). De plus, il serait très intéressant de comprendre pourquoi le modèle de type Bode-Nyquist que nous avons tenté échoue. Il est surprenant qu'un tel modèle donne de mauvais résultats, alors qu'il nous semble plus adapté que le modèle élémentaire.

Sur ce critère d'instabilité, une perspective importante et intéressante nous semble aussi de mieux comprendre le ratio de puissance acoustique dissipé par l'organe, c'est à dire les amplitudes que nous avons obtenues sur la représentation des valeurs propres de la matrice énergétique. Nous avons commencé une adimensionnalisation très satisfaisante avec le nombre de Mach pour un orifice donné, mais nous avons montré que cette adimensionnalisation doit encore prendre en compte les caractéristiques géométriques des diaphragmes. L'intérêt serait d'obtenir une compréhension plus fine des phénomènes d'interaction acoustique-écoulement locaux. Un moyen envisageable serait d'utiliser une analogie aéroacoustique, par exemple l'analogie de Howe.

Approfondissement de la méthode multimodale

L'obtention d'un mode hydrodynamique instable par la méthode multimodale est satisfaisante, mais sa présence ne nous semble pas tout à fait comprise. La présence de cette instabilité semble due au critère de Rayleigh, c'est à dire la présence d'un point d'inflexion virtuel sur le profil d'écoulement. Cependant, nous avons du mal à comprendre l'application de ce critère sur un profil discrétisé d'écoulement.

Les problèmes secondaires rencontrés et que nous avons rapportés sur la méthode multimodale sont les autres perspectives d'approfondissement de la méthode.

Étude d'un élargissement brusque

Enfin, il faut noter que la comparaison des géométries cartésiennes et cylindriques est appropriée avec cette méthode multimodale. Comme ce genre d'étude est rare dans la littérature, il semble intéressant d'utiliser cette méthode pour mieux comprendre la différence entre ces 2 géométries.

Appendix A

Measurements on orifices: potentially whistling frequencies

In this appendix, all the measurements made are presented in the potentially whistling eigenvalue form.

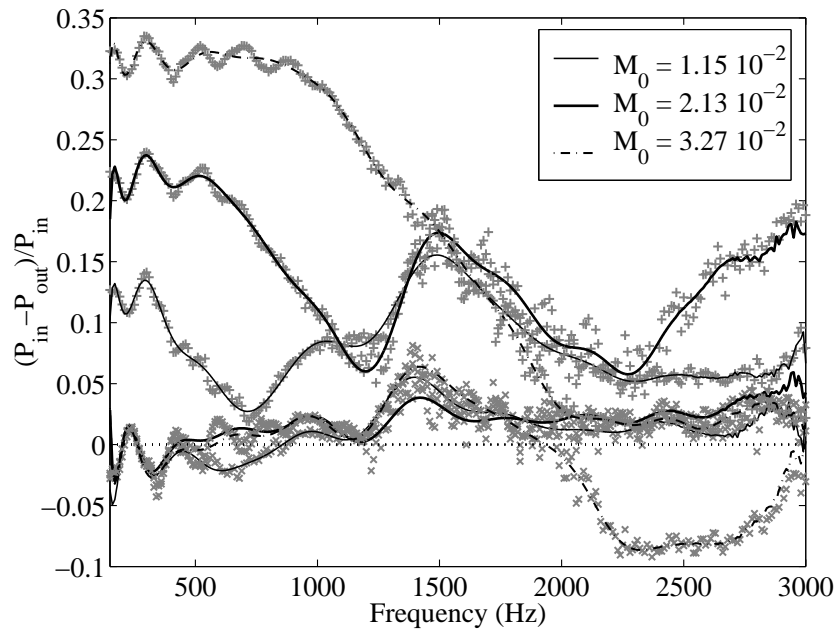


Figure A.1: The eigenvalues of the acoustic power ratio, obtained for orifice $t = 3$ mm, $d = 20$ mm (CC1).

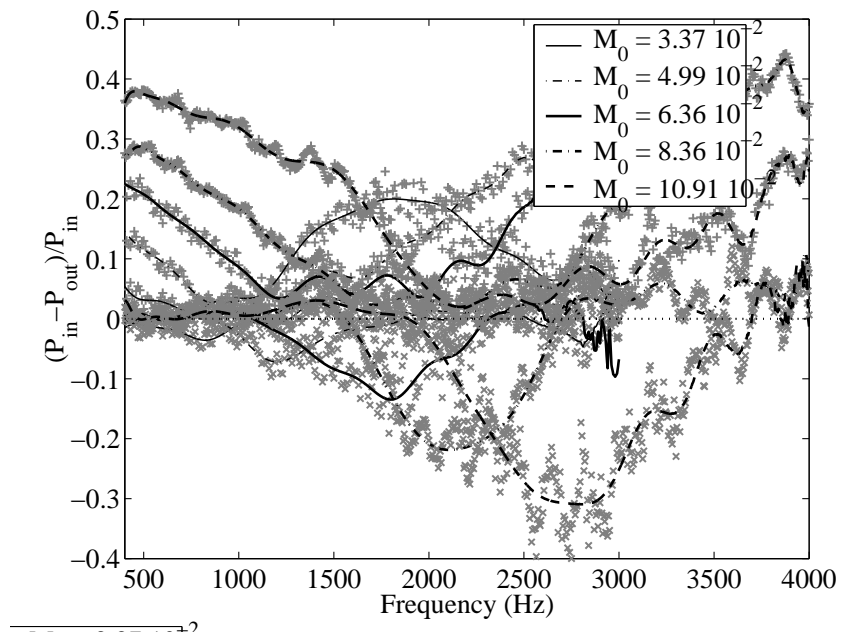


Figure A.2: The eigenvalues of the acoustic power ratio, obtained for orifice $t = 5$ mm, $d = 23$ mm (CC2).

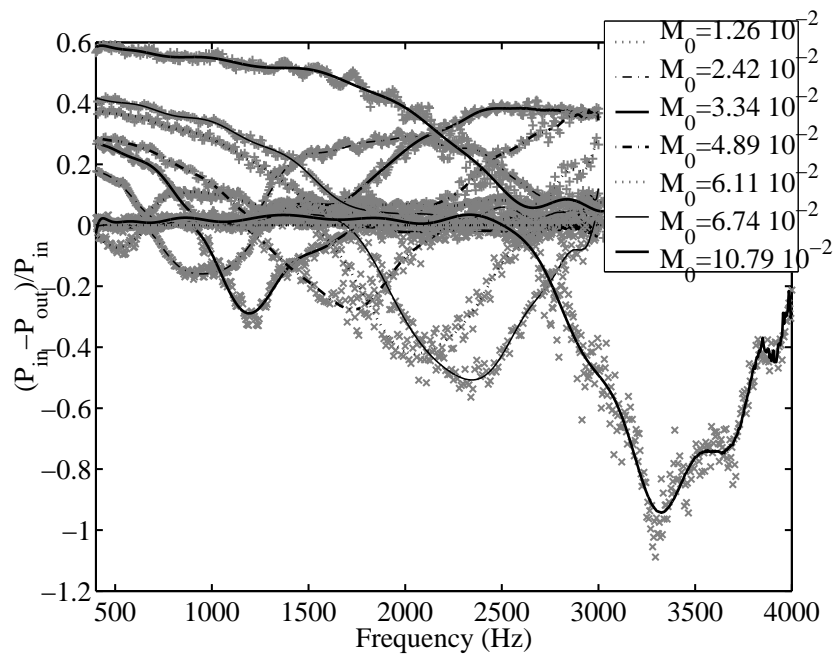


Figure A.3: The eigenvalues of the acoustic power ratio, obtained for orifice $t = 5$ mm, $d = 21$ mm (CC3).

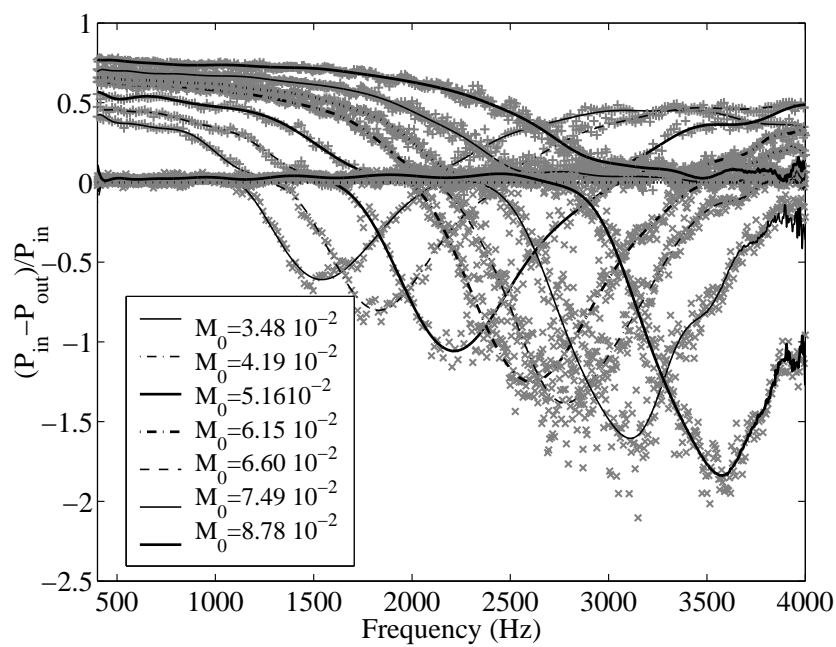


Figure A.4: The eigenvalues of the acoustic power ratio, obtained for orifice $t = 5$ mm, $d = 19$ mm (CC4).

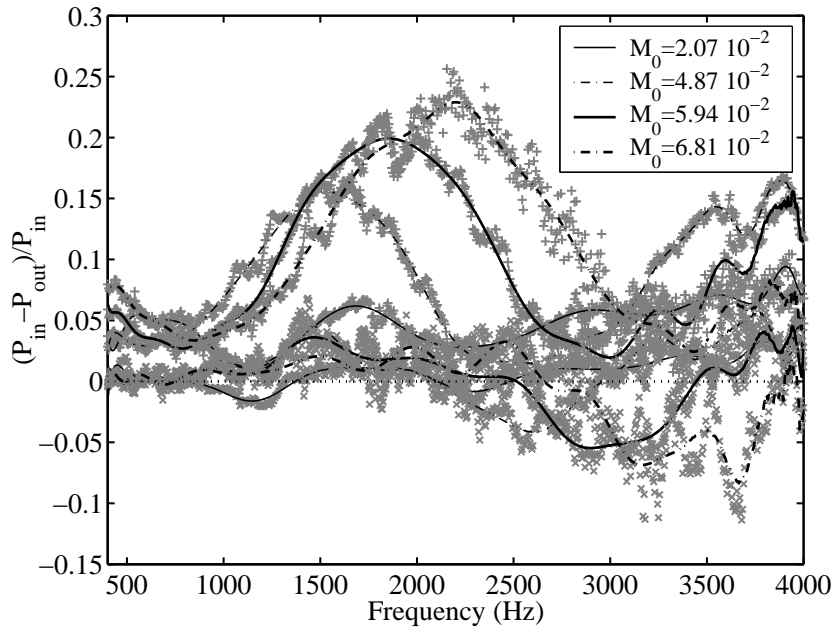


Figure A.5: The eigenvalues of the acoustic power ratio, obtained for orifice $t = 7$ mm, $d = 24$ mm (CC5).

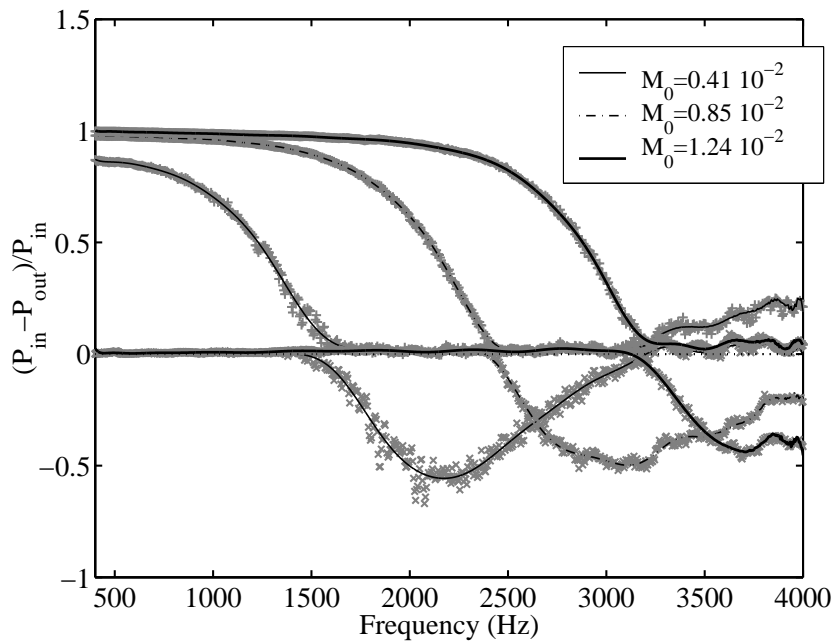


Figure A.6: The eigenvalues of the acoustic power ratio, obtained for orifice $t = 3$ mm, $d = 10$ mm (CC6).

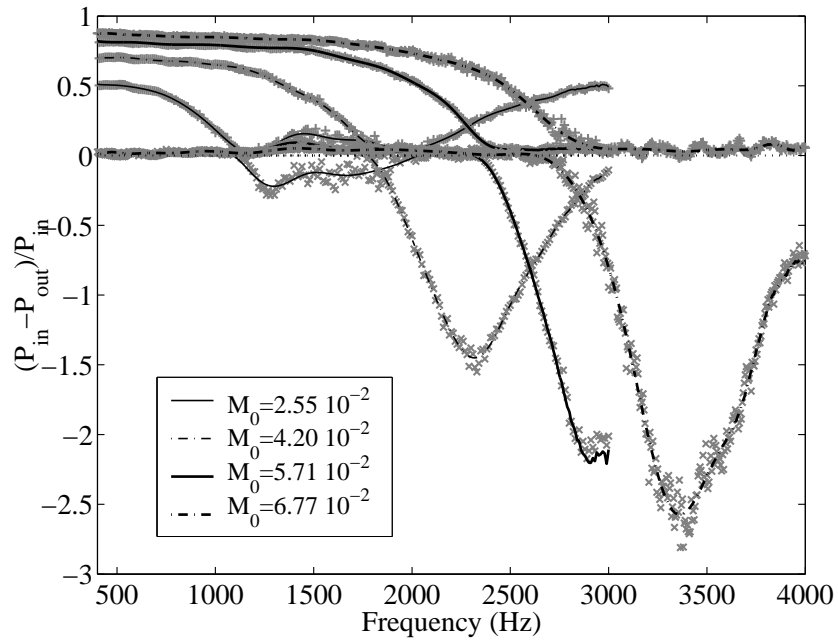


Figure A.7: The eigenvalues of the acoustic power ratio, obtained for orifice $t = 5$ mm, $d = 17$ mm (CC7).

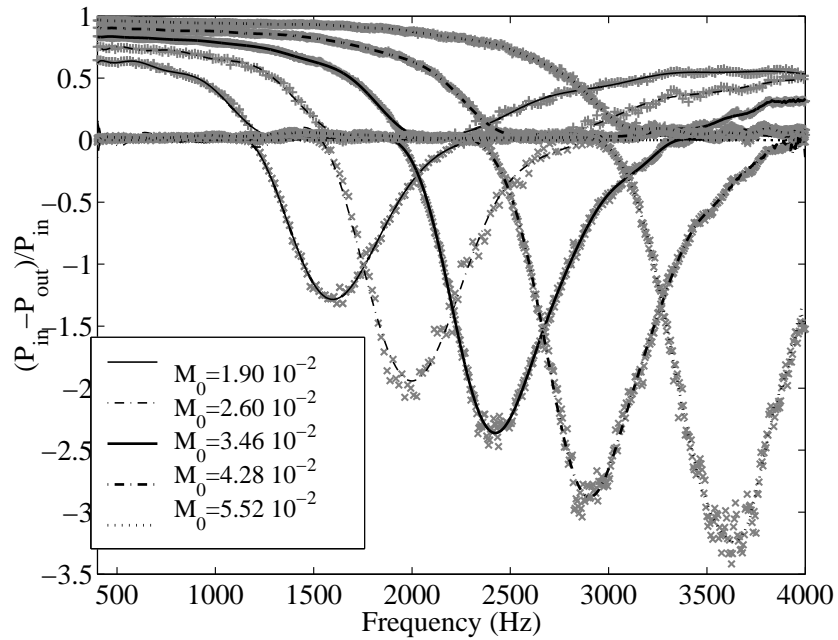


Figure A.8: The eigenvalues of the acoustic power ratio, obtained for orifice $t = 5$ mm, $d = 15$ mm (CC8).

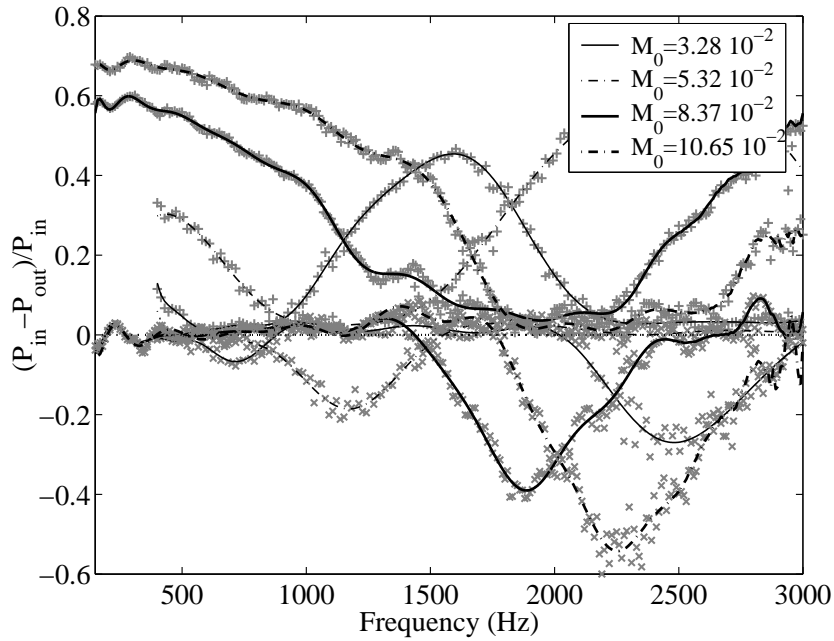


Figure A.9: The eigenvalues of the acoustic power ratio, obtained for orifice $t = 8$ mm, $d = 20$ mm (CC9).

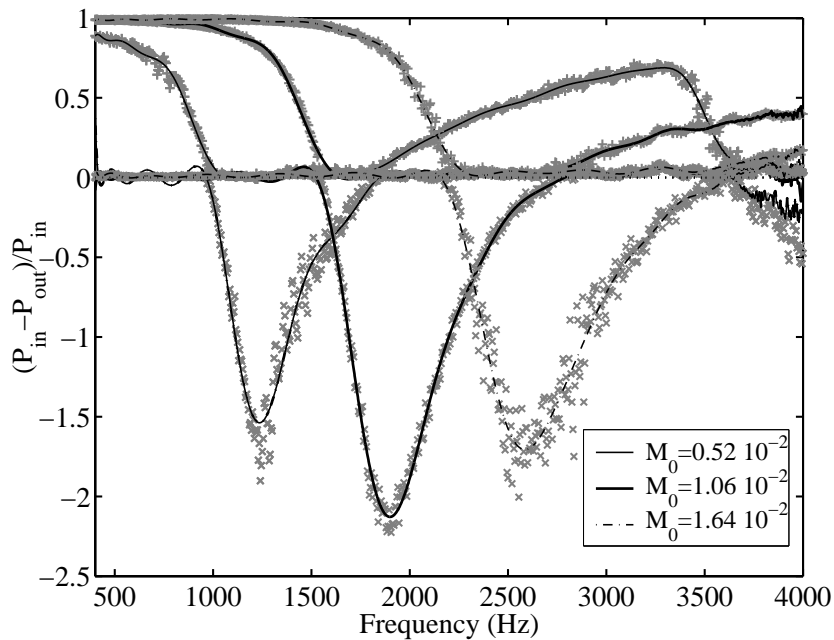


Figure A.10: The eigenvalues of the acoustic power ratio, obtained for orifice $t = 5$ mm, $d = 10$ mm (CC10).

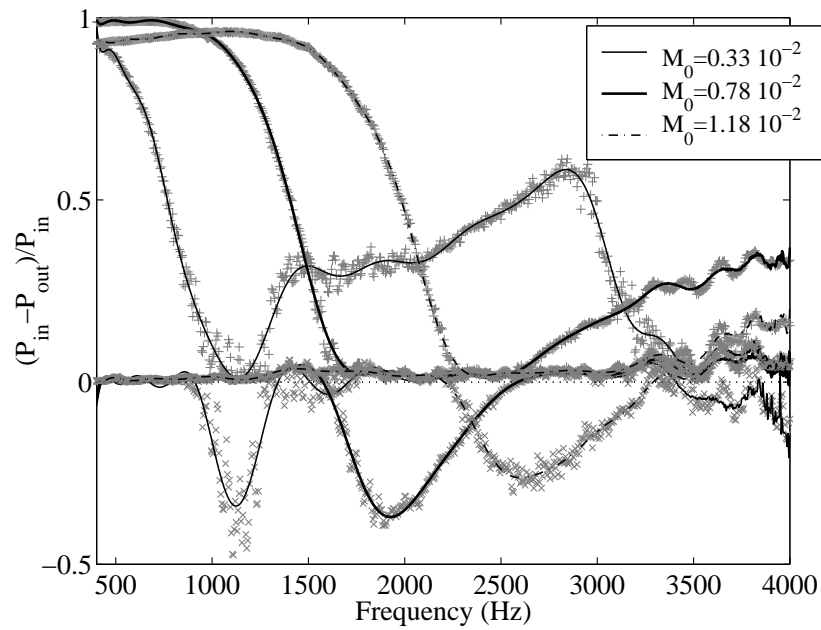


Figure A.11: The eigenvalues of the acoustic power ratio, obtained for orifice $t = 5$ mm, $d = 8$ mm (CC11).

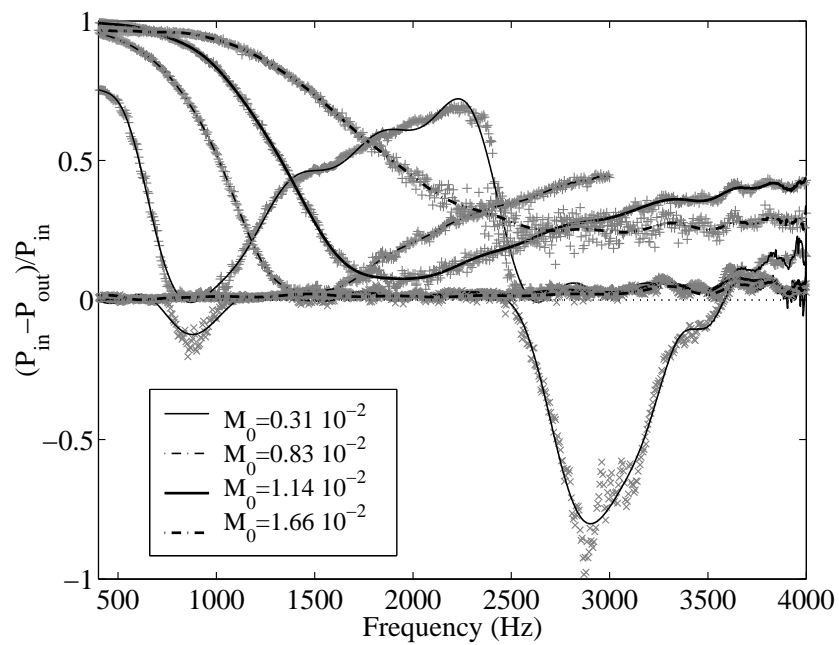


Figure A.12: The eigenvalues of the acoustic power ratio, obtained for orifice $t = 6$ mm, $d = 9$ mm (CC12).

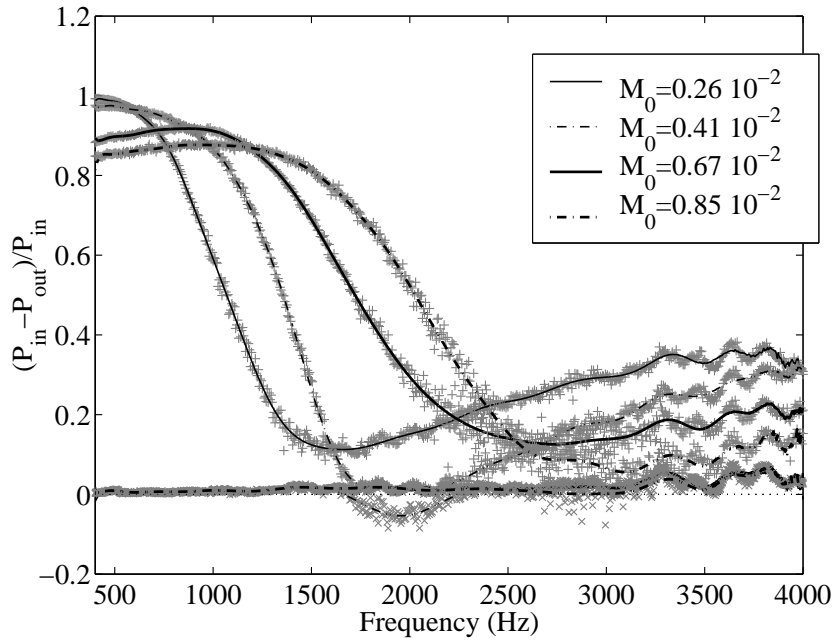


Figure A.13: The eigenvalues of the acoustic power ratio, obtained for orifice $t = 5$ mm, $d = 7$ mm (CC13).

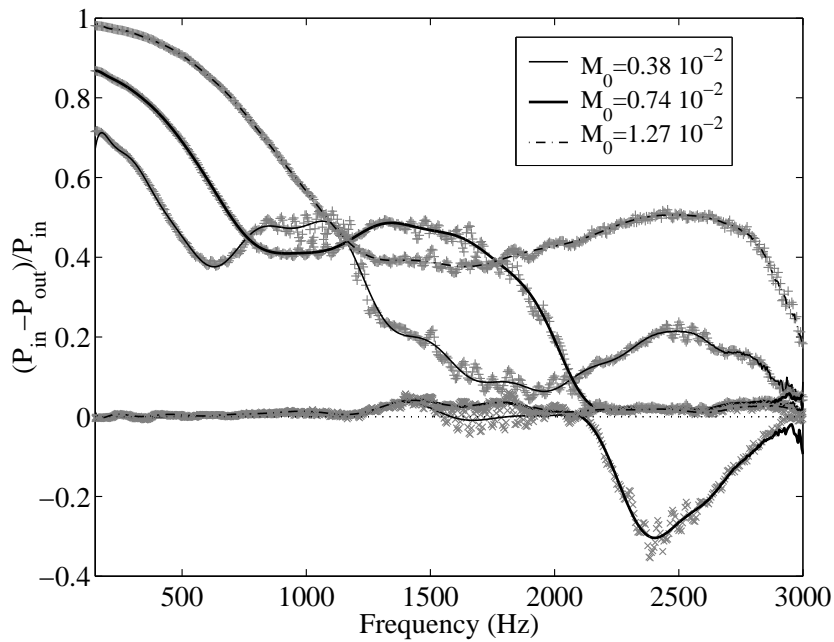


Figure A.14: The eigenvalues of the acoustic power ratio, obtained for orifice $t = 10$ mm, $d = 10$ mm (CC14).

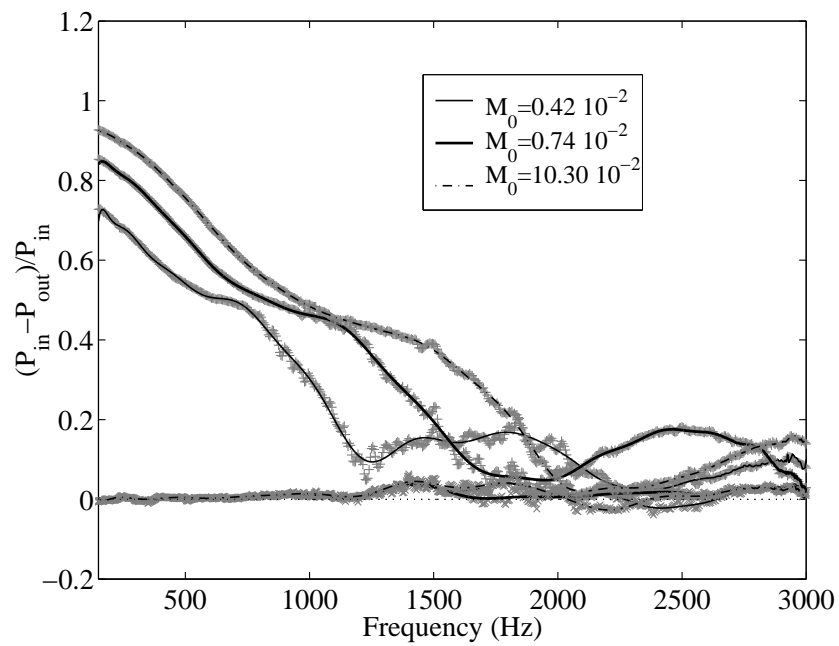


Figure A.15: The eigenvalues of the acoustic power ratio, obtained for orifice $t = 15$ mm, $d = 10$ mm (CC15).

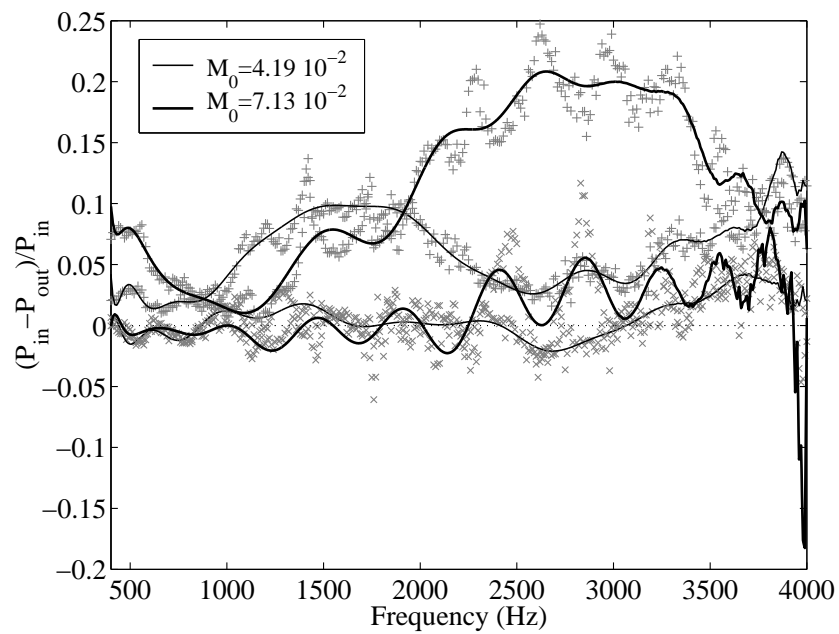


Figure A.16: The eigenvalues of the acoustic power ratio, obtained for orifice $t = 5$ mm, $d = 25$ mm (CC16).

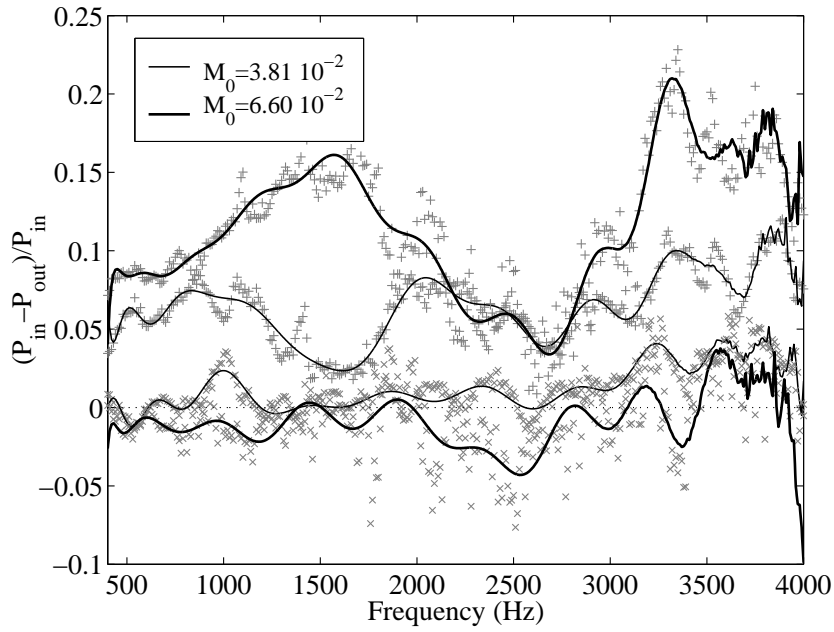


Figure A.17: The eigenvalues of the acoustic power ratio, obtained for orifice $t = 10$ mm, $d = 24$ mm (CC17).

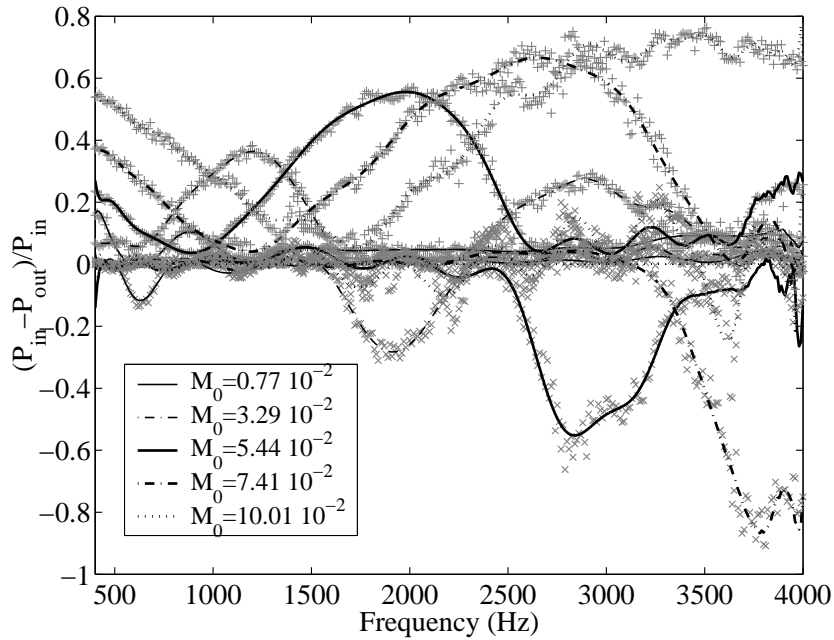


Figure A.18: The eigenvalues of the acoustic power ratio, obtained for orifice $t = 10$ mm, $d = 20$ mm (CC18).

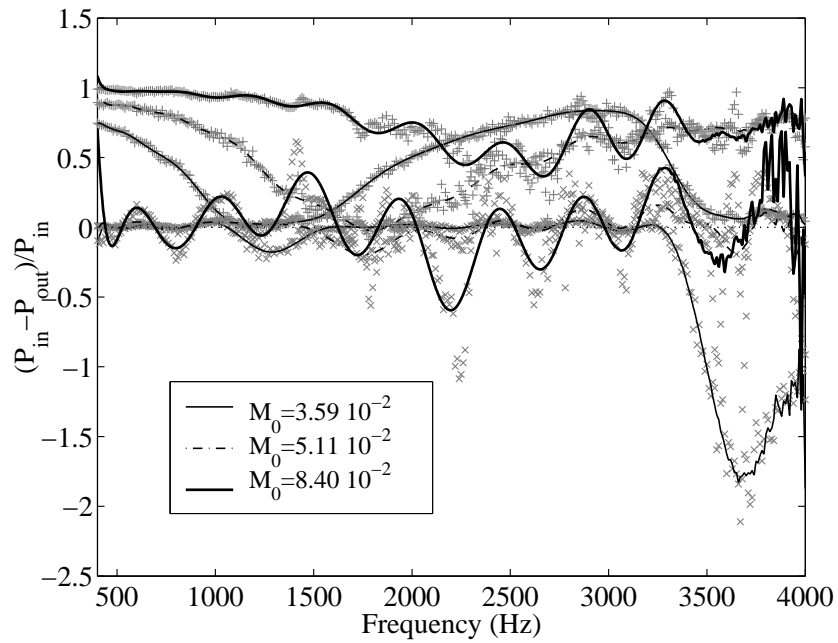


Figure A.19: The eigenvalues of the acoustic power ratio, obtained for orifice $t = 10$ mm, $d = 15$ mm (CC19).

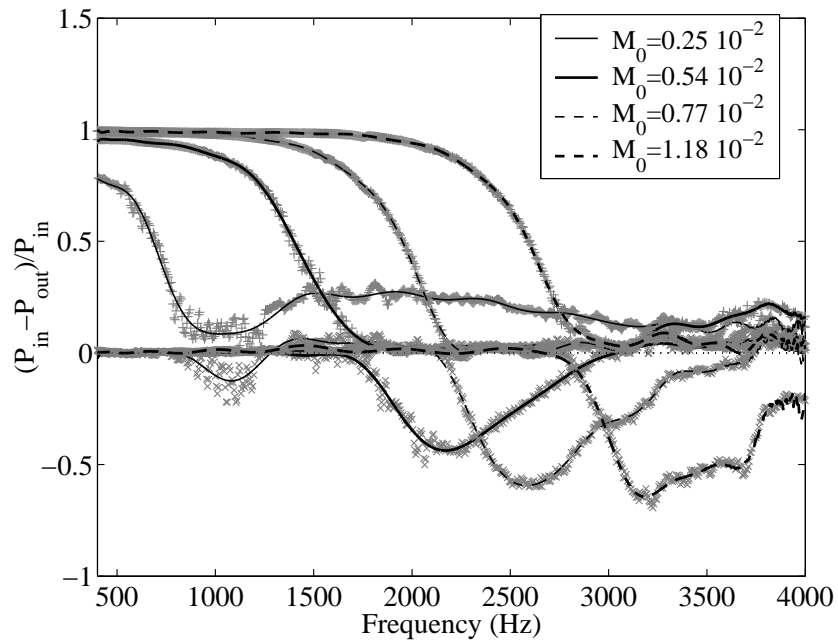


Figure A.20: The eigenvalues of the acoustic power ratio, obtained for orifice $t = 5$ mm, $d = 10$ mm (CCb2) with the bevel downstream.

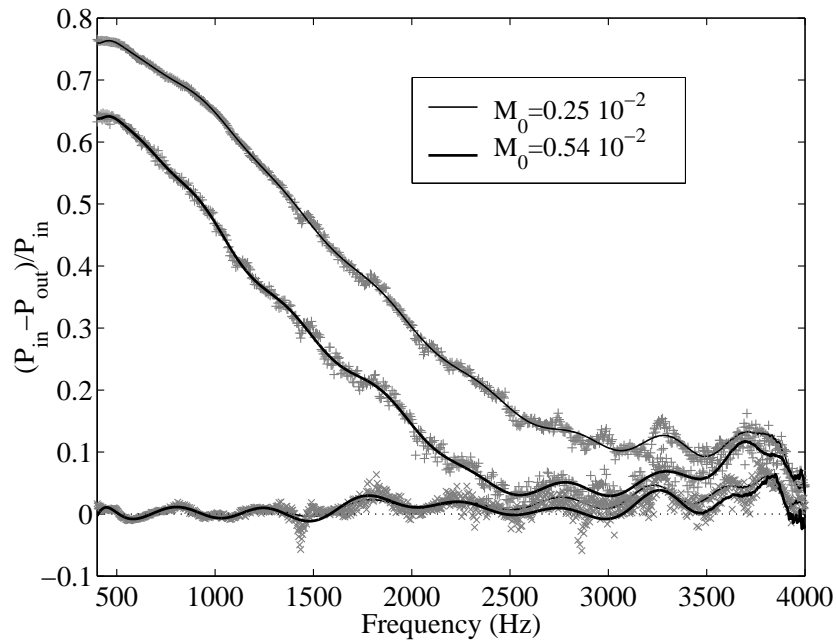


Figure A.21: The eigenvalues of the acoustic power ratio, obtained for orifice $t = 5$ mm, $d = 10$ mm (CCb2) with the large bevel upstream.

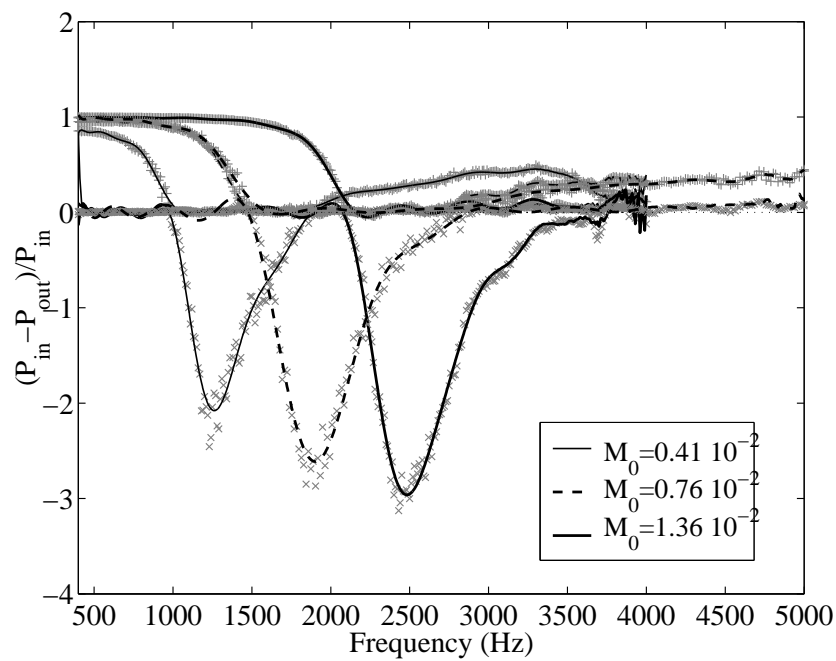


Figure A.22: The eigenvalues of the acoustic power ratio, obtained for orifice $t = 5$ mm, $d = 10$ mm (CCb4) with the small bevel downstream.

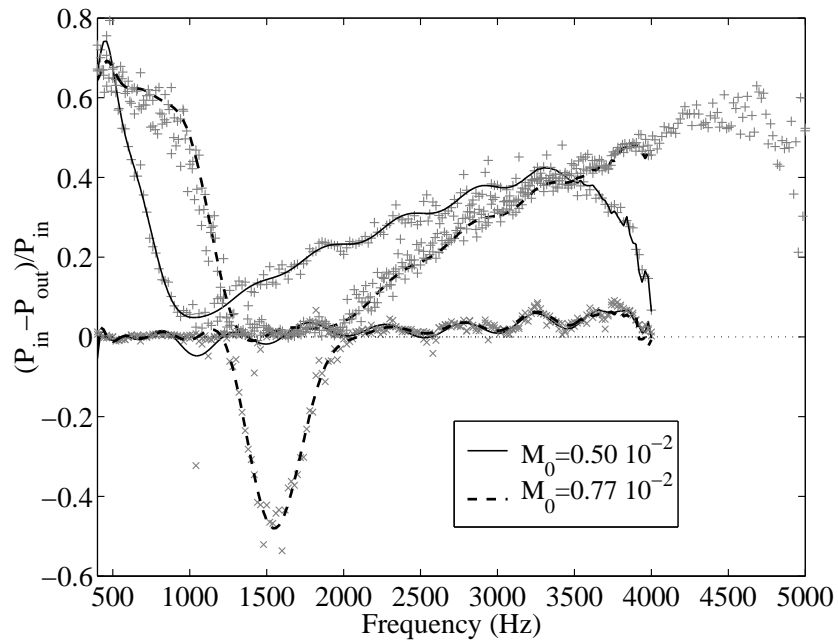


Figure A.23: The eigenvalues of the acoustic power ratio, obtained for orifice $t = 5$ mm, $d = 10$ mm (CCb4) with the small bevel upstream.

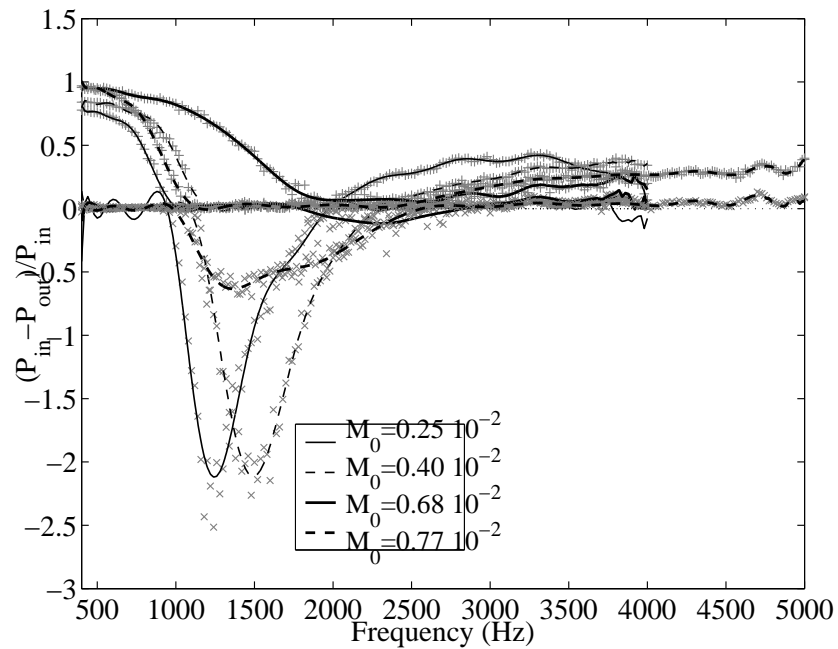


Figure A.24: The eigenvalues of the acoustic power ratio, obtained for orifice $t = 5$ mm, $d = 10$ mm (CCb5: 2 beavels).

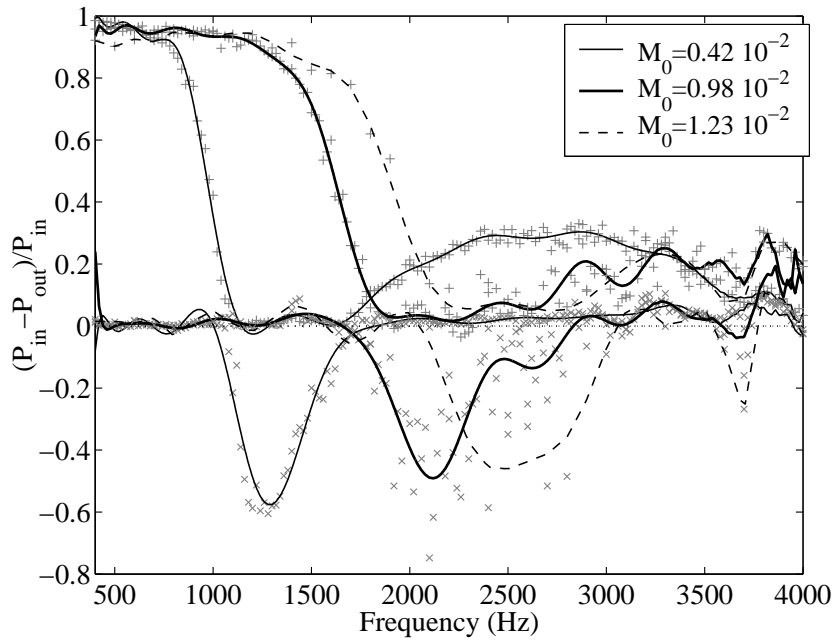


Figure A.25: Potentially whistling eigenvalues of smile shaped slit F1: $t = 5$ mm, $S_d = 63$ mm².

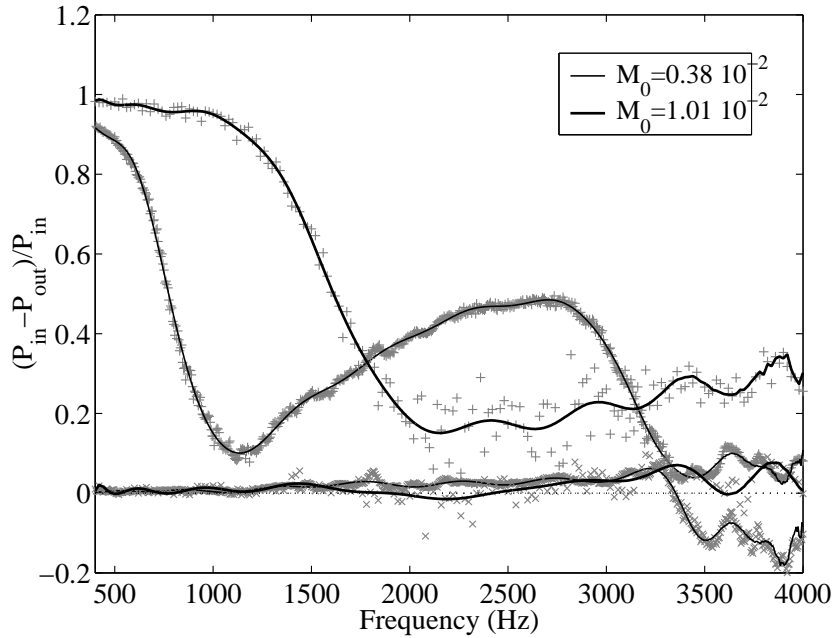


Figure A.26: Potentially whistling eigenvalues of smile shaped slit F2: $t = 5$ mm, $S_d = 63$ mm².

Appendix B

Measurements on double orifice: potentially whistling frequencies

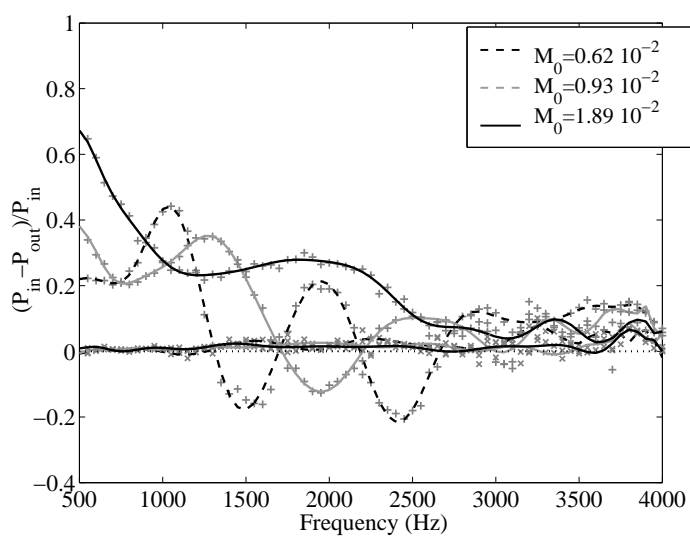


Figure B.1: Eigenvalues of the acoustic power ratio from the whistling criterion for configuration: $b = 1.2$, $c = 3$, $L = 2$ (CCb6+CC22) - various Mach numbers.

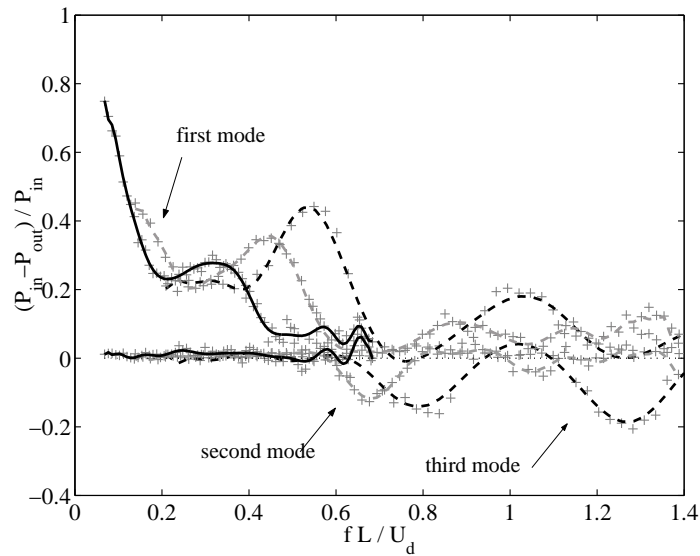


Figure B.2: Strouhal number of the potentially whistling eigenvalues from the whistling criterion for configuration: $b = 1.2$, $c = 3$, $L = 2$ (CCb6+CC22) - various Mach numbers.

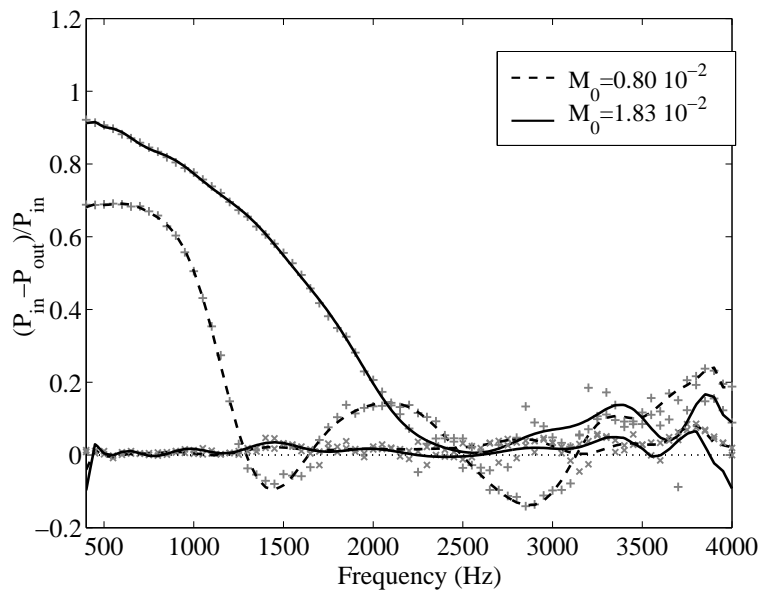


Figure B.3: Eigenvalues of the acoustic power ratio from the whistling criterion for configuration: $b = 1.5$, $c = 3$, $L = 1$ (CCb6+CC8) - various Mach numbers.

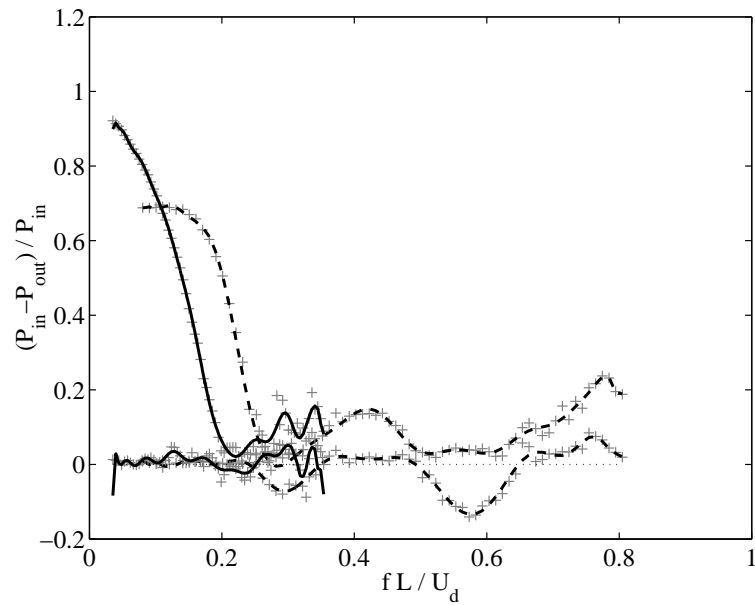


Figure B.4: Strouhal number of the potentially whistling eigenvalues from the whistling criterion for configuration: $b = 1.5$, $c = 3$, $L = 1$ - various Mach numbers (CCb6+CC8).

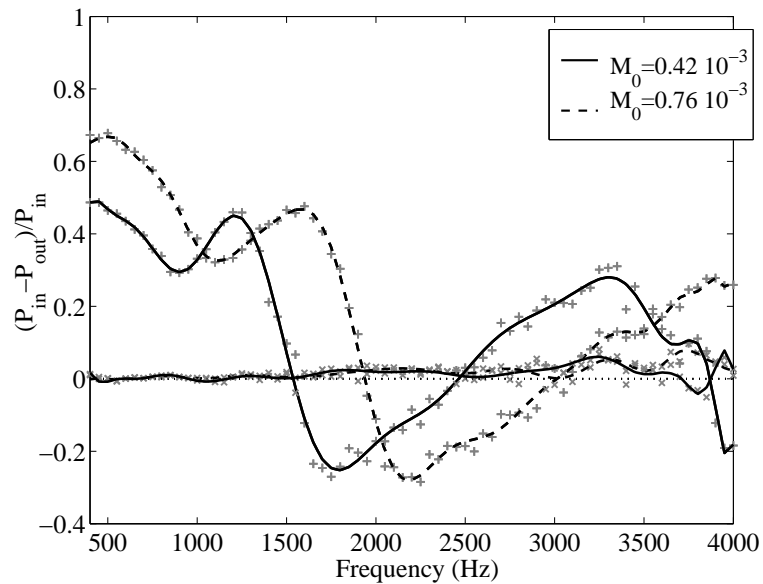


Figure B.5: Eigenvalues of the acoustic power ratio from the whistling criterion for configuration: $b = 2$, $c = 3$, $L = 2$ (CCb6+CC18) - various Mach numbers.

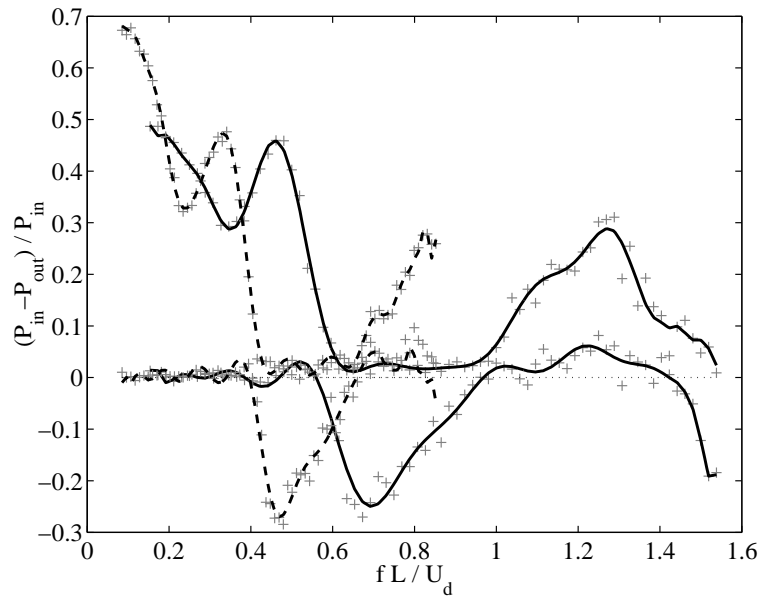


Figure B.6: Strouhal number of the potentially whistling eigenvalues from the whistling criterion for configuration $b = 2$, $c = 3$, $L = 2$ (CCb6+CC18) - various Mach numbers.

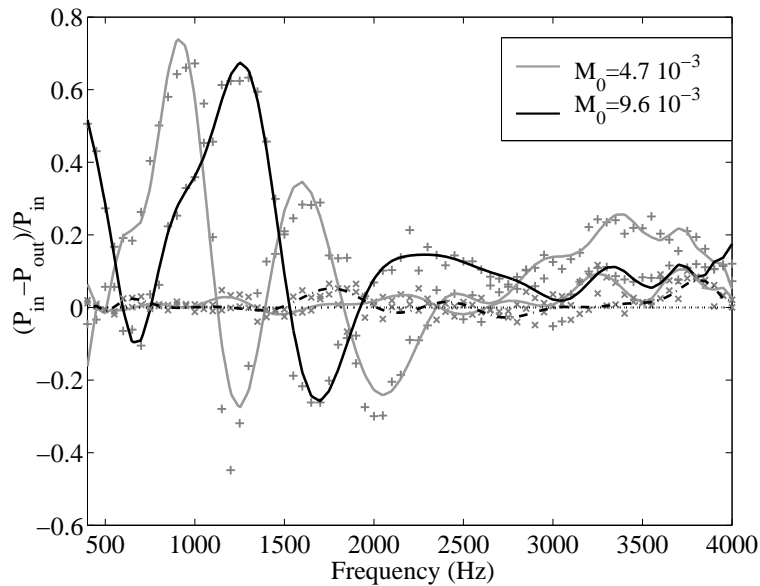


Figure B.7: Eigenvalues of the acoustic power ratio from the whistling criterion for configuration CCb6+CC18+CC9: $b = 2$, $c = 3$, $L = 3.6$.

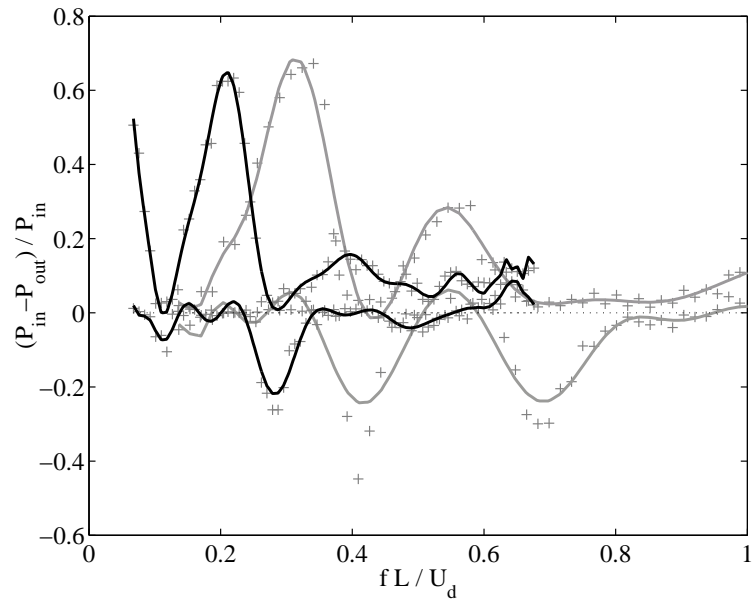


Figure B.8: Strouhal number of the potentially whistling eigenvalues from the whistling criterion for configuration $b = 2$, $c = 3$, $L = 3.6$ (CCb6+CC18+CC9) - various Mach numbers.

Appendix C

Acoustical propagation equations under sheared mean flow

This section presents the demonstration of the acoustical propagation equation under sheared mean flow $M_0(y)\mathbf{e}_x$ (that is incompressible mean flow). Viscosity and entropy variations are also neglected.

Fluid mechanics equations

The equations of fluid mechanics are applied to the general quantities (dimensional): the pressure p , the velocity \mathbf{v} and the fluid density ρ . The viscosity is neglected:

- Mass conservation equation:

$$\frac{\partial \rho}{\partial t} + (\mathbf{v} \cdot \nabla) \rho = -\rho \operatorname{div}(\mathbf{v}). \quad (\text{C.1})$$

- Momentum conservation equation:

The fluid is considered as perfect: Euler equations are considered:

$$\rho \frac{\partial \mathbf{v}}{\partial t} + \rho (\mathbf{v} \cdot \nabla) \mathbf{v} = -\nabla p \quad (\text{C.2})$$

Linearization of Navier Stokes equations

The previous fluid mechanics equations are linearized at first order, giving acoustic equations. We introduce: $\mathbf{v} = \mathbf{U}_0(y) + \mathbf{v}'$, $\rho = \rho_0 + \rho'$, $p = p_0 + p'$.

The mean flow is supposed of the form: $\mathbf{U}_0(y) = U_0(y)\mathbf{e}_x$. It is incompressible.

At initial state, the fluid is considered as uniform, so that ρ_0 is a constant of space and time.

The flow is assumed isentropic, and at uniform entropy at the initial state, so that: $c_0^2 = \frac{p'}{\rho'}$.

- Mass conservation equation:

$$\frac{\partial \rho'}{\partial t} + (\mathbf{U}_0(y) \cdot \nabla) \rho' + (\mathbf{v}' \cdot \nabla) \rho_0 = -\rho_0 \operatorname{div}(\mathbf{v}') - \rho' \operatorname{div}(\mathbf{U}_0(y)) \quad (\text{C.3})$$

From the assumptions, $\text{div}(\mathbf{U}_0(y)) = 0$, $(\mathbf{v}' \cdot \nabla)\rho_0 = 0$ and $c_0^2 = \frac{p'}{\rho'}$. The previous equation reduces to:

$$\frac{\partial p'}{\partial t} + (\mathbf{U}_0(y) \cdot \nabla)p' = -\rho_0 c_0^2 \text{div}(\mathbf{v}') \quad (\text{C.4})$$

In 2D Cartesians, one has: $(\mathbf{U}_0(y) \cdot \nabla)\rho' = U_0(y) \frac{\partial \rho'}{\partial x}$ and $\text{div}(\mathbf{v}') = \frac{\partial v'_x}{\partial x} + \frac{\partial v'_y}{\partial y}$, hence:

$$\frac{\partial p'}{\partial t} + U_0(y) \frac{\partial p'}{\partial x} = -\rho_0 c_0^2 \left(\frac{\partial v'_x}{\partial x} + \frac{\partial v'_y}{\partial y} \right). \quad (\text{C.5})$$

In 2D cylindrical, one has: $(\mathbf{U}_0(r) \cdot \nabla)\rho' = U_0(r) \frac{\partial \rho'}{\partial z}$ and $\text{div}(\mathbf{v}') = \frac{v'_r}{r} + \frac{\partial v'_r}{\partial r} + \frac{\partial v'_z}{\partial z}$, hence:

$$\frac{\partial p'}{\partial t} + U_0(r) \frac{\partial p'}{\partial z} = -\rho_0 c_0^2 \left(\frac{v'_r}{r} + \frac{\partial v'_r}{\partial r} + \frac{\partial v'_z}{\partial z} \right). \quad (\text{C.6})$$

- Momentum conservation equation:

The linearization gives:

$$\rho_0 \frac{\partial \mathbf{v}'}{\partial t} + \rho' \frac{\partial \mathbf{U}_0}{\partial t} + \rho' (\mathbf{U}_0 \cdot \nabla) \mathbf{U}_0 + \rho_0 (\mathbf{v}' \cdot \nabla) \mathbf{U}_0 + \rho_0 (\mathbf{U}_0 \cdot \nabla) \mathbf{v}' = -\nabla p' \quad (\text{C.7})$$

In 2D Cartesians: $\frac{\partial \mathbf{U}_0}{\partial t} = 0$, $(\mathbf{U}_0(y) \cdot \nabla) \mathbf{U}_0(y) = \mathbf{0}$, $(\mathbf{v}' \cdot \nabla) \mathbf{U}_0(y) = v'_y \frac{dU(y)}{dy} \mathbf{e}_x$, $\mathbf{U}_0(y) \cdot \nabla = U(y) \frac{\partial}{\partial x}$, $\nabla p' = \frac{\partial p'}{\partial x} \mathbf{e}_x + \frac{\partial p'}{\partial y} \mathbf{e}_y$. Hence in the longitudinal and transversal direction, one gets:

$$\rho_0 \frac{\partial v'_x}{\partial t} + \rho_0 U(y) \frac{\partial v'_x}{\partial x} + \rho_0 v'_y \frac{dU(y)}{dy} = -\frac{\partial p'}{\partial x}, \quad (\text{C.8})$$

$$\rho_0 \frac{\partial v'_y}{\partial t} + \rho_0 U_0(y) \frac{\partial v'_y}{\partial x} = -\frac{\partial p'}{\partial y}. \quad (\text{C.9})$$

In 2D cylindrical: $\nabla p' = \frac{\partial p'}{\partial r} \mathbf{e}_r + \frac{\partial p'}{\partial z} \mathbf{e}_z$. Hence in the longitudinal and transversal direction, one gets:

$$\rho_0 \frac{\partial v'_r}{\partial t} + \rho_0 U_0(r) \frac{\partial v'_r}{\partial r} = -\frac{\partial p'}{\partial r}, \quad (\text{C.10})$$

$$\rho_0 \frac{\partial v'_z}{\partial t} + \rho_0 U_0(r) \frac{\partial v'_z}{\partial z} + \rho_0 v'_r \frac{dU_0(r)}{dr} = -\frac{\partial p'}{\partial z}. \quad (\text{C.11})$$

Propagation equation: Lilley equation

The propagation equation in pressure is obtained by multiplying $\frac{D}{Dt}$ with the mass conservation equation (Eq. C.8 in Cartesians, Eq. C.9 in cylindrical).

In 2D Cartesians, as $\frac{D}{Dt} \left(\frac{\partial}{\partial y} \right) = \frac{\partial}{\partial y} \left(\frac{D}{Dt} \right) - \frac{dU}{dy} \frac{\partial}{\partial x}$, one gets:

$$\frac{D^2 p'}{Dt^2} - c_0^2 \Delta p' = 2\rho_0 c_0^2 \frac{dU(y)}{dy} \frac{\partial v'_y}{\partial x}, \quad (\text{C.12})$$

with $\Delta p' = \frac{\partial^2 p'}{\partial x^2} + \frac{\partial^2 p'}{\partial y^2}$ and $\frac{D}{Dt} = \frac{\partial}{\partial t} + U(y) \frac{\partial}{\partial x}$.

The propagation equation in the variable p' is (known as Lilley equation, see Bailly (1994)):

$$\frac{D}{Dt} \left(\frac{D^2}{Dt^2} - c_0^2 \Delta \right) p' + 2c_0^2 \frac{dU(y)}{dy} \frac{\partial^2 p'}{\partial x \partial y} = 0 \quad (\text{C.13})$$

If the flow is uniform: $dU/dy = 0$, the classical propagation equation of order 2 in derivative is obtained. In the case of a sheared flow: $dU/dy \neq 0$, it is of order 3 in derivative.

In 2D axisymmetric, it takes a similar form, only the expression of the Laplacian differs from the Cartesians case:

$$\frac{D}{Dt} \left(\frac{D^2}{Dt^2} - c_0^2 \Delta \right) p' + 2c_0^2 \frac{dU(r)}{dr} \frac{\partial^2 p'}{\partial z \partial r} = 0 \quad (\text{C.14})$$

where $\Delta p' = \frac{1}{r} \frac{\partial p'}{\partial r} + \frac{\partial^2 p'}{\partial r^2} + \frac{\partial^2 p'}{\partial z^2}$ and $\frac{D}{Dt} = \frac{\partial}{\partial t} + U(r) \frac{\partial}{\partial z}$.

C.0.0.1 Equation of the modes: Pridmore-Brown equation

A time-frequency dependence of the variables in $e^{j\omega t}$ is assumed. Solutions are demonstrated (see section 2.2.5.2) to take the form: $e^{j(\omega t - kx)}$. Lilley equation becomes then what is known as Pridmore-Brown equation, that is the equation of the modes in a duct with a sheared flow:

$$(\omega - kU) \left[(\omega - kU)^2 + c_0^2 \Delta \right] p' + 2c_0^2 k \frac{dU(y)}{dy} \frac{\partial p'}{\partial y} = 0. \quad (\text{C.15})$$

That is, if $\omega - kU \neq 0$:

$$\Delta p' + \frac{2k \frac{dU(y)}{dy}}{\omega - kU} \frac{\partial p'}{\partial y} - \left(\frac{\omega - kU}{c_0} \right)^2 p' = 0. \quad (\text{C.16})$$

In 2D Cartesians:

$$\frac{\partial^2 p'}{\partial y^2} + \frac{2k \frac{dU(y)}{dy}}{\omega - kU} \frac{\partial p'}{\partial y} + \left[\left(\frac{\omega - kU}{c_0} \right)^2 - k^2 \right] p' = 0. \quad (\text{C.17})$$

In 2D axisymmetric:

$$\frac{\partial^2 p'}{\partial r^2} + \left[\frac{1}{r} + \frac{2k \frac{dU(y)}{dy}}{\omega - kU} \right] \frac{\partial p'}{\partial r} + \left[\left(\frac{\omega - kU}{c_0} \right)^2 - k^2 \right] p' = 0. \quad (\text{C.18})$$

Appendix D

Demonstration of the continuity of the acoustic variables at the expansion

This section presents the demonstration of the continuity of the acoustic variables p', ρ', v'_x, v'_y and of their derivative $\partial d/\partial dx$ at the crossing of the expansion. The geometry is given in Fig. 2.1). The flow is assumed non-viscous, isentropic, and the mean flow is assumed incompressible.

D.1 Continuity of the acoustic variables

Laws of mass conservation, momentum conservation in the x-direction and in the y-direction, and energy conservation, give the fluid mechanics equations, at the expansion:

$$\rho_I v_{x,I} = \rho_{II} v_{x,II}, \quad (\text{D.1})$$

$$\rho_I v_{x,I}^2 + P_I = \rho_{II} v_{x,II}^2 + P_{II}, \quad (\text{D.2})$$

$$(\rho_I v_{x,I}) \cdot v_{y,I} = (\rho_{II} v_{x,II}) \cdot v_{y,II}, \quad (\text{D.3})$$

$$h_I + \frac{v_{x,I}^2 + v_{y,I}^2}{2} = h_{II} + \frac{v_{x,II}^2 + v_{y,II}^2}{2}, \quad (\text{D.4})$$

where h is the enthalpy: $dh = dp/\rho$ for isentropic flow.

Eq. D.3 is simplified using Eq. D.1:

$$v_{y,I} = v_{y,II}. \quad (\text{D.5})$$

Linearized at first order, those equations give the acoustic equations:

$$\rho'_I v_{x,I} + \rho_I v'_{x,I} = \rho'_{II} v_{x,II} + \rho_{II} v'_{x,II}, \quad (\text{D.6})$$

$$\rho'_I v_{x,I}^2 + 2\rho_I v_{x,I} v'_{x,I} + P'_I = \rho'_{II} v_{x,II}^2 + 2\rho_{II} v_{x,II} v'_{x,II} + P'_{II}, \quad (\text{D.7})$$

$$v'_{y,I} = v'_{y,II}, \quad (\text{D.8})$$

$$\frac{p'_I}{\rho_I} + v_{x,I} v'_{x,I} = \frac{p'_{II}}{\rho_{II}} + v_{x,II} v'_{x,II}, \quad (\text{D.9})$$

As the flow is isentropic, $p' = c_0^2 \rho'$. The assumption of incompressibility imposes $\rho'_I = \rho'_{II} = \rho_0$. The pattern of the flow gives also: $v_{x,I} = v_{x,II} = U_0(y)$. After some calculations, Eq. D.6 and D.9 give the continuity of v'_x, p', ρ' :

$$v'_{x,I} = v'_{x,II}, \quad p'_I = p'_{II}, \quad \rho'_I = \rho'_{II}. \quad (\text{D.10})$$

Eq. D.8 gives the continuity of v'_y :

$$v'_{y,I} = v'_{y,II}, \quad (\text{D.11})$$

and Eq. D.9 is automatically satisfied by those conditions.

D.2 Continuity of the derivatives of the acoustic variables

As there is no discontinuity in the y-direction, the derivatives of the acoustic variables in the y-direction are continuous.

The continuity for the derivative in the x-direction can be demonstrated. Mass conservation, momentum conservation in the x-direction and y-direction, linearized at first order give:

$$\frac{\partial \rho'}{\partial t} + \rho_0 \frac{\partial \rho v'_x}{\partial x} + U_0 \frac{\partial \rho'}{\partial x} + \rho_0 \frac{\partial v'_y}{\partial y} = 0, \quad (\text{D.12})$$

$$\rho_0 \left(\frac{\partial v'_x}{\partial t} + U_0 \frac{\partial v'_x}{\partial x} + v'_y \frac{dU_0}{dy} \right) = - \frac{\partial p'}{\partial x}, \quad (\text{D.13})$$

$$\rho_0 \left(\frac{\partial v'_y}{\partial t} + U_0 \frac{\partial v'_y}{\partial x} \right) = - \frac{\partial p'}{\partial y}. \quad (\text{D.14})$$

Eq. D.14 gives the continuity of the derivative of v'_y :

$$\frac{\partial v'_{yI}}{\partial x} = \frac{\partial v'_{yII}}{\partial x}. \quad (\text{D.15})$$

Eq. D.12 and D.13 give the continuity of the derivative of v'_x and p' :

$$\frac{\partial v'_{yI}}{\partial x} = \frac{\partial v'_{yII}}{\partial x}, \quad \frac{\partial p'_I}{\partial x} = \frac{\partial p'_{II}}{\partial x}. \quad (\text{D.16})$$

Appendix E

Acoustic analysis method

We assume that only plane waves propagate in the pipe. First, cross-spectral density functions $G_{pp_{ref}}$ are used. They are well suited to acoustic analysis, because they eliminate non-propagating noise present in time measurements. Indeed, if we decompose time pressure measurements $p(t)$ into a non-propagating signal $p^{\text{non prop}}(t)$ and a propagating one, we have:

$$p(t) = p^+(t) + p^-(t) + p^{\text{non prop}}(t). \quad (\text{E.1})$$

Having defined and fixed a reference sensor and applying the cross-spectral density functions, we get an expression where the non-propagating pressure is removed because it is not correlated to the propagating pressure:

$$G_{p(t)p_{ref}(t)}(\omega) = G_{p^+(t)p_{ref}(t)}(\omega) + G_{p^-(t)p_{ref}(t)}(\omega). \quad (\text{E.2})$$

Second, we define quantities $G_{pp_{ref}}/\sqrt{G_{p_{ref}p_{ref}}}$ which can be handled like Fourier Transforms, and which are almost independent of the reference pressure. Indeed, if we assume a perfect coherence between the point of observation and the reference sensor, we have

$$\frac{|G_{pp_{ref}}|^2}{G_{pp} G_{p_{ref}p_{ref}}} = 1. \quad (\text{E.3})$$

In this case the quantity $G_{pp_{ref}}/\sqrt{G_{p_{ref}p_{ref}}}$ does not depend on the reference sensor. In practice, the reference sensor is taken closest to the points of observation.

Finally, we calculate plane waves. Considering two consecutive sensors, denoted n and $n+1$, plane waves propagation and the linearity characteristics of the cross-spectral density function give

$$G_{p_{n+1}^+p_{ref}}(\omega) = G_{p_n^+p_{ref}}(\omega) e^{-j\omega\tau}, \quad (\text{E.4})$$

$$G_{p_{n+1}^-p_{ref}}(\omega) = G_{p_n^-p_{ref}}(\omega) e^{+j\omega\tau}, \quad (\text{E.5})$$

with τ being the time of flight of the wave between the two sensors. For the sake of ease, we note p_n for $G_{p_n p_{ref}}/\sqrt{G_{p_{ref} p_{ref}}}$. By means of Eqs. (E.2), (E.4) and (E.5), we get the plane wave spectra:

$$p_n^+(\omega) = \frac{p_n(\omega) e^{+i\omega\tau} + p_{n+1}(\omega)}{2j \sin(\omega\tau)}, \quad (\text{E.6})$$

$$p_n^-(\omega) = \frac{p_n(\omega) e^{-i\omega\tau} + p_{n+1}(\omega)}{-2j \sin(\omega\tau)}, \quad (\text{E.7})$$

for upstream measurements ($1 \leq n \leq 2$) and downstream measurements ($4 \leq n \leq 9$). These spectra are expressed in $\text{Pa}/\sqrt{\text{Hz}}$.

The reflection coefficient is defined as p^-/p^+ downstream of the orifice, and by p^+/p^- upstream, because we assume the source of sound to be located in the region of the orifice. For example, if a zero pressure condition is located far downstream of the orifice, and if T is the time of flight toward this pressure node, the reflection coefficient at this current point is $-e^{-2j\omega T}$.